LITHIUM-ION CELL MODELING, STATE ESTIMATION, AND FAULT DETECTION CONSIDERING STATE OF HEALTH FOR BATTERY MANAGEMENT SYSTEMS

By

GEETIKA VENNAM

Bachelor of Technology in Electrical Engineering
SASTRA University
Thanjavur, India
2014

Master of Science in Electrical Engineering
Oklahoma State University
Stillwater, Oklahoma
2017

Submitted to the Faculty of the
Graduate College of the
Oklahoma State University
in partial fulfillment of
the requirements for
the Degree of
DOCTOR OF PHILOSOPHY
December, 2022

LITHIUM-ION CELL MODELING, STATE ESTIMATION, AND FAULT DETECTION CONSIDERING STATE OF HEALTH FOR BATTERY MANAGEMENT SYSTEMS

Dissertation Approved:

Dr. Avimanyu Sahoo

Dissertation Advisor

Dr. Gary G. Yen

Dr. Hamid Nazaripouya

Dr. He Bai

ACKNOWLEDGMENTS

First and foremost, I would like to express my sincere gratitude to my advisor, Dr. Avimanyu Sahoo, for his continuous support and guidance during my Ph.D. study. I am extremely grateful for his invaluable advice, continuous support, patience, immense knowledge, and plentiful experience that have encouraged me in all the time of my academic research and daily life. Without his tremendous understanding and encouragement over the past few years, it would be impossible for me to complete my study.

Secondly, I would like to thank my Ph.D. committee members: Dr. Gary G. Yen, Dr. Hamid Nazaripouya, and Dr. He Bai, for their kind help and guidance during my Ph.D. study at OSU.

Finally, I would like to thank my mother, husband, grandparents, uncle, friends, and other family members for their immense patience and support during my Ph.D. time. Without their constant help and support, this journey to Ph.D. would not be possible.

Acknowledgments reflect the views of the author and are not endorsed by committee members or Oklahoma State University.

Name: GEETIKA VENNAM

Date of Degree: DECEMBER, 2022

Title of Study: LITHIUM-ION CELL MODELING, STATE ESTIMATION, AND FAULT DETECTION CONSIDERING STATE OF HEALTH FOR BATTERY MANAGEMENT SYSTEMS

Major Field: ELECTRICAL ENGINEERING

Abstract: Lithium-ion batteries (LIBs) with high energy density and longer cycle life enable a comparable driving range per charge for electric vehicles (EVs) with their gas counterparts. However, the LIBs are very sensitive to variations in operating conditions, such as overcharge/discharge, high/low temperatures, and mechanical abuse. A battery management system (BMS) is employed to orchestrate safe and reliable operation by monitoring the voltage, current, temperature, state of charge (SOC), and state of health (SOH) and optimizing the charging and discharging cycles. The SOC and SOH, which determine the performance of the LIB, are governed by several stress-inducing factors, such as operating temperature, C-rate, aging, and internal faults. So, it is important to estimate the SOC and SOH in real time, considering the factors affecting the degradation of the battery. On the other hand, an internal fault in LIB leads to thermal runaway. Early detection and diagnosis of these faults are necessary to avoid catastrophic failures of LIBs.

In this dissertation, we developed health-inclusive dynamic models for simultaneous state and parameter estimations and fault detection (FD) schemes. First, we proposed a nonlinear parameter-varying equivalent circuit model (ECM) integrated with the parameter dynamics for simultaneous state and parameter estimation using nonlinear observer-based approaches. Second, the proposed model is extended to integrate the SOH and thermal behavior with ECM. The SOH-coupled nonlinear electric-thermal-aging model comprehends the interplay between the SOC and SOH and couples the ECM dynamics with capacity fade. The proposed model is further extended by integrating the ohmic resistance dynamics for simultaneous SOC, SOH, and parameter estimation using filtering algorithms. Finally, two FD schemes, based on the SOC-based and SOH-coupled models, are proposed to detect internal (thermal and side-reaction) faults by tracking the temperature and parameter residuals of the battery. Adaptive thresholds are designed to account for modeling uncertainties and the effect of degradation in the residuals and avoid false positives. In addition, a novel neural network-based observer is proposed to learn the fault dynamics and estimate the SOC, SOH, and core temperature under internal faults. Experimental and numerical validation results are presented to corroborate the designs.

TABLE OF CONTENTS

Chapter Page

LIST OF TABLES

LIST OF FIGURES

CHAPTER I

INTRODUCTION

Lithium-ion batteries (LIBs) were conceived in 1980 by Mizushima, Jones, Wiseman, and Goodenough [5]. Today, LIBs are one of the most popular energy-storing devices constituting approximately one-third of all batteries [6]. LIBs have been at the forefront of applications advancing into the field of electric vehicles (EVs). High energy density, low self-discharge rate, and longer life [5] of LIBs made it the common choice for powering both high- and low-power equipment. For instance, the recent plug-in EVs [7], with the LIB as the primary power source, successfully bridge the gap between the average EV range and their gas-powered counterparts. The new EV variants can also provide a range of 300 miles per charge. On the other hand, the EV community is also working relentlessly to reduce charging time to a level close to gas-powered vehicles' fueling time. With the introduction of high-power superchargers (450 kW) [8], the current charging time is reduced to 15 minutes to reach 80% of the state of the charge (SOC) level. These advancements in LIB and EVs are alleviating the user's *range anxiety* and paving the way for their ubiquitous acceptance.

However, stress-inducing factors, such as high charging current and low/high operating temperature, aggravate the battery's degradation (capacity loss). So, there is a necessity for an efficient and improved battery design along with furnishing tools to control such complex systems. In addition, it is well known that the volatility of internal constituents, flammability, reactivity, and toxicity of the electrolyte, which is the flip side of the high energy density LIBs, make them thermally unstable at high temperatures and reduces life when operating at low temperatures [9]. The low tolerance to abuse (over-charging/discharging) and vulnerability to thermal runway jeopardize user safety, which is a primary concern. A battery management system (BMS) is employed for a LIB's safe operation, power, and energy management. The state-of-the-art BMSs are augmented with advanced SOC and state of health (SOH) estimation tools along with other traditional functions, such as voltage, current, temperature monitoring, and cell balancing. A standard architecture of BMS with various SOC and SOH estimation functionality is shown in Figure 1. The list of all abbreviations used throughout the dissertation is presented in Table 1.

1.1 Modeling of LIB

A dynamical model of LIB is necessary to monitor the battery behavior and estimate the states, such as SOC and SOH, and efficient power and energy management. The classical battery models include, electrochemical model [10], mathematical/analytical model [11], and equivalent circuit model (ECM) [12].

An electrochemical model, by its name, deals with material microstructure, physio-

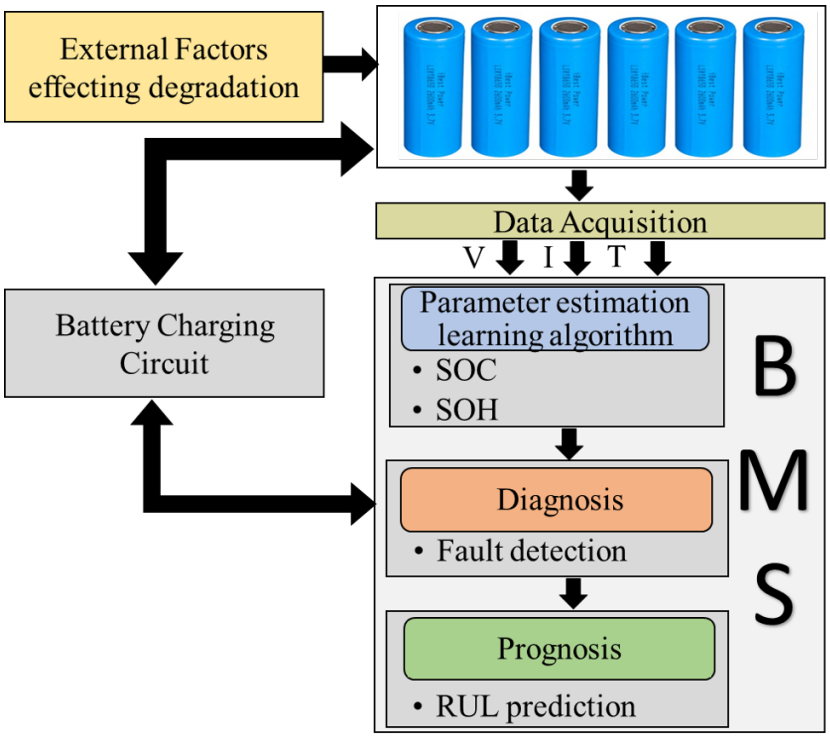

Figure 1: The architecture of the BMS with SOC and SOH estimation, fault diagnosis and prognosis.

Table 1: List of all abbreviations.

ANN	Artificial neural network	ICL	Irreversible capacity loss
BMS	Battery management system	KF	Kalman filter
CEI	Cathode electrolyte interface	LIB	Lithium-ion battery
CFD	Capacity fade deviation percentage	LLI	Loss of lithium inventory
DNN	Deep neural network	ML	Machine learning
DOD	Depth of discharge	NLO	Nonlinear observer
DVA	Differential voltage analysis	OCV	Open circuit voltage
ECM	Equivalent circuit model	PF	Particle filter
EIS	Electrochemical impedance spectroscopy	PDF	Probability density function
EKF	Extended Kalman filter	P2D	Pseudo 2D
ETA	Electro-thermal-aging	RLS	Recursive least square
EVs	Electric vehicles	RUL	Remaining useful lifetime
FL	Fuzzy logic	SEI	Solid electrolyte interface
FD	Fault detection	SOC	State of charge
GPR	Gaussian process regression	SOH	State of health
GRA	Grey relational analysis	SP	Single particle
HI	Health indicator	SVM	Support vector machine
ICA	Incremental capacity analysis	UPF	Unscented particle filter

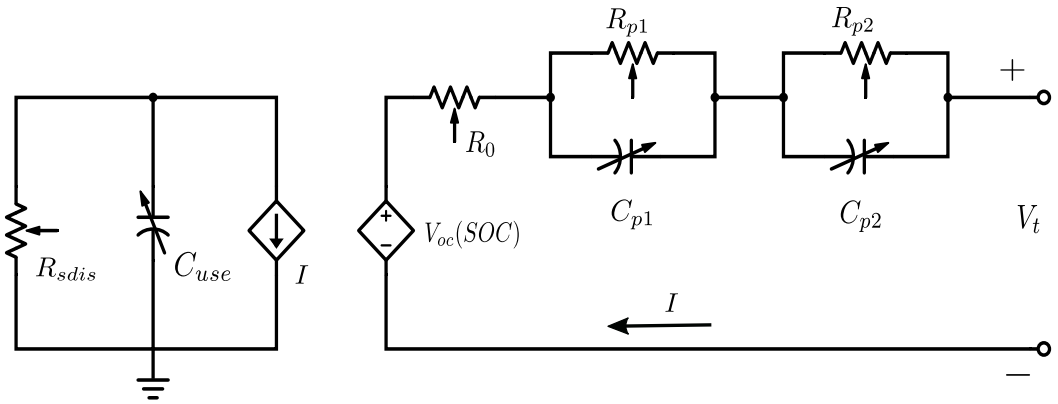

Figure 2: The 2-RC ECM of LIB [2].

chemical process, and mathematical expressions concerning the electrochemical process inside the battery. These models are derived from porous electrodes and concentrated solution theories. The chemical reactions give in-depth knowledge to the researcher to analyze the battery's performance and have greater potential in capturing battery dynamics. However, these models suffer from computational complexity due to involving large time-varying spatial partial differential equations [13]. On the other hand, analytical models use simple mathematical or stochastic functions to reproduce external behavior without exploiting the real physical principles of the underlying system. Therefore, the mathematical models cannot provide accurate voltage measurements with drive cycle input currents [14]. On the other hand, ECMs are less complex, easy to implement and provide a fair accuracy compared to analytical and electrochemical models. Therefore, based on the application requirement, the most widely used battery models are ECM [2] and single particle (SP) electrochemical model [15], which is a simplified version of the electro-chemical model. The readers are suggested to refer [16, 17] and the references therein for more details on battery modeling.

In this dissertation, we focus on ECM due to its computation efficiency and ease of implementation in BMS. There are different types of lumped parameter ECMs proposed in the literature. These models include internal resistance (rint), hysteresis, Randle, 1-RC, and 2-RC models and their combinations. A detailed description of each model is given in [18]. The RC models can be further categorized as impedance- [19], run-time- [20], and Thevenin-based [21] models. A detailed description of these models is given in [2] and the references therein. The circuit components of the above-said models are extracted from the measured voltage responses for different charging and discharging cycles [22].

Among all ECMs, the 2-RC model is more accurate and has been shown to capture all the terminal characteristics and nonlinear dynamics of the battery [18]. A detailed discussion on modeling of LIB (2-RC) by describing each component of ECM taking into account all the chemical reactions occurring inside a LIB, can be found in [23]. The 2-RC ECM of a LIB [2], obtained by combining Thevenin and run-time-based models, is shown in Figure 2. In general, the ECM parameters, i.e., $R_0, R_{p1}, C_{p1}, R_{p2}$ and C_{p2} are linked to physics-based electrochemical model parameters of the LIB [24] as detailed below.

- R_0 represents the total ohmic resistance in the cell. It accounts for the electrical conductivity of the electrodes, electrolyte, separator, and surface film layer resistance

on the electrode due to the solid electrolyte interface (SEI).

- R_{p1} and C_{p1} represent the short time constant in voltage response. They account for the charge transfer resistance and the capacitance between the electrolyte and electrode, respectively.
- R_{p2} and C_{p2} represent the long time constant in voltage response. They account for the Warburg impedance, i.e., the diffusion of the lithium ions between the active material and electrolyte.
- $V_{oc}(SOC)$ is an ideal voltage source, which varies with SOC.
- R_{sdis} represents the self-discharging resistance of LIB.
- C_{use} represents the usable capacity, which is the extracted energy from the battery.
- V_t represents the terminal voltage of the battery.

The left part of the 2-RC electric circuit in Figure2 is the energy balance circuit, representing the battery lifetime. The right part of the circuit is the voltage response circuit, which serves as the transient and steady-state response of the battery. The 2-RC model is widely used in literature to estimate the SOC using various estimation schemes, such as coulomb counting (CC) [25], extended Kalman filter (EKF) [24], linear and nonlinear observers (NLO) [26], and artificial neural networks (ANN) [27]. Although most of these approaches can estimate the SOC effectively, the inherent assumption of time invariance of ECM parameters may lead to an erroneous SOC. In practice, the battery parameters vary non-linearly [28] with SOC and temperature both during charge and discharge cycles. In addition, the internal parameters of the cell also change with the changes in SOH. Several variables, such as C_{rate}, aging, and electrochemical side reactions inside the cell accelerate the degradation [29]. Therefore, the recent LIB models focus on integrating time-varying parameters and the battery's health to capture the dynamics of the cell over its lifetime and improve the accuracy of SOC and SOH estimation, presented next.

1.2 Overview of SOC and SOH Estimation Methods

SOC is the ratio of the remaining capacity to the fully charged capacity of the battery. The SOC estimation in LIBs dates back to the early 1980s. An accurate SOC estimation is the most crucial part of the BMS design in EVs. This not only provides information on the useful energy but also prevents the battery from overcharging/discharging. Therefore, the SOC estimation has attracted considerable interest, and ample reviews on SOC estimation schemes are available in the literature [30, 31]. The classifications of different SOC estimation methods are shown in Figure 3. The direct measurement method estimates the SOC using the physical properties. Bookkeeping estimation methods (CC [25]) use the battery charge and discharge current as input. In model-based methods (EKF [24], linear and NLOs [26, 32]), the battery parameters and SOC are estimated using adaptive filters and observers. The intelligent methods (ANN [27]) are based on the statistical relations between the input and output data and require higher computation time and storage space.

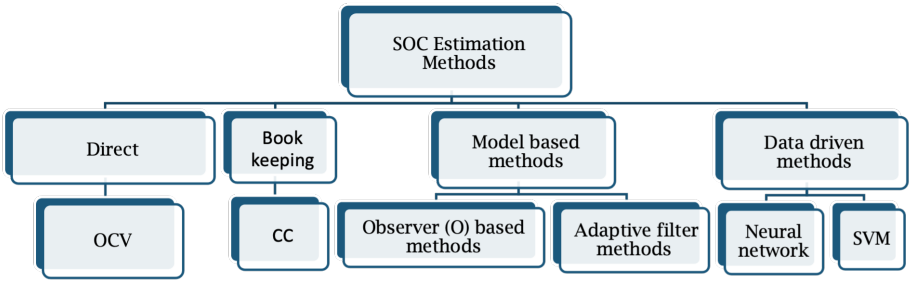

Figure 3: SOC estimation methods.

On the other hand, SOH is a figure of merit of a battery cell/pack's present condition compared to its ideal conditions. SOH linearly refers to capacity loss and power loss (the internal resistance increment), which quantifies the aging phenomena of LIB. SOH estimation is challenging and might not always be accurate due to the dependency on the time-varying internal degradation mechanisms. These inter-related degradation mechanisms include SEI layer formations [4], metal dissolution, loss of contact between the active materials and current collector or carbon network (both cathode and anode), lithium (Li) metal plating, dendrite formations, and mechanical degradation of the electrodes (particle cracking). Although there are several results available on modeling and analysis of internal degradation mechanisms (refer to Section II) and their interplay, they are not yet fully understood and is an active research area.

Primarily there are three SOH estimation methods, i.e., 1) experimental; 2) model-based; and 3) data-driven, proposed in the literature [33, 34, 35]. Figure 4 summarizes all the SOH estimation schemes available in the literature for the above three categories. Experimental methods constitute direct/indirect measurement-based approaches (EIS, open circuit voltage (OCV), incremental capacity analysis (ICA), differential voltage (DVA)) and book-keeping method (CC). The SOH is estimated by correlating the physical measurements and properties of the battery. The large test/measurement time precludes the real-time implementation of the experimental methods in BMS. Model-based methods overcome these limitations and improve the accuracy of SOH estimation by considering the effects of both internal and external aging factors. However, obtaining an accurate model is often challenging. Therefore, data-driven methods, such as analytical and machine learning, were proposed, which use a large amount of experimental data to learn the black-box model of the battery to estimate and predict SOH.

Surveys on empirical, model-based (recursive least square (RLS), Kalman filter (KF)), direct measurement (static measurement, electrochemical impedance spectroscopy (EIS)), and filter-based methods (EKF, particle filter (PF)) are available in the literature for a long time [33, 34, 35, 36, 37, 38, 39]. Likewise, intelligent SOH estimation methods using neural networks (NN), support vector machine (SVM), genetic algorithm (GA) along with model-based methods (RLS, EKF) are reviewed in [40, 41]. For real-time applications, online SOH estimation methods utilizing NN, fuzzy logic (FL), and deep NN (DNN) [42] in combination with degradation mechanisms were discussed in [37]. Similar reviews addressing different SOH estimation methods focusing on battery chemistry, data processing mode, processing time, algorithm, characteristics, accuracy, strength, and weakness are also presented in [38,

39]. Recently, data-driven SOH estimation techniques using "big data" analytics, which has gained attention for their application in EVs with high accuracy, are reviewed in [35, 43]. For more details on SOH-estimation methods, refer to Section II. In addition to the SOC and SOH estimation, the detection of internal faults is another important function of the BMS for safe operation and longevity of the battery, and an overview is presented next.

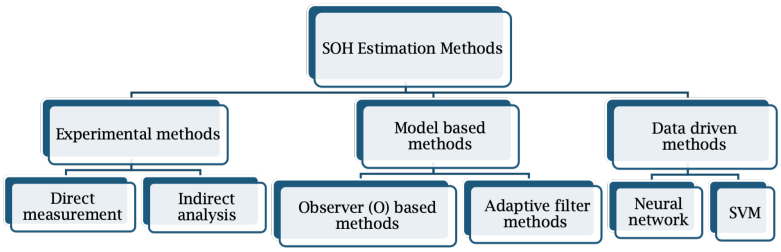

Figure 4: SOH estimation methods.

1.3 Fault Diagnostics and Prognostics of LIBs

Lithium-ion cells are more complex due to their compact size and internal electrochemical reactions. The complex manufacturing process, leading to miniature defects and side reactions inside the cell, may result in internal faults [44]. These faults usher their way, causing high internal pressure and temperature, which may lead to ignition and explosion (thermal runaway). To ensure safety and reliability and avoid catastrophic failures in LIB, BMS must have the capability of diagnosing these internal failures in addition to external faults. Although external faults can be detected from sensor measurement, the placement of sensors for measuring internal changes and detecting internal faults in a LIB is cost and space prohibitive. Therefore, internal fault detection (FD) schemes must rely on advanced noninvasive algorithms.

The BMS is equipped with algorithms to detect external faults, such as voltage drift, overcharge current, and high-temperature [26]. Several model-based FD schemes [45, 46, 47, 48, 49, 50, 51] are proposed in the literature to detect external faults, which use output error as a residual to detect a fault in the system. A fault is detected when this residual exceeds the threshold value. Although these FD schemes [45, 46, 47, 48, 49, 50, 51] could detect and isolate various external faults (sensor and actuator, overcharge/discharge fault, electrochemical) in LIB, these approaches do not address internal and thermal faults especially internal thermal resistance fault which is reflected in core temperature dynamics. Therefore, these FD schemes may not be able to detect and isolate faults. There are several model-based FD schemes presented in the literature [52, 53, 54, 55] to address thermal faults in LIBs. However, the model-based FD scheme [55] requires a physics of failure mechanism to estimate the core temperature and detect thermal faults in the battery. In addition, the model-based FD approaches [52, 53, 54, 55] do not estimate the SOC and SOH during faults. Estimating SOC and SOH during faults eases the user's range anxiety and predicts the health degradation of the battery, which is still an open problem, along with detecting internal side reaction faults, i.e., faults due to internal degradation phenomenon (such as dendrite growth, SEI layer formation, lithium plating [29]).

In the model-based approaches, the ECM parameters are considered to be constant. A constant parameter ECM may lead to false positives due to the incapability of differentiating between the parameter change and fault. Additionally, the internal degradation phenomenon (dendrite growth, SEI layer formation, lithium plating [29]) and external factors such as C_{rate}, temperature, depth of discharge (DOD) affect the battery ECM parameters (especially R_0). Therefore, the ECM parameters variation must be coupled with SOH, i.e., the use of the battery's electro-thermal-aging (ETA) dynamics for FD, which is still an open problem. On the other hand, the model-based approach also uses a constant threshold for FD. Since the LIB parameters vary as the SOH changes, a constant threshold approach may not differentiate between the degradation and faults from the residuals. Further, modeling uncertainties can trigger false positives under constant threshold [56]. A constant threshold also fails to detect faults of smaller magnitude (incipient stage) in normal operating conditions [56]. Therefore, the threshold for model-based FD must be adaptive to accommodate the internal parameter variation due to aging and modeling uncertainty for FD.

1.4 Organisation of the Dissertation

Motivated by the limitations of the available LIB models, SOC, SOH and parameter estimation, and FD, in this dissertation, we have proposed SOH-coupled nonlinear parameter varying models and associated observer/filtering schemes for state and parameter estimation and FD. They are organized as individual chapters in the dissertation.

The dissertation consists of five chapters, and each chapter portrays a sequential development of the research work as outlined in Figure 5. Chapter II presents an in-depth review of internal and external degradation mechanisms at both the anode and cathode and the SOH estimation of LIB. Chapter III, Section 3.2 discusses the details of developing a SOC-dependent ECM, where parameters are considered to be varying with the SOC of the battery. The SOC-dependent model is extended in Section 3.3, where SOC and SOH dynamics are coupled to develop a SOH-coupled ETA model. This makes the SOH-coupled model states and parameters vary with the SOH of the battery. Experimental studies are shown in Section 3.3 to validate the SOH-coupled models. Chapter IV details the FD scheme based on both the SOC-dependent and SOH-coupled ETA to detect internal faults in LIBs. The FD scheme using the SOH-coupled model is detailed in Section 4.3 and 4.4 to estimate faulty states and detect thermal and side reaction faults in LIBs. Adaptive threshold design is also presented in Section 4.3 and 4.4 to facilitate FD in the presence of parameter changes due to degradation, modeling uncertainties, and exogenous input disturbances. Finally, the conclusions are drawn, and future works are described in chapter V.

1.5 Contribution of the Dissertation

The overall contributions can be summarized as follows

- An in-depth review of the SOH estimation methods that incorporate studies on different internal and external aging mechanisms, discussed in Section 2.2 and 2.3, respectively, and the recently developed machine learning-based approaches to estimate SOH (Section 2.4).

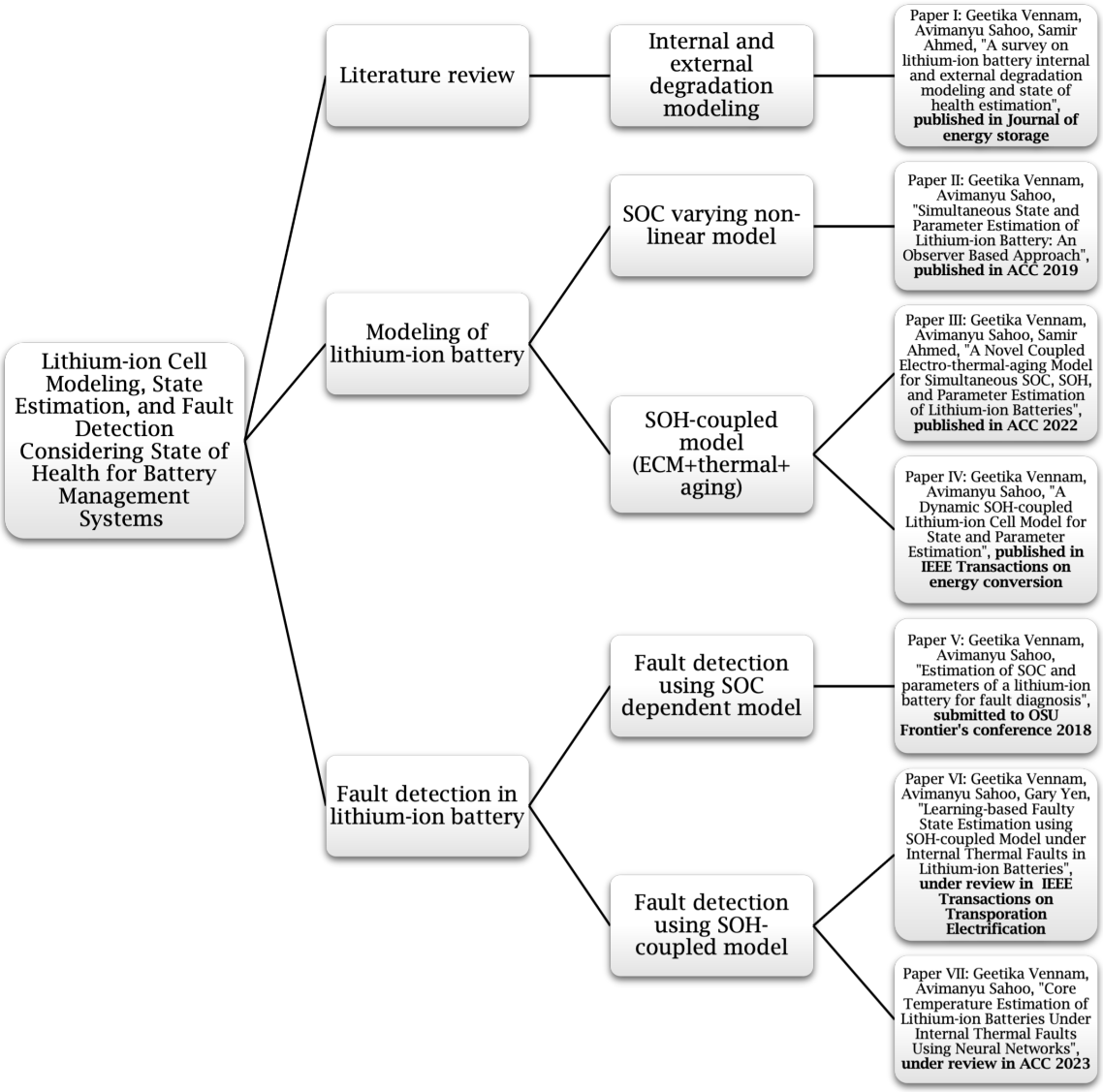

Figure 5: Organisation of the dissertation.

- Development of nonlinear SOC-based parameter varying model, which is used for simultaneous estimation of the SOC and internal battery parameters for both charge and discharge cycles.
- Development of a SOH-coupled ETA model with coupled SOC-SOH dynamics is used for simultaneous estimation of SOC, SOH, and parameters of the LIB.
- Development of the model-based FD scheme based on the SOC-dependent model to detect internal (side-reaction) faults in LIBs.
- Development of the NN-based fault learning scheme based on the SOH-coupled model to estimate the faulty core temperature and detect the thermal faults in LIB.
- Development of a learning-based FD scheme based on a SOH-coupled model to estimate

the faulty states (SOC, SOH, core temperature) and detect thermal and side reaction faults in LIB.

- Design adaptive threshold generator to differentiate between the degradation and faults from the residuals and account for the modeling uncertainties and exogenous input disturbances in no-fault conditions in the FD scheme.

The next chapter presents a detailed literature review on LIB internal and external degradation modeling and SOH estimation.

CHAPTER II

A REVIEW OF LITERATURE ON LITHIUM-ION BATTERY INTERNAL AND EXTERNAL DEGRADATION MODELING AND STATE OF HEALTH ESTIMATION

BMS is an integral part of the LIB for safe operation and power management. The advanced BMSs also provide SOC and SOH information. Accurate estimation of the SOC and SOH from a sparse set of input and output measurements (voltage, current, and surface temperature) is challenging due to the internal inter-related complex electrochemical side reactions. Several factors, such as charge rate, operating temperature, internal aging, abnormal charging-discharging cycles, and internal faults, adversely affect the LIB's health. To aid the development of intelligent and robust BMS with the capability of health-conscious decision-making, a deep understanding of the internal degradation mechanisms and the effect of external degradation-inducing factors are of primary importance. This chapter presents an in-depth review of internal and external degradation mechanisms at both anode and cathode of LIB with their corresponding mathematical models and correlation with SOH metrics (capacity and power fade). Different electrochemical models integrated with the internal degradation mechanisms and their governing equations are discussed and summarized. The effects of the external aging factors on capacity and power fade and the dominant degradation mechanism under cycling and stored conditions are also reviewed and tabulated for quick reference. Recent developments in BMSs capability for SOH estimation using advanced and intelligent algorithms under various internal degradation conditions are also presented. Finally, the challenges in modeling, estimation of SOH, and several future research directions for developing self-learning and smart BMS are provided.

2.1 Introduction

There are several SOH estimation methods presented in literature [33, 34, 35, 36, 38, 39]. The focus of all the above review papers is on the SOH estimation process only without incorporating discussions on the internal degradation mechanisms. Since the SOH metrics (capacity and power fade) are orchestrated by both the internal and external degradation-inducing factors and the mechanisms, a review that can explicitly discuss the correlations will be of paramount importance to the LIB research community. Although a few of the recent reviews [35, 36] provided insights into internal aging mechanisms, such as loss of active material (LAM), SEI layer formation, and loss of Li inventory (LLI), these reviews did not discuss the modeling approaches for internal degradation mechanisms at anode and cathode, which can be integrated with traditional model-based schemes to quantify SOH more accurately. Furthermore, reviews on recently developed advanced SOH estimation

methods tethered with internal and external degradation are not available.

Motivated by the lack of a comprehensive review of LIB's degradation and its correlation with the SOH metrics and estimation, we present an in-depth review of the internal degradation mechanisms along with their mathematical models. We also review the advanced/emerging SOH estimation methods considering both the internal and external aging effects to identify the trend and research gap which hinders the development of intelligent BMS with health-conscious decision-making capability. To the authors' best knowledge, this is the first time such a review encompassing internal degradation and health estimation is presented.

Contributions: The key contributions of this chapter are the review of 1) modeling studies on internal degradation mechanisms at both anode and cathode and their relation to SOH metrics, 2) different electrochemical models integrated with the internal degradation mechanisms, along with their governing equations, for commercially available graphite and metal anodes, 3) the individual and combined contributions of external aging factors to capacity and power fade along with the dominant degradation mechanism under cycling and stored conditions, 4) advanced SOH estimation methods accounting for the influence of both internal and external aging factors, and 5) empirical models of capacity and power fade for calendar and cycle life aging with different cathode chemistry. Finally, we provide recommendations and future directions for intelligent BMS development with self-learning capabilities.

The chapter is organized as follows. The internal degradation mechanisms and their modeling are discussed in Section 2.2. The external factors affecting the degradation of LIB are discussed in Section 2.3. Section 2.4 deals with advanced SOH estimation methods. Finally, the review concludes in Section 2.6 with some recommendations and future direction in Section 2.5. The list of all nomenclature used throughout the dissertation is presented in Table 2.

Table 2: List of all nomenclature.

A	Cross sectional area (m^2)	R_g	Universal gas constant ($\mathrm{J\,K^{-1}\,mol^{-1}}$)
Ah	Ampere-hour throughput	R_j	Radius of the particle (m)
$c_{\bar{k}}$	Concentration of species $\bar{k}$ ($\mathrm{mol\,m^{-3}}$)	R_l	Rate of homogeneous reaction ($\mathrm{mol\,cm^{-2}\,s^{-1}}$)
C_{loss}	Capacity loss	$R_{0_{inc}}$	Increase in internal resistance of the battery
c_0	Li^+ bulk concentration ($\mathrm{mol\,m^{-3}}$)	$s_{\bar{k}l}$	Stoichiometric coefficient for species in reaction l
C_{rate}	Charge/discharge rate of the battery	T	Temperature (K)
C_{rated}	Nominal/rated capacity of the battery (A h)	T_a	Ambient temperature (K)
$c^-_{1,j}$	Surface concentration of the sphere ($\mathrm{mol\,m^{-3}}$)	T_c	Core temperature (K)
c_+	Normalized concentration of Li-ions ($\mathrm{mol\,m^{-3}}$)	t_+	Transference number
D_{eff}	Effective diffusivity ($\mathrm{m^2\,s^{-1}}$)	V	Molar volume of Li ($\mathrm{m^3\,mol^{-1}}$)
$D_{\bar{k}}$	Solvent diffusivity in SEI phase ($\mathrm{m^2\,s^{-1}}$)	V_{oc}	Open circuit voltage potential (V)
D^0_s	Arrhenius diffusion constant	V_t	Terminal voltage of the battery (V)
E_a	Activation energy ($\mathrm{J\,mol^{-1}}$)	y_{tip}	Dendrite tip position (m)
F	Faraday's constant ($\mathrm{C\,mol^{-1}}$)	z	Coordinate direction normal to the anode (m)
I	Charge or discharge current (A)	α_c	Cathodic transfer coefficient
i_{Lf}	Flat limiting current density ($\mathrm{A\,m^{-2}}$)	ρ_e	SEIs electronic resistivity ($\Omega\,\mathrm{m}$)
i_n	Current density normal to dendrite tip ($\mathrm{A\,m^{-2}}$)	ΔSOC	SOC variation
L	Thickness/growth of SEI layer (m)	ξ	Electric permittivity of the film ($\mathrm{C\,V^{-1}\,m^{-1}}$)
n	Number of moles of electrons	Φ, ϵ	Phase filed variables, values ranging $0-1$
$N_{\bar{k}}$	Molar flux of the species ($\mathrm{mol\,cm^{-2}\,s^{-1}}$)		

2.2 Internal Degradation Mechanisms and their Modeling

The LIB is composed of four components, namely cathode, anode, electrolyte, and separator and its performance are dependent on various properties of its components. The characteristics of different LIB materials along with their applications are given in Table. 3. The health degradation is caused by different mechanical, thermal, and chemical processes occurring inside the battery. Modeling and controlling these processes is complicated and involved, yet is very useful for accurate and efficient SOH estimation. The modeling of the internal degradation mechanisms includes modeling different internal chemical reactions contributing to changes in SOH indicators. Figure 6, adopted from [3], depicts various internal degradation mechanisms for LIB including anode (SEI-layer formation, electrode fracture, Li plating, dendrite formation) and cathode degradation. In this section, we have discussed various anode and cathode degradation mechanisms and their corresponding mathematical models.

Table 3: Lithium-ion battery's material characteristics and applications.

LIB's name	**Electrodes**	**Key benefits**	**Limitations**	**Applications**
Lithium Cobalt Oxide (LCO)	$LiCoO_2$/gr[1]	High specific energy	Low inherent safety; due to the low thermal stability of cobalt-oxide, cycle life is relatively modest, and high cost.	Sony
Lithium iron phosphate (LFP)	$LiFePo_4$/gr[1]	Durability, good thermal stability, inherent safety and reliance on abundant eco-friendly materials, low cost	Sensitive to temperature variation, and low specific energy in the range of 90-140Wh/Kg	BYD
Lithium manganese spinel (LMO)	$LiMn_2O_4$/gr[1]	Low internal resistance yields in a relatively high specific power, LMO batteries have a longer cycle life than LCO, typically in the range of 1000–1500 cycles, inherently safe	Lower energy density, in the range of 100–140 Wh/kg	Nissan
Lithium nickel cobalt aluminum oxide (NCA)	Li[2]/gr[1]	Outstanding specific energy in the range of 200–250 Wh/kg as well as high specific power	Marginally safe, and high cost.	Tesla, Daimler
Lithium nickel, manganese cobalt oxide (NMC)	Li[3]/gr[1]	High specific energy	Compared to NCA, the NMC battery has a lower energy density typically in the range of 140–200 Wh/kg, and high cost	Toyota, Volkswagen, General Motors
Lithium titanate (LTO)	(LMO,NCA)/Li[4]	Highly safe, long life cycle span	Low specific energy in the range of 30–110 Wh/kg	Honda, Samsung, Toshiba

gr[1]-graphite,Li[2]-$Li(Ni_085CO_0,1Al_005)0_2$, Li[3]-$Li(Ni_0,33Mn_0,33Co_033)O_2$, Li[4]=$Li_4Ti_5O_{12}$.

2.2.1 Anode Degradation

Solid electrolyte interface (SEI) layer formation

The SEI layer formation at the electrode-electrolyte interface was first introduced in 1979 [57]. The solvents (intercalated Li) and Li-salt (electrolyte) forms a passivating layer (products of decomposed electrolyte) at the active electrode surface and grows in width substantially with consecutive charge and discharge cycles. This layer allows Lithium-ion transportation across the electrode and electrolyte and restricts electron tunneling, preventing continuous electrolyte decomposition. The SEI layer also protects against anode corrosion and maintains

the battery's chemical and electrochemical stability by prohibiting further electrolyte reduction during cycling. Despite the above advantages of the SEI layer, active Li and electrolyte materials are consumed during layer formation, and the internal resistance also increases, which are the orchestrating factors for capacity fade and low power density, respectively.

The SEI layer is formed during the first charge-discharge cycles of the battery on the anode (carbon electrodes), as shown in Figure 6.

It is one of the main aging factors of a graphite electrode (the most common choice of the anode) [58]. The reduction reactions and considerable volume expansion of the anode materials cause the SEI to be more unstable than on the cathode [59]. Over the years, extensive studies on anode SEI films have been reported in the literature.

The SEIs complicated structure, due to the electrolyte reduction reactions near the electrode surface, and the structural–property relationships play an essential role in modeling the SEI layer. These factors make the modeling process complex, leading to trial-and-error-based approaches [60]. In [57], a first attempt is made to model the SEI. The electron leakage through the SEI layer is considered a constraint for SEI growth. A growth rate SEI layer model is given by [57] ,

$$\frac{dL}{dt_{storage}} = \frac{\bar{K} V_{oc}}{\rho_e L} \tag{2.2.1}$$

where L is the thickness/growth of the SEI layer, $t_{storage}$ is storage time, $\bar{K}$ is constant, V_{oc} is open circuit potential, and ρ_e is the SEIs electronic resistivity. Since SEI is formed during the first charge-discharge cycle of the battery, it is also necessary to consider model equations that describe Li's mass transport in solid phases. The diffusion of Li-ions in an active solid particle is, in general, expressed using Fick's law [61], given by

$$\frac{\partial c_{\bar{k}}}{\partial t} = D_{\bar{k}} \left(\frac{\partial^2 c_{\bar{k}}}{\partial z^2} + \frac{2}{z} \frac{\partial c_{\bar{k}}}{\partial z} \right) \tag{2.2.2}$$

where $c_{\bar{k}}$ is the concentration of species $\bar{k}$, $D_{\bar{k}}$ is the solvent diffusivity in the SEI phase, z is the coordinate direction normal to the anode, and t is the time variable. A one-dimensional solvent diffusion model through the SEI layer is adopted in [62]. Film growth rate, resistance, and irreversible capacity loss (ICL) are estimated using a simplified dilute solution theory by considering the transport of both Li+ ions and electrons through the SEI. The material balance equation in [61] is modified in [62] to account for variable film thickness ($L(t)$), as follows,

$$\frac{\partial c_{\bar{k}}}{\partial t} - \frac{\partial L}{\partial t} \frac{\partial c_{\bar{k}}}{\partial \xi} \frac{\xi}{L(t)} + \frac{1}{L(t)} \frac{\partial N_{\bar{k}}}{\partial \xi} + \sum_l s_{\bar{k}l} R_l = 0 \tag{2.2.3}$$

where $\frac{\partial L}{\partial t}$ is the film growth rate, $N_{\bar{k}}$ is the molar flux, R_l is the rate of homogeneous reaction in the film, $s_{\bar{k}l}$ is the stoichiometric coefficient for species in reaction l, and ξ is the electric permittivity of the film. If the film growth rate $\frac{\partial L}{\partial t}$ is slow, the second term in (2.2.3) can be neglected, and (2.2.2) is recovered to describe the transport of solution species limited to solid diffusion [61]. A similar one-dimensional model, which considers both solvent diffusion and kinetics of SEI formations [63], is developed in [64].

All the above models, focusing on the SEI layer formation process, lack in predicting the cycling behavior of LIB at different operating conditions along with the associated SEI

growth processes. A multi-physical pseudo 2D (P2D) [63, 65, 66, 67, 68] SEI layer model, focusing on bridging the transport processes (charge balance, mass balance, energy balance) with elementary reaction-based SEI growth, is developed in [63]. Here, the diffusion rate-determining passive film thickness is given as,

$$L(t) = 2\lambda\sqrt{D_s^0 e^{\frac{-E_a}{R_g T}} t} \tag{2.2.4}$$

where D_s^0 is Arrhenius diffusion constant, E_a is the activation energy, R_g is the universal gas constant, T is the temperature, and $\lambda = \frac{c_+ e^{-\lambda^2}}{\sqrt{\pi} C_{Li_2C0_3} erf(\lambda)}$. Unlike the 1-D model, the concentration of Li [69] inside the solid phase is solved at each node point (j) along the radial coordinate, which is given by [69]

$$\frac{\partial c_{\bar{k},j}}{\partial t} = \frac{D_{\bar{k},j}}{z^2} \frac{\partial}{\partial_z} (z^2 \frac{\partial c_{\bar{k},j}}{\partial z}). \tag{2.2.5}$$

A similar P2D model coupled with the 1D porous electrode model is developed in [65]. The proposed multiscale and multi-physics model reveals the effects of diffusivity, temperature, and kinetics on SEI growth.

The major limitation of the P2D model is the coupled nonlinear partial differential equations and high computational complexity. To overcome this limitation, an SP model [70] was introduced. Electrodes are represented by a single spherical particle whose surface area is equivalent to the solid phase's active area in the porous electrode. This model considers a lumped parameter approach and reduces (2.2.5) to a first-order partial differential equation [70] given by

$$\frac{\partial c_{\bar{k},j}}{\partial t} + \frac{15 D_{\bar{k},j}}{R_j^2} (c_{\bar{k},j} - c_{1,j}^-) = 0, \tag{2.2.6}$$

where $c_{1,j}^-$ is the surface concentration of the sphere, and R_j is the average radius of the particles that constitute the electrode. Eq. (2.2.6) also eliminates the dependence on the spatial variable z. In [71], the SP electrochemical model coupled with thermal dynamics is developed to include temperature in SEI layer modeling. This coupled model can be used to provide insight into controlling the major technological hurdles of current interest, i.e., capacity loss under low temperatures, much-reduced performance at subzero temperatures, and thermal runaway at high temperatures. Moreover, from the properties and functionalities, the SEI growth rate is also determined by modeling the electron tunneling and presented in [65].

Dual-layer SEI emerges from different electrolyte decomposition reactions. The studies on dual-layer SEIs are obtained by adding a second SEI formation reaction. The two layers of SEI differ in chemistry and morphology and grow simultaneously. Analysis of each SEI layer provides us with information on fluctuations in SEI thickness and the relation to the rate-limiting transport mechanism in the solid SEI phase. Opposed to single-layer SEIs, dual-layer SEI formations consider two transport mechanisms, i.e., solvent diffusion and charge transport. Studies revealing the behavior of such dual layer structures are discussed in [72, 73, 74]. In [74], a double layer at the SEI-electrolyte and the particle-SEI interface are included in a model-based study of the aging-dependent processes. The physicochemical SP model in [71] has been extended by introducing a new aging model, which includes the SEI,

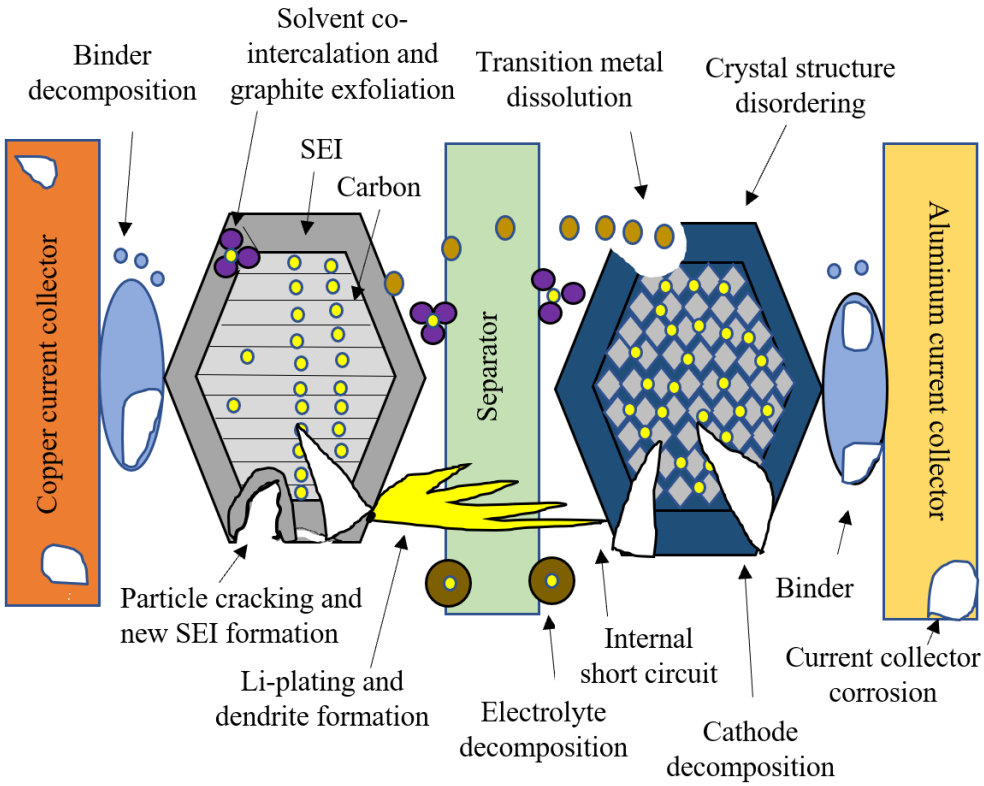

Figure 6: Internal degradation mechanisms in Lithium-ion cells adopted from [3].

to analyze the degradation of the LIB. The initial thickness of the SEI (L_0), is represented as [74],

$$L_0 = \frac{V_{SEI} R_a}{3\epsilon_{s,a} A_{cell} d_a} \tag{2.2.7}$$

where $\epsilon_{s,a}$ is the anode solid phase volume fraction, R_a is anode particle radius, d_a is the thickness of the anode, $V_{SEI} = \frac{n_{loss} M_{Li_2CO_3}}{2\rho_{Li_2CO_3}}$, with n_{loss} as the amount of lost Li, $M_{Li_2CO_3}$ and $\rho_{Li_2CO_3}$ as the molar mass and density of Li carbonate, respectively, and A_{cell} is the area of the cell.

The SEI layer modeling discussed above plays a prominent role in determining the SOH of LIBs. However, SEI is permeable to Li-ions. So, during the charging and discharging of the battery, large stresses are generated due to the volume expansions and contractions of the anode. Cycling also induces graphite exfoliation due to the interaction between the solvent and graphite after diffusion through the SEI. These phenomena result in the electrode's fracture and further growth of fresh SEI, leading to the capacity fade of the battery. The fracture mechanism and mechanical fatigue of the batteries are discussed next.

Fracture

The volume expansion and contraction of the electrodes during charging and discharging of the battery, respectively, build up internal stress leading to fractures/cracks on the electrodes. Upon cycling the battery, the fracture on the electrode surfaces grows gradually. The SEI layer grows on the newly exposed electrode surfaces consuming Li. It also increases the

existing SEI thickness, resulting in additional Li loss and an increase in resistance. Thus, this mechanical degradation caused by diffusion-induced stresses (DIS) is another significant contributor to capacity fading.

The DIS on electrodes has been studied and modeled in [75, 76]. A stress generation model is developed in [75] to predict fractures in active electrode material of Lithium-ioncells based on two regimes (one-phase and two-phase material). Stresses calculated based on these regimes indicate that high-rate applications require smaller particles (particle size) and avoid a two-phase regime to prevent over-discharge. Although DIS modeled in [75] are helpful in analyzing stresses and increasing mechanical durability, the model lacks the inclusion of concentration dependence of Young's modulus, which significantly affects peak stress and stress evolution in the electrodes. The above limitation was later addressed in [76]. The models in [75, 76] focused on understanding the host particle pulverization, i.e., DIS causing large Li concentration gradients at host electrode particles during high C_{rate} , where C_{rate} is the measurement of the charge and discharge current with respect to its nominal capacity. However, the study failed to explain higher coulombic loss during low C_{rate} than during storage, which can be attributed to the SEI layer's possible mechanical degradation.

Fractures of the SEI layer, which are caused due to exertion of large-magnitude stresses during the expansion/contraction of an electrode particle, is studied in [77]. The authors concluded that the stresses experienced by the SEI leading to fracture and reforming at low C_{rate} as the dominant mechanism of cell capacity loss. The mathematical formulation relating SEI cracking to capacity fade during cycle aging is given as [77],

$$C_{cycloss} = a(\Delta SOL)^2 \tag{2.2.8}$$

where ΔSOL is the state of lithiation swing, $a > 0$ is a constant and a function of diffusion properties of Li in the electrode material, rate of reaction, temperature, number of Li atoms involved in the reaction, radius of particles, and mechanical properties of SEI and electrode material. Recently [78], the evolution of DISs and concentration of Li-ions have been evaluated using an analytical model to determine the SEIs fracture mechanism and the fatigue in LIBs. In [79], the battery's capacity loss is examined as capacity fade deviation percentage (CFD) and it is also shown that, as the CFD increases, the crack propagation is dominant along with the influence of SEI layer growth on the battery capacity loss.

Besides SEI layer formation and fracture, the other side reaction requiring attention to extend the existing coupled chemical/mechanical degradation models is Li plating. The determination of Li plating is crucial for efficient battery operation without compromising its life and safety. Li plating mechanism and modeling approaches to study capacity loss induced by itself are discussed next.

Lithium-ion plating

Li plating occurs after a few charge and discharge cycles [9], where the SEI layer grows at the anode reducing the porosity of anodes. The porosity reduction leads to a local potential gradient rise at the anode-electrolyte interface, promoting Li metal formation at the narrow gap between the anode and the electrolyte. Li plating occurs when the negative electrode surface potential falls below zero volts with respect to Li/Li^+ reference electrode.

The Li-ions are inclined to form metallic Li, particularly at low temperatures and during charging. Low temperatures ($5°C$) usually lead to decreased diffusion of Li within the SEI and graphite, which can overlay the electrode with Li plating [80, 81]. In general, the deposited metallic Li is reversible. However, Li dendrites can lose contact with the active material during the oxidation process leading to dead Li in the cell. Furthermore, the plated metallic Li is also highly reactive and forms an irreversible SEI with the electrolyte. Conversely, Li stripping occurs if the negative electrode potential reaches a positive value during the discharge process.

Li plating decreases the amount of cyclable Li-ions or increases the amount of frozen Li in the SEI layer between the electrodes which manifests itself as a reduction in capacity. The Li metal also increases Li plating's positive feedback, leading to an increase in battery resistance. Thus, the modeling of Lithium-ionplating is essential in analyzing aging and safety issues at lower temperatures.

Physicochemical models predict the onset of Li deposition and the possible amount of deposited metallic Li. An initial approach to describe the conditions for Li deposition during overcharge is presented in [82]. Here Doyle's model [66] is extended to include a side reaction described by the Butler-Volmer equation. Modifying this model, a reduced-order control-oriented cell degradation model is developed in [83]. Further, the model in [82] is also modified by the authors in [84] to include the effects of temperature (Arrhenius law-Section 2.3.1). A similar physics-based LIB aging model is presented in [9] by accounting for Li plating and SEI growth and predicting the transition from linear to nonlinear aging after extended cycling. The material balance equation employed for Li-metal is expressed as [9],

$$\frac{\partial C_{Li}}{\partial t} = -\frac{j_{lpl}}{F}(1-\beta) \tag{2.2.9}$$

where C_{Li} is the molar concentration of Li metal per unit volume of the electrode, j_{lpl} is the transfer current density of Li deposition reaction, and parameter β is introduced, which denotes the fraction of plated Li that becomes SEI.

In addition, the degradation effects caused by Li-plating and Li-stripping simultaneously at low temperatures are also not discussed. Later, the authors in [85] developed a quantitative detection method for Li plating and included a study of electrochemical models incorporated with both Li plating and stripping reactions to investigate the process at low temperatures ($-5°C$). Further, less complicated reduced-order models are developed in [86] to quantify the negative electrode potentials to predict Li plating's onset by considering the degradation effects, such as LLI, LAM, growth of plated Li, and secondary SEI and consumption of electrolyte solvents.

Dendrites

Li-dendrites are electrode surface protrusions that grow under activation and deposit on the electrode's flat surface during the diffusion process. These protrusions are often a result of Li-plating at the anode. Dendrites usually resemble a tree-like structure and grow only above critical over potential values. The different growth sites for the dendrite include screw dislocations, nuclei of higher indices, or twinned structures [87]. Therefore, the formation of dendrites causes irreversible consumption of Li inventory and increases the charge transfer

resistance due to the accumulation of dead Li [88]. Dendrites formation can also penetrate the separator and short-circuit the electrodes, which further aggravates Li metal's exothermic reactions with the electrolyte.

The formation and growth of Li dendrites can be categorized into two groups as 1) tip-growth mode [89], and 2) root-growth mode [90]. The modeling and analysis of tip growth are extensively researched compared to root growth. It is based on Fick's law (2.2.2), incorporating various other effects, such as electric current, surface energy, and mechanical deformation. The first attempt was made in [91] to simulate the electrochemical dendrite growth and proposed a comprehensive mathematical model of the time evolution of dendrite tip height (2.2.10) and growth velocity in Li-polymer batteries, given by [91]

$$\frac{\partial y_{tip}}{\partial t} = \frac{V}{F} i_n(y_{tip}, t) \tag{2.2.10}$$

where y_{tip} is the dendrite tip position, V is the molar volume of Li, F is Faraday's constant, and i_n is current density normal to dendrite tip.

A simplified modeling approach analyzing the various over potentials underplay at the dendrite tip and the flat electrode surface is developed in [89]. The modeling work constitutes liquid electrolytes, and the analysis of various over potentials leads to a simplified dendrite tip current density expression in terms of various system parameters, such as operating current density, electrodeposition kinetics, and transport properties, when compared to the computationally complex expression in [91]. The current density expression is given as [89]

$$\frac{i_t}{i_f} = -\frac{1}{bc_0} ln[e^{-bc_0} + \frac{i_f}{i_{Lf}}(1 - e^{-bc_0})]^{-\frac{\alpha_c}{n}} \tag{2.2.11}$$

where α_c is the cathodic transfer coefficient, ratio i_t/i_f represents the ratio of the dendrite tip current density to the current density on the flat surface, i_{Lf} is flat limiting current density, n is the number of moles of electrons, c_0 is the Li^+ bulk concentration, and the parameter b represents the concentration dependence of the diffusion coefficient. Later this model is extended to quantify the dendritic growth (i_t/i_f) during Li electrodeposition at a sub-ambient temperature [92].

All these models involve the solutions to the Nernst Planck equations [93] in the electrode or electrolyte, coupled with the electrochemical reactions at the electrode-electrolyte interfaces, given by

$$\frac{\partial c_+}{\partial t} = \frac{\partial}{\partial x}[D^{eff}\frac{\partial c_+}{\partial x} + \frac{(1 - t_+)I}{FA}] \tag{2.2.12}$$

where c_+ is the normalized concentration of Li-ions in an electrolyte, D_{eff} is effective diffusivity, t_+ is the transference number, A is the cross-sectional area, constant current I applied between $x = 0$ and $x = l_{cell}$ with l_{cell} is the length of a cell.

The electrode-electrolyte interface positions in the above models are assumed to be fixed, making them difficult to capture the complex moving interfaces and their morphological changes during the electrochemical processes, such as the Li dendrite growth in the cell. To overcome the above limitation, a phase-field method is proposed in [94] to simulate the continuous phase transition (evolution process) at the solid-liquid interface and Li dendrite's

growth process. In this method, the Nernst Planck equation in (2.2.12) is modified to include the phase filed variables Φ and ϵ as follows [94],

$$\frac{\partial c_+}{\partial t} = \Delta[D^{eff}\Delta c_+ + \frac{D^{eff}c_+}{R_g T} nF\Delta\Phi] + r_t \tag{2.2.13}$$

where r_t is the source term containing phase field variable ϵ given as $r_t = -\bar{K}_1 \frac{\partial \epsilon}{\partial t}$, $\bar{K}_1$ is the accumulation constant. All the modeling approaches proposed above provide deep insights into the physics of the formation and growth of Li dendrites on Li metal electrodes. Studies related to the Li dendrite formation on graphite electrodes at room temperatures and low charge rates are given in [95, 96, 97, 98]. Unlike graphite electrodes where Li plating may be reversible, Li metal anodes cause irreversible Li-dendrite formation, interfacial side reactions, volume change, and low coulombic efficiency [98]. Figure 7 depicts the dominant aging mechanisms at graphite anode. Cathode degradation is discussed in the next subsection.

2.2.2 Cathode Degradation

Recent studies [99] suggest that active cathode material loss also plays a vital role in the battery's degradation process. Causes of cathode degradation include the deactivation of active materials due to changes in the particle's surface structure and the electronic disconnection between the active materials and a current collector [99]. Further, the cathode material loss due to the DISs [100] also aids the degradation process. These stresses lead to the formation of cracks and an inactive layer on the surface of the cathode, referred to as cathode electrolyte interface (CEI), which leads to LLI.

The evolution of the cracks on the cathode is discussed in [101, 102]. The electrode performance was found to be fading due to the fatigue caused by alternating tensile and compressive stresses during the lithiation and delithiation cycles of the battery, respectively. It is found that the non-uniform intercalation and de-intercalation currents also cause stress between the particles in the electrode. In another effort, [101], the evolution of stress and strain energy inside the cathode is investigated analytically by integrating electrochemistry and mechanics. It is observed from the multi-scale mechanical-electrochemical model [101] that an electrochemically inoperative region in an electrode causes stress built-up. The model also addresses the issues arising due to fractures in the cathode.

On the other hand, the quantitative relationship between stress and cathode material loss is studied in [103] along with the influence of other side reactions, such as Li-plating and SEI layer formations. The authors proposed a coupled electrochemical-mechanical-thermal degradation model to include the effects of external factors such as C_{rate} and ambient temperature. A similar detailed non-invasive investigation on the complex interaction between cathode dissolution, CEI growth, particle cracking in both anode and cathode, and SEI growth to understand the aging behavior of the batteries is given in [104].

A summary of all the internal degradation mechanisms discussed above and the software used for their modeling approaches are given in Table. 4. It can be concluded that mechanical degradation (fracture), Li plating, and cathode degradation contribute to the battery's capacity fade. SEI growth is responsible for both capacity and power fade. Apart from dissecting and relating the internal degradation mechanisms to SOH, it is also necessary to

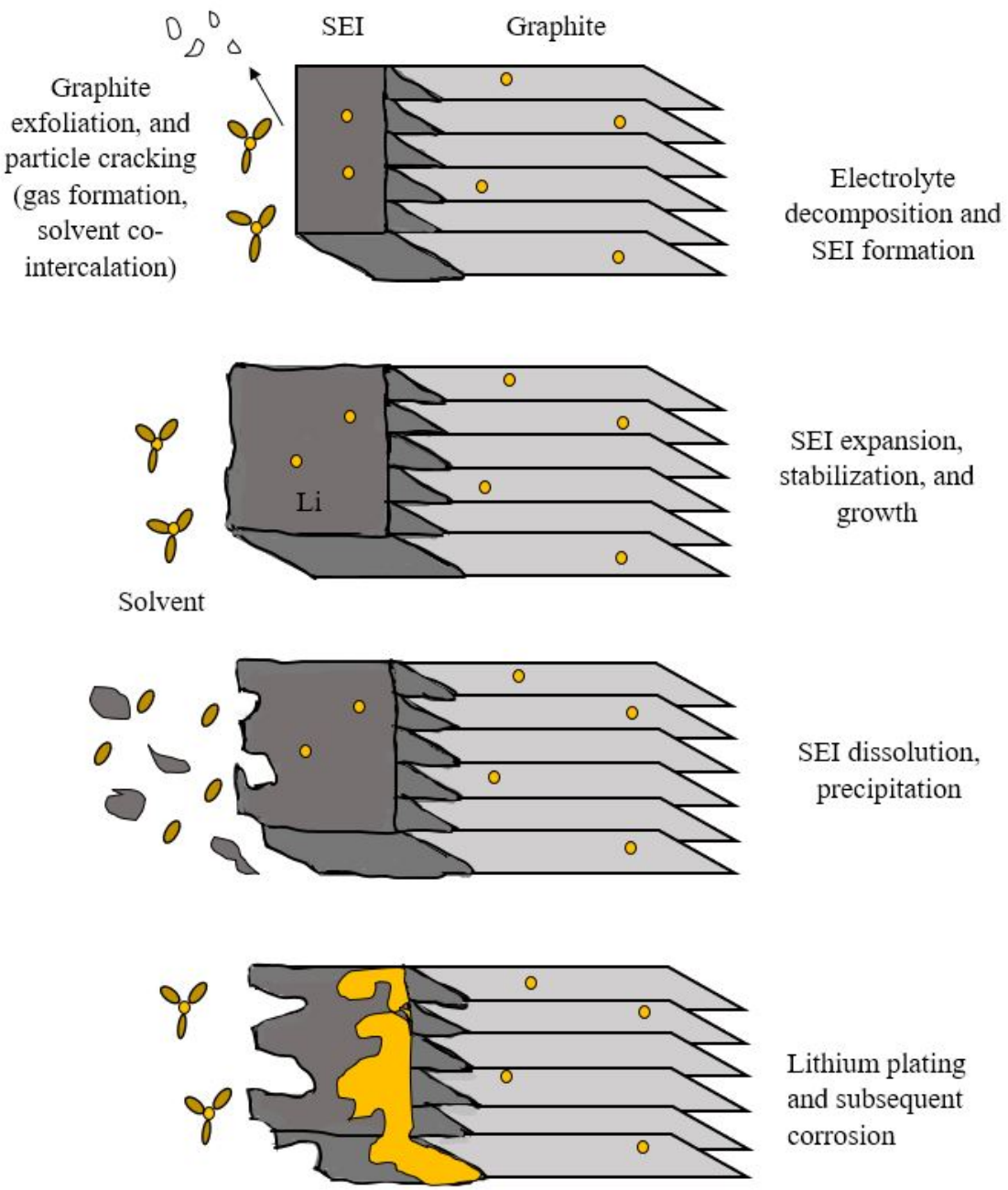

Figure 7: The aging effects on the anode (carbon/graphite) adopted from [4] with author's permission.

reflect on the external factor's contribution to capacity fade and resistance rise in LIBs. The effects of different external aging factors on SOH metrics are discussed in the next section.

2.3 External Factors Affecting the Degradation of the Battery

Degradation of the battery occurs in every stage of its life in different proportions with usage and external operating conditions. Battery degradation can be classified into cycle

Table 4: A summary of internal degradation mechanisms and their modeling approaches.

Internal degradation	Modeling approaches	References	Remarks	Software
SEI	Parabolic models/one-dimensional model	[57, 62, 64, 105]	The models account for variable film thickness and provide a broad, and fundamental understanding of the SEI; models focused on the SEI layer formation process while the battery level models are simplified.	CFD[105].
	A multi-physical pseudo 2D (P2D) model	[63, 65, 66, 68]	Coupled SEI growth model with the accurate battery level model are provided for a more accurate prediction than 1D models; models have long simulation time due to a large number of nonlinear equations and coupled nonlinear partial differential equations.	COMSOL Multiphysics[63]
	Single particle (SP) model	[70, 74, 79]	The models improve computational run time without compromising accuracy; can be simulated quickly but suffers precision at high C_{rate} due to the lack of electrolyte physics and degradation is not taken into account.	MATLAB[74, 106]
Fracture	Coupled chemical/mechanical degradation model	[107, 108, 109, 110]	The models couples electrochemistry, chemical degradation (including SEI formation), and fracture mechanics so as to clarify the life performance of a Lithium-ioncell, the models have high prediction accuracy with reduced computation complexity; fracture of the SEI can lead to the reduction of the electrolyte (that penetrates through the cracks) regenerating the SEI and henceforth increasing its thickness.	COMSOL Multiphysics[107]
Li plating	Physicochemical models	[9, 82, 84]	Li plating occurs at higher currents or lower ambient temperature; anode polarization and Li intercalation kinetics play a crucial role in determining the propensity of Li deposition; deposition of metallic Li on the surface of the anode particles together with the initiation of dendritic growth of Li is the most probable cause for a short circuit.	CFD[84]
	Reduced order models	[83, 111]	The models are simple enough to be executed quickly on an inexpensive embedded systems processor.	COMSOL Multiphysics[83]
Dendrite growth	Tip growth-physical models	[89, 91, 112]	The dendrite growth is always slowed by lowering the current density; Li dendrites can detach from the electrode surface, leaving loose Li crystals called "dead" Li, which is a major source of battery energy density loss; unlike the SEI layer, Li dendrite formation is not acclaimed.	COMSOL Multiphysics[112]
	Phase field modeling	[94, 113, 114]	The models are used for modeling temporal and spatial microstructure evolution of materials undergoing a wide variety of processes, such as phase transformations, deformation, and particle coarsening.	COMSOL Multiphysics[114]
Cathode degradation	Chemical/mechanical degradation model	[101, 102]	Cathode degradation is caused due to changes in the surface structure of particles and the electronic disconnection between the active materials and a current collector; models are useful for gaining insight into possible degradation mechanisms and could be more robust than pure empirical approaches; models are computationally complex and have many parameters which may be unknown.	COMSOL Multiphysics[101]

CFD-computational fluid dynamics

aging and calendar aging [33]. The calendar-aging corresponds to the consequence of battery storage and cycle aging is associated with the usage. Battery temperature, charge/discharge rate, DOD, time, voltage effects during cycling, and SOC during rest periods are the major factors [35] for battery aging. All the above external aging factors responsible for Li loss and increased inner resistance are discussed independently in the next subsections.

2.3.1 Effect of Charging/Discharging rate (C_{rate}) and Temperature

C_{rate} is defined as the charge/discharge rate at which the battery is cycled. Studies on the influence of charging C_{rate} and cut-off voltages on the aging of batteries are presented in [115, 116]. In both these studies charging current has been shown as the deciding factor of loss of LAM, during which the crystal structures of the active material are easily fatigued and damaged. High charging C_{rate} also leads to Li-plating on the anode [117]. Similarly, the discharge capacity significantly falls at a higher discharge rate [118, 119]. The degradation mechanisms at a high discharge rate is similar to the ones at a high charge rate.

The temperature (T) dependency of aging is, in general, described by the Arrhenius equation and studied in the vast amount of literature [120, 121, 122, 123, 124], given by

$$\bar{k}_1 = \bar{k}_0 e^{\frac{-E_a}{R_g T}} \tag{2.3.1}$$

where $\bar{k}_0$ is a rate constant, and $\bar{k}_1$ is kinetic reaction rate. Despite a temporary increase in the battery's performance at high temperatures, there is an occurrence of secondary side reactions in terms of corrosion inside the battery. This corrosion degrades the battery faster with LLI, causing capacity fade. High temperatures also cause the thickening of SEI film and degradation of the cathode [125], resulting in increased power fade (resistance rise). In [121], the authors found that the Warburg elements and cell impedance increased with cycling at a higher temperature, but they did not significantly affect the SOH. In real-life applications, temperature fluctuations combined with the discharge rate have a cumulative effect on the battery's capacity fade.

On the other hand, low-temperature [126] conditions engender a loss of material diffusion and alter the battery chemistry. During low-temperature charging, issues, such as Li plating, dendrite growth, and damage to the crystal structure of active material are reported [84, 125, 127] due to the high polarization of the anode. This further leads to a significant drop in efficiency at high discharge rates, adversely affecting the SOC and SOH.

2.3.2 Effect of Depth of Discharge, State of Charge, Time, and Voltage

Cycle depth or DOD is a critical degradation governing factor. DOD is defined as the ratio of the amount of charge released to the battery's nominal capacity. The battery's cycle life reduces at high DOD due to severe structural and volumetric changes leading to LAM. Thus, deep cycles cause disproportional or exponential aging [128, 129] than small cycle depths [130]. The influence of DOD on the cycle performance of LIB also varies with different cathode materials [128].

The SOC variation, i.e., change of SOC (ΔSOC), significantly affects aging during cycling. The power loss increases as ΔSOC value is high [131]. At high SOC, i.e., at higher terminal voltages, the SEI layer thickens with the electrolyte decomposition and Lithium-ion deposition, leading to a higher aging rate [132]. The combination of high SOC and low-temperature charging also accelerates the aging phenomenon as a non-linear function of time [133] with the occurrence of Lithium-ion deposition side reaction. On the other hand, low SOC causes corrosion of anode copper current collectors and structural disordering of cathode active material dramatically, leading to accelerated aging of LIB [134]. Further, batteries exhibit different aging behavior at the same operating temperatures with different

SOC levels [81]. It is concluded that the cycling between 45% and 55% SOC has the smallest effect on both capacity loss and resistance increase [133].

Storage time also plays a critical role in battery degradation. The calendar-aging is, in general, due to SEI formation in a carbon-based anode [4, 135]. As discussed in the previous section, SEI growth increases internal resistance. As the SEI thickness grows with aging [62, 79]), the power fade increases. In some of the earlier works, this aging process was linear with respect to time [136]. In later studies, the SEI growth rate is found to be a function of the square root of time ($\sqrt{t}$) [137]. This $\sqrt{t}$ dependency usually represents the incremental capacity loss (ICL) due to SEI growth and is often governed by the diffusion process.

Nonetheless, the charging and discharging voltages impact the battery's aging phenomenon with more capacity degradation and resistance increase [115]. High cathode voltages cause electrolyte oxidation, and cathode decomposition [138]. On the other hand, low cathode potentials retards the accelerated aging of the battery. In [115], the authors discussed the impact of reducing cut-off voltage on retarded capacity loss and LLI of LIB. A high or low operating voltage window (ΔV) is also shown to affect the aging mechanisms inside the battery [139]. High ΔV causes the LAM of the graphite anode, and low ΔV results in high discharge cut-off voltages and irreversible structural changes to the graphite anode.

Other factors, such as external abuse, mechanical [111] stress, pressure [140], and choice of the anode, cathode, and electrolyte [141, 142], cause the formation, growth, and thickening of the SEI layer accelerating the aging in LIBs. In summary, high/low temperatures, high C_{rates}, high SOC, and ΔV are the common external aging factors of LIB [139]. A cause and effect diagram for the health degradation of LIBs discussed above is shown in Figure 8. The SOH estimation processes, in regard to the above internal and external degradation mechanisms, are discussed in the next section.

2.4 SOH Estimation Methods

The SOH is quantified using two metrics, namely, the capacity fade and power fade. Capacity fade is defined as the ratio of current capacity to the nominal/rated capacity (C_{rated}) of the battery [133]. The resistance rise ($R_{0_{inc}}$) is used as the indicator of power fade and is expressed as

$$R_{0_{inc}} = \frac{R_{bat} - R_{BOL}}{R_{BOL}} \tag{2.4.1}$$

where R_{BOL} is the beginning of life resistance, and R_{bat} is the current resistance of the battery. From (2.4.1), the SOH is quantified as,

$$\text{SOH}\% = \left(\frac{R_{EOL} - R_{bat}}{R_{EOL} - R_{BOL}}\right) 100\% \tag{2.4.2}$$

where R_{EOL} is battery end of life (EOL) internal resistance. The changes in these metrics are caused by both external and internal degradation mechanisms and age. SOH is a multivariate function of these degradation mechanisms making the estimation a challenging task. Since the SOH can not be measured directly, it is, in general, estimated using various filtering-based approaches. The SOH estimation schemes can be broadly classified as 1) experimental, 2) model-based, and 3) data-driven methods.

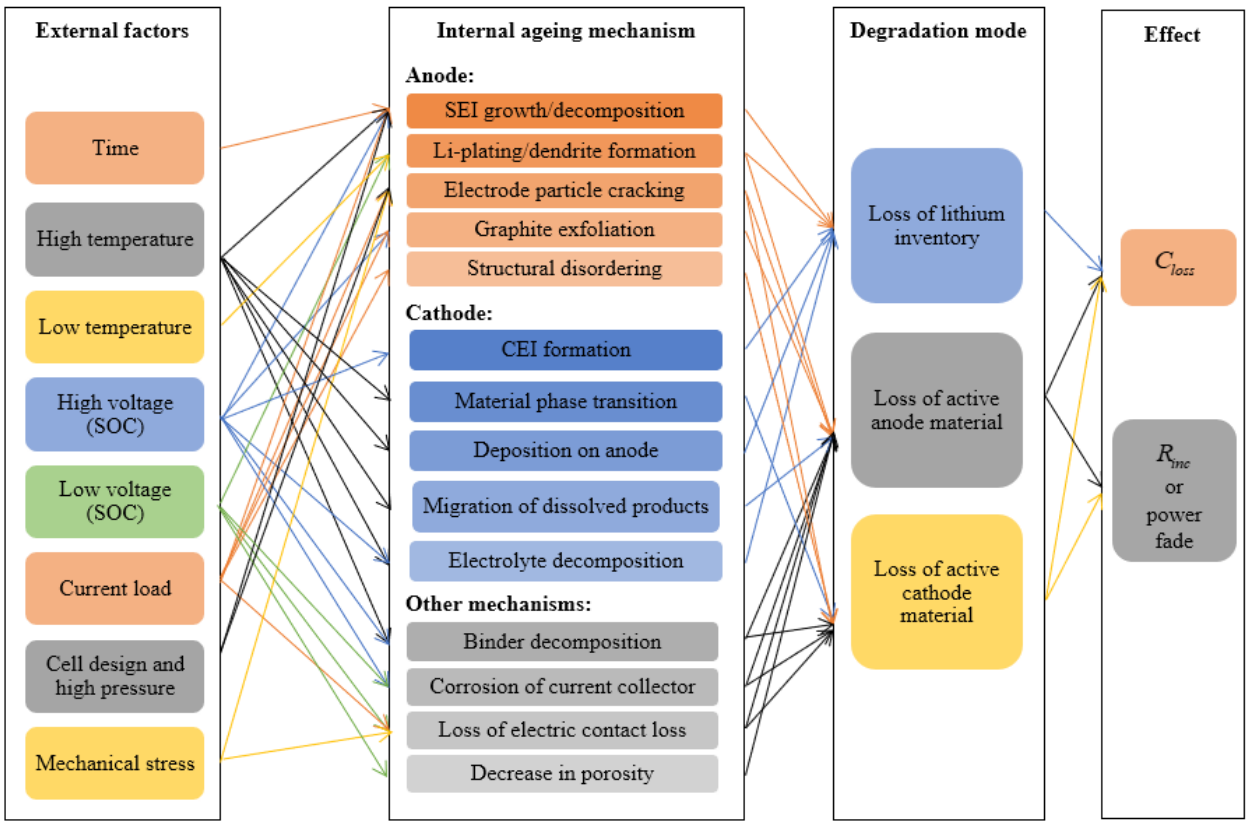

Figure 8: Cause and effect of degradation mechanisms adapted from [3], where CEI is cathode electrolyte interface, SEI is solid electrolyte interface, SOC is state of charge.

Experimental methods constitute direct/indirect measurement-based approaches. The SOH is estimated by correlating these physical measurements to the properties of the battery. The large test/measurement time precludes the real-time implementation of the experimental methods in BMS. Model-based methods, on the other hand, overcome these limitations and improve the accuracy of SOH estimation by considering the effects of both internal and external aging factors. As discussed above in Section 2, obtaining an accurate model is often challenging. Therefore, data-driven methods, such as analytical and machine learning, were also proposed, which use a large amount of experimental data for learning the black-box model of the battery to estimate and predict SOH.

There are a significant amount of reviews available in the literature (refer to [33, 34, 35, 36, 37, 38, 39], and the references therein) on the above SOH estimation approaches. Unlike the existing reviews, our focus in this section is to present a survey of the SOH estimation methods that incorporates studies on different aging mechanisms, discussed in Section 2.2 and 2.3, and the recently developed machine learning-based approaches. The primary goal is to identify future trends and directions in health-conscious intelligent battery management for LIB's safety, longevity, and autonomy.

2.4.1 Experimental Methods

To circumvent the issue of time-intensive tests and measurements for OCV-based SOH estimation schemes [143], ICA [144] and DVA [145] techniques are introduced. The ICA and DVA approaches examine the OCV variations to track the internal chemical reactions and aging mechanisms. These approaches analyze cell voltage responses in different duty regimes, which is the key to understanding cell behavior and degradation. The gradient of the capacity with respect to the voltage ($\frac{dC_n}{d\mathrm{OCV}}$) defines the incremental capacity (IC), whereas the gradient of voltage with respect to the capacity, i.e., $\frac{d\mathrm{OCV}}{dC_n}$ defines the differential voltage (DV) [146]. The voltage plateaus in the OCV curves are converted to recognizable peaks and valleys in ICA and DVA, respectively. The valleys in the DV curve represent the phase transitions of the electrode active material, while a peak indicates a single phase of the active material.

The influence of external aging factors (DOD, SOC, C_{rate}) on aging are identified by ICA [147] and DVA [148] through four main observations [149]: a) simultaneous decrease of all peaks, b) voltage shift of the peaks, c) decrease of a specific peak, and d) new peaks arising. As discussed in Section 2.3, these observations can be correlated to the four main degradation modes: LLI [150], LAM_{anode} [147], $\mathrm{LAM}_{cathode}$ [151], and degree of lithiation [148]. A systematic approach to identify LIB degradation modes, based on the ICA by analyzing their corresponding IC and peak area main features is presented in [152].

Studies on the identification of degradation modes leading to capacity loss are presented in [147, 150, 153, 154, 155, 156]. The IC curves are used to identify two-stage capacity loss, which is caused by LAM on both the anode and a cathode [153], whereas the DVA is used to find the side reactions on anode [154]. Furthermore, [157] illustrates the correlation between capacity loss and DV curves at different SOC levels, cycling, and storage conditions for real-time BMS implementation. The effects of charge/discharge rate and DOD are included in [147, 155] for effective SOH estimation with the lesser computational load. In [147] the linear relationship between the IC peak and the remaining capacity is used to provide a quantitative correlation between the peak value and the SOH of the LIB. ICA and DVA are also employed to extract parameters, such as LLI and LAM, from the IC and DV curves to establish the multi indicators system of SOH [150, 156].

All the above analyses used capacity as a health factor for SOH evaluation. The authors in [158] combined DVA and alternating current impedance to analyze the increase of ohmic and polarization resistance (power fade). The increase in ohmic resistance is attributed to the lack of electrolyte and increased separator resistance. SEI layer growth and deterioration of the ionic kinetics result in polarization resistance growth. A similar model-free SOH calculation method by fusion of the CC method and DVA is proposed in [159]. The authors in [160] explore the aging behavior of the LIB module using EIS, charge/discharge curve, ICA, and average Fréchet distance (AFD). An increase in internal resistance is employed as a health metric. Other similar SOH estimations using ICA and DVA analysis are presented in [144, 145, 161, 162]. Although, ICA and DVA are used for online SOH estimation [144, 150, 163], these curves are susceptible to measurement noise [155], they require a constant and low current to discharge the battery, and ICA/DVA can only be used under a fully charged/discharged process.

2.4.2 Model-Based SOH Estimation with Internal Degradation

In model-based schemes, the battery physics-based models, i.e., electrochemical, thermal [164], ECM, and their combinations [165], along with degradation models are used to design filters (KF, EKF, unscented KF) and/or observers (Luenberger, sliding mode, and nonlinear) to estimate the SOH. These models can be implemented in a wide range of operating conditions and can provide accurate battery behavior and internal parameter changes.

In recent times, the SOH is estimated more accurately by integrating the internal degradation models, discussed in Section 2.2, with electrochemical models of the LIB. Although SP models are the most commonly used electrochemical models, they do not consider the concentration and potential distribution in the electrolyte phase costing the model's accuracy at high C_{rate}. To overcome this limitation, an advanced SP model is proposed in [166] by considering the electrolyte physics of the battery. Later, the advanced SP model in [166] is adopted by [79] to integrate a capacity degradation model with chemical and mechanical degradation, i.e., SEI layer formation coupled with crack propagation. This integrated model can predict battery capacity loss (C_{loss}) as a function of cycle number and temperature, including SEI layer growth coupled with mechanical fatigue. The capacity loss (LLI) is analyzed in four stages [108] of the SEI layer's evolution under chemical and mechanical stress, such as 1) SEI layer's initial formation, 2) growth of the initially formed SEI layer, 3) SEI layer formation on newly formed surfaces due to fracture/cracking, and 4) growth of the new SEI layers on the fractured surfaces.

The advanced SP models in [79, 166] are further reduced and simplified in [167] for online SOH estimation in BMS. This new SP-based comprehensive degradation model includes degradation physics of both anode (coupled chemical/mechanical degradation) and cathode (metal dissolution) and could predict cycling capacity with less than 2% error. The degradation model can also address two main requirements for model-based BMS, i.e., rapid and accurate battery response prediction. On the other hand, a simplified P2D electrochemical model [168] considering side reactions, such as LLI and LAM, is also proposed for SOH prediction. The OCV-SOC relation is updated by integrating the aging effects and is applied to the ECM-based SOC estimator. This OCV-SOC correlation is further utilized as a link between ECM and the electrochemical model. The equilibrium potentials are then used to monitor SOH.

Further, for SOH prediction under various operating temperatures, two types of electrochemical models (P2D and SP) are presented in [169] along with degradation models, such as SEI and Li plating. The side reactions are coupled with reduced order P2D for the anode and SP model for the cathode. Here, a PF is used to estimate aging parameters as a function of time and electrode thickness, and SOH with respect to capacity and power fade in real time. The aging of the battery is also analyzed at different temperatures, C_{rate}, and current profiles. Similarly, the anode SEI growth aging model is coupled with the SPM in [170] to predict the capacity fade of LFP cells with 1.3% error. The operating range of the aging formula at different temperatures and SOC is also determined. However, several other degradation mechanisms (fracture, cathode degradation) are yet to be integrated with these electrochemical models.

In addition, ECM models integrated with empirical aging models (refer to Section 2.4.3) is also proposed to predict battery performance under various operating conditions. In

[171], an ECM model that integrates the electrical, thermal, and aging aspects of an NMC battery [172] is proposed to estimate SOH. An empirical model is proposed in [173] to predict the voltage profiles of an LFP battery cell at various SOH, SOC, and temperature conditions. Similar ETA models are employed in [174, 175] to develop health-conscious optimal battery charging algorithms. A mechanistic model that can synthesize a variety of cell aging scenarios based on degradation modes is presented in [151] with wide applicability to various cell chemistries, designs, and operating modes. The model consists of a modified ECM capable of simulating the different degradation modes via a synthetic approach based on the behavior of electrodes reflected by the study of the DV and IC curves. The model is also able to simulate complicated degradation modes at any C_{rate} and predict capacity loss, EOL, SOC, IC, and DV signatures, without any ambiguity.

2.4.3 Data-Driven Methods

Data-driven methods have recently become a research hot spot for their ability to estimate the SOH without the knowledge of electrochemical reaction, explicit physics-based battery model, and physics of the failure mechanism. Unlike model-based methods, data-driven methods depend only on aging data and are discussed in detail in the following subsections.

Analytical methods

Analytical models correlate the aging of a battery with the operation time [43]. These models use capacity loss and power loss as SOH metrics for modeling. Most of these models represent C_{loss} and $R_{0_{inc}}$ as a function of SOC, Ah, and T [176] and is expressed as,

$$C_{loss}(Ah, \text{SOC}, T) = h_c(\text{SOC}, T).Ah^{z_1} \tag{2.4.3}$$

where $z_1 = 0.48$, $Ah = C_n \times cycle_{number} \times \text{DOD}$ [177]. At each C_{rate}, Ah is directly proportional to time, so instead of using t as a variable in (2.4.3), Ah is used to quantify and correlate the capacity fading behaviors for different C_{rate}. The function $h_c(.)$ is a non-linear capacity severity function, which depends on the aging factors and C_{rate} (only at high charge/discharge rates) [176] and represented by

$$h_c(.) = a_c(\text{SOC})e^{(\frac{-E_{ac}}{R_g T})} \tag{2.4.4}$$

where E_{ac} is the cell activation energy defined for the capacity fade process. The fitting parameters of the $a_c(.)$ are given in [176].

Similarly, the increase in internal resistance $R_{0_{inc}}$ (power fade) as a function of charge throughput is expressed as

$$R_{0_{inc}}(Ah, \text{SOC}, C_{rate}, T) = h_R(\text{SOC}, C_{rate}, T)Ah \tag{2.4.5}$$

where $h_R(.)$ is a non-linear resistance severity function that depends on the aging factors as investigated in [176] and is given by

$$h_R(.) = a_R(\text{SOC}, C_{rate})e^{(\frac{-E_{aR}}{R_g T})} \tag{2.4.6}$$

where E_{aR} is the cell activation energy, defined for the resistance increase process. The fitting parameters of the $a_R(.)$ are detailed in [176].

A summary of empirical models for capacity and power fade of LIB with different cathode chemistry developed with extensive experimentation under controlled environments [133, 172, 176, 177, 178, 179, 180, 181] is presented in Table. 5. The table presents the analytical life-cycle models for two commonly used battery chemistry, i.e., LFP and NMC. In both LFP [177] and NMC [176] batteries, the effect of temperature in cycle-life models is obtained using Arrhenius correlation and power law relation with time or Ah.

Table 5: Summary of empirical models for capacity and power fade of LIB with different cathode chemistry.

Calendar aging	**Cycle aging**
Type of cathode used: NMC [133]	Type of cathode used: NMC [133]
$C_{calloss} = ((7.543V_t - 23.75)10^6 e^{-\frac{6976}{T}})t^{0.75}$	$C_{cycloss} = (7.348 \times 10^{-3}(\varnothing V_t - 3.667)^2 + 7.600 \times 10^{-4} + 4.081 \times 10^{-3}\Delta\text{DOD})\sqrt{Ah}$
$R_{calinc} = ((5.270V_t - 16.32)10^5 e^{-\frac{5986}{T}})t^{0.75}$	$R_{cycinc} = (2.153 \times 10^{-4}(\varnothing V_t - 3.725)^2 - 1.521 \times 10^{-5} + 2.798 \times 10^{-4}\Delta\text{DOD})\sqrt{Ah}$
Type of cathode used: NMC pouch cell [172]	Type of cathode used: NMC-LMO cathodes [176]
$C_{calloss} = (-0.0064 \times 1.1484^{\frac{V_t - V_0}{\Delta V_t}} \times 1.5479^{\frac{T - T_0}{\Delta T}})t^{0.5}$	$C_{cycloss} = a_{cyc}(\text{SOC})e^{(\frac{-E_{ac}}{R_g T})}Ah^{0.48}$
$R_{calinc} = (0.0484 \times 1.0670^{\frac{V_t - V_0}{\Delta V_t}} \times 1.5665^{\frac{T - T_0}{\Delta T}})t^{0.5}$	$R_{cycinc} = a_{Rcyc}(\text{SOC}, C_{rate})e^{(\frac{-E_{aR}}{R_g T})}Ah$
Type of cathode used: LFP [182]	Type of cathode used: LFP [181]
$C_{calloss} = a_{cal}(T, \text{SOC})(1 + \frac{C_{calloss}(t)}{C_{rated}})^{-\alpha(T)}$	$C_{cycloss} = (-5.31 \times 10^{-5} + 8.36 \times 10^{-6}\Delta\text{SOC} + 2.69 \times 10^{-8}e^{C_{rate}}) \times nc^{1.36}$
Type of cathode used: Nano phosphate LFP [178]	Type of cathode used: Nano phosphate LFP [178]
$C_{calloss} = (0.019\text{SOC}^{0.823} + 0.5195)\times (3.258 \times 10^{-9}T^{5.087} + 0.295) \times t^{0.8}$	$C_{cycloss} = (0.00024e^{0.02717T}) \times 0.02982 \times \text{DOD}^{0.4904} \times nc^{0.5}$
$P_{calfade} = (\frac{0.000375\text{SOC} + 0.1363}{0.155})0.003738e^{0.06778T}t$	$P_{cycfade} = \frac{1}{3}(5.78 \times 10^{-4}e^{0.03T} + 1.22 \times 10^{-7})2.918\times 10^{-5}e^{0.08657\text{DOD}} \times nc^{(0.00434T - 0.008\text{DOD} - 0.1504)}$
Type of cathode used: LFP [179]	Type of cathode used: LFP [179]
$C_{calloss} = 3.087 \times 10^{-7}e^{0.05146T}t^{0.5}$	$C_{cycloss} = 6.87 \times 10^{-5}e^{0.027T}nc^{0.5}$
$PPC_{caldec} = 1.71 \times 10^{-29}e^{0.195T}t^{-0.026T + 9.85}$	$PPC_{cycdec} = 3.24 \times 10^{-5}e^{0.03T}nc^{0.00434T - 0.65}$
Type of cathode used: LFP [180]	Type of cathode used: LFP [177]
$R_{calinc} = 6.9656 \times 10^{-8}e^{0.05022T}2.987e^{0.006614\text{SOC}}t^{0.8}$	$C_{cycloss} = 30330 \times e^{\frac{-31700 + 370.3C_{rate}}{R_g T}} \times Ah^{0.55}$

Note: $C_{calloss}$, and $C_{cycloss}$ in % represent capacity loss during calendar and cycle aging respectively, R_{calinc}, and R_{cycinc} in % represent resistance increase during calendar and cycle aging respectively, $P_{calfade}$, and $P_{cycfade}$ in % represent power fade during calendar and cycle aging respectively, PPC_{caldec}, and PPC_{cycdec} in % represent pulse power capability decrease during discharge pulse during calendar and cycle aging respectively, nc is number of cycles, ΔV_t is change in voltage (V_t), V_0 is initial/reference voltage, ΔT is change in temperature, T_0 is initial/reference temperature, ΔDOD is the depth of discharge or cycle depth in the range of $(0-1)$, ΔSOC is the state of charge in the range of $(0-1)$, E_{ac} is the cell activation energy defined for the capacity fade process, E_{aR} is the cell activation energy, defined for the resistance increase process, fitting parameters of the $a_{cyc}(.)$ and $a_{Rcyc}(.)$ are given in [176], a_{cal} is the kinetic dependence of the capacity fade evolution with T, SOC is given in [182], $(1 + \frac{C_{calloss}(t)}{C_{rated}})^{-\alpha(T)}$ with $\alpha(T) > 0$ is given in [182] which can be related to the diffusion limitation of solvent molecule inside SEI layer which tends to decrease the capacity fade rate. $Li(NiMnCo)O_2$ =NMC cathode, $LiFePo_4$ =LFP cathode, $NMC - L_iMn_2O_4(LMO)$ =NMC-LMO blended cathodes.

It is well known that the LFP cathode cells present better durability, and inherent safety, and rely on abundant, eco-friendly materials [183]. However, the major limitations of LFP cells are low specific energy and dramatic changes in the OCV-SOC curve, as the SOCs drop to 0% and rise to 100%, and wide flat OCV plateau in the middle SOC regions. Therefore, the cycle-aging for LFP [179, 181] are found to vary with the number of cycles (nc). Compared to LFP cells, aging in NMC cells [133, 172] includes the effect of storage voltage, time,

and temperature during calendar-aging and DOD, SOC, C_{rate} and Ah for cycle-aging. Note that the NMC batteries, discussed in Table 5, constitute pouch cells instead of cylindrical cells. The primary limitation of all the semi-empirical models presented in Table 5 is that they don't reflect the contributions of the internal degradation mechanisms explicitly in the expressions.

Recent studies [184, 185, 186, 187] consider a subset of the degradation mechanisms (eg., SEI formation and growth) to represent analytical aging models. Three semi-empirical models of the three aging modes (LLI, LAM_{anode}, $\text{LAM}_{cathode}$) are quantified by the established OCV model in [186], along with the development of the mapping models with SOH, ohmic resistance, and polarization resistance evolution. The authors established a clear mapping from external stress to internal aging mechanism to external behavior. Although several empirical methods based on the DV curve have been proposed in [157, 163], the features used to estimate the capacity are sensitive to the relatively high initial SOC and charging current, which was redressed in [187]. However, in [187], the correlations between the extracted features and battery aging mechanisms, such as the LLI, LAM_{anode}, and $\text{LAM}_{cathode}$ are not completely elucidated, especially for the battery with NMC cathode. Later, the authors in [150] extracted six characteristic parameters revealing LAM_{anode}, and $\text{LAM}_{cathode}$ and LLI from the IC curve to establish the multi-indicators system describing battery SOH for NMC LIB, which enables ICA to be used in on-board applications. In addition, LLI is found to be the dominant factor causing a capacity loss for batteries under 20% DOD.

Machine learning methods

Machine learning approaches use SOH data to fit a model, which can be used for future prediction. The machine learning methods used for SOH estimation are ANN [188, 189], SVM [190, 191, 192], and fuzzy logic [193, 194]. ANN is one of the approximation methods which can fit complex non-linear functions. In [189], a robust algorithm for ANN is presented, predicting SOH at different operating conditions. However, the main limitation of ANNs includes the requirement of a large amount of training data and the training method, which significantly affect the accuracy. Furthermore, the identification and optimization of the model topology of ANN remain an open technical challenge [43]. Other probabilistic approaches, such as gaussian process regression (GPR) [195], relevant vector machine (RVM) [196] are also used in literature to estimate the SOH of the battery. However, the above methods are mostly affected by the phenomenon of capacity regeneration and cannot make long-term predictions. Recently, deep learning became popular in battery health prediction due to its powerful ability to achieve accurate long-term degradation predictions [197].

DNN, convolutional NNs (CNN), and recurrent NNs (RNN) are introduced for system modeling, time series forecasting, and natural language processing [198]. These deep learning technologies eliminate the need for data labeling and feature engineering by extracting higher-level features from input data using multiple layers. Recent studies [198, 199, 200] have reported using these technologies to establish a relationship between the features of battery degradation from the battery characterization data and the SOH of the battery. In [199], a deep CNN is used to estimate the capacity of a battery, whose unique features include local connectivity and shared weights. A similar investigation on models of three different families of NN architectures, such as feed-forward NN (FNN), CNN, and long short-term memory

NN (LSTMNN) are proposed in [200] for battery capacity estimation. LSTMNN is found to outperform other model architectures in estimating battery capacity more accurately because of its simpler structure and its ability to interpret variable-sized time-series battery data in an efficient manner. On the other hand, in [198], a two-stream hybrid gate recurrent unit (GRU)-CNN is employed to build a time series prediction problem for SOH estimation. All these studies use voltage, current, and temperature during the charging as inputs to learn the model and predict the SOH of the battery with good accuracy. In all the above techniques, future capacity values are predicted based on the trained model until the capacity reaches the EOL (20% capacity loss).

In real-time applications, it is difficult to measure battery capacity directly due to incomplete discharge. In addition, identifying internal aging mechanisms inducing capacity/power fade through data-driven methods is cumbersome. Therefore, some health indicators (HIs) are extracted from the measured parameters (voltage, current, temperature, and time interval) to estimate SOH using data-driven approaches. They are especially important for data-driven methods as battery internal aging mechanisms are known to be manifested by these HIs [201]. A novel method to predict RUL based on the optimized health indicators and online model correction with transfer learning is presented in [197]. GPR is used to optimize the threshold for HIs and determine the EOL of LIB. The SOH of the battery is evaluated using grey relational analysis (GRA) in [146]. The HIs were extracted from the partial IC curves for GRA. A voltage-temperature health feature extraction method for batteries is proposed in [202]. Another approach using partial voltage profiles and GPR is also proposed to extract voltage-dependent health features. In [203], HIs are extracted to estimate the SOH under general discharging conditions, such as CC, pulse current, and dynamic current, and using these HIs as input features, linear regression (LR), SVM, RVM, and GPR, are employed to predict the SOH of the battery. Recent studies [201, 204] also include significant dimensional reduction of HIs. A HIs extraction and optimization using IC curves are presented in [201]. An improved GPR is applied for battery capacity estimation.

In recent times, hybrid methods [205], which combine similar or different methods, have also become the main research focus to improve SOH estimation and RUL prediction. Hybrid data-driven and model-based approaches are two notable ones [206, 207, 208, 209]. In [210], an aging phenomenon based on the rain-flow cycle counting method combined with a deep-learning algorithm is presented. This hybrid method extracts the battery aging trajectory and provides an aging index to improve the SOH estimation accuracy. An ensemble of data-driven strategies is also proposed [146, 211, 212, 213, 214] to improve the accuracy further and reduce the computational load. A comparison of all the emerging SOH estimation methods along with their accuracy is given in Table. 6. We can observe that hybrid approaches are compelling, more accurate, and reliable for SOH estimation of LIBs.

In the next section, we summarize the above studies and provide recommendations for future research direction to develop intelligent BMSs with health-conscious decision-making capabilities.

2.5 Discussion and Future Recommendations

From the above studies, the internal degradation steps starting from SEI formation to lithium plating can be summarized as follows: 1) SEI layer grows in width substantially at the anode

Table 6: A comparison of emerging SOH estimation methods.

Methods	References	Key benefits	Limitations	Accuracy
Data-driven approach	[188, 189]	Simple structure, easy to identify parameters, easy to implement, strong ability to consider nonlinearities, high prediction accuracy, non-parametric, robust to outliers, low prediction time.	Easy to cause under-fitting problems due to its linear regression type, potential overfitting problems, poor generalization ability, bad long-term prediction ability, poor uncertainty management ability, performance highly depends on the training process.	RMSE $\approx$ 0.0203
Hybrid methods	[212, 215]	Prediction accuracy is high and avoids the estimation error from the model mismatch, and enhances the model's adaptability to varying operating conditions	Computation is complicated and depends on experimental data, restricts its applicability under more complex aging conditions when combined with model-based methods.	MARE $\approx$ 0.27%,RMSE $\approx$ 0.0037
Empirical methods	[178, 180]	Easy to be built up and quick to produce predictions, simple structure easy of extracting model parameters, the low computational effort.	Extensive laboratory tests over the entire operating range are required, poor robustness, low accuracy, difficulty to develop suitable laboratory aging tests to analyze the interaction between different aging processes and link them to life expectancy on an experimental basis, low generalizability, and developed models are restricted to a specific battery type and operating conditions.	$R^2 \approx 0.963$, ARE $\approx$ 9.72%
Physics-based models	[74, 103]	High accuracy, linked to the underlying physics of the battery.	Heavy computation load, difficult model parameterization.	RMSE $\approx$ 0.002
DVA/ICA-based methods	[146, 147]	Easy to monitor and implement in BMS for online applications, indicative of the intercalation process.	Limited to low current rates, sensitive to measurement noise and temperature, heavy data requirements of voltage and current measurements.	ME $\approx$ 4%, RMSE $\approx$ 6.4
Physics-based degradation mechanisms + Big data	[216, 217]	Highly accurate, implementable in online BMS applications, vast quantities of data are processed and treated with high accuracy at the same time.	It needs a large amount of data to train and the accuracy depends on the model used.	RMSE $\approx$ 5%
Deep neural network	[198, 200]	Automates the feature learning process from large amounts of data, learning highly representative features that carry the most useful information of the data	It needs a large amount of data to train.	ME $\approx$ 4.3%, RMSE $\approx$ 4.69%

RMSE-Root mean square error, MARE-Mean absolute relative error, ARE-Average relative estimation error, ME-Maximum estimation error

with consecutive charge and discharge cycles. 2) Due to SEIs permeability to Li-ions, large stresses are generated leading to fractures of electrodes. 3) SEI layer formation and its growth lead to a reduction in the anode's porosity, which further results in Li-plating or Li-metal formation at the narrow gap between the anode and the electrolyte. 4) Li-plating again results in protrusions on the electrode surface leading to dendrites. It is well established that

the dominant aging mechanisms for graphite anode LIBs are SEI formation, which increases the impedance and the consumption of Li ions [218]. Additionally, lithium metal plating could also contribute to accelerated aging, causing a further increase in capacity and power fade. It can be concluded that while the fracture, lithium plating, and dendrite formation leads to the loss of active lithium resulting in capacity loss, the SEI layer formation affects both the capacity loss and power fade. On the other hand cathode materials in LIBs are significantly affected by both cycling and calendar life. The characteristics of the cathode may differ from one chemistry to another due to their sensitivities to aging. Thus, the degradation mechanisms can be clustered into LLI, LAM_{anode}, $\text{LAM}_{cathode}$ and increase of the faradic and ohmic resistances [3].

Capacity loss is caused by LAM and LLI, and recent studies [219] have shown that LLI is prominent when compared to LAM. LLI is caused due to irreversible Li-plating and SEI layer formation and its growth [58]. Li-ions are inclined to form metallic Li at low temperatures which decreases the amount of cyclable Li-ions that manifests itself as a capacity loss. Consequently, low-temperature charging accelerates the aging phenomenon of LIB [133]. Although, Li-plating can be reduced by an optimized charging process [220], SEI formation and its growth is prudent and also unavoidable. While LLI can take place alone, LAM takes place simultaneously with LLI [152] and lead to both capacity and power fade. LAM can originate from three basic sets of conditions: structural changes during cycling, chemical decomposition or dissolution reactions and surface film modification [157]. On the other hand, ohmic resistance increase is the result of various sources of LLI and LAM [152].

It is evident that the modeling and estimation of the above internal degradation processes are complex due to the interplay among these degradation mechanisms. From the perspective of modeling, recent studies on the continuum model [74] and atomistic-scale mechanisms [221] can be a powerful combination for predicting SEI growth and parameters, such as conductivity. Continuum models, which incorporate chemical/electrochemical kinetics and transport phenomena to produce more accurate predictions than empirical models, provide deeper insight into the cell. These models will provide a new perception of structural growth and the transport of ions in the SEI, and need further research.

In recent times, these electrochemical degradation models, discussed in Section 2, are integrated with the electrochemical SP model [74, 103, 222] for improved SOH estimation. Results on the integration of SEI, fracture, cathode dissolution, CEI growth, and particle cracking in both anode and cathode for SOH estimation are available in literature [104]. However, several internal degradation mechanisms, such as Li-plating and Li-dendrites, are yet to be integrated while estimating the health of LIB. Although Li-plating on graphite anodes is partly reversible [223], Li dendrite could still form on the graphite anodes during fast charging and overcharging conditions, especially in a long-range EV [95]. Further, the studies [9, 79, 85, 86] incorporating advanced SP and reduced-order P2D models are partially comprehensive in considering the combination of various degradation mechanisms to understand the aging effects along with predicting C_{loss} of the battery. These integrated model-based approaches for SOH estimation have improved the SOH estimation accuracy significantly, but still in the infant stage and an open area of future research.

External factors, such as high C_{rate}, high SOC, or low temperatures accelerate the battery's degradation [9] by affecting the internal degradation mechanisms, as discussed in Section 2.3. Analytical aging models [133, 172, 176, 177, 184, 185] are used to represent

the capacity and power fade of the battery under various operating conditions for different battery chemistry, as discussed in Table 5. Semi-empirical aging models, representing the degradation modes of the LIB [186] at different operating conditions, lay the foundations for understanding the interconnection between external stress, internal aging mechanism, and external behavior (capacity/power fade). Therefore, several ECMs [171, 174, 175] are integrated with these analytical models to predict the battery's life-cycle performance. The recent efforts, in [224], to use an improved P2D model to obtain a relationship between the ECM electrical and electrochemical parameters suggest SOH-integrated ECM modeling approaches for more reliable, accurate, and cost-effective solution for SOH estimation, when compared to basic electrochemical models [79]. Integrating or reflecting the contributions of internal degradation mechanisms with empirical models could further improve the SOH estimation results and can be another research direction.

Further, the internal battery parameters, both in electrochemical and ECM, are time-varying. The parameters vary with change in SOC, capacity, and power fade. Therefore, constant parameters ECM, integrated with empirical aging models, lacks accuracy in SOH estimation. Incorporating parameter-varying ECMs for SOC [225] and SOH estimation will further improve the estimation accuracy. Development of filters or learning schemes to estimate/learn the time-varying parameters can provide a more reliable prediction of SOH. However, estimating or learning the time-varying parameters in real time is a challenging problem and could be an area of future research.

On the other hand, machine-learning-based approaches are gaining interest. Both shallow and deep learning-based approaches are also applied to LIB's SOC and SOH estimation. Recently, Deep learning schemes such as CNN, RNN, FNN, GRU-CNN, and LSTMNN are used in predicting the SOH of LIB with good accuracy due to their potent capability to make accurate long-term degradation predictions [197, 198]. One of the primary limitations of these machine-learning approaches is the unavailability of a large amount of degradation data for implementation. To circumvent the issue of large SOH data, real-time online machine learning-based approaches are promising. The learning schemes must use the online measured data to update the learned models with lesser computation requirements. Further, the recent developments in computationally efficient real-time learning [226, 227] in the control research community can be leveraged to learn the complex nonlinear LIB model with the reduced computational requirement.

Another alternative to the data-hungry machine learning approaches is the hybrid methods, such as ICA-data-driven [146, 213], model-based-data-driven [215]), and GPR. These methods are found to be more accurate, compelling, and reliable estimation methods than traditional learning-only algorithms. They have more significant potential, compatibility, and adaptability to varying operating conditions for industrial applications. ICA/DVA methods have also been developed for onboard battery SOC and SOH estimation [228]. Recently, GPR based method is an emerging data-driven approach. It is a bayesian non-parametric probability approach with remarkable performance in non-linear mapping. The non-parametric GPR-based model is considerably convenient to implement onboard with the support of voltage and temperature measurements [202]. GPR is used to extract HI's which unmasks the battery's internal aging mechanisms to estimate the SOH of LIBs [201, 203, 204]. Unlike other data-driven methods, such as SVM, and ANN, GPR brings statistical thought into machine learning, which helps the approach be more accurate. It is also capable of

dealing with issues, such as small sample and prediction uncertainty representation for battery degradation modeling and prognosis [202]. The hybrid approaches are also one of the promising areas of future research for the adaptability and autonomy of BMSs in battery health prediction.

2.6 Conclusion

In this chapter, an in-depth review of different internal and external degradation mechanisms of LIB along with emerging SOH estimation methods is provided. The inter-relations among these degradation mechanisms and their effects on capacity and power fade are also discussed. Although there are several models developed for these internal degradation mechanisms, further research is required to understand the distinguished effects of external degradation-inducing factors on these internal degradation mechanisms.

In the next chapter, we will discuss two different modeling approaches for LIBs a) the SOC-based ECM along with simultaneous SOC and parameter estimation and b) the SOH-coupled ETA model along with the simultaneous estimation of SOC, SOH, and parameter of LIB.

CHAPTER III

SOC AND SOH COUPLED MODELING OF LITHIUM ION CELL

In this chapter, two different modeling approaches for LIBs are presented. Section 3.2 discusses the development of ECM based SOC dependent non-linear model and Section 3.3 discusses the development of the SOH-coupled ETA model. Both these models are used for simultaneous state and parameter estimation in LIBs.

3.1 Introduction

LIBs are widely accepted among other energy storage devices due to their high energy density and long cycle life [5]. However, stress-inducing factors, such as high charging current and low/high operating temperature, aggravate the battery's degradation. So, there is a necessity for an efficient and improved battery design along with furnishing tools to monitor and control such a complex system that will pave the way for their ubiquitous acceptance.

There are two aspects to a battery system: 1) battery design and manufacturing and 2) BMS. The latter is the primary focus of this paper. The key issues to consider while designing a BMS are efficient monitoring, control, and optimal thermal management schemes to mitigate thermal runaway and accelerated aging. Therefore, the reliable functioning of the BMS depends on the accuracy of the SOC, SOH, core temperature, and RUL estimation.

From the SOC estimation point of view, various estimation schemes as discussed in Section 1.2 are available in the literature. On the other hand, accurate identification of internal model parameters is also necessary for fault and stress detection and SOH estimation [33] along with SOC. The adaptive estimation techniques [32], [229], [230], to identify the parameters and estimate the SOC of LIB, in general, consider the parameters to be constant. Although a few results on time-varying parameter [24], [231] estimation is available, the authors in [24], [231] assumed one of the important parameter, i.e., ohmic resistance, R_0, is constant during dynamic computations. Further, the authors in [28] proposed a nonlinear SOC-varying model of LIB only for the discharging cycle and proposed a KF-based approach to estimate the SOC. In this paper [28], the authors' also considered R_0 as a constant parameter during dynamic computations. The internal resistance is a key parameter to determine the SOH and varies with SOC, C-rate, and number of cycles. Further, the ECM parameters are different for the charge and discharge cycles.

SOH estimation, on the other hand, provides the user with information about the degradation behavior of the battery. The most commonly used SOH indicators include variation in battery capacity [165], DC resistance [165], and impedance [36]. SOH due to capacity fade is generally defined as the ratio between the remaining capacity and the initial nominal capacity of the battery. Several variables, such as C_{rate}, SOC, temperature, and electrochem-

ical side reactions inside the cell accelerate the degradation [29]. The internal parameters of the cell change with the change in SOH. Thus, estimation of SOH along with SOC and internal parameters of the cell will allow health-conscious orchestration of charge/discharge profile and thermal management, directing towards safer operation and longer life. There are several SOH estimation methods [29] studied in the literature as discussed in Section 1.2. Among them, model-based estimators, which use the cell's dynamic model, have been extensively studied [225, 232].

Several ETA models [174, 233, 234, 235, 236, 237, 238, 239] have also been proposed considering the effect of aging factors (temperature, C_{rate}, DOD) to track the battery's degradation. The thermal battery model, introduced in [233], is used to study the real-time control of battery cooling by capturing the core and surface temperatures of the cylindrical cell. The model can also predict the transient thermal behavior of cells under various stresses and duty cycles. Later in [234], the authors presented an electro-thermal model by fusing two sub-models: the 2RC ECM and the two-state thermal model developed in [233]. These sub-models are coupled through heat generation, SOC, and temperature-dependent electrical parameters of A123 $LiFePO_4$/graphite battery. The electro-thermal model is further extended in [174] to include the aging dynamics of the $LiFePO_4$/graphite battery adopted from [177]. An empirical aging model [177] reflecting the cycle life aging of $LiFePO_4$/graphite battery is integrated with the electro-thermal model developed in [234] and employed for optimizing charging protocols for three illustrative charge paradigms, such as minimum-time, minimum-aging, and balanced charge.

Later, the ETA model developed in [174] is adopted in [235] to estimate the core and surface temperature of the battery. The authors accounted for the effect of temperature on model parameters and aging. Besides, a similar modification of the thermal-aging model is presented in [236], where the internal temperature of the battery is set to a constant assuming a high-performance battery thermal management system. Although the ETA models proposed in [174, 235, 236] estimate the SOH and temperature of the battery, the aging dynamics used in these models do not include the dependence on one of the main aging factors, i.e., SOC. A modified aging model [1] for $LiFePO_4$/graphite battery accounting for the dependence of SOC is adopted in [237] to capture the effects of charging behavior on capacity loss and derive optimal charging patterns for LIBs.

Although a considerable effort has been put into developing the ETA models [174, 235, 236, 237] to capture aging behavior, the ECM employed in [174, 235, 236, 237] is not coupled with the capacity fade dynamics of the battery. The authors in [238] sketched the SOC coupling with capacity fade dynamics of the battery using simplified ECM while developing a coupled model of the battery pack. The model in [238] assumes constant ECM parameters, limiting its dynamical accuracy, and adopts a capacity fade model without the effect of change in the C_{rate} of the battery. However, the ECM parameters are affected by temperature, C_{rate}, and mechanical stress [29]. In addition, the 1RC ECM used in [238] ignores some of the transient behaviors compared to the 2RC model [2].

Besides SOC, SOH, and temperature [239], estimation of the time-varying and nonlinear parameters of the ETA model is of paramount importance to track the battery's internal degradation, capture power fade, and be nifty in fault detection and isolation. Traditionally, adaptive control approaches are used to estimate parameters of constant parameter models, and then the model is used to design an observer to estimate the states. The primary

limitations of these two-step approaches are that the adaptive algorithm needs to run several times throughout a battery's life to update model parameters to account for the degradation and lacks accuracy in estimating the time-varying parameters. Developing a SOH-coupled model integrated with parameter dynamics, especially the internal resistance, will simplify parameter estimation schemes.

Motivated by the limitations, In the first part of this chapter, we first propose a novel nonlinear state-space model of the LIB, as a switched system, for both charging and discharging cycles. The SOC-dependent nonlinear electric circuit parameters are redefined as the states of the model such that an observer-based approach can be used to estimate the parameters. Then, a NLO design is presented for the switched system to estimate the SOC and the non-linearly varying internal parameters both for charge and discharge cycles.

In the later part of this chapter, we propose two SOH-coupled nonlinear ETA models. The first model comprehends the interplay between the SOC and SOH and couples the parameter-varying ECM dynamics with capacity fade. This makes the ECM model states (SOC) and parameters vary with SOH while existing models assume constant ECM parameters. Then, the SOH-coupled ECM model is integrated with the thermal model of the battery to develop the ETA model. In the second step, the proposed SOH-coupled model is extended to include the dynamics of the ohmic resistance to track the evolution of the internal resistance as an indicator of internal degradation. This extended model allows us to use an observer to estimate both the states and parameters simultaneously in run-time. One of the other advantages of this approach is that the model can now be learned online using a NN for plug-and-play applications in BMS, whose outputs will be both the internal parameters and the states of the cell.

The proposed SOH-coupled and extended nonlinear models are validated with experimental data and numerical simulation. Numerical comparison results are also presented by contrasting our results with the existing uncoupled models [174, 235] and experimental results for capacity fade till the EOL of the battery [240]. Finally, an EKF [241] based state estimation scheme, using the proposed ETA models, is employed to simultaneously estimate the battery's SOC, SOH, temperatures, and ohmic resistance. The SOH estimation results till EOL at different C_{rates} and temperatures are also presented. The model has potential applications in fault diagnostics and prognostics, where the progression of the internal faults is reflected in the battery's internal resistance. The preliminary idea of the paper is presented in [241].

Contributions: The main contributions of the chapter are: 1) development of a novel nonlinear time-varying SOC-based state-space model of the LIB, 2) simultaneous estimation of the SOC and internal battery parameters for both charge and discharge cycle, and 3) the development of a SOH-coupled ETA model with coupled SOC and SOH dynamics, which reflects SOH's impact on ECM parameters, 4) extended SOH-coupled ETA model by incorporating ohmic resistance dynamics, and 5) numerical and experimental validation of the proposed SOH-coupled and the extended models.

The next section discusses the development of a SOC-based model to estimate the SOC and time-varying parameters of the battery simultaneously.

3.2 SOC Varying Model of LIB

SOC and SOH estimation, along with parameter identification of a LIB, are the primary steps toward the development of an efficient BMS. In this section, first, a novel nonlinear state space representation of the ECM of LIB, with SOC-varying electrical parameters, is presented as a switched system, i.e., for both charging and discharging cycles. Second, an NLO is designed to simultaneously estimate the SOC and SOC-varying internal parameters of the ECM. The uniform ultimate boundedness (UUB) of the NLOs state estimation error is guaranteed using Lyapunov stability analysis. In the later part of the section, numerical simulation results are also presented to corroborate the efficacy of modeling and simultaneous estimation scheme.

The remaining section is organized as follows. Section 3.2.1 presents a brief background on LIB ECM and formulates the problem. In Section 3.2.2, the novel SOC based nonlinear switched system model is presented followed by the NLO design. Simulation results are included in Section 3.2.3 followed by the conclusion in Section 3.4.

3.2.1 Background and Problem Formulation

The 2RC ECM of the LIB as shown in Figure 2 is widely adopted for SOC estimation because of reasonable accuracy and ease of implementation. For estimation of the SOC, the ECM is, in general, represented as a linear dynamical system with a nonlinear output equation, given by

$$\begin{aligned} \dot{x} &= Ax + Bu \\ y &= V_{OC}(SOC) + x_2 + x_3 + R_0 u \end{aligned} \tag{3.2.1}$$

where $x = \begin{bmatrix} x_1 & x_2 & x_3 \end{bmatrix}^T \in \mathbb{R}^3$ is the state vector with $x_1 = SOC$, $x_2 = V_{c_{p1}}$, $x_3 = V_{c_{p2}}$, $u = I$ is the control input, and the output $y = V_0 \in \mathbb{R}$ is the terminal voltage. $V_{oc}(SOC)$ is the open circuit voltage which varies with SOC, and C_{use} represents the usable capacity of the battery. The internal dynamics $A \in \mathbb{R}^{3\times3}$ and the control coefficient function $B \in \mathbb{R}^{3\times1}$ are given by $A = \begin{bmatrix} 0 & 0 & 0 \\ 0 & -1/R_{p1}C_{p1} & 0 \\ 0 & 0 & -1/R_{p2}C_{p2} \end{bmatrix}$ and $B = \begin{bmatrix} -1/C_{use} & 1/C_{p1} & 1/C_{p2} \end{bmatrix}^T$. This representation assumes the ECM parameters to be constant over the life of the battery. The following assumption is in general used while developing the model.

Assumption 3.2.1 *[2] The effect of R_{sdis} on the transient behavior of the battery is negligible .*

Traditionally, KF or NLO [24] based approaches are utilized for estimating the SOC of the battery. The model parameters are identified using online adaptive techniques [229] and used in designing the KF and observers. Although the model in (3.2.1) can effectively estimate the SOC, the inherent assumption of time-invariance of parameters [230] may lead to an erroneous SOC value.

In practice, the battery parameters vary non-linearly [28] with SOC, temperature, C-rate, age, and capacity loss both during charge and discharge cycles. Adaptive estimation

of constant parameters is not suitable for the accurate estimation of SOC and SOH of the battery over its life cycle. Further, online estimation of change in ECM parameters, due to the above-mentioned effects, will be useful for fault and stress detection and developing a metric for SOH. Therefore, the problem at hand is twofold: 1) the development of a nonlinear parameter varying model for LIB which can be used to accurately estimate SOC and 2) the design of a higher order NLO for estimating the SOC, and time-varying parameters, simultaneously. Solutions to the above problems are presented in the next section. Since the model parameters are different during the charge and discharge cycle, a switched system approach is utilized to develop a nonlinear parameter-varying model.

3.2.2 SOC-Dependent Model and Nonlinear Observer Design

The ECM parameters of a battery vary with SOC, temperature, current direction and C-rate [242]. In this section, a novel nonlinear state space representation is presented considering the SOC-dependent ECM parameters both for charging and discharging. A non-linear switched dynamical system representation is proposed. Further, a higher-order NLO design for the switched system is presented to simultaneously estimate the states and parameters.

Reformulation of state space model

The SOC-dependent ECM parameters of the LIB, using the HPPC test data [24], can be expressed as

$$\begin{aligned}
R_0 &= a_0 e^{(-(\frac{SOC-b_0}{c_0})^2)} + d_0 e^{(-(\frac{SOC-e_0}{j_0})^2)} + \gamma_0 e^{(-(\frac{SOC-q_0}{s_0})^2)} \\
R_{p1} &= a_1 e^{(-(\frac{SOC-b_1}{c_1})^2)} + d_1 e^{(-(\frac{SOC-e_1}{j_1})^2)} + \gamma_1 e^{(-(\frac{SOC-q_1}{s_1})^2)} \\
R_{p2} &= a_2 e^{(-(\frac{SOC-b_2}{c_2})^2)} + d_2 e^{(-(\frac{SOC-e_2}{j_2})^2)} + \gamma_2 e^{(-(\frac{SOC-q_2}{s_2})^2)} \\
C_{p1} &= a_3 e^{(-(\frac{SOC-b_3}{c_3})^2)} + d_3 e^{(-(\frac{SOC-e_3}{j_3})^2)} + \gamma_3 e^{(-(\frac{SOC-q_3}{s_3})^2)} \\
C_{p2} &= a_4 e^{(-(\frac{SOC-b_4}{c_4})^2)} + d_4 e^{(-(\frac{SOC-e_4}{j_4})^2)} + \gamma_4 e^{(-(\frac{SOC-q_4}{s_4})^2)}
\end{aligned} \tag{3.2.2}$$

where $a_i, b_i, c_i, d_i, e_i, j_i, \gamma_i,$ and s_i for $i = 0, 1, 2, 3, 4$ are the coefficient of approximation. The discharge and charge coefficients are listed in the Table 7 and Table 8, respectively, in Section 3.2.3. The approximated open circuit voltage $V_{oc}(SOC)$ is represented as

$$\begin{aligned}
V_{oc}(SOC) = r_0 + r_1 SOC + r_2 SOC^2 + r_3 SOC^3 + r_4 SOC^4 \\
+ r_5 SOC^5 + r_6 SOC^6 + r_7 SOC^7 + r_8 SOC^8 + r_9 SOC^9
\end{aligned} \tag{3.2.3}$$

where r_i for $i = 0, 1, 2, \cdots, 9$ are constant coefficients given in Table 9 in Section 3.2.3.

Remark 3.2.1 *Note that the coefficients $a_i, b_i, c_i, d_i, e_i, j_i, \gamma_i,$ and s_i for $i = 0, 1, 2, 3, 4$ are different for discharging and charging cycles.*

It is clear from (3.2.2) and (3.2.3), that the ECM parameters and the terminal voltage are highly nonlinear and vary with SOC. Before presenting the nonlinear model of the ECM, the following assumption is necessary.

Assumption 3.2.2 *[243] The rate of change of charging and discharging current is zero, i.e., $dI/dt = 0$.*

The assumption is trivial since the current during the charging and discharging cycles is slowly varying and a high sampling rate of the data acquisition device. Redefine the state vector for charge and discharge cycle $x = [x_1 \;\; x_2 \;\; x_3 \;\; x_4 \;\; x_5 \;\; x_6 \;\; x_7 \;\; x_8 \;\; x_9 \;\; x_{10} \;\; x_{11}]^T$ where $x_1 = SOC, x_2 = \dot{x_1}, x_3 = V_{c_{p1}}, x_4 = V_{c_{p2}}, x_5 = R_0, x_6 = \frac{1}{C_{p1}}, x_7 = \frac{1}{R_{p1}}, x_8 = \frac{1}{C_{p2}}, x_9 = \frac{1}{R_{p2}}, x_{10} = \frac{1}{C_{use}}$, and $x_{11} = V_0$. The state space representation of the charge and discharge condition of the ECM can be expressed as

$$\begin{aligned} \dot{x} &= \begin{cases} f_c(x) + g_c(x)u & u < 0 \\ f_d(x) + g_d(x)u & u > 0 \end{cases} \\ y &= Cx \end{aligned} \tag{3.2.4}$$

where $f_{(.)}(x)$ and $g_{(.)}(x)$ are the internal dynamics and control coefficient vector functions respectively. The subscript c and d denotes the charging and discharging condition, respectively. The discharge current is taken as positive while modeling. The output vector $C = \begin{bmatrix} 0 & 0 & 0 & 0 & 0 & 0 & 0 & 0 & 0 & 0 & 1 \end{bmatrix}$.

The charge and discharge dynamics can be expressed as a switched dynamical system in an input affine form as

$$\begin{aligned} \dot{x} &= f_{q(u)}(x) - g_{q(u)}(x)u \\ y &= Cx \end{aligned} \tag{3.2.5}$$

where $q(u) \in \{c, d\}$ is the switching index function that denotes the charging and discharging cycle of LIB. The vector functions $f_{q(u)}(x) = [0 \;\; 0 \;\; f_3(x) \;\; f_4(x) \;\; 0 \;\; 0 \;\; 0 \;\; 0 \;\; 0 \;\; 0 \;\; f_{11}(x)]^T \in \mathbb{R}^{11}$, and $g_{q(u)}(x) = [-x_{10} \;\; 0 \;\; x_6 \;\; x_8 \;\; g_5(x) \;\; g_6(x) \;\; g_7(x) \;\; g_8(x) \;\; g_9(x) \;\; 0 \;\; g_{11}(x)]^T \in \mathbb{R}^{11}$, where

$$\begin{aligned}
&f_3(x) = -x_3x_6x_7, \;\; f_4(x) = -x_4x_8x_9, \\
&f_{11}(x) = -f_3(x) - f_4(x), \\
&g_5(x) = -(-2(a_0/c_0)((x_1 - b_0)/c_0)e^{(-(\frac{x_1-b_0}{c_0})^2)} - 2(d_0/j_0)((x_1 - e_0)/j_0)e^{(-(\frac{x_1-e_0}{j_0})^2)} \\
&\qquad - 2(\gamma_0/s_0)((x_1 - q_0)/s_0)e^{(-(\frac{x_1-q_0}{s_0})^2)})x_{10}, \\
&g_6(x) = (-2(a_3/c_3)((x_1 - b_3)/c_3)e^{(-(\frac{x_1-b_3}{c_3})^2)} - 2(d_3/j_3)((x_1 - e_3)/j_3)e^{(-(\frac{x_1-e_3}{j_3})^2)} \\
&\qquad - 2(\gamma_3/s_3)((x_1 - q_3)/s_3)e^{(-(\frac{x_1-q_3}{s_3})^2)})x_{10}x_6^2, \\
&g_7(x) = (-2(a_1/c_1)((x_1 - b_1)/c_1)e^{(-(\frac{x_1-b_1}{c_1})^2)} - 2(d_1/j_1)((x_1 - e_1)/j_1)e^{(-(\frac{x_1-e_1}{j_1})^2)} \\
&\qquad - 2(\gamma_1/s_1)((x_1 - q_1)/s_1)e^{(-(\frac{x_1-q_1}{s_1})^2)})x_{10}x_7^2, \\
&g_8(x) = (-2(a_4/c_4)((x_1 - b_4)/c_4)e^{(-(\frac{x_1-b_4}{c_4})^2)} - 2(d_4/j_4)((x_1 - e_4)/j_4)e^{(-(\frac{x_1-e_4}{j_4})^2)} \\
&\qquad - 2(\gamma_4/s_4)((x_1 - q_4)/s_4)e^{(-(\frac{x_1-q_4}{s_4})^2)})x_{10}x_8^2, \\
&g_9(x) = (-2(a_2/c_2)((x_1 - b_2)/c_2)e^{(-(\frac{x_1-b_2}{c_2})^2)} - 2(d_2/j_2)((x_1 - e_2)/j_2)e^{(-(\frac{x_1-e_2}{j_2})^2)} \\
&\qquad - 2(\gamma_2/s_2)((x_1 - q_2)/s_2)e^{(-(\frac{x_1-q_2}{s_2})^2)})x_{10}x_9^2, \\
&g_{11}(x) = -x_6 - x_8 + \frac{g_5(x)}{x_{10}}x_2 - (r_1 + 2r_2x_1 + 3r_3x_1^2 + 4r_4x_1^3 + 5r_5x_1^4 + 6r_6x_1^5 \\
&\qquad + 7r_7x_1^6 + 8r_8x_1^7 + 9r_9x_1^8)x_{10}.
\end{aligned}$$

Remark 3.2.2 *The above state space representation uses SOC-dependent circuit parameters as states of the system. Therefore, the change in parameters can be estimated using observer-based approaches.*

For ease of implementation on board an embedded processor, the discrete-time representation of the dynamics in (3.2.5) can be expressed as

$$\begin{aligned} x_{k+1} &= \bar{f}_{q(u)}(x_k) - \bar{g}_{q(u)}(x_k)u_k \\ y_k &= \bar{C}x_k \end{aligned} \tag{3.2.6}$$

where $x_k \in \mathbb{R}^{11}$, $u_k \in \mathbb{R}$ and $y_k \in \mathbb{R}$ are the state, control input, and output at time instant $k \in \mathbb{N}$, $\mathbb{N} = 1, 2, 3 \cdots$ with a sampling period T, i.e., $t = kT$. Euler's approximation is used to convert (3.2.5) to (3.2.6) where $\bar{f}_{q(u)}(x_k) \in \mathbb{R}^{11}$ and $\bar{g}_{q(u)}(x_k) \in \mathbb{R}^{11}$ are the discrete internal dynamics and control coefficient function, and $\bar{C}$ is the output matrix. The NLO design is presented next.

Nonlinear observer design

The discrete dynamics in (3.2.6) can be rewritten as

$$\begin{aligned} x_{k+1} &= Kx_k + (\bar{f}_{q(u)}(x_k) - Kx_k) - \bar{g}_{q(u)}(x_k)u_k \\ &= Kx_k + \Pi_{q(u)}(x_k) - \bar{g}_{q(u)}(x_k)u_k \end{aligned} \tag{3.2.7}$$

where $K \in \mathbb{R}^{n\times n}$ is a Schur matrix and $\Pi_{q(u)}(x_k) = \bar{f}_{q(u)}(x_k) - Kx_k$.

The non-linear switched observer can be represented by

$$\hat{x}_{k+1} = K\hat{x}_k + \Pi_{q(u)}(\hat{x}_k) - \bar{g}_{q(u)}(\hat{x}_k)u_k + L_{q(u)}(y_k - \hat{y}_k) \tag{3.2.8}$$

where $L_{q(u)} \in \mathbb{R}^{n\times 1}$ is the observer gain.

The state estimation error dynamics are given by

$$\tilde{x}_{k+1} = K\tilde{x}_k + \tilde{\Pi}_k - \tilde{\bar{g}}_k u_k + L_{q(u)}\bar{C}\tilde{x}_k \tag{3.2.9}$$

where the state estimation error $\tilde{x}_k = x_k - \hat{x}_k$ and $\tilde{\Pi}_k = \Pi_{q(u)}(x_k) - \Pi_{q(u)}(\hat{x}_k)$, and $\tilde{\bar{g}}_k = \bar{g}_{q(u)}(x_k) - \bar{g}_{q(u)}(\hat{x}_k)$. The output error is $\tilde{y}_k = y_k - \hat{y}_k = \bar{C}\tilde{x}_k$.

The next theorem guarantees the uniform ultimate boundedness of the state estimation error.

Theorem 3.2.1 *Consider the dynamics of the battery (3.2.7) along with the observer* (3.2.8)*. Let Assumptions 3.2.1 and 3.2.2 hold and there exists a positive definite matrix P satisfying the Lyapunov equation $K^TPK - P = -Q$. Then, the state estimation error is locally uniformly ultimately bounded.*

Proof. The proof is routine and can be completed using a common Lyapunov function. ■

As a preliminary numerical validation, the next section presents the simulation results for simultaneous SOC and parameter estimation using the dynamics in (3.2.5) and the proposed NLO.

3.2.3 Simulation Results and Discussion

A polymer LIB of nominal capacity of $10Ah$ is selected for the simulation purpose. The experimental data presented in [24] is used for reformulating the state space model and estimating the states and parameters of the LIB. The charging and discharging current of $30A$, as shown in Figure 9, is used as an input. Further, a discharge current of $10A$ is used to drop the SOC by 10% in each cycle [24].

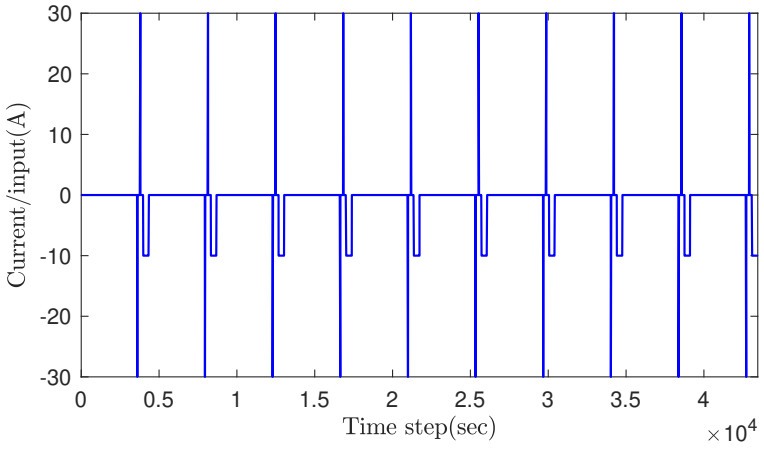

Figure 9: Current (I) during charging and discharging conditions.

Table 7: Coefficients of parameters in discharge condition for SOC-varying model.

$a_0 = 0.0039$	γ_1= 0.0009	d_3=5201	j_1 = 0.554
b_0 = 0.1133	q_1=0.8234	e_3= 0.7096	c_3=0.0833
c_0 = 0.1363	s_1=0.2778	j_3= 0.4034	s_4=0
d_0 =0.0043	a_2= 20.12	γ_3=0	e_1= -0.4803
e_0= 0.5204	b_2= -0.2707	q_3= 0	b_3= 0.8145
j_0 = 0.3415	c_2=0.0881	s_3=0	q_4=0
γ_0 = 0.0037	d_2= 0.0011	a_4= 1.96E4	d_1 =0.0069
q_0= 0.9559	e_2=0.8054	b_4=0.5897	a_3= -3821
s_0 = 0.1552	j_2=0.2373	c_4= 0.0744	γ_4=0
a_1 = 73.18	γ_2= 0.0013	d_4=3.20E4	
b_1 = -0.1586	q_2=0.0329	e_4= 0.7789	
c_1= 0.0538	s_2=0.493	j_4= 0.9388	

The simulation parameters were selected as follows. The initial values were selected as $SOC = 0.7$, $V_{cp1} = 0.5$, $V_{cp2} = 0.5$ for the NLO. The battery parameters are calculated from the initial values using (3.2.2) and the coefficients of these parameters are detailed in Table 7, Table 8. The coefficients of parameters detailed in Table 9 are used to define $V_{oc}(SOC)$ relation in the output equation (3.2.1). The observer gain is chosen as $L_{q(u)} = [0.00308 \;\; 0.0001 \;\; 0.0001 \;\; 5 \times 10^{-6} \;\; 1 \times 10^{-6} \;\; 7 \;\; 1.4 \times 10^{-7} \;\; 8 \;\; 0 \;\; 0.003 \;\; 0]^T$.

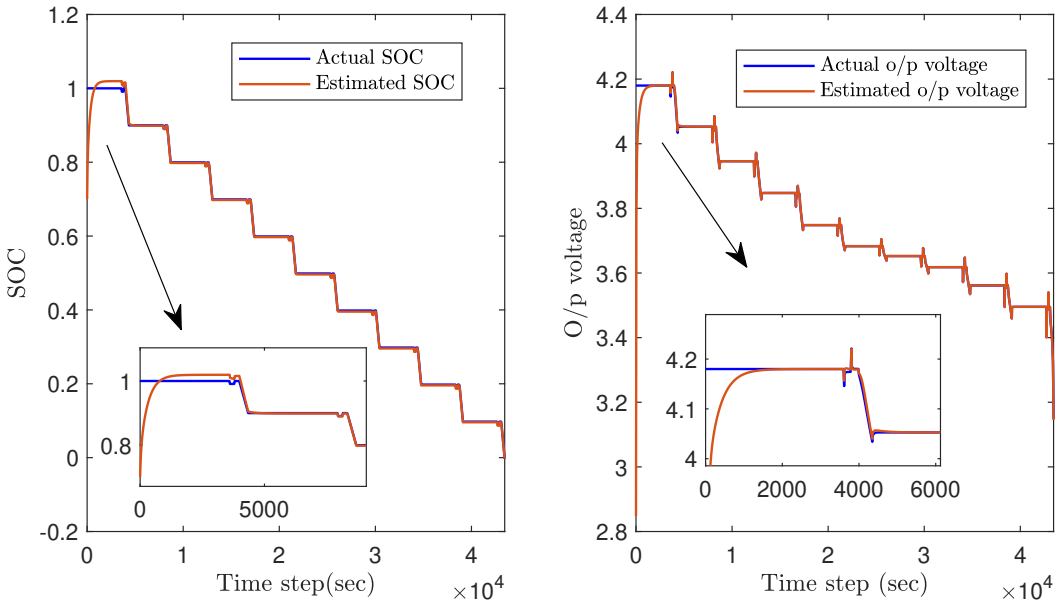

Figure 10: Estimated SOC and output voltage using NLO.

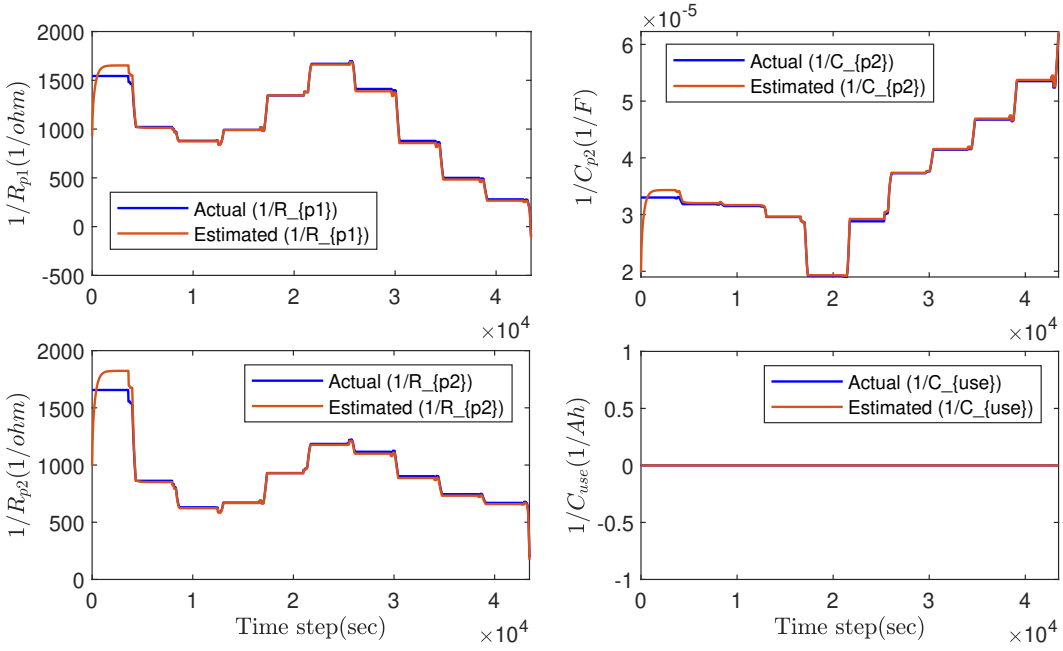

Figure 11: Estimated parameters of LIB using NLO.

Table 8: Coefficients of parameters in charge condition for SOC-varying model.

a_0 =0.0040	γ_1= 0.001204	d_3=3747	j_1 = 0.5055
b_0 = 0.3491	q_1=-0.1257	e_3= 0.4055	c_3=0.1765
c_0=0.579	s_1=0.5632	j_3= 0.1634	s_4=1.475
d_0 =0.0041	a_2= 0.001782	γ_3=1644	e_1=1.302
e_0= 1.217	b_2= -0.1252	q_3= 0.1528	b_3=0.8134
j_0 = 0.4841	c_2=0.1024	s_3=0.1855	q_4= 9.424
γ_0 = 0.0054	d_2= 0.0012	a_4= 2.801E4	d_1 =0.0015
q_0= -0.3046	e_2=-0.0972	b_4=0.8464	a_3= 3779
s_0 = 0.2602	j_2=0.6309	c_4= 0.2426	γ_4=1.69E18
a_1 = 2.2E8	γ_2= 0.0010	d_4=3.484E4	
b_1 = -0.4281	q_2=1.118	e_4= 0.3633	
c_1= 0.0839	s_2=0.3559	j_4= 0.3629	

Table 9: Coefficients of $V_{oc}(SOC)$ for SOC-varying model.

r_0	3.358	r_4	-112.496	r_8	1248.695
r_1	2.523	r_5	-255.813	r_9	-327.932
r_2	-17.736	r_6	1213.788		
r_3	76.748	r_7	-1826.955		

The simulation results are shown in Figure 10 through Figure 13 . From Figure 10, it can be observed that the estimated SOCs and output voltage converge close to the actual values. This shows the ultimate boundedness of the system using NLO. Further, the SOC and output voltage of the battery drops during discharge condition i.e., $30A$ discharge current from Figure 9 and vice-versa as expected. The convergence of SOC and output voltage errors is shown in Figure 13.

The estimated parameters of the battery such as $1/R_{p1}, 1/C_{p2}, 1/R_{p2}, 1/C_{use}$ are shown in Figure 11. Similarly, the estimated states along with parameters of the battery such as $V_{cp1}, V_{cp2}, R_0, 1/C_{p1}$ are shown in Figure 12. From the above figures, we can see that the states along with the parameters of LIB converge close to the actual values proving that the proposed model can efficiently estimate the parameters. From Figure 12 it is observed that the value of R_0 changes with SOC. Also, R_0 varies with temperature and C_{rate} which is included in the next section.

The next section discusses the development of a SOH-coupled model to estimate the SOC and SOH of the battery simultaneously. The proposed model in Section 3.2.2 is extended to a SOH-coupled model by redefining the states of the state space representation in (3.2.5) to include the degradation of the LIB. The extended model integrates the SOC, SOH, and parameters of the battery to facilitate an observer-based approach for SOH estimation.

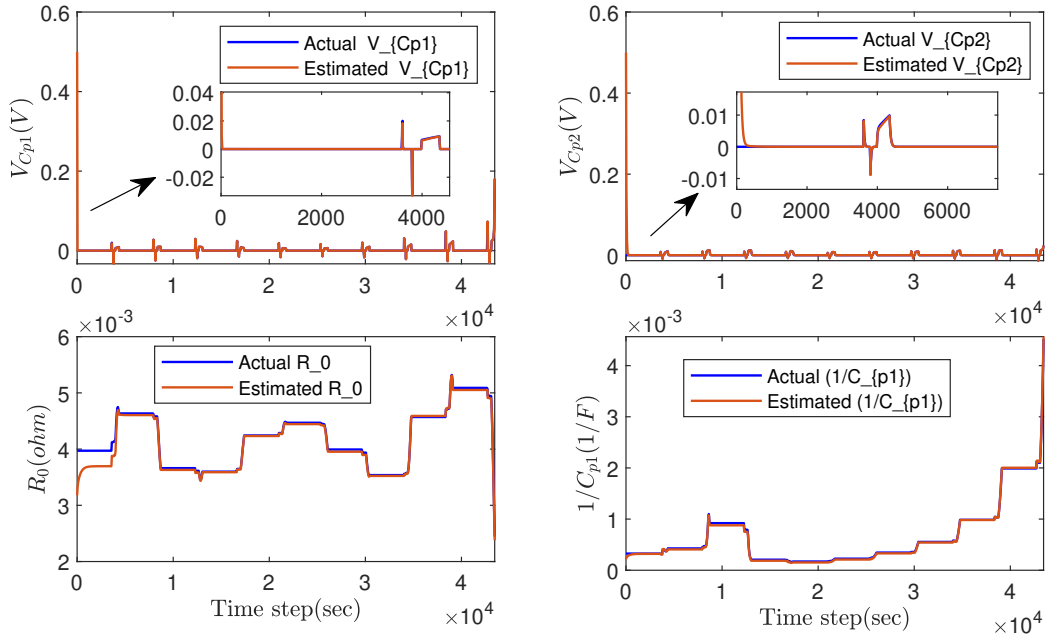

Figure 12: Estimated parameters of LIB using NLO.

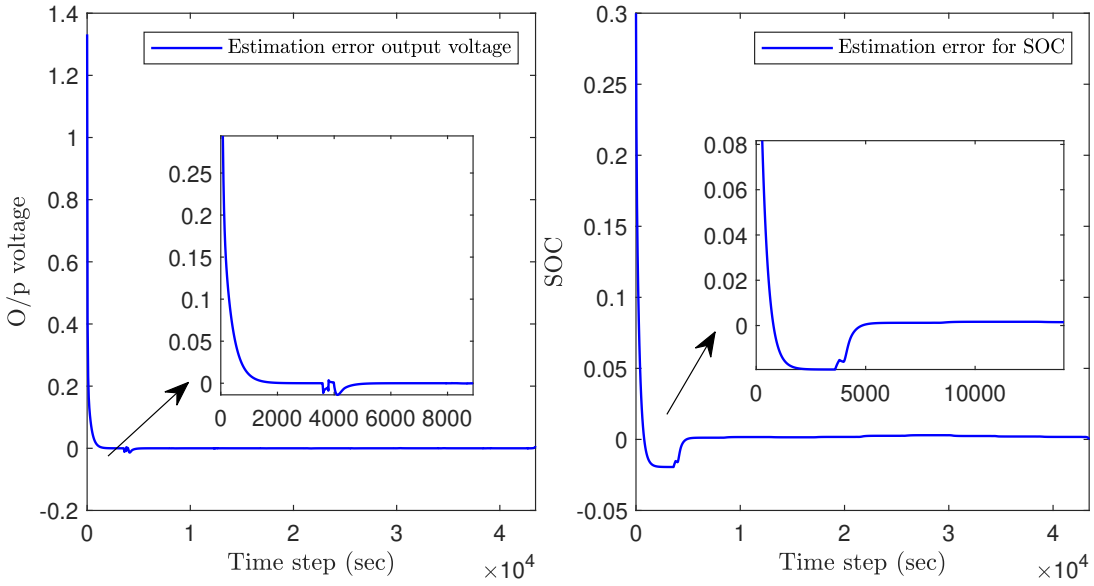

Figure 13: SOC and O/P voltage errors using NLO.

3.3 A Dynamic SOH-Coupled Lithium-ion Cell Model for State and Parameter Estimation

The health assessment of LIBs is critical for BMSs to ensure safe and reliable operation and predict life-cycle. SOH monitoring is challenging since it is governed by several internal and external degradation factors, such as temperature, aging, C_{rate}, and faults. In this section, we propose a SOH-coupled nonlinear ETA model of a $LiFePO_4$/graphite battery, which can be employed to simultaneously estimate the SOC, SOH, temperatures, and internal resistance using a filtering-based approach. The coupling between the ECM and the SOH is established using an empirical capacity fade model of a $LiFePO_4$/graphite battery and its effects on SOC dynamics. In contrast to a constant usable capacity, the proposed model employs a SOH-dependent variable capacity ECM, thereby incorporating the influence of battery aging on the ECM. The SOH-coupled ECM model is then integrated with the thermal model to develop the ETA model. The ETA model is further extended by augmenting the ohmic resistance dynamics to enable monitoring of the evolution of the internal resistance. The proposed SOH-coupled model is validated with numerical simulation and experimental data. Estimation results for SOC, SOH, temperature, and ohmic resistance are included to show the model's potential for monitoring and control applications.

The remaining section is organized as follows. Section 3.3.1 presents a brief background on the ETA model of a LIB and formulates the problem. Section 3.3.3 presents the simultaneous estimation of SOC, SOH, temperature, and internal resistance. The experimental and numerical simulation results are presented in Section 3.3.4, followed by the conclusion in Section 3.4.

3.3.1 Background and Problem Statement

Background

The ECM (in Figure 2) is widely used to determine the terminal characteristics of LIB which is in general, represented as a linear dynamical system with a nonlinear output equation as given in (3.2.1). The parameters $R_0, R_{p1}, C_{p1}, R_{p2}, C_{p2}$, and C_{use} are assumed constant, and the current I is negative for charge and positive for discharge. The CC method represents the SOC dynamics in (3.2.1).

However, the ECM parameters vary with aging factors, such as temperature, C_{rate}, SOC, DOD, and SOH of the battery [2]. Therefore, considering the constant parameter ECM model may lead to inaccurate SOC estimation. Further, to incorporate the thermal and SOH (capacity fade) dynamics along with their effects on the ECM parameters, ETA models of the battery are developed [174]. The ETA model consists of three submodels: 1) a 2-RC varying parameter ECM [2, 244], 2) thermal model [234], and 3) a semi-empirical aging model [174], as described below.

Varying parameter 2-RC ECM model

The state space model in (3.2.1) is redefined to include the aging effects, such as SOC and temperature, on the parameters of the battery. The varying parameter 2-RC model is given

as

$$\begin{aligned}
\frac{dSOC}{dt} &= \frac{-I}{C_{use}} \\
\frac{dV_{c_{p1}}}{dt} &= \frac{-V_{c_{p1}}}{R_{p1}(SOC,T_m)C_{p1}(SOC,T_m)} + \frac{I}{C_{p1}(SOC,T_m)} \\
\frac{dV_{c_{p2}}}{dt} &= \frac{-V_{c_{p2}}}{R_{p2}(SOC,T_m)C_{p2}(SOC,T_m)} + \frac{I}{C_{p2}(SOC,T_m)} \\
V_t &= V_{OC}(SOC) - V_{c_{p1}} - V_{c_{p2}} - R_0(T_m)I
\end{aligned} \tag{3.3.1}$$

where T_m is the average of surface (T_s) and core (T_c) temperature given as $T_m = \frac{T_c+T_s}{2}$. The ECM parameters dependent on SOC and T_m are obtained experimentally and are represented as

$$\begin{aligned}
R_{0_i} &= a_{0_i} e^{\frac{a_{1_i}}{T_m - a_{2_i}}} \\
R_{p1_i} &= (a_{3_i} + a_{4_i}SOC + a_{5_i}SOC^2) e^{\frac{a_{6_i}}{T_m - a_{7_i}}} \\
C_{p1_i} &= a_{8_i} + a_{9_i}SOC + (a_{10_i} + a_{11_i}SOC)T_m \\
R_{p2_i} &= (a_{12_i} + a_{13_i}SOC + a_{14_i}SOC^2) e^{\frac{a_{15_i}}{T_m}} \\
C_{p2_i} &= a_{16_i} + a_{17_i}SOC + a_{18_i}SOC^2 + a_{19_i}SOC^3 + \\
&\quad (a_{20_i} + a_{21_i}SOC + a_{22_i}SOC^2 + a_{23_i}SOC^3)T_m
\end{aligned} \tag{3.3.2}$$

where the subscript $i \in \{c, d\}$ with c and d denote charging and discharging, respectively, and the coefficients $a_{\tau_i} (\tau = 0, \cdots, 23)$ are listed in Section 3.3.4.

Thermal model

The thermal model depicts the dynamics of core temperature (T_c), and surface temperature (T_s), which are expressed as follows [244]:

$$\begin{aligned}
\dot{T}_c &= \frac{T_s - T_c}{R_c C_c} + \frac{Q(t)}{C_c} \\
\dot{T}_s &= \frac{T_a - T_s}{R_u C_s} - \frac{T_s - T_c}{R_c C_s}
\end{aligned} \tag{3.3.3}$$

where $Q(t) = |I(V_{oc}(SOC) - V_t - T_c(t)\frac{dV_{oc}}{dT_c})|$ is the internal heat generation, including joule heating and energy dissipated from electrodes [174], and $\frac{dV_{oc}}{dT_c}$ is the entropic coefficient. The heat generated from the entropic heat is neglected ($\frac{dV_{oc}}{dT_c} = 0$). $R_c(K/W), R_u(K/W), C_c(J/K)$, and $C_s(J/K)$ are the heat conduction resistance, convection resistance, core heat capacitance, and surface heat capacity, respectively. The ambient temperature is denoted by T_a.

Capacity fade model of the lithium-ion battery

The SOH (capacity fade) can be expressed as

$$SOH(t) = SOH(t_0) - \frac{\int_{t_0}^{t} |I(\tau)| d\tau}{2N(SOC, C_{rate}, T_c)C_{use}}. \tag{3.3.4}$$

where t_0 denotes the initial time. Consequently, $SOH = 1$ corresponds to a new battery. A 20% capacity loss is considered the EOL. The time derivative of (3.3.4) yields the battery aging (capacity fade) dynamics and can be written as

$$\dot{SOH}(t) = -\frac{|I(t)|}{2N(SOC, C_{rate}, T_c)C_{use}} \tag{3.3.5}$$

where N denotes the number of cycles until the EOL, which can be found using the expression

$$N(SOC, C_{rate}, T_c) = \frac{3600Ah_{total}(SOC, C_{rate}, T_c)}{C_{use}} \tag{3.3.6}$$

with Ah_{total} is the total amount of charge that can flow in and out of the battery during its operation. The Ah_{total} can be computed from the capacity loss model, obtained experimentally in [1], and is given by

$$C_{loss} = (\alpha SOC + \beta)e^{\frac{E_a + \eta C_{rate}}{R_g T_c}}(Ah)^z \tag{3.3.7}$$

where C_{loss} is a function of the SOC, C_{rate}, and T_c. The variables α and β are severity factor functions, whose values depend on SOC and are given in Table 10. The constant $\eta = 152.5$ models the C_{rate} dependence, R_g is the ideal gas constant, Ah is the accumulated charge throughput, $E_a = 31500$ J mol^{-1} is the activation energy, and the power-law factor $z = 0.57$. Based on the capacity loss (3.3.7), we can compute the Ah_{total} as

Table 10: Optimal values of α, β [1].

$SOC\%$	α	β
$SOC\% < 45$	2896.6	7411.2
$SOC\% \geq 45$	2694.5	6022.2

$$Ah_{total} = \left[\frac{20}{(\alpha SOC + \beta)e^{\frac{-E_a + \eta C_{rate}}{R_g T_c}}}\right]^{\frac{1}{z}}. \tag{3.3.8}$$

The ETA dynamics are formed by combining (3.3.1), (3.3.3), and (3.3.5), and can be expressed as

$$\begin{aligned}
\frac{dSOC}{dt} &= \frac{-I}{C_{use}} \\
\frac{dV_{c_{p1}}}{dt} &= \frac{-V_{c_{p1}}}{R_{p1}(SOC, T_m)C_{p1}(SOC, T_m)} + \frac{I}{C_{p1}(SOC, T_m)} \\
\frac{dV_{c_{p2}}}{dt} &= \frac{-V_{c_{p2}}}{R_{p2}(SOC, T_m)C_{p2}(SOC, T_m)} + \frac{I}{C_{p2}(SOC, T_m)} \\
\dot{T}_c &= \frac{T_s - T_c}{R_c C_c} + \frac{I(V_{oc}(SOC) - V_t)}{C_c} \\
\dot{T}_s &= \frac{T_a - T_s}{R_u C_s} - \frac{T_s - T_c}{R_c C_s} \\
\dot{SOH}(t) &= -\frac{|I(t)|}{2N(SOC, C_{rate}, T_c)C_{use}}.
\end{aligned} \tag{3.3.9}$$

Problem statement

The ETA model in (3.3.9) has two primary limitations: 1) it uses a constant capacity C_{use} and 2) it does not incorporate parameter dynamics. The battery's charge holding capacity (SOC) and parameters vary with the capacity fade of the battery. The usable capacity C_{use} keeps diminishing from the design/nominal capacity as the battery cycles/ages [235]. The ECM model in (3.3.1) uses the CC method to estimate the SOC with constant C_{use}, which decouples the SOC dynamics from capacity fade (SOH), i.e., the C_{use} is not affected by the capacity fade. This will lead to a lower SOC value while estimating and, therefore, adversely affect the charging and discharging level of the cell. Since the ECM parameters are functions of SOC, as given in (3.3.2), the inaccurate SOC value leads to wrong ECM run-time parameters and terminal voltage. Therefore, the SOC dynamics must account for the interplay between the C_{use} and capacity fade.

Besides estimation of the states (SOC, voltages across the capacitors, temperatures, and capacity fade) by the BMS, ECM parameter estimation is also crucial to comprehend power fade and internal behaviors. The ohmic resistance R_0 plays a significant role in determining the power fade of the battery, and it can be used to detect internal degradation and faults [29]. In general, estimating time-varying parameters is challenging, and conventional adaptive estimation techniques may not be useful. Integration of the ohmic resistance dynamics in the model (3.3.9) will provide another degree of freedom in estimating the power fade and internal degradation as a state estimation problem.

In summary, the problem in hand is threefold: 1) the development of a nonlinear SOH-coupled ETA model, which can be used to estimate SOC, SOH, surface, and core temperatures accurately, 2) extending the SOH-coupled model by incorporating the dynamics of R_0 to estimate it as a state, and 3) numerically and experimentally validation of the models. Solutions to the above problems are presented next.

3.3.2 SOH-Coupled Nonlinear Electro-Thermal-Aging Model of LIB

In this section, we have proposed a SOH-coupled dynamic model of the LIB by using the correlation between the capacity fade and usable capacity. Then, we extended the model by integrating the dynamics of ohmic resistance.

SOH-coupled nonlinear ETA model

The proposed coupled ETA model of the LIB cell, shown in Figure 14, depicts the interdependence among the three sub-models (3.3.1), (3.3.3), and (3.3.5). The ECM in Figure 14 a) is coupled with thermal in Figure 14 b) and the capacity fade model of the battery in Figure 14 c). The capacity fade, core, and surface temperature are functions of SOC and $V_{oc}(SOC)$.

Similarly, the thermal model in Figure 14 b) is coupled with ECM in Figure 14 a) and the capacity fade model in Figure 14 c). Therefore, the T_c and T_s are fed to both ECM and capacity fade model. Since the usable capacity C_{use} decreases with the capacity fade, as shown in Figure 14 c), the SOH is fed back to the ECM in Figure 14 a). To couple the SOC dynamics with capacity fade, we can integrate the effect of SOH in (3.3.4) with C_{use} in

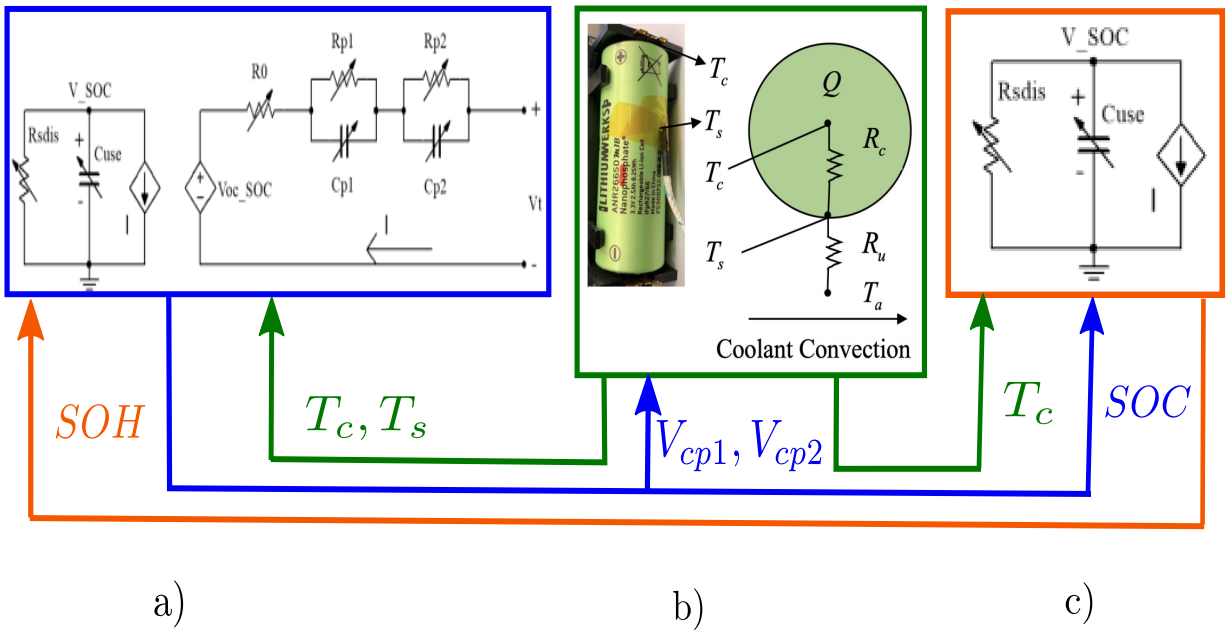

Figure 14: SOH-coupled model of LIB a) ECM, b) thermal model, c) capacity fade model.

(3.3.1) to rewrite the SOC dynamics [238] as

$$S\dot{O}C(t) = \frac{-I(t)}{SOH(t)C_{use}}. \tag{3.3.10}$$

Remark 3.3.1 *Since the charge holding capacity of the battery reduces with aging, the product of $SOH \times C_{use}$, as in (3.3.10), will result in 0% SOC for fully discharged condition and 100% SOC for the fully charged condition during every cycle throughout the life. This will result in an accurate estimation of SOC when compared to constant C_{use}, which leads to a low SOC value with an increase in cycle numbers.*

A SOH-coupled ETA model can be developed by redefining (3.3.9) and taking into account the modified dynamics of SOC in (3.3.10). The state space representation of the SOH-coupled nonlinear ETA model can be expressed in non-affine form as

$$\begin{aligned} \dot{x} &= f^s(x,u) \\ y &= h^s(x,u) \end{aligned} \tag{3.3.11}$$

where $x = [x_1 \;\; x_2 \;\; x_3 \;\; x_4 \;\; x_5 \;\; x_6]^T$ with $x_1 = SOC$, $x_2 = V_{c_{p1}}$, $x_3 = V_{c_{p2}}$, $x_4 = T_c, x_5 = T_s, x_6 = SOH$, $T_m = \frac{x_4+x_5}{2}$, $x \in \mathbb{R}^6$ and the control input $u = [I \;\; T_a]^T \in \mathbb{R}^2$. The output vector $h^s(x,u) = [V_{OC}(x_1) - x_2 - x_3 - R_0(x_4,x_5)u_1 \quad x_5]^T \in \mathbb{R}^2$ and $f^s(x,u) =$

$$\begin{bmatrix} \frac{-u_1}{x_6 C_{use}} \\ \frac{-x_2}{R_{p1}(x_1,x_4,x_5)C_{p1}(x_1,x_4,x_5)} + \frac{u_1}{C_{p1}(x_1,x_4,x_5)} \\ \frac{-x_3}{R_{p2}(x_1,,x_4,x_5)C_{p2}(x_1,,x_4,x_5)} + \frac{u_1}{C_{p2}(x_1,x_4,x_5)} \\ \frac{-x_4}{R_c C_c} + \frac{x_5}{R_c C_c} + \frac{u_1(Voc(x_1)-V_t)}{C_c} \\ \frac{x_4}{R_c C_s} - \frac{x_5}{R_u C_s} - \frac{x_5}{R_c C_s} + \frac{u_2}{R_u C_s} \\ \frac{-u_1}{2N(x_1,C_{rate},x_4)C_{use}} \end{bmatrix}.$$

Remark 3.3.2 *The ETA dynamics of the LIB in* (3.3.11) *depict that the ECM, thermal, and aging models are coupled with each other. Consequently, the effect of SOH on C_{use} will also be reflected in the ETA model states and parameters.*

Extended SOH-coupled ETA model

In this subsection, we extended the SOH-coupled model in (3.3.11) to include dynamics of the ohmic resistance, which is primarily governed by the temperature.

It can be seen from Tables 12 and 13 that the coefficients $a_{0_i}, a_{1_i}, a_{2_i}$ of the R_{0_i} expression in (3.3.2) are close to each other for both charging and discharging conditions. For the BMS application, we have averaged these coefficients to obtain a common coefficient, both for charging and discharging, to represent R_{0_i}, which is given as

$$R_{0_i} = a_{0_v} e^{\frac{a_{1_v}}{T_m - a_{2_v}}} \tag{3.3.12}$$

where the coefficients $a_{0_v}, a_{1_v}, a_{2_v}$ are the average of $\{a_{0_c}, a_{0_d}\}$,$\{a_{1_c}, a_{1_d}\}$,$\{a_{2_c}, a_{2_d}\}$, respectively.

The dynamics of the internal resistance R_0 from (3.3.12) can be expressed as

$$\dot{R}_0 = -a_{0_v} a_{1_v} e^{\frac{a_{1_v}}{\frac{x_4+x_5}{2} - a_{2_v}}} \frac{\dot{x}_4 + \dot{x}_5}{2} \frac{1}{(\frac{x_4+x_5}{2} - a_{2_v})^2} \tag{3.3.13}$$

Redefining the extended state vector for the model in (3.3.11) to include the new state R_0 as $x = [x_1 \;\; x_2 \;\; x_3 \;\; x_4 \;\; x_5 \;\; x_6 \;\; x_7]^T$ where $x_7 = R_0$, the reformulated state space model in (3.3.11) in non-affine form is given as

$$\begin{aligned} \dot{x} &= f^p(x, u) \\ \bar{y} &= h^p(x, u) \end{aligned} \tag{3.3.14}$$

where $h^p(x,u) = [V_{oc}(x_1) - x_2 - x_3 - x_7 u_1 \quad x_5]^T$, and $f^p(x,u) =$

$$\begin{bmatrix} \frac{-u_1}{x_6 C_{use}} \\ \frac{-x_2}{R_{p1}(x_1,,x_4,x_5)C_{p1}(x_1,x_4,x_5)} + \frac{u_1}{C_{p1}(x_1,x_4,x_5)} \\ \frac{-x_3}{R_{p2}(x_1,,x_4,x_5)C_{p2}(x_1,,x_4,x_5)} + \frac{u_1}{C_{p2}(x_1,x_4,x_5)} \\ \frac{-x_4}{R_c C_c} + \frac{x_5}{R_c C_c} + \frac{u_1(Voc(x_1)-V_t)}{C_c} \\ \frac{x_4}{R_c C_s} - \frac{x_5}{R_u C_s} - \frac{x_5}{R_c C_s} + \frac{u_2}{R_u C_s} \\ \frac{-u_1}{2N(x_1,C_{rate},x_4)C_{use}} \\ f_7(x) \end{bmatrix}$$, where $f_7(x)$ is the right-hand side of the (3.3.13).

Remark 3.3.3 *The model assumes the rate of change of charging and discharging current is zero, i.e., $dI/dt = 0$ [225]. This is a trivial assumption since the data acquisition system used in the BMS has, in general, a very high sampling rate.*

Remark 3.3.4 *The state space representation in* (3.3.14) *uses SOH-dependent ECM parameter R_0 as a state of the system. Therefore, the change in parameter can be estimated using any observer-based approaches along with SOC, SOH, and temperatures. Note that the SOH-coupled model does not include power fade dynamics. Therefore, the R_0 changes only reflect the capacity fade and temperature effects.*

3.3.3 Simultaneous State and Parameter Estimation

In this section, we have presented the simultaneous states (SOC, SOH, T_c, T_s) and parameter (R_0) estimation scheme using the models proposed in the previous section and an EKF.

For the ease of on-board BMS implementation, the discrete-time representation of the SOH-coupled ETA model in (3.3.14) can be expressed as

$$\begin{aligned} x_{k+1} &= f^H(x_k, u_k) \\ y_k &= h(x_k, u_k) + v_k \end{aligned} \tag{3.3.15}$$

where the nonlinear function $f^H(x_k, u_k)$ is the discrete internal dynamics, and $h(x_k, u_k)$ is the output function with observation noises v_k at time instant $k \in \mathbb{N}$ with a sampling period T, i.e., $t = kT$. In the simplest form, Eulers' approximation can be used to convert (3.3.14) to (3.3.15). Other higher-order approaches may also be employed. For completeness, we have presented the discrete-time EKF algorithm below in Algorithm 1. The EKF algorithm

Algorithm 1 Extended Kalman filter algorithm.

Step 1: Initialization $k = 0$

Initialize state vector and covariance matrix

$\hat{x}_0^- = E(x_0), P_0^- = E[(x_0 - \hat{x}_0^-)(x_0 - \hat{x}_0^-)^T]$

Step 2: Computation $k = 1, 2, ...$

Prediction Step:

$\hat{x}_{k|k-1} = f(\hat{x}_{k-1|k-1}) + g(\hat{x}_{k-1|k-1})u_k$ ▷ Predicted state estimate

$\hat{y}_k = h(\hat{x}_{k|k-1}, u_k)$

$P_{k|k-1} = F_k P_{k-1|k-1} F_k^T + Q_k$ ▷ Predicted covariance estimate

Update Step:

$\tilde{y}_k = y_k - \hat{y}_k$ ▷ Error

$S_k = H_k P_{k|k-1} H_k^T + R_k$ ▷ Residual covariance

$K_k = P_{k|k-1} H_k^T S_k^{-1}$ ▷ Optimal kalman gain

$\hat{x}_{k|k} = \hat{x}_{k|k-1} + K_k \tilde{y}_k$ ▷ Updated state estimation

$P_{k|k} = (I - K_k H_k) P_{k|k-1}$ ▷ Updated covariance estimation

[241] uses two steps to estimate the states: 1) update and 2) predict step. The estimated state vector is denoted by $\hat{x}_k$, and the control input and output, respectively, are denoted by the u_k and y_k. The output residual is defined as $\tilde{y}_k = y_k - \hat{y}_k$ with $\hat{y}_k$ as the estimated output of the EKF.

The prediction step is used to estimate state $\hat{x}_k$ and covariance matrix $P_{k|k-1} \in \mathbb{R}^{n \times n}$. The update step is used to update the state and covariance estimates using the Kalman gain $K_k \in \mathbb{R}^n$, residual covariance matrix $S_k \in \mathbb{R}^{m \times m}$, measurement variance matrix $R_k \in \mathbb{R}^{m \times m}$, and measurement matrix H_k. The state transition and observation matrices F_k^H and H_k, respectively, are given by

$$\begin{aligned} F_k^H &= \frac{\partial f^H}{\partial x}|_{\hat{x}_{k-1|k-1}, u_k} \\ H_k &= \frac{\partial h}{\partial x}|_{\hat{x}_{k|k-1}, u_k}. \end{aligned} \tag{3.3.16}$$

The model validation and state and parameter estimation results for SOH coupled models developed in (3.3.11) and (3.3.14) are presented next.

3.3.4 Simulation and Experimental results

In this section, we have presented both simulation and experimental results to validate the proposed models developed in Section 3.3.2 and the state estimation scheme proposed in Section 3.3.3. First, the SOH-coupled model is validated via simulation by comparing it with the existing uncoupled models, and then the experimental validation is presented using an actual drive cycle current as input. Second, the extended model is validated using experimental data under the same drive cycle. Finally, the state estimation results using EKF with two different drive cycles are presented.

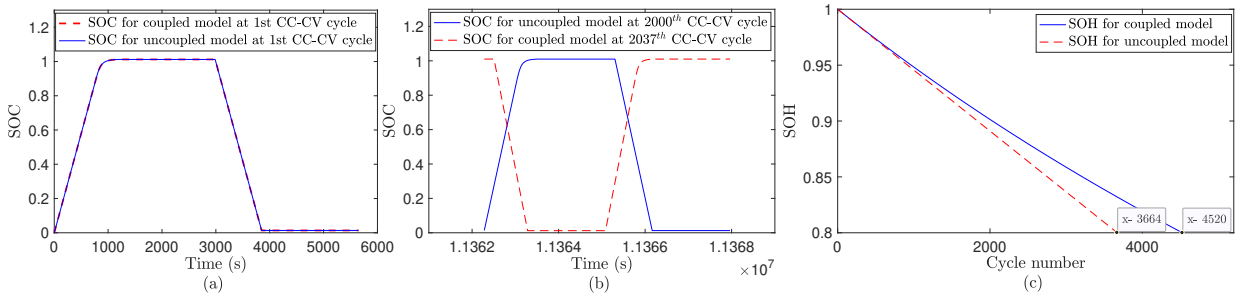

Figure 15: Comparison results between SOH coupled model (3.3.11) and the SOH uncoupled model (3.3.9) for $10A$ (approx. $4.17C_{rate}$) CC-CV cycling at $T_a = 25°C$; a) SOC for the first charge-discharge cycle, b) SOC for a time window at approximate mid-life, c) SOH decay for EOL cycle.

SOH-coupled model validation

In this subsection, we present comparison results between the SOH-coupled model in (3.3.11) and the ETA model in (3.3.9) [174, 235]. The initial state vector was selected as $x = [0\ 0.1\ 0.1\ 10\ 25\ 1]^T$ with sampling time of $1s$. A 10A constant current constant voltage (CC-CV) charge-discharge cycle was used as an input for both the proposed SOH coupled model (3.3.11) and uncoupled model (3.3.9) to observe the battery degradation over the life.

Figure 15 a) and b) depict the comparison between the evolution of SOC for both models to illustrate the difference between the number of charge-discharge cycles. From Figure 15 (a), it can be seen that the SOCs during the first charge and discharge cycle are the same for both the coupled and uncoupled models with the same initial conditions. This similarity is due to the SOH value being 100% for a new cell. Figure 15 (b) depicts the SOC curves for both models for a time window at approximate mid-life. It can be observed that although the time window for both the models is the same, the proposed coupled model was at its 2037^{th} charge-discharge cycle, whereas the uncoupled model was at its 2000^{th}.

It can be observed from (3.3.4) that as the battery ages, the denominator term $(SOH * C_{use})$ keeps diminishing. This leads to a shorter charge and discharge time to reach the current full capacity with the same CC-CV charging. However, since the uncoupled model

uses constant C_{use} throughout the battery's cycle life, the charge/discharge times are the same for each cycle and longer, leading to less cycle number in the same time window, as shown in Figure 15 (b).

Figure 15 c) depicts the comparison results for SOH decay to EOL (80%) of the battery for both uncoupled and coupled models. It can be observed that the SOH for the uncoupled model (3.3.9) decays to EOL faster than the proposed coupled model (3.3.11). The EOL for the uncoupled model is achieved at 3664 cycles when compared to 4520 cycles for the proposed coupled model. This is because the constant C_{use} in SOC dynamics of the uncoupled model (3.3.9) makes the cell charge up to the constant rated capacity until EOL leading to a lesser number of cycles. On the other hand, the proposed coupled model's SOC dynamics take capacity fade into account and always limit the charging/discharging to the current charge-holding capacity of the battery and, hence, depict a higher cycle number to reach EOL.

Furthermore, we have compared the number of cycles till the EOL of the uncoupled and the proposed model with experimental validation results in [240], shown in Figure 16 a), b). The EOL charge-discharge cycle number, with the input of 10A at 65^0C, of the coupled model (3.3.11) is found to be 457 cycles, as shown in Figure 16 a), which is more closer to the experimental results presented in [240], i.e., at 0.8 SOH the number of cycles is greater than 450 cycles at $65°C$. On the other hand, the uncoupled model (3.3.9) EOL cycle number is 405, as shown in Figure 16 b), which is lower than the experimental results in [240] as discussed above. This implies that the proposed SOH-coupled model (3.3.11) more accurately represents the actual cell dynamics and number of cycles of operation.

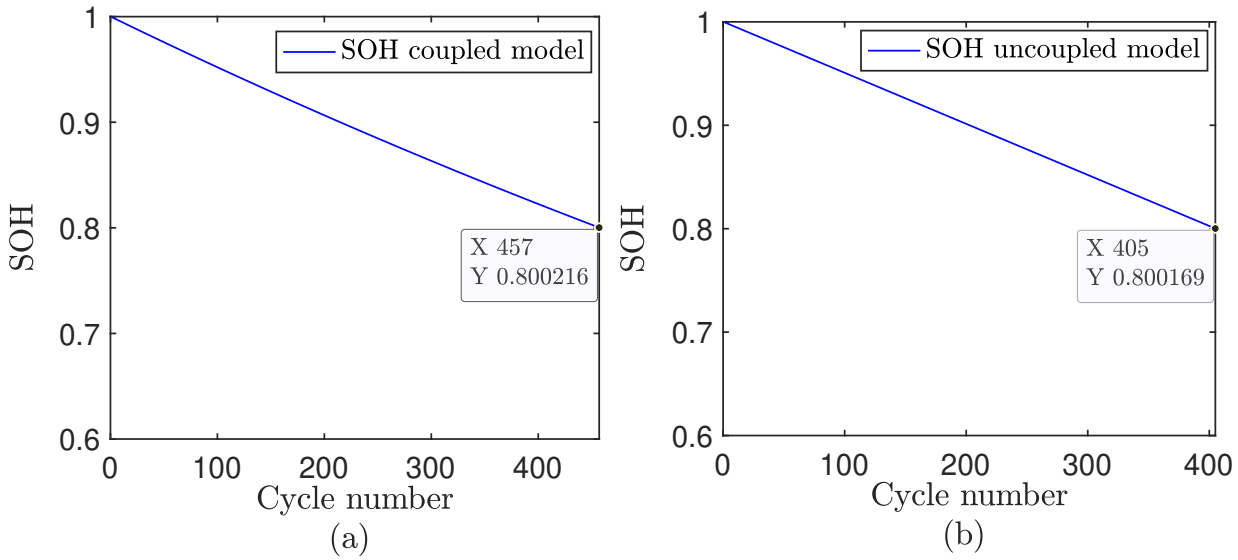

Figure 16: SOH decay $(4.17C_{rate}, 65°C)$ for a) coupled and b) uncoupled model.

Experimental validation

In this subsection, experimental studies are conducted on cylindrical A12326650 $LiFePO_4$/graphite cells with a capacity of 2.5 Ah. Maccor 4300M battery testing system, shown in Figure 17,

is used for the experiments. All the tests were conducted in the environmental Chamber. The testing system records the battery's measured data (voltage, current, and temperature) to the computer. We imported the recorded current and voltage to Matlab/Simulink to validate the proposed coupled models in (3.3.11) and (3.3.14). First, the capacity of the

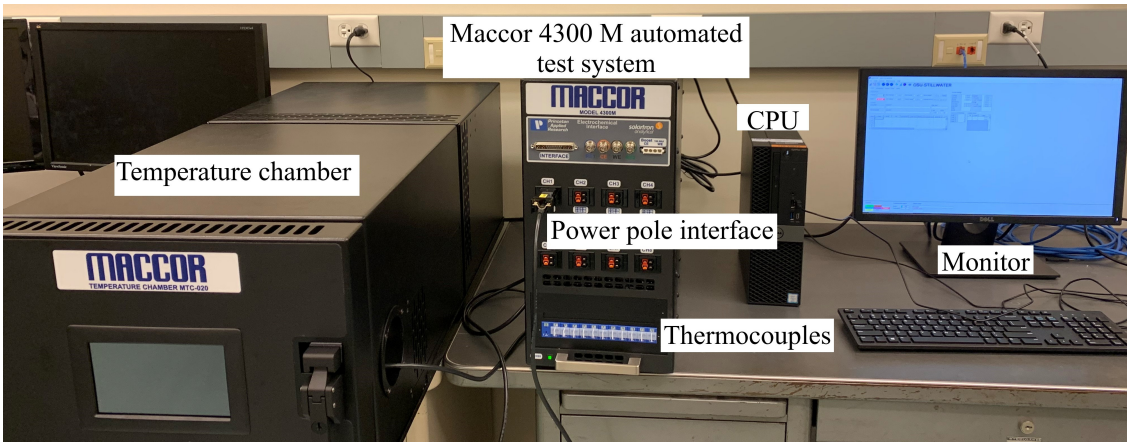

Figure 17: Maccor testing equipment.

cell is measured experimentally by cycling the battery at a low rate (C/20) and found to be 2.4Ah. Next, the $V_{oc}(SOC)$ curve is obtained from the OCV-SOC test as follows,

1. The cell was fully discharged to 0% SOC following the standard CC-CV protocol as shown in Figure 18.
2. Then, the batteries were rested for 2h and charged with C/20 in the intervals of 10%SOC.
3. The OCV of batteries was measured after 2h rest after each 10% SOC increment.
4. Steps 3) and 4) were repeated until the batteries were charged to 100%SOC.
5. Steps 3), 4), and 5) were repeated for discharge protocol.

Figure 19 depicts the V_{oc} varying with SOC for both charge and discharge cycles. The average of these curves is used to model the $V_{oc}(SOC)$ curve. It can be seen that $V_{oc}(SOC)$ has an almost linear behavior in the region between 10% and 100% SOC and exponentially drops while the SOC is below 10% [245]. Although V_{oc} varies with temperature, the authors in [246] showed that V_{oc} variation with temperature is minimal in $LiFePO_4$ cells. Therefore, the OCV-SOC test is carried out at a constant $(25°C)$ temperature. From the experimental data, the V_{oc} and SOC relation can be approximated as

$$\begin{aligned} V_{oc}(SOC) = p_0 + p_1 SOC + p_2 SOC^2 + p_3 SOC^3 + \\ p_4 SOC^4 + p_5 SOC^5 + p_6 SOC^6 + \\ p_7 SOC^7 + p_8 SOC^8 \end{aligned} \tag{3.3.17}$$

where the coefficients p_ξ, $\xi = 0, \cdots, 8$, are listed in Table 11. Likewise, pulse charging

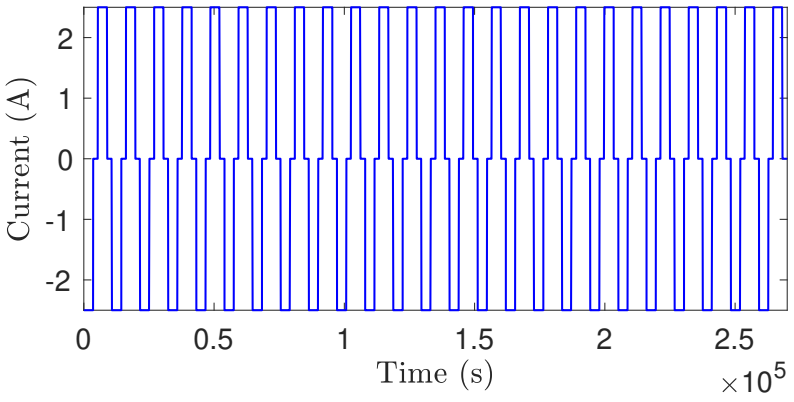

Figure 18: CC-CV current at $1C_{rate}$.

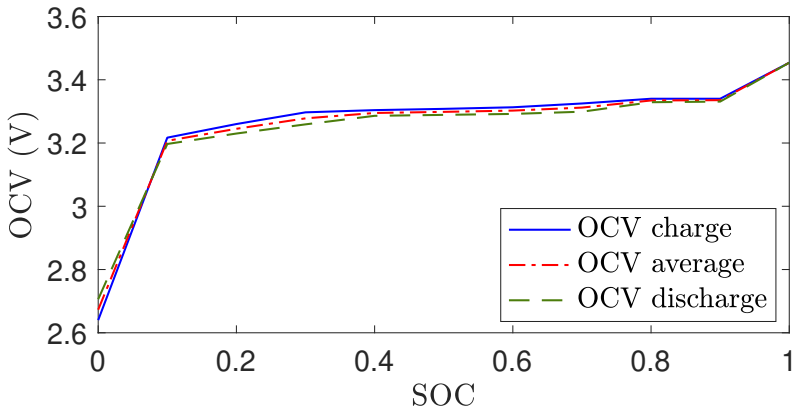

Figure 19: OCV varying with SOC for charge and discharge cycle.

Table 11: Coefficients of $V_{oc}(SOC)$ for SOH-coupled model.

$p_0 = 2.6716$	$p_3 = 530.5705$	$p_6 = -2041.9950$
$p_1 = 12.4519$	$p_4 = -1428.5355$	$p_7 = 982.9183$
$p_2 = -111.8739$	$p_5 = 2249.9804$	$p_8 = -192.7344$

and discharging currents, as shown in Figure 20, are used to extract the parameters of the ECM [244] at different temperatures ($15°C$, $25°C$, $35°C$, and $45°C$). The ECM parameters are identified using the pulse-relaxation experiments [244], i.e., the voltage response curves during the rest period (pulse-relaxation) at each SOC and temperature are used to compute R0 and other parameters of ECM. The ECM parameters are then characterized as functions of SOC and temperature for both charge and discharge, as given in (3.3.2). The coefficients for the parameters given in (3.3.2) are listed in Table. 12 and 13. The parameters of the single cell lumped thermal model are adopted from [234], such as $Ru = 3.08$, $Rc = 1.94$, $Cc = 62.7$, $Cs = 4.5$, and $Rg = 8.314$ [244]. The SOH model parameters are given in Section 3.3.1. The A12326650 cell is cycled using a drive cycle current, as shown in Figure 21, and

Table 12: Coefficients of parameters in charge condition for SOH-coupled model.

a_{0_c} =0.00374	a_{8_c}=2700	a_{16_c}= 3.295E4
a_{1_c} = 45.19	a_{9_c}= -3152	a_{17_c}=5.078E5
a_{2_c}=-19.82	a_{10_c}= 39.99	a_{18_c} = -1.271E6
a_{3_c} =0.0005564	a_{11_c}=15.79	a_{19_c}=7.433E5
a_{4_c}= -0.001371	a_{12_c}=0.002505	a_{20_c}=4039
a_{5_c} = 0.002355	a_{13_c}= -0.002719	a_{21_c}=-1.384E4
a_{6_c}= 220.4	a_{14_c}= 0.008104	a_{22_c}=2.434E4
a_{7_c}=-51.55	a_{15_c}=15.55	a_{23_c}= -1.422E4

Table 13: Coefficients of parameters in discharge condition for SOH-coupled model.

a_{0_d} =0.003304	a_{8_d}=-971.6	a_{16_d}= 0.001499
a_{1_d} = 53.82	a_{9_d}= 3892	a_{17_d}=-3.648E5
a_{2_d}=-19.21	a_{10_d}= 83.94	a_{18_d} = 1.487E6
a_{3_d} =0.002477	a_{11_d}=-71.61	a_{19_d}=-1.129E6
a_{4_d}= -0.006782	a_{12_d}=0.007987	a_{20_d}=746.4
a_{5_d} = 0.005186	a_{13_d}= -0.01778	a_{21_d}=2.027E4
a_{6_d}= 132.5	a_{14_d}= 0.01273	a_{22_d}=-6.325E4
a_{7_d}=-23.39	a_{15_d}=23	a_{23_d}= 4.447E4

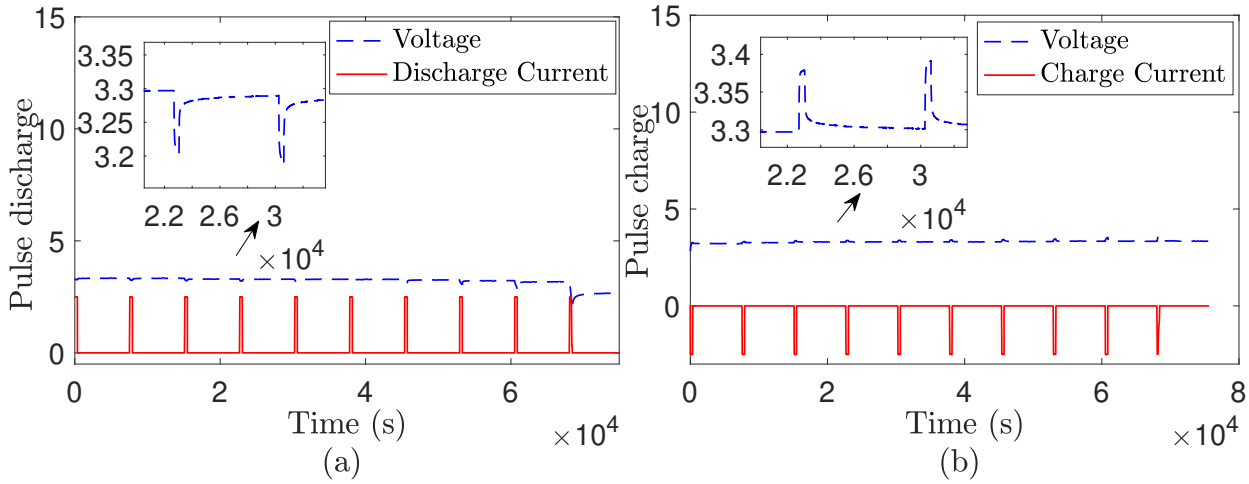

Figure 20: a) Pulse discharge voltage and current profile, b) pulse charge voltage and current profile.

the same current is used as an input to the proposed coupled model (3.3.11). Figure 22 (a) depicts the comparison results of the model voltage output with experimentally measured voltage. The model output tracks the experimentally obtained voltage with RMSE 0.0063V. Correspondingly, the comparison results for measured and model surface temperatures are

given in Figure 22 (b). The model tracks the experimentally measured surface temperature with RMSE 0.0926°C.

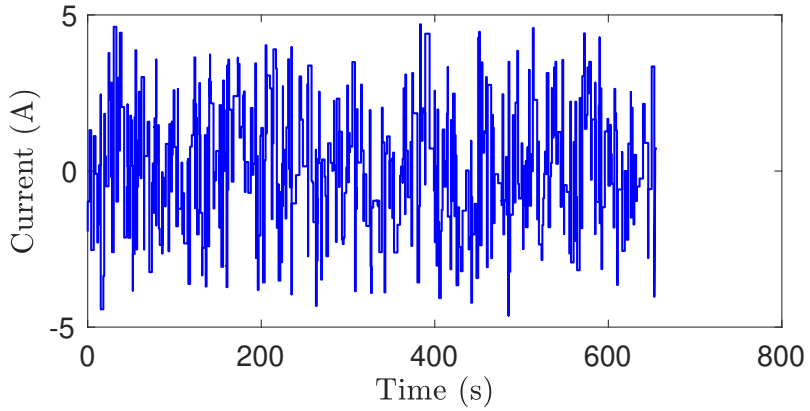

Figure 21: Drive cycle current.

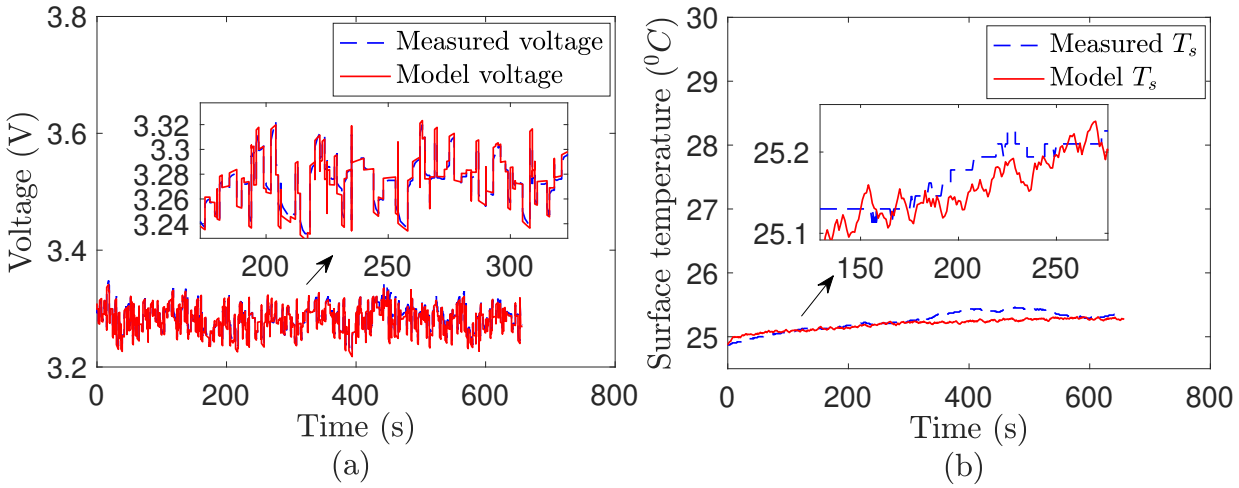

Figure 22: Comparison results with drive cycle input current: a) SOH-coupled model (3.3.11) output voltage with an experimentally measured terminal voltage of the A123 battery under the same input current, b) SOH-coupled model (3.3.11) surface temperature with an experimentally measured surface temperature of the A123 battery under the same input current.

Validation of the extended model

Similar to the experimental validation of the proposed model (3.3.11), the extended model (3.3.14) is validated under the same drive cycle current. The output voltage tracks the experimentally obtained voltage with RMSE 0.0054V, and the model surface temperature tracks the experimentally measured surface temperature with RMSE 0.1°C. To avoid redundancy, the plots for the above comparison results are not included in the paper. Instead, the comparison results between the measured R_0 and model R_0 at $T_a \approx 25°C$ are presented in

Figure 23. The R_0 obtained from experiments approximated as in (3.3.12) for both charge and discharge cycles is compared with the model state R_0. From Figure 23, it can be seen that the model state R_0 tracks the measured values with RMSE $7.7E-8\Omega$. The SOC, SOH,

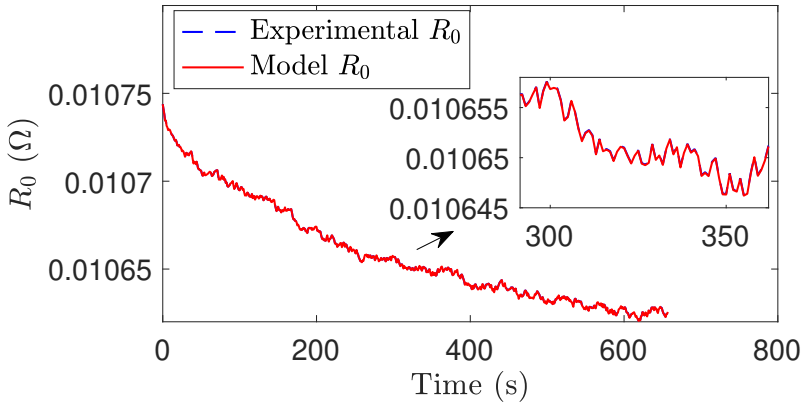

Figure 23: Comparison results with drive cycle input current for measured R_0 using (3.3.12) and Model R_0 from the SOH coupled model (3.3.14).

T_c, T_s, and R_0 estimation results using EKF are presented next.

Table 14: Output voltage RMSEs at different $C_{rates}, T_a = 25°C$.

C_{rate}	RMSE	SOH	Cycle number
1	0.0029	0.8	9803
3	0.0038	0.8	6279
5	0.0040	0.8	3924
10	0.0042	0.8	1393

Simultaneous state and parameter estimation

In this subsection, two different drive cycle currents are used for simultaneous state and parameter estimation using EKF.

First, the drive cycle input current, as shown in Figure 21, is used for EKF estimation of voltage, T_c, SOC, and SOH for the proposed model (3.3.11), which is given in Figure 24 a), b) and Figure 25 a) and b), respectively. The initial value vector was chosen as $\hat{x}_0 = [0.33\ 0.002\ 0.002\ 24.7\ 24.7\ 0.98]^T$, $P = diag[2, 0.04, 0.04, 0.01, 0.01, 0.023], Q = 0.000001 * ones(6, 6)$, and $R = 1E-7\mathbf{I}$. It can be clearly seen that the EKF is able to estimate the state close to the actual values. The output voltage, T_c, SOC, and SOH estimation errors are within a 1% band with RMSEs 0.0011, 0.0065, 0.0015, and 0.0060, respectively.

Second, an Urban Dynamometer Driving Schedule (UDDS) current profile, as shown in Figure 26 a), is used as an input to the proposed coupled model (3.3.11). Figure 26 b) and Figure 27 a) and b) depict the estimation results for voltage, SOC, and SOH, respectively.

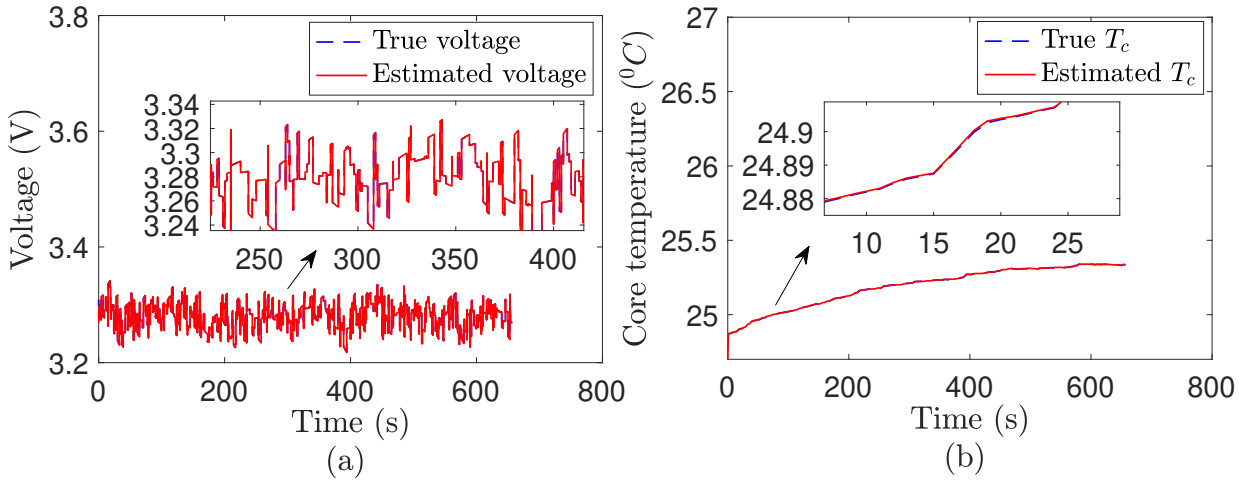

Figure 24: Comparison results with drive cycle input current a) SOH-coupled model (3.3.11) output voltage and estimated voltage using EKF under the same input current, b) Core temperature from the model and EKF under the same input current.

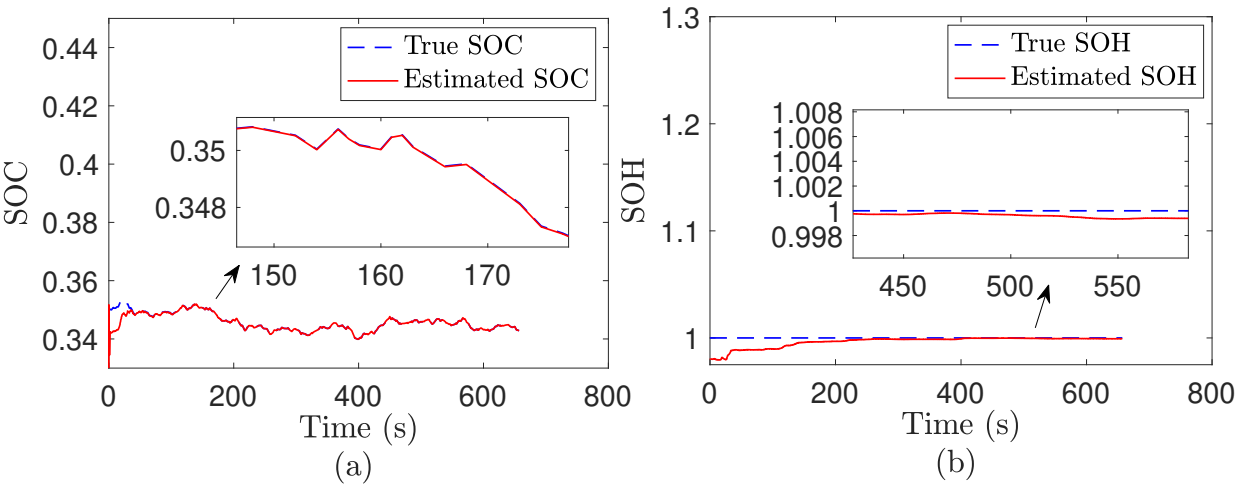

Figure 25: Comparison results with drive cycle input current a) SOC from the model (3.3.11) and EKF under the same input current, and b) SOH from the model and EKF under the same input current.

It can be observed that the estimated voltage and states (SOC, SOH) converge close to the actual value. The output voltage, SOC, and SOH estimation errors are within the 1% band with RMSEs 0.0016, 0.0014, and 0.0085, respectively. This implies that the proposed model can be employed for characterizing the SOH of LIB under real-driving scenarios. Next, the comparison results for EKF estimation of R_0 for the extended model (3.3.14) are given in Figure 28 under the drive cycle input current as shown in Figure 21. The R_0 estimation error is within a 1% band with RMSE $1.963E-4$.

Finally, we present simulation results at high C_{rates} and different temperatures to evaluate the proposed model (3.3.11) and EKF using CC-CV input current. The initial value

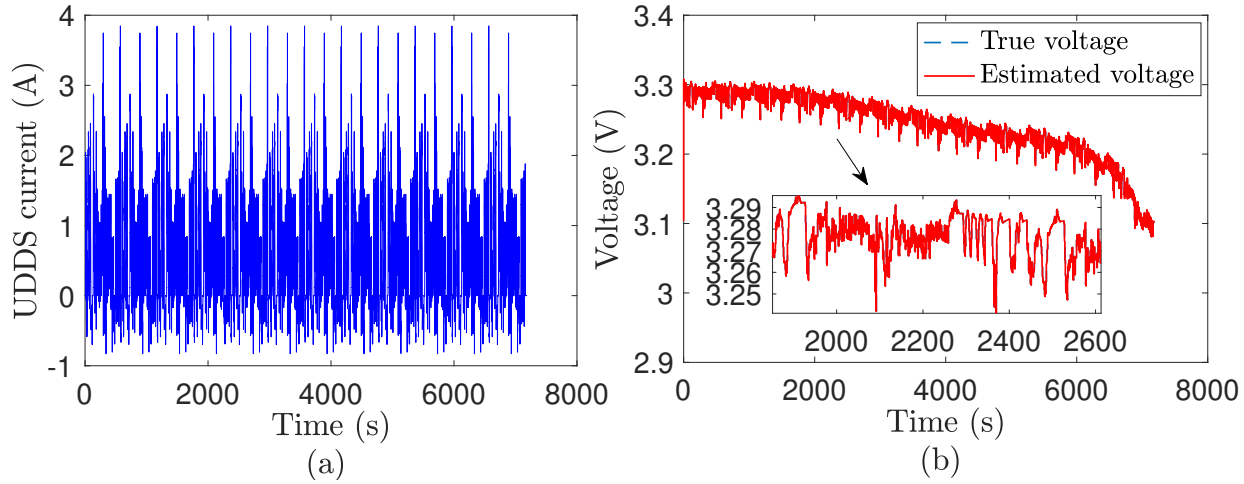

Figure 26: a) UDDS input current, b) Comparison results for output voltage from SOH-coupled model (3.3.11) and EKF under the same UDDS current.

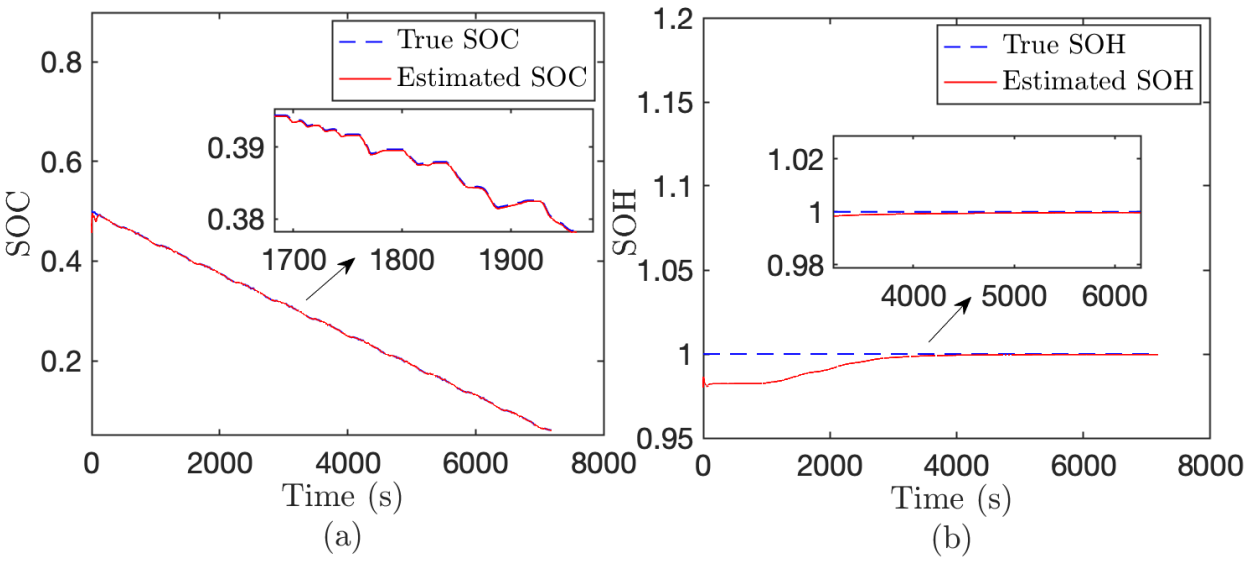

Figure 27: Comparison results with UDDS current a) SOC from the model (3.3.11) and EKF under the same input current, and b) SOH from the model and EKF under the same input current.

vector was chosen as $\hat{x}_0 = 0.1 * [x(1)\ x(2)\ x(3)\ 2 * x(4)\ 2 * x(5)\ 7.9 * x(6)]^T$, $P = 1E4 * diag[1, 4, 4, 10, 18, 1E-9], Q = 0$, and $R = 1E-7 * diag[1, 1]$. Figure 29 a), b), c), and d) depict the SOH estimation using EKF for the coupled model (3.3.11) at different C_{rates} ($C_{rate} = 1, 3, 5, 10$), and temperatures ($T_a = 35°, 45°, 55°C, 65°C$). Here, it can be observed from Figure 29 a), b), c), and d) that the estimated SOH converges close to the actual value at all C_{rates}. Table 14 presents the output voltage RMSEs at different C_{rates} with SOH decay to 0.8. It is found from Figure 29 a) at $1C_{rate}$, SOH decays to 0.8 after 9803 CC-CV cycles of the battery, Figure 29 b) SOH decays to 0.8 after 6279 CC-CV cycles of the battery at $3C_{rate}$,

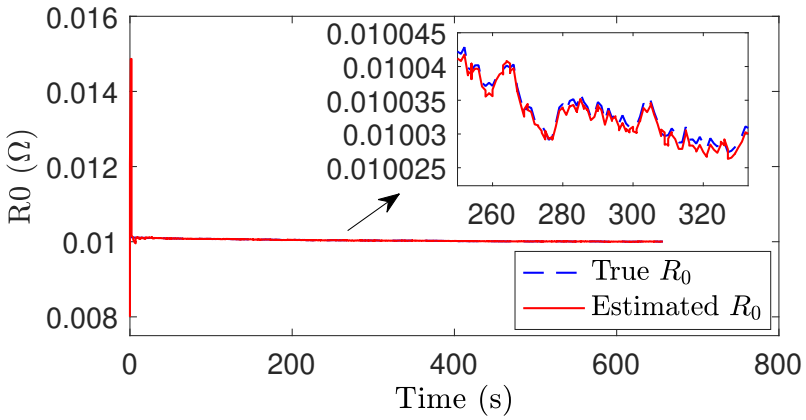

Figure 28: Comparison results for R_0 from the SOH-coupled model (3.3.14) and EKF under the same drive cycle current.

Figure 29 c) SOH decays to 0.8 after 3924 CC-CV cycles of the battery at $5C_{rate}$, whereas in Figure 29 d) it took 1393 cycles for the SOH to decay to 0.8 at $10C_{rate}$. Consequently, as the C_{rates} increases, SOH decays faster at the same $T_a = 25°C$, reducing the life of the battery. Additionally, variation in SOH at different ambient temperatures $(35°, 45°,$ and $55°C, 65°C)$

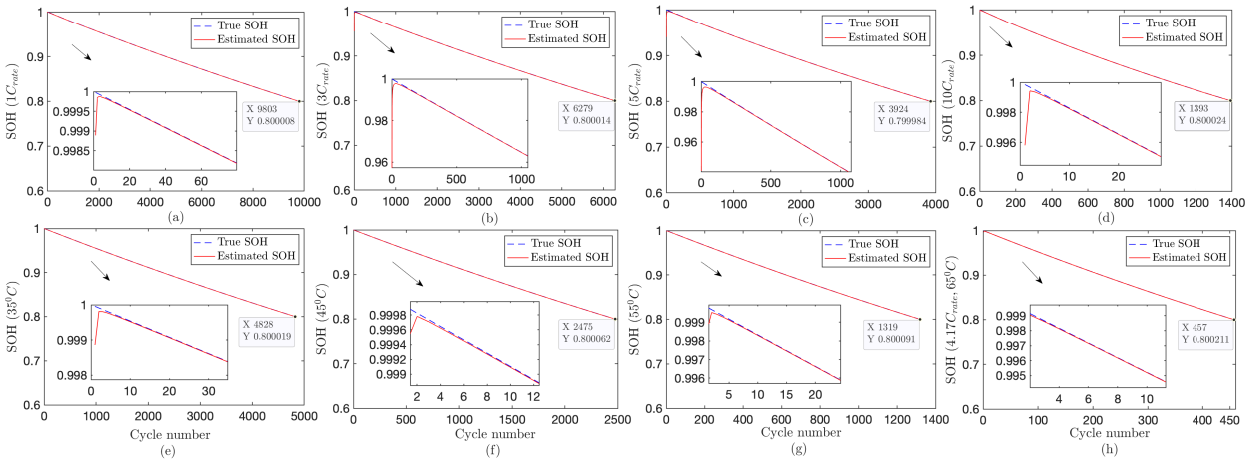

Figure 29: Comparison of SOH until EOL at different C_{rate}. a) $1C_{rate}$, b) $3C_{rate}$, c) $5C_{rate}$ d) $10C_{rate}$. Comparison of SOH until EOL at different T_a at 1_{crate}. e) $35°C$, f) $45°C$, g) $55°C$, and h) $4.17C_{rate}$ $65°C$.

at $1C_{rate}$ is also depicted in Figure 29 e), f), g), and h). In Figure 29 e) SOH decays to 0.8 at $1C_{rate}$ as the battery is cycled through 4828 CC-CV cycles at $T_a = 35°$ with RMSE 0.0030, whereas in Figure 29 f) SOH decays to 0.8 at $1C_{rate}$ as the battery is cycled through 2475 CC-CV cycles at $T_a = 45°$ with RMSE 0.0029. In Figure 29 g), SOH decays to 0.8 at $1C_{rate}$ as the battery is cycled through 1319 CC-CV cycles at $T_a = 55°$ with RMSE 0.0030, and SOH decays to 0.8 as the battery is cycled through 457 CC-CV cycles at $4.17C_{rate}$ at $T_a = 65°C$ with RMSE 0.0040, as shown in Figure 29 h). Consequently, it can be observed that SOH decay is fast at $T_a = 45°C$ and $55°C$ when compared to $T_a = 25°C$, which is due

to the increase in resistance at higher operating temperatures [121].

3.4 Conclusion

In Section 3.2, an ECM-based state space representation of LIB with SOC-dependent parameters is presented along with an NLO. The NLO is used to estimate states and parameters simultaneously. The simulation results validated the estimation accuracy of the NLO. Section 3.3 proposed a dynamic SOH-coupled nonlinear ETA model. In addition, we also extended the SOH-coupled model by augmenting the ohmic resistance dynamics, allowing simultaneous state and parameter estimation using a filter or an observer-based approach. Both the models are validated experimentally and numerically, and comparison results at different C_{rates} and ambient temperatures are also presented to show the effectiveness of the proposed coupled models. EKF is used to estimate the critical battery states such as SOC, SOH, core, and surface temperatures. This will improve the BMS capability for efficient thermal management and health-conscious decision-making. Moreover, estimating the time-varying ohmic resistance can be used as an indicator for internal degradation/fault.

The next chapter discusses the FD schemes based on: a) SOC dependent model as discussed in Section 3.2.2 to detect internal (side-reaction) faults, b) the SOH-coupled model as discussed in Section 3.3.2 to detect thermal and side reaction faults in LIBs along with estimating the core temperature, SOC and SOH of the battery during faults.

CHAPTER IV

FAULT DIAGNOSIS OF LITHIUM-ION BATTERY

In this chapter, FD schemes using two different models of LIBs are presented. Section 4.2 uses SOC dependent model as discussed in Section 3.2.2 to detect internal (side-reaction) faults. Section 4.3 and Section 4.4 use a SOH-coupled model as discussed in Section 3.3.2 to detect thermal and side reaction faults for LIBs using an adaptive threshold generator. A NN learning scheme is proposed to learn the physics of fault mechanism and estimate the core temperature and detect thermal faults in Section 4.3. A modified NN-based learning scheme in Section 4.3 is proposed in Section 4.4 to learn the faults and estimate core temperature, SOC, and SOH during faults. The NN learning scheme modified in Section 4.4 is also used to detect thermal and side reaction faults in LIB. In this chapter all the faults considered are additive faults.

4.1 Introduction

The past decade has seen a growing trend towards next-generation LIBs in EVs due to their high energy density, high coulombic efficiencies, and low self-discharge [247]. However, safety and reliability have been major concerns for these devices. A BMS ensures battery safety, power, and energy management. Key functions of advanced BMS include monitoring internal states, such as SOC and SOH, and battery charging. Developing an accurate battery model and effective SOC and SOH estimation algorithms is crucial in battery behavior analysis and thermal management, extending the battery's run-time and preventing overcharge/over-discharge.

There are two battery models – ECM [2, 225] and electrochemical model [15] – proposed in the literature that are employed to estimate the SOC and the SOH. The ECM is used widely due to its ease of implementation and fair accuracy when compared to the electrochemical models. The latter suffers from computational complexity due to involving large time-varying spatial partial differential equations. To further improve the ECM, electro-thermal models [234] also have been incorporated to exploit the coupling between the thermal and electrical dynamics (ECM) of LIB. Recently the electro-thermal model is further extended in [174, 241, 248] to include the aging effects of the cell as discussed in chapter III.

On the other hand, advanced BMSs are incorporated with fault diagnosis algorithms to detect faults, such as voltage drift, overcharge/over-discharge current, and high-temperature [26]. The FD schemes include co-relation-based [249], model-based [250], data-driven, and hybrid [251] approaches. In a correlation-based approach, the correlation coefficients of cell voltages are captured and compared for FD in LIB. Among the above FD methods, model-based fault diagnosis of dynamic systems is widely used. The performance of the

model-based approaches highly depends on the model accuracy with which they maintain robustness against cell-inconsistencies in all operating conditions.

Model-based FD schemes [45, 46, 47, 48, 50, 51] use output error as a residual to detect a fault in the system. A fault is said to occur when this residual exceeds the threshold value. The authors in [45] presented a FD and isolation scheme for sensor faults using an EKF. Diagnosis of overcharge/over-discharge and electrochemical faults using EKF and sliding mode observer (SMO) are presented in [46] and [47], respectively. The author in [48] used a UKF to diagnose parameter-based faults in LIB. The authors in [50] present simultaneous fault isolation and estimation schemes using Leuenberger and learning observers. Multiple-model adaptive estimation (MMAE) technique for diagnosing overcharge/over-discharge faults is presented in [51].

Although the above said FD schemes [45, 46, 47, 48, 49, 50, 51] could detect and isolate various kinds of faults (sensor and actuator, overcharge/discharge fault, electrochemical) in LIB, the authors in [45], [48] considered the parameters to be constant for a healthy model of the battery, which is not practical. Similarly in [51] the OCV vs. SOC curve is considered to be linear which is non-linear and may reduce the accuracy of the battery model. In [50] the authors considered the ohmic resistance, i.e., R_0, of the battery to be constant during dynamic computations, which varies with SOC and is an important parameter to estimate SOH. Thus, considering the parameters to be constant, may reduce the accuracy of the battery model.

On the other hand the aforementioned FD schemes [45, 46, 47, 48, 50, 51] do not address LIB's internal/thermal faults. The internal faults cause high internal pressure and temperature leading to thermal runaway. The catastrophic failures in LIB can be circumvented by early detection and diagnosis of internal faults. The authors in [52, 53, 54, 55, 252] address internal thermal faults in LIBs. In [52, 55, 252], the authors used two state electro-thermal model to detect internal thermal faults using core and surface temperatures as residuals and adaptive threshold to account for the uncertainties in the battery model. Since core temperature is not available for direct measurement, the SOC [52] information and internal resistance estimates from the observer [55, 252] are used to compute the core temperature. In addition, the authors in [55] used an online battery internal resistance estimator to represent the changes in core temperature due to fault. As a result, the algorithm requires a better understanding of the physics of the failure mechanism.

Although the above model-based schemes [52, 53, 54, 55, 252] could detect internal thermal faults, they do not consider the effect of SOH on ECM and the thermal dynamics of the battery. The ECM and thermal parameters vary with internal degradation phenomenon [29], and external factors [29], such as C_{rate}, temperature, and DOD, may render these FD schemes ineffective. In addition, core temperature estimations must also include the change in resistance and SOC due to the normal and accelerated change in health caused by degradation and internal faults. The above models [52, 55, 252] also do not address the side reaction faults, such as dendrite growth, SEI layer formation, and lithium plating [29]). These faults reflect changes in the battery's SOC, SOH, voltage, and core and surface temperatures.

Therefore, deployment of a SOH-coupled ETA model [241] for FD and design of the adaptive threshold for residuals accounting for health degradation of the battery will help reduce the false alarms due to the degradation of the battery. It will also improve the accuracy of SOC, SOH, core temperature, and parameter (R_0) estimation under the fault

conditions.

Motivated by the above limitations, in the first part of this chapter, we propose a novel nonlinear state space model of an ECM of LIB to estimate the SOC and internal parameters using EKF. The ECM parameters are considered to be non-linear and SOC dependent. Further, a model-based FD scheme using the EKF as an observer is presented. Faults such as over-charge/over-discharge, sensor, internal short circuit, and external abuse lead to an increase in the internal temperature of LIB [44]. This temperature rise affects the internal ohmic resistance of the battery. Therefore, we consider the Arrhenius dependency of the parameters (internal/ohmic resistance i.e., R_0) on the average temperature of LIB [56] to develop the model-based FD scheme for thermal faults. The output residuals are generated by comparing the faulty battery and the estimated outputs. When the residual exceeds a predefined threshold value, a fault is detected. The simulation results prove the accuracy of the proposed thermal FD scheme.

In the second part of this chapter, we reformulated the SOH-coupled ETA model presented in Section 3.3.2 to incorporate the voltage dynamics for FD and core temperature estimation. An NLO is designed to simultaneously estimate the states (SOC, SOH, core, and surface temperature) and internal resistance (R_0). The observer output and the battery's measured voltage and surface temperature are compared to generate residuals for thermal FD. An adaptive threshold generator, used for the detection of faults, is designed by accounting for the parameter changes due to health degradation of the battery in no-fault conditions and unmodeled dynamics. This enables separating the changes in the residuals due to the fault in the battery and the degradation due to capacity fade.

Upon detection of the internal faults, a second NN-based observer to learn the internal fault dynamics is proposed and employed to estimate the faulty states, including core temperature. A Lyapunov-based update law is designed to train the NN weights online. The weight update scheme uses the estimated core temperature (i.e., the core temperature in the healthy condition from the first observer) along with the measured surface temperature (battery output) to address the challenges in learning with only measured output. This also guarantees faster learning of NN weights and convergence of the NN weight estimation error. The core temperature estimate under the fault conditions from the NN-based fault observer is compared against the healthy observer estimates to isolate the internal thermal faults. Finally, the simulation results prove the accuracy of the proposed thermal FD and learning scheme.

In the last part of the chapter, we used the reformulated SOH coupled model for FD and SOC, SOH, and core temperature estimation. Then a NLO is designed to estimate the healthy states (SOC, SOH, core and surface temperature, and parameter (R_0)) of LIB. The residuals for model-based FD are generated by comparing the measured outputs, such as output voltage and surface temperature, and observer outputs. Later on, the adaptive threshold generator is designed to account for unmodeled dynamics and the parameter changes due to health degradation in no-fault conditions of the battery. This has allowed the adaptive threshold generator to distinguish residuals due to the fault and the degradation (capacity fade).

Upon detection of an internal fault, a second NN-based observer is introduced to learn the internal fault dynamics. The employed observer learns the faults and estimates the faulty states, including SOC, SOH, and core temperature. We introduce an online Lyapunov-based

update law using the measured and estimated healthy states to train the NN weights. Using the Lyapunov stability theory, we guarantee the convergence of the observer state and NN weight estimation errors. These state estimates from NN-based observers during a fault can be further used to isolate internal thermal faults, optimize charge/discharge cycles, and predict the RUL of the battery. Finally, numerical simulation results are presented to prove the efficacy of the proposed FD and learning scheme.

Contributions: The main contributions of this chapter are 1) develop a SOC-based model as discussed in Section 3.2.2 to estimate SOC and parameters of the battery simultaneously, 2) develop an EKF-based FD scheme to detect internal (thermal) faults, 3) reformulation of a SOH-coupled ETA model for FD, 4) development of an NLO to detect internal thermal and side reaction faults in LIB and the convergence proof, 5) design of an adaptive threshold generator to account for the parameter changes due to aging, and modeling uncertainties in no-fault conditions to detect the faults, 6) introduction of an NN-based fault observer to learn thermal runaway and internal thermal resistance faults and estimating the core temperature, and 7) design of an NN-based fault observer to learn internal thermal and side-reaction faults and estimate the SOC, SOH, and core temperatures under fault conditions. Analytical and numerical validation results using Lyapunov stability analysis and computer simulation are also presented to corroborate the designs.

The next section discusses the FD scheme using the SOC-based model (Section 3.2.2) to detect internal thermal faults in LIBs.

4.2 Fault Diagnosis via SOC-Dependent Parameter Varying Model

In this section, a parameter estimation and FD scheme for Lithium-ion batteries (LIBs) is presented to detect internal faults at an embryonic stage using SOC dependent model. The change in parameters due to internal faults of the LIB is captured by using an EKF. First, a novel nonlinear state space model of the LIB using the ECM is developed. An EKF is employed as an observer to estimate the SOC and internal parameters, which are the states of the proposed state space model. Then, a model-based FD scheme is employed to detect the thermal fault of the battery by comparing the model output with the faulty battery. Finally, numerical simulation results are presented showing the convergence of the observer estimation error and detection of the fault.

The rest of the section is organized as follows. Section 4.2.1 briefly describes the problem statement and LIB modeling using $2RC$ ECM. Section 4.2.2 details the model-based FD scheme. Simulation results followed by a conclusion are discussed in Section 4.2.3 and Section 4.5 respectively.

4.2.1 Problem Statement and Modeling of Lithium-ion Battery

In this section, a novel continuous-time nonlinear model of the LIB is developed and the equivalent discrete-time representation is presented

Problem statement

A $2RC$ ECM model, shown in Figure 2, is widely used to represent the LIB. The ECM is obtained by combining Thevenin and run-time models [2]. The dynamics of the LIB in state space form is given in (3.2.1).

This representation leads to a linear state equation with a nonlinear output equation [243]. However, the ECM parameters are SOC dependent and nonlinear [24]. Therefore, a linear representation and parameter estimation approach may lead to inaccurate SOC estimation. Since most of the FD schemes utilize the deviation of parameters from the nominal value, a linear representation will be less accurate and may lead to false positives. Therefore, the problem at hand is to develop a nonlinear model of the battery which is capable of estimating the nonlinear internal parameters and can be used for FD. A solution to the above problem is presented next.

Nonlinear model of LIB

To simultaneously estimate the states and parameters, a nonlinear state space model of LIB is presented by defining the time-varying nonlinear internal parameters as state variables. The assumptions 3.2.1 and 3.2.2 are recalled to proceed further.

Defining the state vector $x = \begin{bmatrix} x_1 & x_2 & x_3 & x_4 & x_5 & x_6 & x_7 & x_8 & x_9 \end{bmatrix}^T$ where $x_1 = SOC, x_2 = V_{c_{p1}}, x_3 = V_{c_{p2}}, x_4 = R_0, x_5 = \frac{1}{C_{p1}}, x_6 = \frac{1}{R_{p1}}, x_7 = \frac{1}{C_{p2}}, x_8 = \frac{1}{R_{p2}}, x_9 = \frac{1}{C_{use}}$. The state space representation of ECM from (3.2.1) along with parameters as states can be expressed as,

$$\dot{x} = f(x) + g(x)u \tag{4.2.1}$$

$$y = h(x, u) \tag{4.2.2}$$

where $x \in \mathbb{R}^9$, and $u \in \mathbb{R}$ are the state and control input vector, respectively. The nonlinear internal dynamics is $f(x) \in \mathbb{R}^9$, the control coefficient function $g(x) \in \mathbb{R}^9$, and output $y = V_o \in \mathbb{R}$. Based on the experimental results presented in [24], the SOC-dependent ECM internal parameters, i.e., $R_0, R_{p1}, R_{p2}, C_{p1}, C_{p2}$, for both charge and discharge conditions are obtained as an exponential function. The coefficients are presented in Table 7 and Table 8. The output function $h(x, u) = V_{OC}(x_1) - x_2 - x_3 - x_4 u$. From the experimental result in [24], the $V_{oc}(SOC)$ which is a function of SOC and obtained as a ninth-order polynomial given as in (3.2.3).

Using Euler's approximation, the discrete-time state space representation of (4.2.1), and (4.2.2) can be expressed as,

$$\begin{aligned} x_{k+1} &= \bar{f}(x_k) + \bar{g}(x_k)u_k \\ y_k &= h(x_k, u_k) \end{aligned} \tag{4.2.3}$$

where $x_k \in \mathbb{R}^9$, $u_k \in \mathbb{R}$ and $y_k \in \mathbb{R}$ are the state, control input, and output at time instant $k \in \mathbb{N}, \mathbb{N} = 1, 2, 3 \cdots$ with a sampling period T, i.e., $t = kT$. The internal dynamics $\bar{f}(x_k) = x_k + Tf_{ekf}(x_k) \in \mathbb{R}^9$, and control coefficient function $\bar{g}(x_k) = Tg_{ekf}(x_k) \in \mathbb{R}^{9\times 1}$ where $f_{ekf}(x_k) = \begin{bmatrix} 0 & f_1(x_k) & f_2(x_k) & 0 & 0 & 0 & 0 & 0 & 0 \end{bmatrix}^T$ and $g_{ekf}(x_k) = [-x_{9k} \;\; x_{5k} \;\; x_{7k} \;\; f_3(x_k) \;\; f_4(x_k) \;\; f_5(x_k)$

$f_6(x_k)\ \ f_7(x_k)\ \ 0]^T$ with

$$
\begin{aligned}
f_1(x_k) &= -x_{2k}x_{5k}x_{6k},\\
f_2(x_k) &= -x_{3k}x_{7k}x_{8k},\\
f_3(x_k) &= -(-2a_0(x_{1k}-b_0/c_0)e^{(-(\frac{x_{1k}-b_0}{c_0})^2)} - 2d_0(x_{1k}-e_0/j_0)e^{(-(\frac{x_{1k}-e_0}{j_0})^2)}\\
&\quad - 2g_0(x_{1k}-q_0/s_0)e^{(-(\frac{x_{1k}-q_0}{s_0})^2)})x_{9k},\\
f_4(x_k) &= (-2a_3(x_{1k}-b_3/c_3)e^{(-(\frac{x_{1k}-b_3}{c_3})^2)} - 2d_3(x_{1k}-e_3/j_3)e^{(-(\frac{x_{1k}-e_3}{j_3})^2)}\\
&\quad - 2g_3(x_{1k}-q_3/s_3)e^{(-(\frac{x_{1k}-q_3}{s_3})^2)})x_{9k}x_{5k}^2,\\
f_5(x_k) &= (-2a_1(x_{1k}-b_1/c_1)e^{(-(\frac{x_{1k}-b_1}{c_1})^2)} - 2d_1(x_{1k}-e_1/j_1)e^{(-(\frac{x_{1k}-e_1}{j_1})^2)}\\
&\quad - 2g_1(x_{1k}-q_1/s_1)e^{(-(\frac{x_{1k}-q_1}{s_1})^2)})x_{9k}x_{6k}^2,
\end{aligned}
$$

$$
\begin{aligned}
f_6(x_k) &= (-2a_4(x_{1k}-b_4/c_4)e^{(-(\frac{x_{1k}-b_4}{c_4})^2)}\\
&\quad - 2d_4(x_{1k}-e_4/j_4)e^{(-(\frac{x_{1k}-e_4}{j_4})^2)} - 2g_4(x_{1k}-q_4/s_4)e^{(-(\frac{x_{1k}-q_4}{s_4})^2)})x_{9k}x_{7k}^2,\\
f_7(x_k) &= (-2a_2(x_{1k}-b_2/c_2)e^{(-(\frac{x_{1k}-b_2}{c_2})^2)} - 2d_2(x_{1k}-e_2/j_2)e^{(-(\frac{x_{1k}-e_2}{j_2})^2)}\\
&\quad - 2g_2(x_{1k}-q_2/s_2)e^{(-(\frac{x_{1k}-q_2}{s_2})^2)})x_{9k}x_{8k}^2,
\end{aligned}
$$

where $a_i, b_i, c_i, d_i, e_i, j_i, g_i,$ and s_i for $i = 0, 1, 2, 3, 4$ are the coefficient of parameters for both charge and discharge conditions given in Table 7 and Table 8 respectively. The output equation $h(x_k, u_k) = V_{OC}(x_{1k}) - x_{2k} - x_{3k} - x_{4k}u_k$.

Remark 4.2.1 *The state space representation of the ECM in (4.2.3) uses functions of the circuit parameters as states of the model. This allows an EKF to estimate the nonlinear parameters. Further, the estimated parameters can be used for the model-based FD scheme presented next.*

4.2.2 Model-Based Fault Detection Scheme

In this section, first, the EKF is presented to estimate the SOC and internal parameters. Then, a model-based FD scheme is presented using EKF as an observer.

SOC and parameter estimation using EKF

The following standard assumption is necessary for the parameter assumption.

Assumption 4.2.1 *The sampling time T is selected such that the system in* (4.2.3) *is observable.*

The proposed model in (4.2.3) can be expressed with zero mean Gaussian and observation noise as follows,

$$
\begin{aligned}
x_k &= \bar{f}(x_{k-1}) + \bar{g}(x_{k-1})u_k + w_k\\
y_k &= h(x_k, u_k) + v_k
\end{aligned}
\tag{4.2.4}
$$

where $w_k \in \mathbb{R}^9$ and $v_k \in \mathbb{R}$ are zero-mean Gaussian process and observation noises with covariance Q_k and R_k, respectively. The EKF acts as an observer for the system in (4.2.4) which is represented as follows,

The prediction step is given by

$$\begin{aligned} \hat{x}_{k|k-1} &= \bar{f}(\hat{x}_{k-1|k-1}) + \bar{g}(\hat{x}_{k-1|k-1})u_k \\ \hat{y}_k &= h(\hat{x}_{k|k-1}, u_k) \\ P_{k|k-1} &= F_k P_{k-1|k-1} F_k^T + Q_k. \end{aligned} \tag{4.2.5}$$

where $\hat{x}_k$ and $\hat{y}_k$ are the estimated states and output of the EKF. The update step can be written as

$$\begin{aligned} \tilde{y}_k &= y_k - \hat{y}_k \\ S_k &= H_k P_{k|k-1} H_k^T + R_k \\ K_k &= P_{k|k-1} H_k^T S_k^{-1} \\ \hat{x}_{k|k} &= \hat{x}_{k|k-1} + K_k \tilde{y}_k \\ P_{k|k} &= (I - K_k H_k) P_{k|k-1} \end{aligned} \tag{4.2.6}$$

where $\tilde{y}_k$ is the output residual, $P_{k|k-1} \in \mathbb{R}^{n \times n}$ is the predicted covariance matrix, $S_k \in \mathbb{R}$ is the residual covariance matrix and, $K_k \in \mathbb{R}^n$ is the Kalman gain. The matrix functions

$$\begin{aligned} F_k &= \frac{\partial \bar{f}}{\partial x}|_{\hat{x}_{k-1|k-1}} + \frac{\partial \bar{g}}{\partial x}|_{\hat{x}_{k-1|k-1}} u_k \\ H_k &= \frac{\partial h}{\partial x}|_{\hat{x}_{k|k-1}} \end{aligned} \tag{4.2.7}$$

with $H_k = \begin{bmatrix} h_9 & -1 & -1 & -u_k & 0 & 0 & 0 & 0 & 0 & 0 & 0 \end{bmatrix}$ and $h_9 = \frac{\partial V_{oc}(\hat{x}_{1k})}{\partial \hat{x}_{1k}} - \frac{\partial \hat{x}_{4k}}{\partial \hat{x}_{1k}} u_k$. The model-based FD scheme is presented next by comparing the measured and estimated outputs obtained using EKF.

Model-based fault detection scheme

The model-based FD scheme for a single lithium-ion cell is presented in Figure 30. The dynamics of the faulted system are represented by

$$\begin{aligned} x_k &= \bar{f}(x_{k-1}) + \bar{g}(x_{k-1})u_k + w_k + \eta(x_k) \\ y_k &= h(x_k, u_k) + v_k \end{aligned} \tag{4.2.8}$$

where $\eta(x_k)$ is the fault dynamics added to the battery dynamics.

An EKF, given in (4.2.5), is utilized as an observer which can estimate the battery internal parameters using the proposed state space model in (4.2.8). The advantage of the EKF is that it can estimate the states accurately under disturbances [45].

Remark 4.2.2 *In traditional model-based FD schemes, a fault in the system state can be detected using the observer-based approach. However, the parameter variation due to the fault can not be estimated. In the proposed approach, the EKF can estimate the internal parameters of the ECM of the battery using the proposed state space representation.*

Since the EKF can estimate the states accurately, in healthy conditions the EKF output matches with the battery output. Thus, the voltage output residual $\tilde{y}$ is zero. Since the EKF uses the healthy model of the battery, in case of an internal fault in the battery, the output will still represent the output of a healthy battery. The output residual $\tilde{y}_k$ will increase. A fault is said to occur when the residual evaluated is greater than a threshold value. The threshold value to indicate fault can be computed based on the run-time maximum values of the internal parameters. It is to note that the EKF can estimate the internal resistance

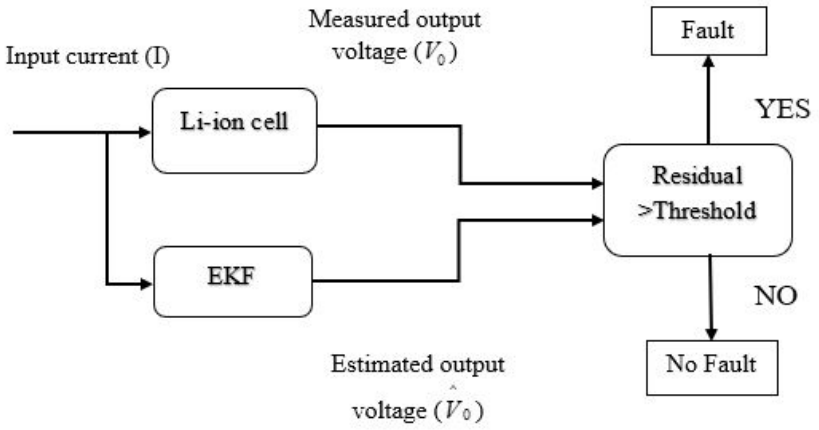

Figure 30: EKF-based fault detection scheme of a lithium-ion cell.

R_0, which is one of the states of the proposed state space model. Therefore, a thermal fault can be easily detected and isolated using the proposed EKF-based approach. To validate the model-based FD scheme in a real world situation, the simulation results are presented using actual driving cycle data in the next section.

4.2.3 Simulation Results and Discussion

Simulations are performed on MATLAB/Simulink platform and presented in this section to show the effectiveness of the proposed model-based FD scheme. The ECM parameters are computed from the experimental data presented in [24] for a polymer LIB of nominal capacity of $10Ah$. These parameters are used for the simulation. First, the SOC and parameter estimation using EKF is discussed.

SOC and parameter estimation

The battery dynamics presented in (4.2.3) with coefficients in Table 7, Table 8 and Table 9 are used for simulation. The initial values of SOC, V_{cp1}, and V_{cp1} are chosen as $0.9, 0.4V$, and $1V$, respectively, and the input current of $30A$ is used for both charging and discharging cycles along with a $10A$ discharge current for 10% drop in SOC value as given in [24]. These current cycles range for a total time period of 43460 sec. A zero mean process and observation noises added to the system dynamics in (4.2.3) are $w_k = 0$ and $v_k = [0, 1]$ i.e., v_k

is a random noise between the values 0 to 1. The simulation results are shown in Figure 31 - Figure 33. The actual output and estimated output voltage are shown in Figure 31. One can

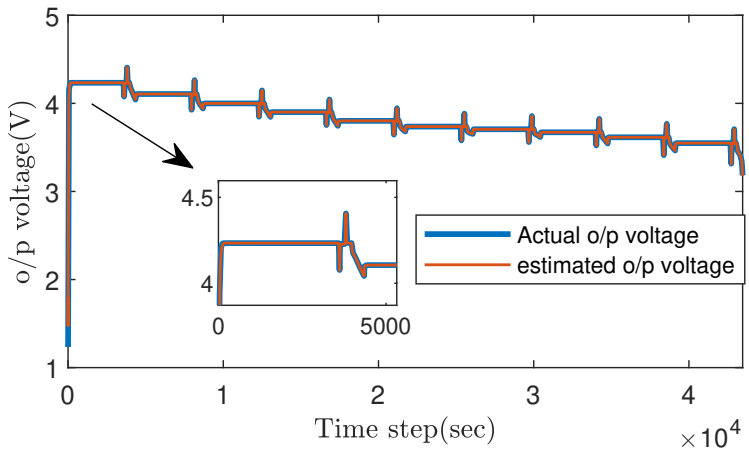

Figure 31: Estimated output voltage of LIB using EKF.

observe from Figure 31 that the estimated output voltage converges to the actual output in the presence of observation noise to the system. One can also see from the zoomed version of Figure 31 that the o/p voltage drops during charging condition (-I) of LIB and vice-versa and also drops at every 10% SOC drop. The decrease in SOC due to battery aging and its estimated value with EKF is shown in Figure 32. It is clear that EKF can estimate the SOC with reasonable accuracy as shown in the zoomed Figure It is important to mention here that the SOC is one of the states of the proposed model.

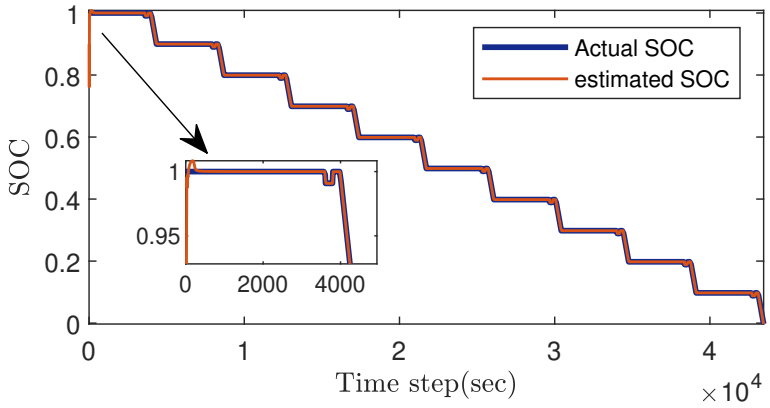

Figure 32: Estimated SOC of LIB using EKF.

Similarly, the SOC-dependent nonlinear internal resistance (R_0), which increases nonlinearly with degradation and aging of the battery, is shown in Figure 33. The estimated values of R_0 converge to the actual values. Note that the R_0 is one of the parameters of the ECM of LIB and is estimated using EKF. This proves the robustness of the proposed state

space representation in the presence of noise in the system. Next, results for the model-based FD scheme are presented.

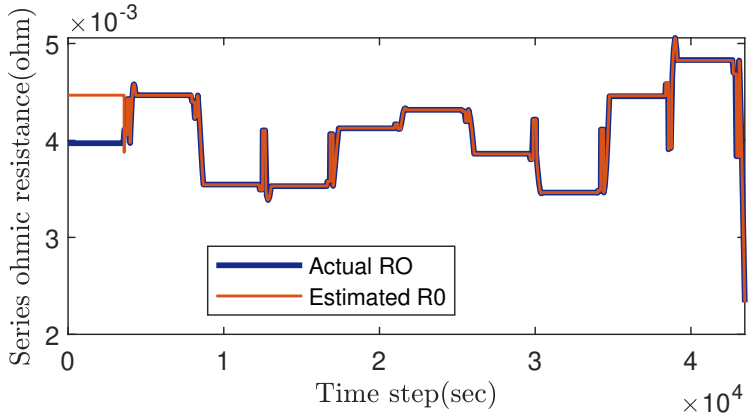

Figure 33: Estimated ohmic resistance R_0 of LIB using EKF.

EKF-based fault detection scheme

To verify the effectiveness of the EKF-based observer for FD, an actual drive cycle, shown in Figure 34, is used as an input current to LIB. A fault is introduced to the system at $t = 2403$ sec i.e., an externally increasing time-varying fault $(0.0000001 * (1 - e^{(0.001*k-10)}))$, $k \in \mathbb{N}$ is added to R_0 which is one of the states of the system. The estimated output voltage using

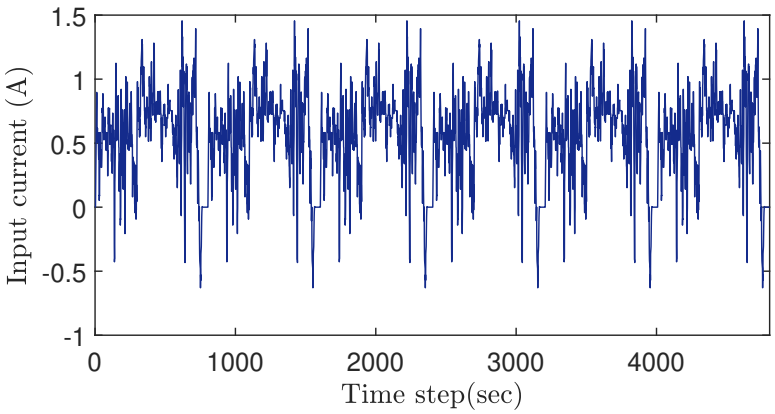

Figure 34: Drive cycle input current.

EKF with a fault in the system is given in Figure 35. It can be seen that EKF estimates the output voltage accurately before the fault occurs. The EKF-based observer is unable to estimate faulted battery output. This is due to the fact that the observer is unaware of the fault in the battery and the battery dynamics change with the fault. This results in a large output residual, which is the difference between the measured and estimated output voltage of LIB.

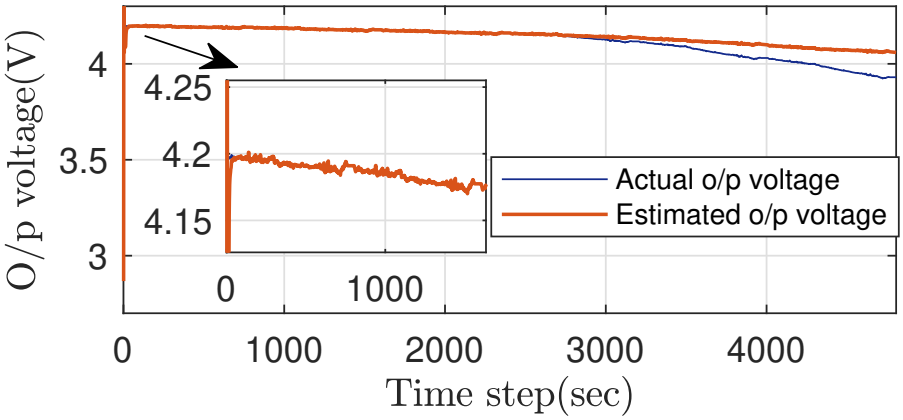

Figure 35: Estimated output using EKF when a fault is introduced at $t = 2403$ sec.

The output residual is shown in Figure 36. Threshold value is chosen to be a constant for the simulation. We can observe from Figure 36 that the residuals are bounded below the threshold value till the fault occurs in the battery i.e., at $t = 2403$ sec. The residual exceeds the threshold value when the fault occurs. Thus, an internal fault is detected in the system and is diagnosed at an incipient stage.

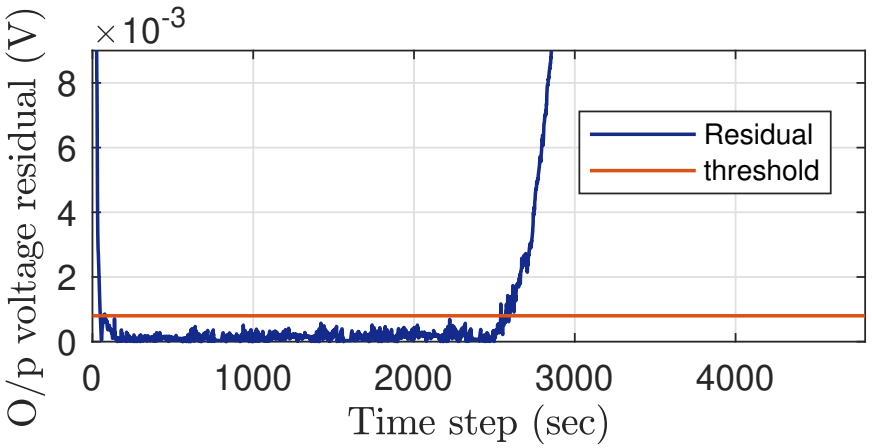

Figure 36: Residual output and a threshold.

The next section discusses the fault diagnosis scheme using the SOH-coupled model (Section 3.3.2) to estimate the core temperature and detect thermal faults in LIBs.

4.3 Core Temperature Estimation of Lithium-ion Batteries Under Internal Thermal Faults Using Neural Networks

In this section, the NN-based FD scheme is proposed to estimate the core temperature and detect the thermal faults in LIB. The estimation of the core temperature of a LIB is of

paramount importance to prevent thermal runaway. This section presents a core temperature estimation scheme for LIBs under internal thermal faults. First, a model-based incipient internal FD scheme using the SOH-coupled ETA model of the LIB is proposed. An NLO is employed to estimate the states and parameters (internal resistance) of the SOH-coupled state space model and generate multiple residuals, such as output voltage and surface temperature. Second, an adaptive threshold is designed to detect convective cooling and internal thermal resistance faults. The adaptive threshold minimizes the false positives due to the battery's health degradation and model uncertainties. Finally, a second network (NN)-based observer to learn the fault dynamics and estimate the core temperature under fault conditions is proposed. Further, the core temperature is used to isolate the internal thermal faults. Analytical and numerical validation results using a Lyapunov-based approach are presented to show the convergence of the state and NN weight estimation errors.

The rest of the section is organized as follows. Section 4.3.1 briefly describes the problem statement and LIB modeling using the SOH-coupled ETA model. Section 4.3.2 and 4.3.2 details the model-based FD and isolation scheme with adaptive threshold design in Section 4.3.2. Section 4.3.3 details the core temperature estimation under fault using NN followed by simulation results in Section 4.3.4 and conclusion in Section 4.5.

4.3.1 Background and Problem Formulation

SOH-coupled LIB model

In this section, a SOH-coupled ETA model [241], developed in Section 3.3.2, is presented for a cylindrical A12326650 $LiFePO_4$/graphite cell. The model is composed of three submodels: a) an ECM, b) a thermal model, and c) an aging model. A reformulated version of the model by incorporating the terminal voltage dynamics can be expressed in a state space form as

$$\begin{aligned} \dot{x} &= f(x) + g(x,u) \\ y_t &= \bar{C}x \end{aligned} \tag{4.3.1}$$

where the state vector $x = [x_1 \;\; x_2 \;\; x_3 \;\; x_4 \;\; x_5 \;\; x_6 \;\; x_7 \;\; x_8]^T$ with $x_1 = SOC$, $x_2 = V_{c_{p1}}$, $x_3 = V_{c_{p2}}$, $x_4 = T_c, x_5 = T_s, x_6 = SOH_c, x_7 = R_0, x_8 = V_t$, $x \in \mathbb{R}^8$, the control input $u = [u_1 \; u_2]^T \in \mathbb{R}^2$ with $u_1 = I$ and $u_2 = T_a$ and y_t is the output vector with output matrix $\bar{C} = \begin{bmatrix} 0 & 0 & 0 & 0 & 1 & 0 & 0 & 0 \\ 0 & 0 & 0 & 0 & 0 & 0 & 0 & 1 \end{bmatrix}$. Thus, the output can be represented as $y_t = [x_5 \; x_8]^T$. The variable I denotes the charging/discharging current, R_0 is total ohmic resistance, T_c and T_s are the core and surface temperatures, respectively, SOH_c represents capacity fade, and C_{use} represents the battery's nominal capacity.

The internal dynamics $f(x) = \Big[\; 0, \;\; \frac{-x_2}{R_{p1}(x_1,x_4,x_5)C_{p1}(x_1,x_4,x_5)}, \;\; \frac{-x_3}{R_{p2}(x_1,,x_4,x_5)C_{p2}(x_1,,x_4,x_5)}, \;\; \frac{-x_4}{R_cC_c} + \frac{x_5}{R_cC_c}, \frac{x_4}{R_cC_s} - \frac{x_5}{R_uC_s} - \frac{x_5}{R_cC_s}, \;\; 0, \;\; \alpha_1(x), \;\; -\alpha_2(x) - \alpha_3(x) \; \Big]^T$ where $R_{p1}(\cdot)$ and $C_{p1}(\cdot)$ are charge transfer resistance and capacitance, and $R_{p2}(\cdot)$ and $C_{p2}(\cdot)$ are diffusion resistance and capacitance of the cell, respectively, which are a function of SOC, T_c, and T_s. The lumped resistances $R_c(K/W)$ and $R_u(K/W)$, and capacitances $C_c(J/K)$ and $C_s(J/K)$ are the heat conduction resistance, convection resistance, core heat capacitance, and surface heat capacity, respectively. The temperature T_a denotes the ambient temperature, and N

denotes the number of cycles until the EOL. The functions $\alpha_1(x) = -a_{1_v} x_7 \frac{\dot{x}_4+\dot{x}_5}{2} \frac{1}{(\frac{x_4+x_5}{2}-a_{2_v})^2}$, $\alpha_2(x) = \frac{-x_2}{R_{p1}C_{p1}}$, $\alpha_3(x) = \frac{-x_3}{R_{p2}C_{p2}}$, with the coefficients $a_{0_v}, a_{1_v}, a_{2_v}$ are the average of $\{a_{0_c}, a_{0_d}\}$, $\{a_{1_c}, a_{1_d}\}$,$\{a_{2_c}, a_{2_d}\}$, respectively. The subscript with c and d denote charging and discharging, respectively. For more details of the model, the readers are encouraged to refer to [241].

The vector function $g(x,u) = \Big[\frac{-u_1}{x_6 C_{use}}, \frac{u_1}{C_{p1}(x_1,x_4,x_5)}, \quad \frac{u_1}{C_{p2}(x_1,x_4,x_5)}, \frac{u_1(V_{oc}(x_1)-x_8)}{C_c}, \frac{u_2}{R_u C_s}, \frac{-u_1}{2N(x_1,C_{rate},x_4)C_{use}}, 0, u_1(-\alpha_1(x) - \beta_1(x) - \beta_2(x) - \beta_3(x)) \Big]^T$ where $\beta_1(x) = \frac{1}{C_{p1}}$, $\beta_2(x) = \frac{1}{C_{p2}}$, $\beta_3(x) = \frac{\beta_4(x)}{x_6 C_{use}}$, $\beta_4(x) = p_1 + 2p_2x_1 + 3p_3x_1^2 + 4p_4x_1^3 + 5p_5x_1^4 + 6p_6x_1^5 + 7p_7x_1^6 + 8p_8x_1^7$, p_i for $i = 0, 1, 2, \cdots, 8$ are constant coefficients given in [241].

The model parameters R_0, R_{p1}, R_{p2}, C_{p1}, and C_{p2} in charge and discharge conditions are obtained experimentally and are given in Section 3.3.4. Since the coefficients of R_0 are close to each other for both charging and discharging conditions, we have averaged these coefficients to obtain a common coefficient. The detailed insights on reformulating the model in (4.3.1) are given in Section 4.4

Remark 4.3.1 *The ECM parameters used in SOH-coupled model* (4.3.1) *are time-varying, i.e., they vary with SOH of the battery cell.*

Problem statement

Model-based FD schemes generate residuals using the actual and estimated outputs and compare them against predetermined constant threshold values to detect faults [46]. Although T_s is measurable in (4.3.1) to generate residuals to detect convective cooling resistance fault, T_c information is also vital in detecting and isolating thermal faults such as internal thermal resistance and thermal runaway fault. In reality, T_c is not measurable, and conventional observer-based techniques don't estimate faulty T_c values.

Additionally, the LIB parameters in (4.3.1) vary with SOH, a constant threshold approach may not be used to differentiate between the degradation and faults from the residuals. Further, modeling uncertainties can also lead to false positives with a constant threshold. Therefore, the threshold for model-based fault detection must be adaptive to accommodate the internal parameter variation due to aging and modeling uncertainty for fault detection.

In summary, the problem at hand is threefold: 1) design a NLO to estimate the healthy states and parameters of the cell, 2) design the adaptive threshold to account for parameters varying with capacity fade and modeling uncertainty, and 3) develop a second NN-based observer to learn the internal fault dynamics to estimate the faulty states including core temperature for better thermal management. Solutions to the above problems are presented next.

4.3.2 Fault Detection Scheme

In this section, we first proposed a model-based fault detection by using the reformulated SOH-coupled model. Then, we introduced an adaptive threshold generator accounting for the internal parameter changes and model uncertainties.

Remark 4.3.2 *Note that the proposed fault detection scheme can be applied to other cell chemistries.*

Fault mapping for detection and isolation

We consider three types of thermal faults, such as convective cooling resistance fault, internal thermal resistance fault, and thermal runaway fault [52] and are listed in Table 15 with their mapping to the internal parameters.

Table 15: Fault mapping for thermal faults.

Actual faults	**Description of fault**	**Fault map**
Fault 1	Convective cooling resistance fault (ΔR_u), which is represented by a significant deviation in the parameter R_u from its nominal value.	$\gamma_1 = 0\ \gamma_2 \neq 0$
Fault 2	Internal thermal resistance fault (ΔR_c), which is modeled by a change in the parameter R_c from its nominal value.	$\gamma_1 \neq 0\ \gamma_2 \neq 0$
Fault 3	Thermal runaway fault, which is modeled by an additional heat-generation term that contributes to the core temperature rise in the battery.	$\gamma_1 \neq 0\ \gamma_2 = 0$

The state space model with the faults in Table 15 can be expressed as

$$\begin{aligned} \dot{x} &= f(x) + g(x,u) + \Gamma(x,u) \\ y_t &= Cx \end{aligned} \tag{4.3.2}$$

where the vector $\Gamma(x,u) = [0\ 0\ 0\ \gamma_1(t)\ \gamma_2(t)\ 0\ 0\ 0]^T$ are the faults added to the dynamics of the battery. The function $\gamma_1(t)$, and $\gamma_2(t)$ represent faults in core temperature and surface temperature dynamics, respectively. The convective cooling resistance fault (failure of the cooling system) can be modeled by $\gamma_2(t)$ and exhibited as an increase in surface temperature residual. Similarly, the thermal runaway faults (overcharging/discharging, short circuit) can be modeled by $\gamma_1(t)$ and exhibit as an increase in core temperature residual. Similarly, the internal thermal resistance fault (inhomogeneous heat dissipation) can be modeled as both $\gamma_1(t)$ and $\gamma_2(t)$ and exhibits as both increases in core and surface temperature residuals. The core and surface temperature changes also affect voltage (4.3.1) in the presence of faults. Therefore internal faults in Table 15 also exhibit as an increase in voltage residual.

Fault detection observer design

The LIB's SOH-coupled dynamics in (4.3.1) can be rewritten as

$$\begin{aligned} \dot{x} &= Kx + f(x) - Kx + g(x,u) \\ &= Kx + \Pi(x) + g(x,u) \end{aligned} \tag{4.3.3}$$

where $K \in \mathbb{R}^{n\times n}$ is a Hurwitz matrix, $\Pi(x) = f(x) - Kx$. Based on (4.3.3) the NLO can be represented by

$$\begin{aligned} \dot{\hat{x}} &= K\hat{x} + \Pi(\hat{x}) + g(\hat{x}, u) + L^T(y - \hat{y}) \\ \hat{y}_t &= C\hat{x} \end{aligned} \tag{4.3.4}$$

where $\hat{x}$ is the estimated state, $L \in \mathbb{R}^{m\times n}$ is the observer gain, and $\Pi(\hat{x}) = f(\hat{x}) - K\hat{x}$.

The observer state estimation error dynamics using (4.3.3) and (4.3.4) can be expressed as

$$\dot{\tilde{x}} = K\tilde{x} + \tilde{\Pi}(x, \hat{x}) + \tilde{g}(x, \hat{x}, u) - L^T C\tilde{x} \tag{4.3.5}$$

where the state estimation error $\tilde{x} = x - \hat{x}$, $\tilde{\Pi}(x, \hat{x}) = \Pi(x) - \Pi(\hat{x})$, $\tilde{g}(x, \hat{x}, u) = g(x, u) - g(\hat{x}, u)$ and the output error $\tilde{y} = y - \hat{y} = C\tilde{x}$. For brevity, we drop the arguments in the functions, i.e., $\tilde{\Pi}(x, \hat{x})$ is $\tilde{\Pi}$, $\tilde{g}(x, \hat{x}, u)$ is $\tilde{g}$, when it is clear.

The next theorem guarantees the asymptotic convergence of the state estimation error $\tilde{x}$ under no-fault conditions. Before introducing the theorem, we need the following trivial assumption.

Assumption 4.3.1 *The functions $\tilde{\Pi}$ and $\tilde{g}$ are continuously differentiable locally Lipschitz functions for any L_π, $L_g > 0$ there exists $r > 0$ such that $\|\tilde{\Pi}\| \leq L_\pi\|\tilde{x}\|$ and $\|\tilde{g}\| \leq L_g\|\tilde{x}\|$ $\forall$ $\|\tilde{x}\| < r$.*

Theorem 4.3.1 *Consider the dynamics of the battery* (4.3.3) *along with the observer* (4.3.4)*. Suppose Assumption 4.3.1 holds. Let there exist a positive definite matrix P satisfying the Lyapunov equation*

$$(K - L^T C)^T P + P(K - L^T C) = -Q \tag{4.3.6}$$

where Q is a positive definite matrix with $(K - L^T C)$ being a stable matrix. Then, the state estimation error $\tilde{x}$ is locally asymptotically stable from any initial $\tilde{x}_0 \in \Omega_x \subset \mathbb{R}^8$, i.e., $\lim_{t\to\infty} \tilde{x} \to 0$.

Proof. The proof can be completed by selecting a Lyapunov function candidate $V = \frac{1}{2}\tilde{x}^T P\tilde{x}$.

The derivative of V along the trajectories of (4.3.5) with the

Lipschitz continuity of the functions $\tilde{\Pi}$ and $\tilde{g}$ from Assumption 4.3.1 can be expressed as

$$\begin{aligned} \dot{V} \leq \frac{1}{2}\tilde{x}^T(P(K - L^T C) + (K - L^T C)^T P)\tilde{x} + \\ \lambda_{max}(P)L_\pi\|\tilde{x}\|^2 + \lambda_{max}(P)L_g\|\tilde{x}\|^2 \end{aligned} \tag{4.3.7}$$

where $\lambda_{max}(P)$ is the maximum eigenvalue of symmetric positive definite matrix P. With simple algebraic manipulation and definition of Euclidean norm, we can get

$$\dot{V} \leq -\tilde{x}^T(\frac{1}{2}Q - \lambda_{max}(P)L_\phi I)\tilde{x} \tag{4.3.8}$$

where $L_\phi = L_\pi + L_g$. By properly selecting the K, L and P, we can ensure $\frac{1}{2}Q - \lambda_{max}(P)L_\phi I > 0$. Thus, from (4.3.8) $\dot{V} < 0$. By Lyapunov theorem, the state estimation errors $\tilde{x}$ converge to zero asymptotically as $t \to \infty$. ■

From the above results, we can also show that the output estimation error also converges to zero asymptotically and is presented in the next corollary.

Corollary 4.3.1 *Let hypothesis of Theorem 4.3.1 hold. Then, the output errors $\tilde{y}$ also converge to zero asymptotically.*

Proof. The proof is a direct result of the Theorem 4.3.1 since C is a constant matrix. ■

The proposed NLO is used to generate output residuals by comparing the battery outputs (terminal voltage, and surface temperature) with the observer outputs. The residuals are compared against an adaptive threshold value designed next to detect the fault. We will need the following assumption to proceed further.

Assumption 4.3.2 *The observer state estimation error in* (4.3.5) *converges before the occurrence of any fault.*

This is a trivial assumption since the observer can be implemented at the commissioning of the cells.

Adaptive threshold design

In this subsection, we designed the threshold values for the output residuals. Unlike the constant threshold values, we proposed adaptive thresholds [52] to account for the changes in residuals due to aging, changes in operating conditions, and unmodeled dynamics (uncertainty) and eliminate false positives.

We can express the changes in the model parameters as the sum of the nominal values and the change, e.g., $R_0 + \Delta R_0, C_c + \Delta C_c, C_s + \Delta C_s, T_a + \Delta T_a$, where ΔR_0, ΔC_s, ΔC_c, and ΔT_a are changes in the parameters due aging and modeling uncertainty. Therefore, the residuals will lead to a non-zero value even under no-fault conditions. The nominal SOH-coupled model in (4.3.3) can be rewritten to include the parameter changes $(\Delta R_0, \Delta C_s, \Delta C_c, \Delta T_a)$ as

$$\begin{aligned} \dot{x} &= Kx + \Pi + g + \chi(x,u) \\ y &= Cx \end{aligned} \tag{4.3.9}$$

where $\chi(x,u) = [\eta_1(x,u), \cdots, \eta_8(x,u)]^T$ is a vector-valued function of parameter changes due to degradation. Note that $\chi(x,u)$ is a state and/or input-dependent vector function.

We can express $\eta_1(x,u), \cdots, \eta_8(x,u)$ as linear in unknown parameter form [52] as

$$\begin{aligned} &\eta_1(x,u) = \eta_{11},\ \eta_2(x,u) = \eta_{21},\ \eta_3(x,u) = \eta_{31} \\ &\eta_4(x,u) = \eta_{41} + \eta_{42}x_4 + \eta_{43}x_5 + \eta_{44}u_1, \\ &\eta_5(x,u) = \eta_{51} + \eta_{52}x_4 + \eta_{53}x_5 + \eta_{54}u_2,\ \eta_6(x,u) = \eta_{61}, \\ &\eta_7(x,u) = \eta_{71} + \eta_{72}x_4 + \eta_{73}x_5,\ \eta_8(x,u) = \eta_{81} + \eta_{82}u_1 \end{aligned} \tag{4.3.10}$$

where $\eta_{11}, \eta_{21}, \cdots, \eta_{81}$ capture the modeling uncertainty i.e., they include the effects of exogenous input disturbances in the system [52]. The change in thermal parameters $(C_c + \Delta C_c)$ is reflected in η_{42}, η_{43}, and η_{44}, $(C_s + \Delta C_s)$ is reflected in η_{52}, η_{53}, and η_{54}, $(T_a + \Delta T_a)$ is reflected in η_{54}, and $(R_0 + \Delta R_0)$ is reflected in η_{44}, η_{72}, η_{73}, and η_{82}. The noise in input current and ambient temperature is reflected in η_{44} and η_{82}, and η_{54}, respectively.

Assumption 4.3.3 *The parameters changes due to degradation and uncertainties, i.e., $\eta_1(x,u),\cdots,\eta_8(x,u)$, are assumed to be bounded, unknown, exogenous (and possibly time-varying) inputs acting on the nominal battery model. For brevity of notation $\chi(x,u)$ is represented as χ.*

From Corollary 4.3.1, the output residuals under no fault and modeling uncertainty conditions converges to zeros asymptotically. The residuals dynamics in the presence of parameter changes due to aging and uncertainity can be expressed as

$$\begin{aligned}\dot{\tilde{y}}_1 &\leq -\sigma_5\tilde{y}_1+\eta_5, \text{and}\\ \dot{\tilde{y}}_2 &\leq -\sigma_8\tilde{y}_2+\eta_8.\end{aligned} \tag{4.3.11}$$

where σ_5, and σ_8 are the convergence rates under no fault conditions. Using the comparison lemma [52], the solutions to (4.3.11) can be computed as

$$\begin{aligned}\tilde{y}_1 &\leq \tilde{y}_1(0)e^{-\sigma_5 t}+\int_0^t e^{-\sigma_5(t-\tau)}\eta_5(\tau)\,d\tau, \text{and}\\ \tilde{y}_2 &\leq \tilde{y}_2(0)e^{-\sigma_8 t}+\int_0^t e^{-\sigma_8(t-\tau)}\eta_8(\tau)\,d\tau.\end{aligned} \tag{4.3.12}$$

From the definitions in (4.3.10), we have $|\eta_5(\tau)|\leq|\eta_{51}|+|\eta_{52}||x_4|+|\eta_{53}||x_5|+|\eta_{54}||u_2|$, $|\eta_8(\tau)|\leq|\eta_{81}|+|\eta_{82}||u_1|$. Since $e^{-\sigma_5 t},e^{-\sigma_8 t}>0,\forall t>0$, we can write $|e^{-\sigma_5 t}|=e^{-\sigma_5 t}$, and $|e^{-\sigma_8 t}|=e^{-\sigma_8 t}$. Further, from Assumption 4.3.3, we have $\eta_{ij}\leq\eta_{ijmax}\forall i,j=1,\cdots,8$. Using Cauchy Schwarz [52] inequality $|ab|\leq|a||b|$, (4.3.12) can be written as

$$\begin{aligned}\tilde{y}_1 &\leq R_{es_{1th}}=\tilde{y}_1(0)e^{-\sigma_5 t}+\int_0^t|e^{-\sigma_5(t-\tau)|}\eta_{5max}\,d\tau,\\ \tilde{y}_2 &\leq R_{es_{2th}}=\tilde{y}_2(0)e^{-\sigma_8 t}+\int_0^t|e^{-\sigma_8(t-\tau)|}\eta_{8max}\,d\tau,\end{aligned} \tag{4.3.13}$$

where $\eta_{5max}=\eta_{51max}+\eta_{52max}|x_4|+\eta_{53max}|x_5|+\eta_{54max}|u_2|$, $\eta_{8max}=\eta_{81max}+\eta_{82max}|u_1|$.

The adaptive thresholds $R_{es_{1th}}$, and $R_{es_{2th}}$ can be calculated as

$$\begin{aligned}R_{es_{1th}} &= \tilde{y}_1(0)e^{-\sigma_5 t}+r_1, and\\ R_{es_{2th}} &= \tilde{y}_2(0)e^{-\sigma_8 t}+r_2\end{aligned} \tag{4.3.14}$$

where r_1,r_2 can be calculated from the filter dynamics as folows

$$\begin{aligned}\dot{r}_1 &= -\sigma_5 r_1+\eta_{5max}, \text{and}\\ \dot{r}_2 &= -\sigma_8 r_2+\eta_{8max}.\end{aligned} \tag{4.3.15}$$

The adaptive thresholds in (4.3.14) prevent any false alarms from being generated in the interval $[0\ \ T]$ prior to the occurrence of a fault, even in the presence of parameters changing due to aging and modeling uncertainty, satisfying $\eta_i(x,u)\leq\eta_{i_{max}}\ \forall i=1,2,\cdots,8$.

Note that from Table 15, the core temperature is an important internal indicator of the fault and thermal runaway. Therefore, in the next section, we have proposed an NN-based learning approach to learn the fault dynamics and estimate the core temperature using a fault observer.

4.3.3 Core Temperature Estimation Under Fault

In order to detect thermal faults with higher confidence and better thermal management, estimation of the core temperature T_c under fault conditions is of paramount importance. In this section, we proposed a second NN-based fault observer, designed by augmenting a NN in the proposed NLO in Section 4.3.2, which can learn the fault dynamics online. Therefore, the output of the observer will estimate the faulty states (SOC, capacitor voltages, internal resistance, and terminal voltages) of the LIB along with the core temperature T_c. The NN-based fault detection scheme is shown in Figure 37.

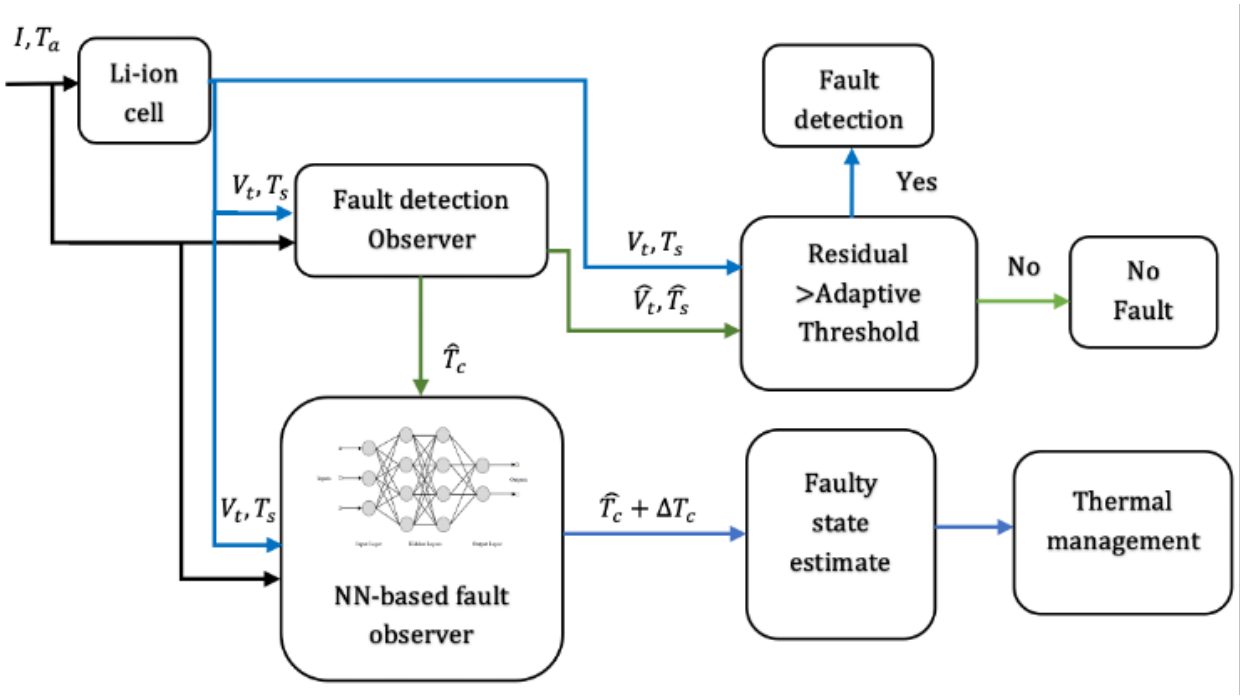

Figure 37: NN-based fault detection scheme.

Consider the state space model of the LIB under thermal fault given in (4.3.2). Since the fault function, $\Gamma(x, u)$ is unknown, we can revoke the universal approximation property of the NNs to approximate the function in a compact set. Alternatively, the function $\Gamma(x, u)$ can be represented in parametric form using a multi-layer NN as

$$\begin{aligned} \dot{x} &= Kx + \Pi(x) + g(x, u) + \theta^T \sigma(x, u) + \epsilon(x, u) \\ y &= Cx \end{aligned} \tag{4.3.16}$$

where $\epsilon(x, u)$ is the measurement error, $\sigma(x, u) \in \mathbb{R}^l$ is the basis function , l is the number of neurons in the NN architecture and $\theta \in \mathbb{R}^{l \times n}$ is NN weights.

Since our goal, in this papers, is to investigate the faults $\gamma_1(t)$ and $\gamma_2(t)$ in the thermal dynamics of the cell, we can express the NN approximator as $\theta^T \sigma(x, u) = [0\ 0\ 0\ \theta_{\gamma_1}^T \sigma_{\gamma_1}(x, u), \theta_{\gamma_2}^T \sigma_{\gamma_2}(x, u)\ 0\ 0\ 0]^T$. Therefore, the dynamics of the T_c and T_s and the redefined outputs

under the fault conditions can be expressed as

$$\begin{aligned}\dot{\zeta} &= A\zeta + B\bar{u} + \theta_\gamma^T \sigma_\gamma(\zeta, u) + \epsilon(\zeta, u) \\ \bar{y} &= \bar{C}\zeta\end{aligned} \tag{4.3.17}$$

where $\zeta = [\zeta_1 \quad \zeta_2]^T$ with $\zeta_1 = T_c, \zeta_2 = T_s$, $\bar{u} = [Q \quad T_a]^T$ with $\bar{C} = \begin{bmatrix} 0 & 1 \end{bmatrix}$, $A = \begin{bmatrix} \frac{-1}{R_c C_c} & \frac{1}{R_c C_c} \\ \frac{1}{R_c C_s} & \frac{-1}{R_u C_s} - \frac{1}{R_c C_s} \end{bmatrix}$, $B = \begin{bmatrix} \frac{1}{C_c} & 0 \\ 0 & \frac{1}{R_u C_s} \end{bmatrix}$.

Based on (4.3.17), the NN-based fault observer can be written as

$$\begin{aligned}\dot{\hat{\zeta}} &= A\hat{\zeta} + B\bar{u} + \hat{\theta}_\gamma^T \sigma_\gamma(\hat{\zeta}, u) + \bar{L}^T \bar{C}\tilde{\zeta} \\ \hat{\bar{y}} &= \bar{C}\hat{\zeta}\end{aligned} \tag{4.3.18}$$

where $\bar{L} \in \mathbb{R}^{1\times n}, n = 2$ is gain matrix obtained from L in (4.3.4) given as $\bar{L} = \begin{bmatrix} L_{51} & L_{52} \end{bmatrix}$, $\hat{\zeta}$ and $\hat{\bar{y}}$ are the estimated state and output vectors, respectively. The state estimation error is given as, $\tilde{\zeta} = \zeta - \hat{\zeta}$.

The state estimation error dynamics in the presence of faults by subtracting (4.3.18) from (4.3.17) can be written as,

$$\dot{\tilde{\zeta}} = A\tilde{\zeta} + \tilde{\theta}_\gamma^T \sigma_\gamma(\hat{\zeta}, u) + \theta_\gamma^T \tilde{\sigma}_\gamma - \bar{L}^T \bar{C}\tilde{\zeta} + \epsilon(\zeta, u) \tag{4.3.19}$$

where $\tilde{\sigma}_\gamma = \sigma_\gamma(\zeta, u) - \sigma_\gamma(\hat{\zeta}, u)$. The weight errors is given as $\tilde{\theta}_\gamma = \theta_\gamma - \hat{\theta}_\gamma$.

We aim to develop an online NN weight tuning rule to update the weights so that the faulty state estimation error and NN weight estimation error converge close to zero. Before introducing the NN weight update law we need the following assumption.

Assumption 4.3.4 *The internal faults are slowly time-varying.*

Since the model-based fault detection scheme can detect faults at an incipient stage, the assumption holds for many faults at their initial stages. In LIB, the major challenge in training the NN weights is the limited available measurement to design the update law, i.e., T_c is not available for measurements. To address this challenge, we employ the estimated healthy state ($\hat{T}_c$) by the NLO in (4.3.4) as a substitute for the state T_c, in addition to the faulty measured T_s. Defining the augmented output vector as the concatenation of the healthy states and faulty measured output as $\bar{X} = [\hat{T}_c, \bar{y}]^T$, the augmented error vector $\Xi = \bar{X} - \hat{\zeta}$ is employed to tune the NN weight estimates.

The weight update law of the NN is developed based on the subsequent stability analysis as

$$\dot{\hat{\theta}}_\gamma = -\sigma_\gamma(\hat{\zeta}, u)\Xi^T \upsilon - \sigma_\gamma(\hat{\zeta}, u)\sigma_\gamma(\hat{\zeta}, u)^T \hat{\theta}_\gamma \Upsilon \tag{4.3.20}$$

where $\upsilon, \Upsilon \in \mathbb{R}^{n\times n}$ are the learning rates.

The temperature $\hat{T}_c$ in $\bar{X}$ is the healthy estimate of T_c obtained from the observer in (4.3.4) and does not account for faults reflecting in T_c. From Theorem 4.3.1, we know that $\hat{x} \to x$ and by Assumption 4.3.2, we can rewrite $\bar{X} = \zeta + \Delta_\zeta$, and $\Delta_\zeta = [\Delta_{T_c}, 0]^T$ represents the change in T_c due to fault. The augmented error vector $\Xi = \tilde{\zeta} + \Delta_\zeta$ is employed to tune the NN weight estimates.

The weight error dynamics in the presence of faults based on (4.3.20) can be written as

$$\dot{\tilde{\theta}}_\gamma = \sigma_\gamma(\hat{\zeta}, u)(\tilde{\zeta} + \Delta_\zeta)^T \upsilon + \sigma_\gamma(\hat{\zeta}, u)\sigma_\gamma(\hat{\zeta}, u)^T \hat{\theta}_\gamma \Upsilon. \tag{4.3.21}$$

The next theorem guarantees uniform ultimate boundedness (UUB) of the faulty state estimation error.

Assumption 4.3.5 *The change in T_c due to fault is assumed to be bounded with $\Delta_{T_c} \leq \kappa\tilde{\zeta}_1$, where κ, is some positive constant.*

Assumption 4.3.6 *Given a constant approximation error $\bar{\epsilon}$ there exists a vector of basis functions $\sigma_\gamma(\zeta, u)$ and NN weight parameter vector θ_γ and positive constants σ_{max} and θ_{max} such that given a compact set Ω, $\|\theta_\gamma\| \leq \theta_{max}$, $\|\epsilon(\zeta, u)\| \leq \bar{\epsilon}$ and $\|\sigma_\gamma(\zeta, u)\| \leq \sigma_{max}$, $\|\tilde{\sigma}_\gamma(\zeta, \hat{\zeta}, u)\| \leq 2\sigma_{max}$, $\|\sigma_\gamma(\hat{\zeta}, u)\| \leq \sigma_{max}$, $\forall(\zeta, u) \in \zeta$.*

Theorem 4.3.2 *Consider the dynamics of the battery (4.3.17) and the observer (4.3.18). Suppose the Assumptions 4.3.2-4.3.6 hold. Let there exists a positive definite matrix $\bar{P}$ satisfying the Lyapunov equation $(A - \bar{L})^T\bar{P} + \bar{P}(A - \bar{L}) = -\bar{Q}$, where $\bar{Q}$ is a positive definite matrix with $(A-\bar{L})$ being a stable matrix. If the weights of NN are updated according to (4.3.20), then the estimation error and the weights error are ultimately bounded, i.e., $\tilde{\zeta}, \tilde{\theta}_\gamma \in L_\infty$.*

Proof. The proof can be completed using a common Lyapunov function $V(Z) = \frac{1}{2}\tilde{\zeta}^T\bar{P}\tilde{\zeta} + \frac{1}{2}tr(\tilde{\theta}_\gamma^T\tilde{\theta}_\gamma))$, where $Z = [\tilde{\zeta}^T \;\; vec(\tilde{\theta}_\gamma)^T]$, $vec(.)$ is the vectorization operator.

The first derivative of the Lyapunov function along the faulty observer state and NN parameter estimation dynamics is given as

$$\begin{aligned}\dot{V}(Z) = {} & \tilde{\zeta}^T\bar{P}\tilde{\theta}_\gamma^T\sigma_\gamma(\hat{\zeta}, u) + \tilde{\zeta}^T\bar{P}\theta_\gamma^T\tilde{\sigma}_\gamma + \tilde{\zeta}^T\bar{P}\epsilon(\zeta, u) + \\ & \frac{1}{2}\tilde{\zeta}^T(\bar{P}(A - \bar{L}^T\bar{C}) + (A - \bar{L}^T\bar{C})^T\bar{P})\tilde{\zeta} + \\ & tr(\tilde{\theta}_\gamma^T(\sigma_\gamma(\hat{\zeta}, u)\tilde{\zeta}^T\upsilon + \sigma_\gamma(\hat{\zeta}, u)\Delta_\zeta^T\upsilon + \\ & \sigma_\gamma(\hat{\zeta}, u)\sigma_\gamma(\hat{\zeta}, u)^T\theta_\gamma\Upsilon - \sigma_\gamma(\hat{\zeta}, u)\sigma_\gamma(\hat{\zeta}, u)^T\tilde{\theta}_\gamma\Upsilon))\end{aligned} \tag{4.3.22}$$

recalling the Assumption 4.3.5 and 4.3.6, the first derivative of the Lyapunov function can be upper bounded as

$$\begin{aligned}\dot{V}(Z) \leq {} & -\frac{1}{2}\lambda_{min}(\bar{Q})\|\tilde{\zeta}\|^2 - \|\Upsilon\|\sigma_{max}^2\|\tilde{\theta}_\gamma\|^2 + \\ & \psi_1\|\tilde{\zeta}\|\|\tilde{\theta}_\gamma\| + \psi_2\|\tilde{\zeta}\| + \psi_3\|\tilde{\theta}_\gamma\|\end{aligned} \tag{4.3.23}$$

where $\psi_1 = \sigma_{max}\lambda_{max}(\bar{P}) + \|\upsilon\|\sigma_{max} + \|\upsilon\|\|\pi\|\sigma_{max}$, $\psi_2 = 2\theta_{max}\sigma_{max}\lambda_{max}(\bar{P}) + \bar{\epsilon}\lambda_{max}(\bar{P})$, $\psi_3 = \|\Upsilon\|\sigma_{max}^2\theta_{max}$ and $\pi = diag[\kappa, 0]$.

Separating the cross terms in (4.3.23) and using Young's inequality, $2|ab| \leq |a|^2 + |b|^2$: we have $2\|\tilde{\theta}_\gamma\|\|\tilde{\zeta}\| \leq \|\tilde{\theta}_\gamma\|^2 + \|\tilde{\zeta}\|^2$, (4.3.23) can be written as

$$\dot{V}(Z) \leq -\frac{\psi_4}{2}\|\tilde{\zeta}\|^2 - \frac{\psi_5}{2}\|\tilde{\theta}_\gamma\|^2 + c_1 + c_2 \tag{4.3.24}$$

where $\psi_4 = \frac{1}{2}\lambda_{min}(\bar{Q}) - \psi_1 > 0$ $\psi_5 = \|\Upsilon\|\sigma_{max}^2 - \psi_1 > 0$, $c_1 = \frac{\psi_2^2}{2\psi_4}$, and $c_2 = \frac{\psi_3^2}{2\psi_5}$.

From (4.3.24), we have $\dot{V}(Z) < 0$ as long as $||\tilde{\zeta}|| > \left(\frac{2(c_1+c_2)}{\psi_4}\right)^{\frac{1}{2}}$ or $||\tilde{\theta}_\gamma|| > \left(\frac{2(c_1+c_2)}{\psi_5}\right)^{\frac{1}{2}}$. The state estimation error $\tilde{\zeta}$ and NN weight estimation error $\tilde{\theta}_\gamma$ remain locally UUB. This completes the proof.

■

4.3.4 Simulation Results and Discussion

Identification of ECM model parameters

Experimental studies conducted on cylindrical A12326650 $LiFePO_4$/graphite cells with a capacity of 2.5 Ah are given in Section 3.3.4. The parameters obtained from these experiments are used for simulation.

Validation of the observer in the presence of uncertainties and no fault

Simulations were performed on MATLAB/Simulink platform and presented in this section to show the effectiveness of the proposed model-based FD scheme. The change in parameters due to SOH degradation in the form (4.3.10) are injected into the plant model. The coefficients were chosen as $\eta_{11} = \eta_{44} = \eta_{54} = \eta_{61} = \eta_{71} = \eta_{72} = \eta_{73} = \eta_{81} = 0, \eta_{21} = 10^{-7}, \eta_{31} = 10^{-6}, \eta_{41} = \eta_{42} = \eta_{43} = \eta_{51} = \eta_{52} = \eta_{53} = 10^{-8}, \eta_{82} = 10^{-4}$.

A drive cycle current in Figure 21 was used to validate the observer. The states and parameters estimated using the observer in the presence of uncertainties are given in Figure 38. All the state estimation errors for SOH, SOC, T_c, T_s, R_0 are within 1% band with RMSEs $0.0024, 0.0013, 0.0036, 0.0038, 1.75E{-}4$, respectively.

Validation of the observer under fault

The same drive cycle current is used as an input to LIBs model in (4.3.2) with $T_a \approx 25°C$. As a preliminary result, in this paper, we focused on the thermal faults occurring in T_c and validated the fault detection and core temperature estimation via the proposed NN-based online fault learning scheme.

Validation results under fault in R_c

The thermal resistance fault affects both the core and surface temperature dynamics, which can be seen from Eq. (4.3.2). Therefore, the fault can be manifested as $\gamma_1, \gamma_2 \neq 0$. An abrupt internal thermal resistance fault $10 * R_c$ is introduced to the system at $t = 400$ sec. The T_s and V_t residuals with adaptive threshold under fault is shown in Figure 39 a), b), respectively. From Figure 39 a) and b), we can observe that the residuals are within the adaptive threshold value before the occurrence of the fault $t = 400$ sec. This further validates the estimation accuracy of the NLO. Upon the occurrence of the fault, the T_s and V_t residuals exceed the adaptive threshold value after $t = 406$ and 409 sec, respectively. This implies the detection of an internal thermal resistance fault and is diagnosed at an incipient stage.

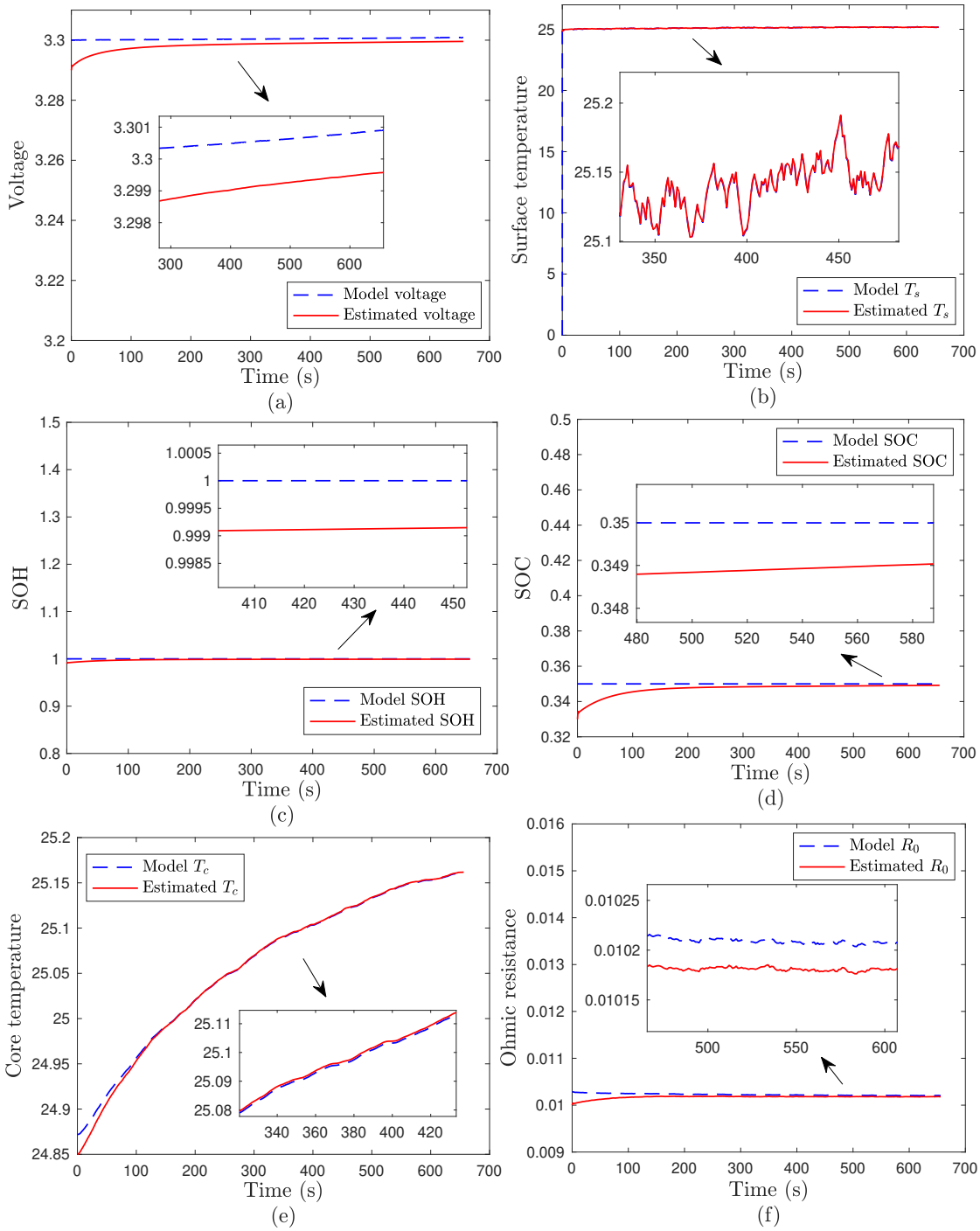

Figure 38: Convergence of estimated states to actual states: a) voltage, b) surface temperature, c) SOH, d) SOC, e) core temperature, and f) ohmic resistance under no-fault condition.

Upon the detection of the fault, the NN is deployed to learn the thermal resistance fault online. The simulation parameters used were $\Upsilon = 0.008 * diag[-.05, -1750], \upsilon = 30\Upsilon$. The NN weight $\hat{\theta}_\gamma$ was initialized at random from a uniform distribution in the interval of [0 0.1].

The number of neurons in the hidden layer is chosen as 10. From Figure 40 a), we can observe that after the fault is detected at $t = 406$ sec, the NN learns the fault dynamics, which can be verified by the convergence of the T_s residual close to zero with RMSE 0.0079. The convergence of the T_c estimation error close to zero with RMSE 0.0096 is shown in Figure 40 (b). Furthermore, the convergence of the estimated NN weight updates is also shown in Figure 40 (c). Therefore, it can be concluded that the NN was able to learn the fault dynamics and estimate the core temperature in the presence of internal thermal resistance fault.

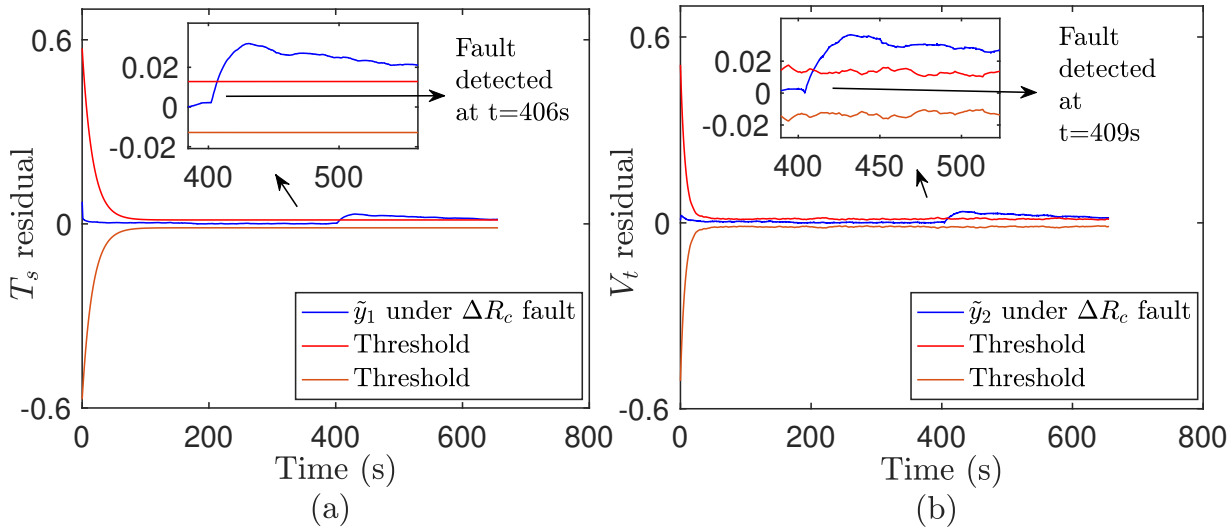

Figure 39: Residual responses under abrupt internal thermal resistance fault injected at 400s a) fault detected at $t = 406s$ and $\tilde{y}_1$ increase beyond the threshold value, b) fault detected at $t = 409s$ and $\tilde{y}_2$ increase beyond the threshold value.

Validation results under multiple thermal faults

From (4.3.2), it can be observed that the thermal resistance and internal heat generation affects both core and surface temperature dynamics. Therefore, the fault can be manifested as $\gamma_1, \gamma_2 \neq 0$. An abrupt thermal resistance fault $0.4R_c$ and additional heat generation term, whose amplitude is 0.018W, are introduced to the system at $t = 400$ sec. The estimated T_s and V_t residuals is shown in Figure 41 a) and b), respectively. From Figure 41 a) and b), we can observe that both the T_s and V_t residuals are within the adaptive threshold value till the fault occurs in the battery, i.e., at $t = 400$ sec. The residual T_s gradually exceeds the threshold after $t = 409$ sec and the residual V_t gradually exceeds the threshold after $t = 410$ sec. Thus, an multiple thermal faults are detected in the system and are diagnosed at an incipient stage.

Upon the detection of the faults, the NN-based fault learning observer is deployed to learn the thermal faults online. The simulation parameters used were $\Upsilon = 0.09 * diag[.008 - 1450], \upsilon = 20\Upsilon$. The NN weight $\hat{\theta}_\gamma$ is initialized at random from a uniform distribution in the interval of [0 0.01]. From Figure 42 a), we can observe that after the fault is detected at

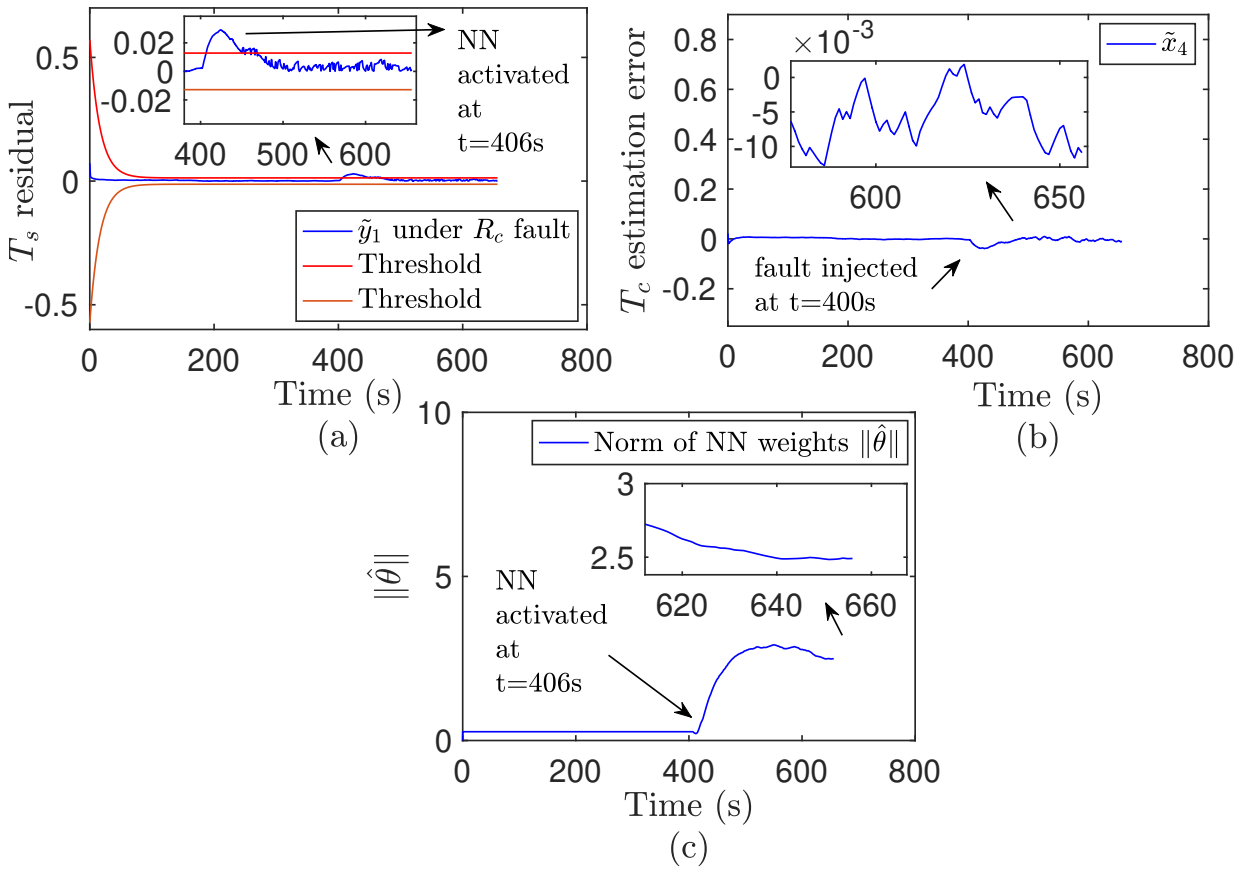

Figure 40: Residual responses with NN under abrupt internal thermal resistance fault injected at 400s a) NN gets activated at $t = 406s$ and brings the $\tilde{y}_1$ below the threshold value, b) NN gets activated at $t = 406s$ and brings back the T_c estimation error close to zero, c) NN weight estimation convergence.

$t = 409$ sec, the NN learns the fault dynamics, which can be verified by the convergence of the T_s residual close to zero with RMSE 0.0042. The convergence of the T_c estimation error close to zero with RMSE 0.0057 is shown in Figure 42 (b). Furthermore, the convergence of the estimated NN weight updates is also shown in Figure 42 (c). Therefore, it can be concluded that the NN was able to learn the fault dynamics and estimate the core temperature in the presence of multiple internal thermal faults.

The next section details the modified FD scheme presented in Section 4.3.2 and 4.3.3 to estimate the states in presence of faults and detect the thermal and side reaction faults in LIBs.

4.4 Learning-based Faulty State Estimation Using SOH-coupled Model Under Internal Thermal Faults in Lithium-ion Batteries

In this section, an NN-based FD scheme in Figure 37 is modified and presented to estimate the core temperature, SOC, and SOH during faults and detect thermal and side reaction

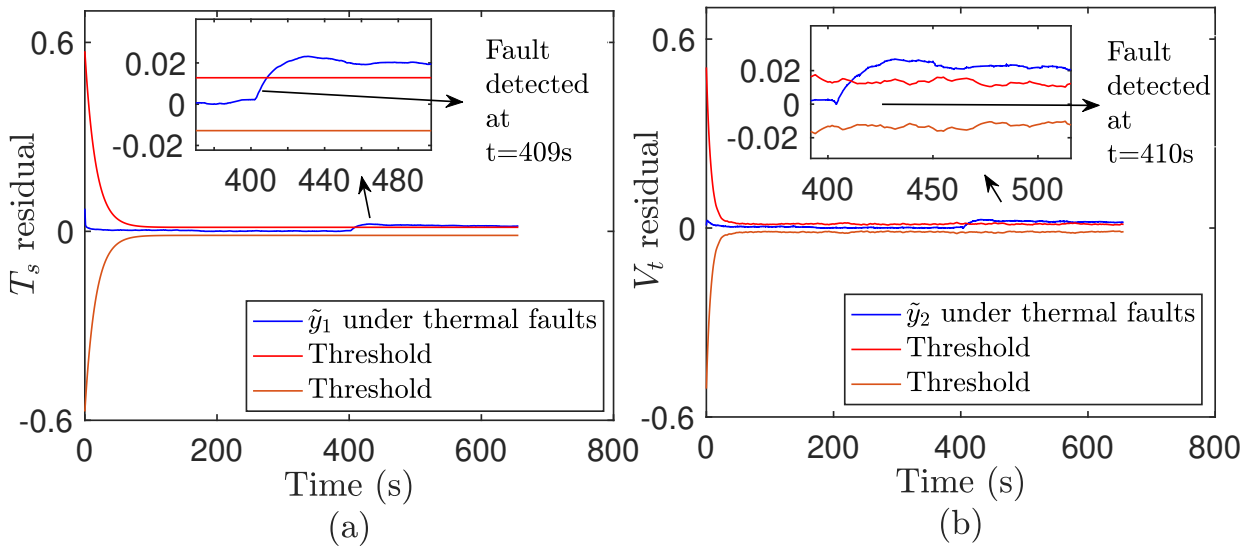

Figure 41: Residual responses under multiple thermal faults injected at 400s a) fault detected at $t = 409s$ and $\tilde{y}_1$ increase beyond the threshold value, b) fault detected at $t = 410s$ and $\tilde{y}_2$ increase beyond the threshold value.

faults at an embryonic stage. Estimating the SOC, SOH, and core temperature under internal faults will significantly improve the BMSs autonomy and accuracy in range prediction. In this section, we present an NN-based state estimation scheme that can estimate the SOC, core temperature, and SOH under internal faults in LIBs. First, we propose a model-based internal fault detection scheme by employing a SOH-coupled ETA of the LIB. Then, a NLO is employed to estimate the proposed SOH-coupled model's healthy states for a residual generation. The fault diagnosis scheme compares the output voltage and surface temperature residuals against the designed adaptive threshold to detect thermal faults. The adaptive threshold effectively alleviates the false positives due to degradation and model uncertainties of the battery under no-fault conditions. Upon detection of a fault, we employ an additional NN-based observer in the second step to learn the faulty dynamics. A novel NN weight tunning algorithm is proposed using the measured voltage, surface temperature, and estimated healthy states. The convergence of the nonlinear and NN-based observer state estimation errors is proven using the Lyapunov theory. Finally, numerical simulation results are presented.

The rest of the section is organized as follows. Section 4.4.1 and 4.4.2 briefly describe the problem statement and SOH-coupled ETA model, respectively. Section 4.4.3 details the model-based FD scheme along with the observer and adaptive threshold design. Faulty state estimation using a learning-based observer is presented in Section 4.4.4 along with stability analysis followed by simulation results in Section 4.4.5 and conclusion and future work in Section 4.5.

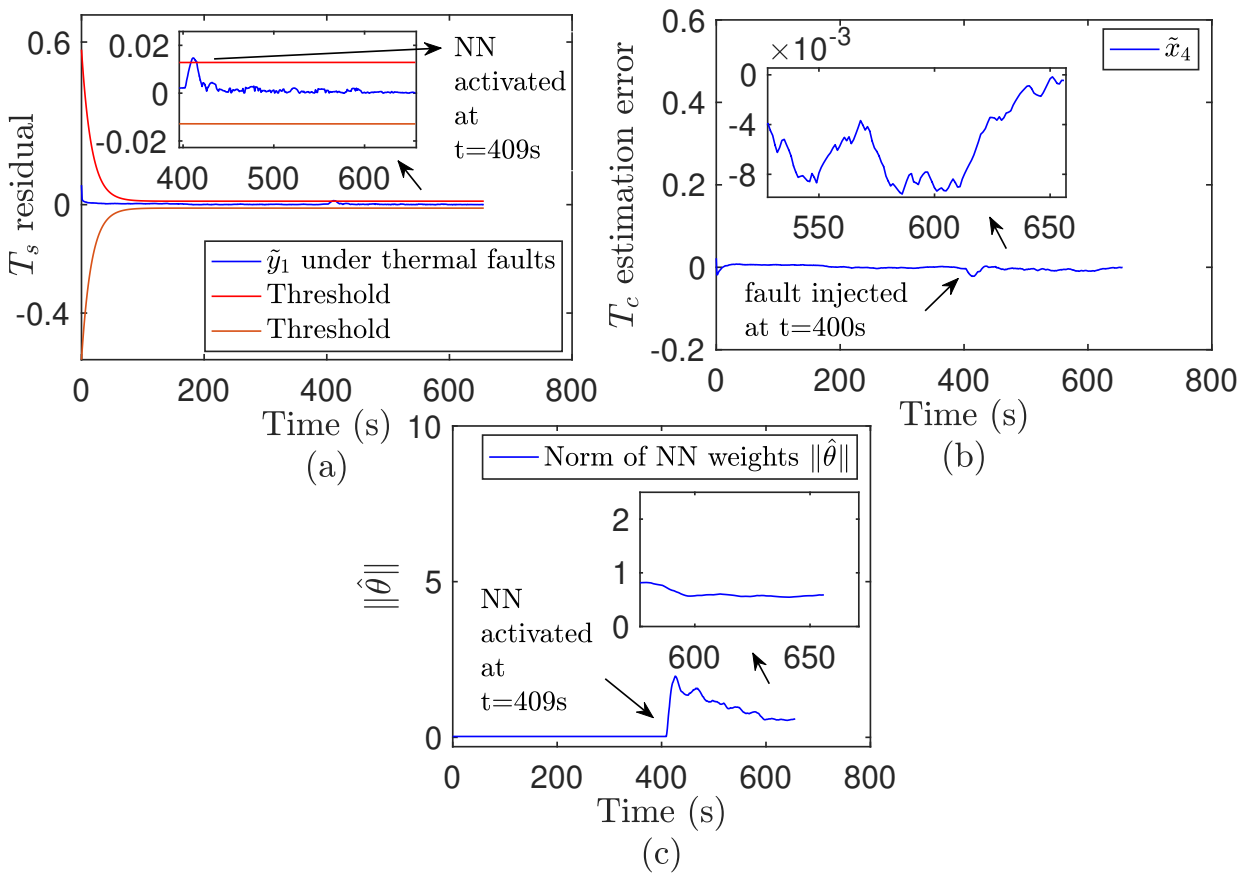

Figure 42: Residual responses with NN under internal thermal resistance and additive heat generation fault injected at 400s a) NN gets activated at $t = 409s$ and brings the $\tilde{y}_1$ below the threshold value, b) NN gets activated at $t = 409s$ and brings back the T_c estimation error close to zero, c) NN weight estimation convergence.

4.4.1 Background and Problem Formulation

This section briefly describes the SOH-coupled ETA model [241] for a cylindrical A12326650 $LiFePO_4$/graphite cell and formulates the problem. The model constitutes three coupled submodels (shown in Figure 14): 1) ECM [2] to capture the terminal behavior of the cell, 2) a thermal model [244] to capture the core (T_c) and surface (T_s) temperatures dynamics, and 3) an aging model [1] to capture the dynamics of capacity fade. Note that we have used the term aging and degradation interchangeably throughout the paper to imply the degradation of the health of the LIB.

The SOH-coupled ETA dynamics presented in Section 3.3 [241] are expressed by

$$\begin{aligned}
\frac{dSOC}{dt} &= \frac{-I(t)}{SOH_c(t)C_{use}} \\
\frac{dV_{c_{p1}}}{dt} &= \frac{-V_{c_{p1}}}{R_{p1}(SOC,T_m)C_{p1}(SOC,T_m)} + \frac{I}{C_{p1}(SOC,T_m)} \\
\frac{dV_{c_{p2}}}{dt} &= \frac{-V_{c_{p2}}}{R_{p2}(SOC,T_m)C_{p2}(SOC,T_m)} + \frac{I}{C_{p2}(SOC,T_m)} \\
\frac{dT_c}{dt} &= \frac{T_s - T_c}{R_c C_c} + \frac{Q(t)}{C_c} \\
\frac{dT_s}{dt} &= \frac{T_a - T_s}{R_u C_s} - \frac{T_s - T_c}{R_c C_s} \\
\frac{dSOH_c}{dt} &= -\frac{|I(t)|}{2N(SOC, C_{rate}, T_c)C_{use}} \\
V_t &= V_{OC}(SOC) - V_{c_{p1}} - V_{c_{p2}} - R_0(T_m)I.
\end{aligned} \tag{4.4.1}$$

Remark 4.4.1 *From the SOH-coupled model in Figure 14, it can be observed that the ECM, thermal, and aging models are coupled with each other. The ECM parameters are coupled with SOH, the heat generation in the thermal model is governed by V_{cp1} and V_{cp2} of the ECM, and the SOH is driven by both SOC and core-temperature T_c.*

The LIB dynamics in (4.4.1) comprehensively represent battery terminal electrical, internal thermal, and capacity fade behavior. In contrast to the traditional model-based fault detection approaches [52], the SOH-coupled model-based fault detection scheme can help disentangle the effect of the fault and the natural aging of the battery on the model output through an adaptive threshold. Moreover, to further improve the model's capability in (4.4.1) for isolation of internal faults (e.g., side-reaction faults), which are primarily reflected in the ohmic resistance of the battery, the internal resistance dynamics are required to be integrated. On the other hand, to orchestrate the safe operation and optimal management of a battery under fault, the BMSs must be capable of learning the fault dynamics and estimating SOC, SOH, and core temperature. This will help in thermal management, accurate estimation of SOC, SOH, and RUL, and also provide avenues to mitigate thermal runaway.

In summary, the problem at hand is fourfold: 1) the development of a nonlinear SOH-coupled ETA model by integrating ohmic resistance dynamics, 2) the design of a NLO to estimate the healthy states and parameters of the cell, 3) the design of the adaptive threshold accounting for parameters variation due to degradation and modeling uncertainties, and 4) the development of a learning-based observer to learn the internal fault dynamics and estimating the faulty states including SOC, SOH, and core temperature. Next, solutions to the above problems are presented.

4.4.2 Model Reformulation

In this section, we have reintroduced the SOH-coupled model integrated with ohmic resistance and terminal voltage dynamics to be used as a model in the fault detection scheme.

The Ohmic resistance varies with the temperature, which is given as [174]

$$R_0 = a_{0_i} e^{\frac{a_{1_i}}{(T_m)-a_{2_i}}}, \tag{4.4.2}$$

where the subscript $i \in \{c, d\}$ with c and d denote charging and discharging, respectively, and the coefficients in charge and discharge condition are obtained experimentally. It can be observed that the coefficients of R_0 are close to each other for both charging and discharging conditions. Therefore, we have averaged these coefficients to obtain a common coefficient for BMS application, both for charging and discharging, given as in (3.3.12). For brevity in notation from now on $R_{p1}(SOC, T_m)$, $C_{p1}(SOC, T_m)$, $R_{p2}(SOC, T_m)$, $C_{p2}(SOC, T_m)$ are $R_{p1}, C_{p1}, R_{p2}, C_{p2}$, respectively.

The dynamics of R_0 can be represented as

$$\frac{dR_0}{dt} = \frac{d}{dt}(a_{0_v} e^{\frac{a_{1_v}}{(T_m)-a_{2_v}}}) = \alpha_1(T_m) \tag{4.4.3}$$

where $\alpha_1(T_m) = -a_{1_v} R_0 \frac{\dot{T}_c+\dot{T}_s}{2} \frac{1}{(\frac{T_c+T_s}{2}-a_{2_v})^2}$. Similarly, we can compute the dynamics of the terminal voltage by taking the first derivative of V_t, expression in (4.4.1) given by

$$\frac{dV_t}{dt} = \alpha_2(x_1) - \frac{dV_{c_{p1}}}{dt} - \frac{dV_{c_{p2}}}{dt} - \alpha_1(T_m) I. \tag{4.4.4}$$

where $x_1 = SOC$, $\alpha_2(x_1) = \frac{dV_{oc}(x_1)}{dt} = (r_1 + 2r_2 x_1^1 + 3r_3 x_1^2 + 4r_4 x_1^3 + 5r_5 x_1^4 + 6r_6 x_1^5 + 7r_7 x_1^6 + 8r_8 x_1^7) \frac{dx_1}{dt}$.

For completeness, by combining (4.4.1), (4.4.3), and (4.4.4), the reformulated SOH-inclusive ETA model can be expressed as

$$\begin{aligned}
\frac{dSOC}{dt} &= \frac{-I(t)}{SOH_c(t) C_{use}} \\
\frac{dV_{c_{p1}}}{dt} &= \frac{-V_{c_{p1}}}{R_{p1} C_{p1}} + \frac{I}{C_{p1}} \\
\frac{dV_{c_{p2}}}{dt} &= \frac{-V_{c_{p2}}}{R_{p2} C_{p2}} + \frac{I}{C_{p2}} \\
\frac{dT_c}{dt} &= \frac{T_s - T_c}{R_c C_c} + \frac{Q(t)}{C_c} \\
\frac{dT_s}{dt} &= \frac{T_a - T_s}{R_u C_s} - \frac{T_s - T_c}{R_c C_s} \\
\frac{dSOH_c}{dt} &= -\frac{|I(t)|}{2N(SOC, C_{rate}, T_c) C_{use}} \\
\frac{dR_0}{dt} &= \alpha_1(T_m) \\
\frac{dV_t}{dt} &= \alpha_2(x_1) - \frac{dV_{c_{p1}}}{dt} - \frac{dV_{c_{p2}}}{dt} - \alpha_1(T_m) I
\end{aligned} \tag{4.4.5}$$

where $y = [T_s \;\; V_t]^T$ denotes the outputs of the system.

Defining the state vector $x = [x_1 \;\; x_2 \;\; x_3 \;\; x_4 \;\; x_5 \;\; x_6 \;\; x_7 \;\; x_8]^T$ with $x_1 = SOC$, $x_2 = V_{c_{p1}}$, $x_3 = V_{c_{p2}}$, $x_4 = T_c, x_5 = T_s, x_6 = SOH, x_7 = R_0, x_8 = V_t$, the state space representation of the SOH-coupled nonlinear ETA model in (4.4.5) can be written in a control affine form as

$$\begin{aligned} \dot{x} &= f(x) + g(x)u \\ y &= Cx \end{aligned} \tag{4.4.6}$$

where the state vector $x \in \mathbb{R}^8$, the control input $u = [u_1 \; u_2]^T \in \mathbb{R}^2$ with $u_1 = I$ and $u_2 = T_a$, and y is the output vector with output matrix $C = \begin{bmatrix} 0 & 0 & 0 & 0 & 1 & 0 & 0 & 0 \\ 0 & 0 & 0 & 0 & 0 & 0 & 0 & 1 \end{bmatrix}$. Thus, the output can be represented as $y = [x_5 \; x_8]^T = [y_1 \; y_2]^T$ and the internal dynamics $f(x) = \begin{bmatrix} 0 \\ \frac{-x_2}{R_{p1}(x_1,x_4,x_5)C_{p1}(x_1,x_4,x_5)} \\ \frac{-x_3}{R_{p2}(x_1,,x_4,x_5)C_{p2}(x_1,,x_4,x_5)} \\ \frac{-x_4}{R_cC_c} + \frac{x_5}{R_cC_c} \\ \frac{x_4}{R_cC_s} - \frac{x_5}{R_uC_s} - \frac{x_5}{R_cC_s} \\ 0 \\ \alpha_1(x) \\ -\alpha_3(x) - \alpha_4(x) \end{bmatrix}$ and $g(x) = \begin{bmatrix} \frac{-1}{x_5C_{use}} & 0 \\ \frac{1}{C_{p1}(x_1,x_4,x_5)} & 0 \\ \frac{1}{C_{p2}(x_1,x_4,x_5)} & 0 \\ \frac{(V_{oc}(x_1)-x_8)}{C_c} & 0 \\ 0 & \frac{1}{R_uC_s} \\ \frac{-1}{2N(x_1,C_{rate},x_4)C_{use}} & 0 \\ 0 & 0 \\ (-\alpha_1(x) - \alpha_2(x) - \beta_1(x) - \beta_2(x)) & 0 \end{bmatrix}$ where $\alpha_1(x) = -a_{1_v}x_7\frac{\dot{x}_4+\dot{x}_5}{2}\frac{1}{(\frac{x_4+x_5}{2}-a_{2_v})^2}$, $\alpha_3(x) = \frac{-x_2}{R_{p1}C_{p1}}$, $\alpha_4(x) = \frac{-x_3}{R_{p2}C_{p2}}$, $\beta_1(x) = \frac{1}{C_{p1}}$, $\beta_2(x) = \frac{1}{C_{p2}}$,$\alpha_2(x) = \frac{\beta_3(x)}{x_5C_{use}}$, $\beta_3(x) = r_1 + 2r_2x_1^1 + 3r_3x_1^2 + 4r_4x_1^3 + 5r_5x_1^4 + 6r_6x_1^5 + 7r_7x_1^6 + 8r_8x_1^7$.

4.4.3 Fault Detection Scheme

Internal fault mapping

We consider four types of faults, such as convective cooling resistance fault, internal thermal resistance fault, thermal runaway fault [52], and side reaction faults [253] for FD using the model in (4.4.6). Table 16 presents different types of faults and their mapping.

The state space model in (4.4.6) with the above faults can be expressed as

$$\begin{aligned} \dot{x}_f &= f(x_f) + g(x_f)u + \Gamma(x_f, u) \\ y &= Cx \end{aligned} \tag{4.4.7}$$

where x_f are the faulty states of the model, the vector $\Gamma(x_f, u) = [0 \; 0 \; 0 \; \gamma_4(t) \; \gamma_5(t) \; 0 \; \gamma_7(t) \; 0]^T$ are the faults added to the dynamics of the battery. The function $\gamma_4(t)$, $\gamma_5(t)$, and $\gamma_7(t)$ represent faults in core temperature, surface temperature, and internal resistance dynamics, respectively.

The convective cooling resistance fault (failure of the cooling system) and thermal runaway faults (overcharging/discharging, short circuit) can be represented by the addition of γ_4 and γ_5 to the dynamics of the battery, respectively. Similarly, the internal thermal resistance fault (inhomogeneous heat dissipation) can be represented by the addition of both γ_4 and γ_5. The internal side reactions faults, such as SEI, dendrite growth, and lithium plating, can be represented by the addition of γ_7, which can be reflected as a growth in ohmic resistance R_0 [29, 253]. In addition, the side reaction faults in LIBs can be attributed to a combination of

Table 16: Fault mapping for thermal and side reaction faults.

Actual faults	**Description of fault**	**Fault map**
Fault 1	Convective cooling resistance fault (ΔR_u), which is represented by a significant deviation in the parameter R_u from its nominal value.	$\gamma_4 = 0$ $\gamma_5 \neq 0$ $\gamma_7 \neq 0$
Fault 2	Internal thermal resistance fault (ΔR_c), which is modeled by a change in the parameter R_c from its nominal value.	$\gamma_4 \neq 0$ $\gamma_5 \neq 0$ $\gamma_7 \neq 0$
Fault 3	Thermal runaway fault, which is modeled by an additional heat-generation term that contributes to the core temperature rise in the battery.	$\gamma_4 \neq 0$ $\gamma_5 = 0$ $\gamma_7 \neq 0$
Fault 4	Internal side reaction fault, which is modeled by the change in the parameter R_0 from its nominal value	$\gamma_4 \neq 0$ $\gamma_5 \neq 0$ $\gamma_7 \neq 0$

factors, such as excessive temperature, detrimental copper plating occurring at the negative electrode, and cell construction and design, which all lead to thermal runaways [254, 253]. Therefore side reaction faults also manifest as temperature rises in the battery which is caused by the occurrence of multiple internal faults, i.e., represented by γ_4 and γ_5.

Remark 4.4.2 *The mapping of the faults (Fault* $1, 2, 3, 4$*) to* $\gamma_4, \gamma_5, \gamma_7$ *is useful in designing the diagnostic scheme, which can further be used for detecting,* γ_4*,* γ_5 *and* γ_7*. The cooling convective resistance fault exhibits an increase in surface temperature residual, the thermal runaway fault exhibits an increase in core temperature residual, the internal thermal resistance fault exhibits both increases in core and surface temperature residual, and side reaction faults exhibit an increase in the core, surface temperature, and voltage residuals. The change in* T_c *and* T_s *also affect voltage* (4.4.1) *in the presence of faults. Therefore internal faults in Table 16 also exhibit an increase in voltage residual.*

SOH-Coupled model-based fault detection scheme

The proposed SOH-inclusive model-based FD scheme is shown in Figure 43. An NLO is used to estimate the states of the SOH-coupled model. Two residuals are generated by comparing the battery outputs (terminal voltage, surface temperature) with the observer outputs. The residuals are compared against an adaptive threshold value (designed in the later part of Section 4.4.3) to detect the fault.

Remark 4.4.3 *Note that the proposed fault detection scheme can be applied to other cell chemistries.*

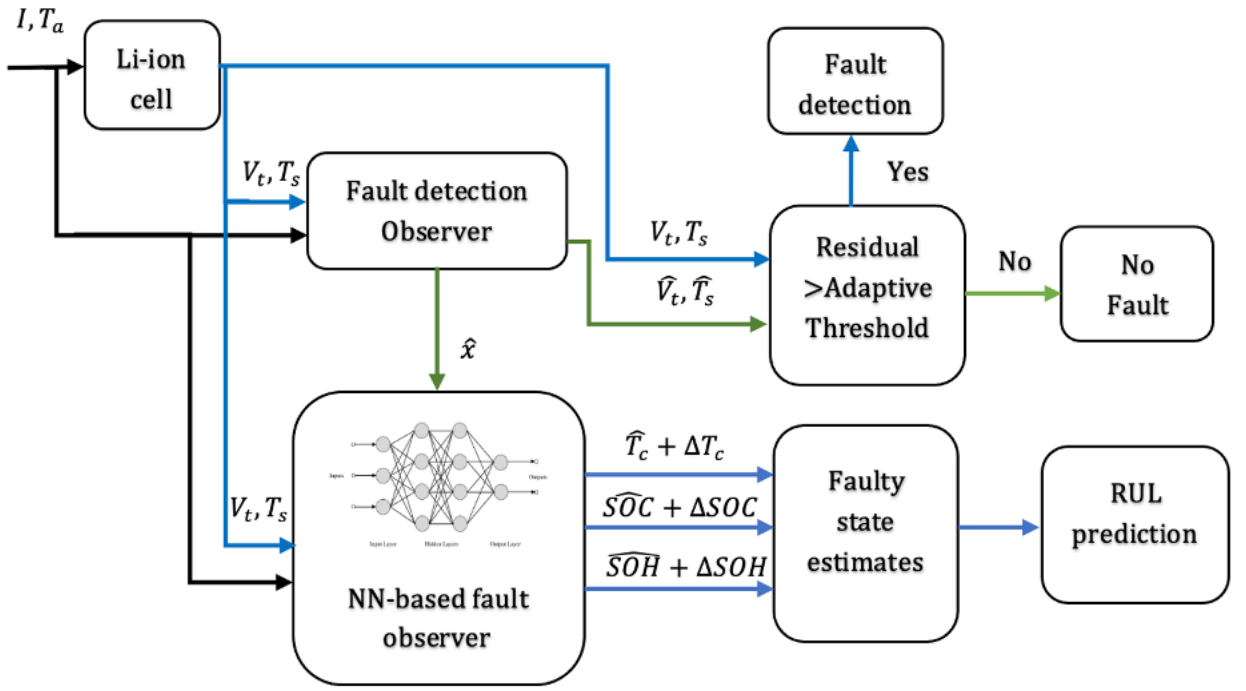

Figure 43: Fault detection scheme of a lithium-ion cell.

Estimation of healthy states via a nonlinear observer

The dynamics in (4.4.6) can be rewritten as

$$\begin{aligned} \dot{x} &= Kx + f(x) - Kx + g(x)u \\ &= Kx + \Pi(x) + g(x)u \end{aligned} \tag{4.4.8}$$

where $K \in \mathbb{R}^{n\times n}$ is a Hurwitz matrix, $\Pi(x) = f(x) - Kx$.

Based on (4.4.8) the NLO can be represented by

$$\begin{aligned} \dot{\hat{x}} &= K\hat{x} + \Pi(\hat{x}) + g(\hat{x})u + L^T(y - \hat{y}) \\ \hat{y} &= C\hat{x} \end{aligned} \tag{4.4.9}$$

where $\hat{x}$ is the estimated state, $L \in \mathbb{R}^{m\times n}$ is the observer gain, and $\Pi(\hat{x}) = f(\hat{x}) - K\hat{x}$.

The state estimation error dynamics using (4.4.8) and (4.4.9) is given by

$$\dot{\tilde{x}} = K\tilde{x} + \tilde{\Pi}(x, \hat{x}) + \tilde{g}(x, \hat{x})u - L^T C\tilde{x} \tag{4.4.10}$$

where the state estimation error $\tilde{x} = x - \hat{x}$, $\tilde{\Pi}(x, \hat{x}) = \Pi(x) - \Pi(\hat{x})$, $\tilde{g}(x, \hat{x}) = g(x) - g(\hat{x})u$ and the output error $\tilde{y} = y - \hat{y} = C\tilde{x}$. For brevity, we drop the arguments in the functions, i.e., $\tilde{\Pi}(x, \hat{x})$ is $\tilde{\Pi}$, $\tilde{g}(x, \hat{x}, u)$ is written as $\tilde{g}$, when it is clear.

Convergence analysis of the observer

The theorem 4.4.1 presented below guarantees the asymptotic convergence of the state estimation error $\tilde{x}$.

Theorem 4.4.1 *Consider the dynamics of the battery* (4.4.8) *along with the observer* (4.4.9). *Let there exist a positive definite matrix* P *satisfying the Lyapunov equation*

$$(K - L^T C)^T P + P(K - L^T C) = -Q \tag{4.4.11}$$

where Q *is a symmetric positive definite matrix with* $(K - L^T C)$ *being a stable matrix. Then, the state estimation error* $\tilde{x}$ *is locally asymptotically stable from any initial* $\tilde{x}_0 \in \Omega_x \subset \mathbb{R}^8$, *i.e.,* $\lim_{t\to\infty} \tilde{x} \to 0$.

Proof. The proof can be completed by selecting a Lyapunov function candidate V, given by

$$V = \frac{1}{2}\tilde{x}^T P \tilde{x} \tag{4.4.12}$$

where $P \in \mathbb{R}^{n\times n}$ is a symmetric positive definite matrix. To complete the proof, we need the following inequalities

Since the functions, Π and g are continuously differentiable, it is routine to check that the functions $\tilde{\Pi}$ and $\tilde{g}$ are continuously differentiable locally Lipschitz functions for any L_π, $L_g > 0$. It implies that there exists $r > 0$ such that $\|\tilde{\Pi}\| \leq L_\pi \|\tilde{x}\|$ and $\|\tilde{g}\| \leq L_g \|\tilde{x}\|$, $\forall\ \|\tilde{x}\| < r$. Further, since the charge and discharge current is finite, without loss of generality, the control input u is upper bounded with $\|u\| \leq u_{max}$, where u_{max} is the maximum absolute value of the charging and discharging currents.

The derivative of V along the trajectories of (4.4.10) is given as

$$\begin{aligned}
\dot{V} &= \tilde{x}^T P \dot{\tilde{x}} = \tilde{x}^T P(K\tilde{x} + \tilde{\Pi} + \tilde{g}u - L^T C\tilde{x}) \\
&\quad + (K\tilde{x} + \tilde{\Pi} + \tilde{g}u - L^T C\tilde{x})^T P\tilde{x} \\
&= \frac{1}{2}\tilde{x}^T (P(K - L^T C) + (K - L^T C)^T P)\tilde{x} + \tilde{x}^T P\tilde{\Pi} + \\
&\quad \tilde{x}^T P\tilde{g}u
\end{aligned} \tag{4.4.13}$$

Recalling the local Lipschitz continuity of the functions $\tilde{\Pi}$ and $\tilde{g}$ and simplifying (4.4.13) yields,

$$\begin{aligned}
\dot{V} \leq \frac{1}{2}\tilde{x}^T (P(K - L^T C) + (K - L^T C)^T P)\tilde{x} + \\
\lambda_{max}(P) L_\pi \|\tilde{x}\|^2 + u_{max}\lambda_{max}(P) L_g \|\tilde{x}\|^2
\end{aligned} \tag{4.4.14}$$

where $\lambda_{max}(P)$ is the maximum eigenvalue of symmetric positive definite matrix P. Using the definition of Euclidean norm, we can express the first derivative as

$$\dot{V} \leq -\frac{1}{2}\tilde{x}^T Q\tilde{x} + \lambda_{max}(P) L_\pi \tilde{x}^T\tilde{x} + \lambda_{max}(P) L_g u_{max} \tilde{x}^T\tilde{x} \tag{4.4.15}$$

where Q is a positive definite matrix satisfying the Lyapunov equation in (4.4.11).

By combining similar terms, we can express (4.4.15) as

$$\dot{V} \leq -\tilde{x}^T (\frac{1}{2}Q - \lambda_{max}(P) L_\phi I)\tilde{x} \tag{4.4.16}$$

where $L_\phi = L_\pi + u_{max} L_g$. By properly selecting the K, L and P, we can ensure $\frac{1}{2}Q - \lambda_{max}(P) L_\phi I > 0$. Thus, from (4.4.16) $\dot{V} < 0$. By Lyapunov theorem, the state estimation errors $\tilde{x}$ converge to zero asymptotically as $t \to \infty$. ■

From the above results, we can also show that the output estimation error also converges to zero asymptotically and presented in the next corollary.

Corollary 4.4.1 *Let hypothesis of Theorem 4.4.1 hold. Then, the output errors $\tilde{y}$ also converges to zero asymptotically.*

Proof. From Theorem 1, the positive definite matrix Q satisfies the Lyapunov equation. Alternatively, we can select a positive definite Q that always guarantees a positive definite matrix P, which can be obtained by solving the Lyapunov equation (4.4.11). Without loss of generality, we can assume $Q = \text{diag}\{q_i\}$, $i = 1, 2, \cdots, 8$, to be diagonal matrix with all diagonal elements positive, i.e., $q_i > 0 \ \forall i$, which satisfies the condition $Q_{red} = \frac{1}{2}Q - \lambda_{max}(P)L_\phi I > 0$. It is routine to check that Q_{red} is also a diagonal matrix.

Recalling (4.4.16), we can express the first derivative of the Lyapunov function as

$$\dot{V} \leq -\tilde{x}^T Q_{red}\tilde{x} \leq -\tilde{x}_5^T\sigma_5\tilde{x}_5 - \tilde{x}_8^T\sigma_8\tilde{x}_8 \tag{4.4.17}$$

where σ_5, and σ_8 are the corresponding diagonal elements of Q_{red}. From (4.4.17), the first $\dot{V} < 0$ and the state errors $\tilde{x}_5, \tilde{x}_8$ converge to zero as $t \to \infty$. Alternatively, the output estimation errors $\tilde{y}_1$, $\tilde{y}_2$ convergences to zero as $t \to \infty$. ■

Next section details the adaptive threshold design.

Adaptive threshold design for fault detection

In this subsection, we designed the FD threshold values for the output residuals. Unlike the constant threshold, we proposed adaptive thresholds [52, 255] to account for the changes in residuals due to aging, changes in operating temperature, and unmodeled dynamics (uncertainties).

The following assumption is needed to proceed further.

Assumption 4.4.1 *The observer in* (4.4.9) *converges before the occurrence of a fault.*

This is a trivial assumption since the observer convergence rate can be selected by designing a proper gain matrix and implemented before commissioning.

For instance, the ECM parameter (R_0) varies with SOH and other degradation-inducing factors, such as T_c, C_{rate}, and DOD. The thermal model parameters, such as C_c, C_s, and T_a, also change with battery aging. We can express these changes in the model parameters as the sum of the nominal values and the change, i.e., $R_0 + \Delta R_0$, $C_c + \Delta C_c$, $C_s + \Delta C_s$, and $T_a + \Delta T_a$, where ΔR_0, ΔC_s, ΔC_c, and ΔT_a are the changes in the parameters due aging and modeling uncertainty. Therefore, the residuals will lead to a non-zero value even under no-fault conditions.

The nominal SOH-coupled model in (4.4.8), under no-fault condition, can be rewritten to include the parameter changes (ΔR_0, ΔC_s, ΔC_c, and ΔT_a) as

$$\begin{aligned} \dot{x} &= Kx + \Pi(x) + g(x)u + \chi(x,u) \\ y &= Cx \end{aligned} \tag{4.4.18}$$

where $\chi(x,u) = [\eta_1(x,u), \cdots, \eta_8(x,u)]^T$ is a vector-valued function of parameter changes due to degradation. Note that $\chi(x,u)$ is a state and/or input-dependent vector function. We can express $\eta_1(x,u), \cdots, \eta_8(x,u)$ as linear in unknown parameter form [52] as

$$\begin{aligned}
&\eta_1(x,u) = \eta_{11},\ \eta_2(x,u) = \eta_{21},\ \eta_3(x,u) = \eta_{31}\\
&\eta_4(x,u) = \eta_{41} + \eta_{42}x_4 + \eta_{43}x_5 + \eta_{44}u_1,\\
&\eta_5(x,u) = \eta_{51} + \eta_{52}x_4 + \eta_{53}x_5 + \eta_{54}u_2,\\
&\eta_6(x,u) = \eta_{61},\\
&\eta_7(x,u) = \eta_{71} + \eta_{72}x_4 + \eta_{73}x_5, \text{and}\\
&\eta_8(x,u) = \eta_{81} + \eta_{82}u_1
\end{aligned} \tag{4.4.19}$$

where $\eta_{11}, \eta_{21}, \cdots, \eta_{81}$ capture the modeling uncertainty i.e., they include the effects of exogenous input disturbances in the system [52]. The change in thermal parameters $(C_c + \Delta C_c)$ is reflected in η_{42}, η_{43}, and η_{44}, $(C_s + \Delta C_s)$ is reflected in η_{52}, η_{53}, and η_{54}, $(T_a + \Delta T_a)$ is reflected in η_{54}, and $(R_0 + \Delta R_0)$ is reflected in η_{44}, η_{72}, η_{73}, and η_{82}. The noise in input current and ambient temperature is reflected in η_{44} and η_{82}, and η_{54}, respectively.

Assumption 4.4.2 *$\eta_1(x,u), \cdots, \eta_8(x,u)$ are assumed to be bounded, unknown, exogenous (and possibly time-varying) inputs acting on the nominal battery model. For brevity of notation $\chi(x,u)$ is χ.*

From Corollary 4.4.1, we have $\dot{\tilde{y}} \leq -\sigma\tilde{y}$, where σ is the convergence rate, i.e., the output residuals under ideal conditions (no-fault and modeling uncertainty) converge to zeros asymptotically. Therefore, the dynamics of the residual in the presence of parameter changes due to aging and uncertainty can be expressed as

$$\begin{aligned}
&\dot{\tilde{y}}_1 \leq -\sigma_5\tilde{y}_1 + \eta_5, \text{and}\\
&\dot{\tilde{y}}_2 \leq -\sigma_8\tilde{y}_2 + \eta_8.
\end{aligned} \tag{4.4.20}$$

where σ_5, and σ_8 are the convergence rates under no fault conditions and defined in (4.4.17). Using the comparison lemma [256], the solutions to (4.4.20) are upper bounded as

$$\begin{aligned}
&\tilde{y}_1 \leq \tilde{y}_1(0)e^{-\sigma_5 t} + \int_0^t e^{-\sigma_5(t-\tau)}\eta_5(\tau)\,d\tau,\\
&\tilde{y}_2 \leq \tilde{y}_2(0)e^{-\sigma_8 t} + \int_0^t e^{-\sigma_8(t-\tau)}\eta_8(\tau)\,d\tau.
\end{aligned} \tag{4.4.21}$$

Applying Cauchy Schwarz [257] inequality $|ab| \leq |a||b|$, (4.4.21) can be written as

$$\begin{aligned}
&\tilde{y}_1 \leq \tilde{y}_1(0)|e^{-\sigma_5 t}| + \int_0^t |e^{-\sigma_5(t-\tau)}||\eta_5(\tau)|\,d\tau, \text{and}\\
&\tilde{y}_2 \leq \tilde{y}_2(0)|e^{-\sigma_8 t}| + \int_0^t |e^{-\sigma_8(t-\tau)}||\eta_8(\tau)|\,d\tau
\end{aligned} \tag{4.4.22}$$

From the definitions in (4.4.19), we have $|\eta_5(\tau)| \leq |\eta_{51}| + |\eta_{52}||x_4| + |\eta_{53}||x_5| + |\eta_{54}||u_2|$ and $|\eta_8(\tau)| \leq |\eta_{81}| + |\eta_{82}||u_1|$. Since $e^{-\sigma_5 t}$, $e^{-\sigma_8 t} > 0, \forall t > 0$, we can write $|e^{-\sigma_5 t}| = e^{-\sigma_5 t}$, and $|e^{-\sigma_8 t}| = e^{-\sigma_8 t}$. Further, from Assumption 4.4.2, we have $\eta_{ij} \leq \eta_{ijmax} \forall i,j = 1, \cdots, 8$.

Using the above upper bounds, we can express (4.4.22) as

$$\begin{aligned}\tilde{y}_1 \leq R_{es_{1th}} &= \tilde{y}_1(0)e^{-\sigma_5 t} + \int_0^t |e^{-\sigma_5(t-\tau)}|\eta_{5max}\, d\tau \\ \tilde{y}_2 \leq R_{es_{2th}} &= \tilde{y}_2(0)e^{-\sigma_8 t} + \int_0^t |e^{-\sigma_8(t-\tau)}|\eta_{8max}\, d\tau\end{aligned} \tag{4.4.23}$$

where $\eta_{5max} = \eta_{51max} + \eta_{52max}|x_4| + \eta_{53max}|x_5| + \eta_{54max}|u_2|$, and $\eta_{8max} = \eta_{81max} + \eta_{82max}|u_1|$.

The adaptive thresholds $R_{es_{1th}}$, and $R_{es_{2th}}$ can be calculated as

$$\begin{aligned}R_{es_{1th}} &= \tilde{y}_1(0)e^{-\sigma_5 t} + \Psi_1, \text{and} \\ R_{es_{2th}} &= \tilde{y}_2(0)e^{-\sigma_8 t} + \Psi_2,\end{aligned} \tag{4.4.24}$$

where Ψ_1, Ψ_2 can be calculated from the filter dynamics

$$\begin{aligned}\dot{\Psi}_1 &= -\sigma_5\Psi_1 + \eta_{5max}, \\ \dot{\Psi}_2 &= -\sigma_8\Psi_2 + \eta_{8max}.\end{aligned} \tag{4.4.25}$$

The adaptive thresholds in (4.4.24) prevent any false alarms from being generated even in the presence of parameters changes due to aging and modeling uncertainty, satisfying $\eta_i(x,u) \leq \eta_{i_{max}}\ \forall i = 1, 2, \cdots, 8$.

The next section provides an NN-based learning approach to learn the fault dynamics and estimate the SOC, SOH, and core temperature using a fault observer.

4.4.4 Faulty State Estimation Using Learning-Based Observer

In this section, we introduce a second observer, which can be implemented after the detection of an internal fault for estimating the faulted states (SOC, SOH, and core temperature).

NN-based observer for faulty state estimation

Considering the state space representation of the LIB under fault conditions in (4.4.7), the fault vector function $\Gamma(x_f, u)$ is difficult to model and often unknown complex nonlinear function of the states and control input. We can revoke the universal approximation property to approximate this function in a compact set. Alternatively, the function $\Gamma(x_f, u)$ can be represented in parametric form using a multi-layer NN as

$$\begin{aligned}\dot{x}_f &= Kx_f + \Pi(x_f) + g(x_f)u + \theta^T\sigma(x_f, u) + \epsilon(x_f, u) \\ y_f &= Cx_f\end{aligned} \tag{4.4.26}$$

where x_f is the faulty state of the model, $y_f = [y_{1f}\ y_{2f}]^T$ is the faulted battery output, $\theta = \begin{bmatrix} \theta_{\gamma_1} & 0 & 0 & ... & 0 \\ 0 & \theta_{\gamma_2} & 0 & ... & 0 \\ . & & & & \\ . & & & & \\ 0 & 0 & ... & 0 & \theta_{\gamma_8} \end{bmatrix}_{ln\times n}$ is the unknown target NN weight matrix with each

$\theta_{\gamma_i}^T \in \mathbb{R}^{1\times l}$ and $\sigma_{\gamma_i} \in \mathbb{R}^{l\times 1}$ $\forall i = 1..8$. The basis or activation function is denoted by $\sigma = \begin{bmatrix} \sigma_{\gamma_1}^T & \sigma_{\gamma_2}^T & \cdots & \sigma_{\gamma_8}^T \end{bmatrix}_{ln\times 1}^T$ where l is the number of neurons in the NN architecture and $\epsilon(x_f, u)$ is the approximation error.

Based on (4.4.26) the NN-based fault observer can be written as

$$\begin{aligned} \dot{\check{x}} &= K\check{x} + \Pi(\check{x}) + g(\check{x})u + \check{\theta}^T\sigma(\check{x}, u) + L^T C\tilde{x} \\ \check{y} &= C\check{x} \end{aligned} \tag{4.4.27}$$

where $\check{x}$ and $\check{y}$ are the state and output estimation vectors in the presence of faults, respectively, and $\hat{\theta}$ represents the estimated NN weights of the output layer of NN. The state estimation error $\tilde{x} = x_f - \check{x}$ is the difference between the faulty battery state and observer state in (4.4.27).

The state estimation error dynamics in the presence of faults, by subtracting (4.4.27) from (4.4.26), can be written as

$$\begin{aligned} \dot{\tilde{x}} = K\tilde{x} + \tilde{\Pi} + \tilde{g}u + \tilde{\theta}^T\sigma(\check{x}, u) + \theta^T\tilde{\sigma}(x_f, \check{x}, u) - \\ L^T C\tilde{x} + \epsilon(x_f, u) \end{aligned} \tag{4.4.28}$$

where $\tilde{\sigma}(x_f, \check{x}, u) = \sigma(x_f, u) - \sigma(\check{x}, u)$. For brevity in notation $\tilde{\sigma}(x_f, \check{x}, u)$ is written as $\tilde{\sigma}$, and the weight errors is given as $\tilde{\theta} = \theta - \hat{\theta}$.

The update law for training $\hat{\theta}$ such that the faulty state estimation error and NN weight estimation error converge close to zero is provided next.

Convergence analysis

Before introducing the NN weight update law, we need the following assumption.

Assumption 4.4.3 *All faults are slowly time-varying and detected at an incipient stage.*

One of the major challenges in training the NN weights in the case of a LIB is the limited available measurement to design the update law. Alternatively, the only outputs available for measurement are the terminal voltage and surface temperature of the battery under fault. To address this challenge, we employ the estimated healthy states ($\hat{x}$) by the NLO in (4.4.9) as a substitute for the states that are not measurable, in addition to the faulty measured output. Defining the augmented output vector as the concatenation of the healthy states and faulty measured outputs as $\bar{X} = [S\hat{O}C, \hat{V}_{cp1}, \hat{V}_{cp2}, \hat{T}_c, y_{1f}, S\hat{O}H, \hat{R}_0, y_{2f}]^T$, the augmented error vector $\Xi = \bar{X} - \check{x}$ is employed to tune the NN weight estimates.

The weight update law, developed based on the subsequent stability analysis, can be represented by

$$\dot{\hat{\theta}} = -\sigma(\check{x}, u)\Xi^T\upsilon - \sigma(\check{x}, u)\sigma(\check{x}, u)^T\hat{\theta}\Upsilon \tag{4.4.29}$$

where $\upsilon, \Upsilon \in \mathbb{R}^{n\times n}$ are the learning gains.

From (4.4.29) it can be observed that $S\hat{O}C, \hat{V}_{cp1}, \hat{V}_{cp2}, \hat{T}_c, S\hat{O}H, \hat{R}_0$ in $\bar{X}$ does not account for faults reflecting in $SOC, V_{cp1}, V_{cp2}, T_c, SOH, R_0$, respectively. From Theorem 4.4.1, we know that $\hat{x} \to x$ and by Assumption 4.4.1, we can rewrite $\bar{X} = x + \Delta_x$, and $\Delta_x = [\Delta_{SOC}, \Delta_{V_{cp1}}, \Delta_{V_{cp2}}, \Delta_{T_c}, 0, \Delta_{SOH}, \Delta_{R_0}, 0]^T$ represents the change in $SOC, V_{cp1}, V_{cp2}, T_c, SOH,$

R_0 due to fault. The augmented error vector $\Xi = \tilde{x} + \Delta_x$ is employed to tune the NN weight estimates.

The weight estimation error dynamics can be written as

$$\dot{\tilde{\theta}} = \sigma(\check{x}, u)(\tilde{x} + \Delta_x)^T \upsilon + \sigma(\check{x}, u)\sigma(\check{x}, u)^T \hat{\theta}\Upsilon \tag{4.4.30}$$

The next theorem guarantees uniform ultimate boundedness (UUB) of the faulty state estimation error. To show the UUB, we will use the following trivial assumptions.

Assumption 4.4.4 *The change in SOC, V_{cp1}, V_{cp2}, T_c, SOH, and R_0 due to fault is assumed to be bounded with $\Delta_{SOC} \leq \kappa_1 \tilde{x}_1$, $\Delta_{V_{cp1}} \leq \kappa_2 \tilde{x}_2$, $\Delta_{V_{cp2}} \leq \kappa_3 \tilde{x}_3$, $\Delta_{T_c} \leq \kappa_4 \tilde{x}_4$, $\Delta_{SOH} \leq \kappa_6 \tilde{x}_6$, and $\Delta_{R_0} \leq \kappa_7 \tilde{x}_7$, where κ_i, $i = 1, .., 4, 6, 7$ are some positive constants.*

Assumption 4.4.5 *Given a constant $\bar{\epsilon}$ there exists a vector of basis functions $\sigma(x, u)$ and weight parameter vector θ and positive constants σ_{max} and θ_{max} such that given a compact set $x \in \Omega_x$, $\|\theta\| \leq \theta_{max}, \|\epsilon(x, u)\| \leq \bar{\epsilon}$ and $\|\sigma(x, u)\| \leq \sigma_{max}, \|\tilde{\sigma}(x, \hat{x}, u)\| \leq 2\sigma_{max}, \|\sigma(\hat{x}, u)\| \leq \sigma_{max}$, $\forall (x, u) \in x$.*

Theorem 4.4.2 *Consider the dynamics of the battery* (4.4.26) *and the observer* (4.4.27)*. Suppose the Assumptions 4.4.1 to 4.4.5 hold. Let there exist a positive definite matrix $\bar{P}$ satisfying the Lyapunov equation $(K - L^T C)^T \bar{P} + \bar{P}(K - L^T C) = -\bar{Q}$. If the weights of NN are updated according to* (4.4.29)*, then $\tilde{x}, \tilde{\theta} \in L_\infty$, the estimation error and the weights error are ultimately bounded.*

Proof. The proof can be completed using a Lyapunov function

$$V(Z) = \frac{1}{2}\tilde{x}^T \bar{P}\tilde{x} + \frac{1}{2}tr(\tilde{\theta}^T \tilde{\theta})) \tag{4.4.31}$$

where $Z = [\tilde{x}^T \quad vec(\tilde{\theta})^T]$, $\bar{P} \in \mathbb{R}^{n \times n}$ is a symmetric positive definite matrix, $vec(.)$ is the vectorization operator.

The derivative of V along the trajectories of (4.4.28) and (4.4.30) is given as

$$\begin{aligned}
\dot{V}(Z) &= \tilde{x}^T \bar{P}\dot{\tilde{x}} + tr(\tilde{\theta}^T \dot{\tilde{\theta}})) \\
&= \tilde{x}^T \bar{P}\tilde{\theta}^T \sigma(\check{x}, u) + \tilde{x}^T \bar{P}\theta^T \tilde{\sigma} + \tilde{x}^T \bar{P}\epsilon(x, u) + \\
&\tilde{x}^T \bar{P}K\tilde{x} + \tilde{x}^T \bar{P}\tilde{\Pi} + \tilde{x}^T \bar{P}\tilde{g}u - \tilde{x}^T \bar{P}L^T C\tilde{x} \\
&+ tr(\tilde{\theta}^T(\sigma(\check{x}, u)\tilde{x}^T \upsilon + \sigma(\check{x}, u)\Delta_x^T \upsilon + \\
&\sigma(\check{x}, u)\sigma(\check{x}, u)^T \theta\Upsilon - \sigma(\check{x}, u)\sigma(\check{x}, u)^T \tilde{\theta}\Upsilon).
\end{aligned} \tag{4.4.32}$$

Recalling the Assumption 4.4.4 and 4.4.5, and the Lyapunov first derivative can be upper

bounded as

$$\begin{aligned}\dot{V}(Z) \leq\ & \tilde{x}^T\bar{P}\tilde{\theta}^T\sigma(\check{x},u) + \tilde{x}^T\bar{P}\theta^T\tilde{\sigma} + \tilde{x}^T\bar{P}\epsilon(x,u)+ \\ & \frac{1}{2}\tilde{x}^T(\bar{P}(K-L^TC)+(K-L^TC)^T\bar{P})\tilde{x} + \tilde{x}^T\bar{P}\tilde{\Pi}+ \\ & \tilde{x}^T\bar{P}\tilde{g}u + tr(\tilde{\theta}^T(\sigma(\check{x},u)(\tilde{x})^T\upsilon + \sigma(\check{x},u)(\psi\tilde{x})^T\upsilon+ \\ & \sigma(\check{x},u)\sigma(\check{x},u)^T\theta\Upsilon - \sigma(\check{x},u)\sigma(\check{x},u)^T\tilde{\theta})\Upsilon) \\ & \leq \sigma_{max}\lambda_{max}(\bar{P})\|\tilde{x}\|\|\tilde{\theta}\| + 2\theta_{max}\sigma_{max}\lambda_{max}(\bar{P})\|\tilde{x}\|+ \\ & \bar{\epsilon}\lambda_{max}(\bar{P})\|\tilde{x}\| - \frac{1}{2}\lambda_{min}(\bar{Q})\|\tilde{x}\|^2+ \\ & \lambda_{max}(\bar{P})L_\pi\|\tilde{x}\|^2 + u_{max}\lambda_{max}(\bar{P})L_g\|\tilde{x}\|^2+ \\ & \sigma_{max}\|\upsilon\|\|\tilde{x}\|\|\tilde{\theta}\| + \sigma_{max}\|\psi\|\|\upsilon\|\|\tilde{\theta}\|\|\tilde{x}\|+ \\ & \sigma_{max}^2\theta_{max}\|\Upsilon\|\|\tilde{\theta}\| - \sigma_{max}^2\|\Upsilon\|\|\tilde{\theta}\|^2\end{aligned} \tag{4.4.33}$$

where $\psi = diag[\kappa_1,\kappa_2,\kappa_3,\kappa_4,0,\kappa_6,\kappa_7,0]$. $\lambda_{min}(\bar{Q})$ is the minimum eigenvalue of symmetric positive definite matrix $\bar{Q}$, $\lambda_{max}(\bar{P})$ is the maximum eigenvalue of symmetric positive definite matrix $\bar{P}$.

Rearranging the terms in (4.4.33) gives,

$$\begin{aligned}\dot{V}(Z) \leq & -\left(\frac{1}{2}\lambda_{min}(\bar{Q}) - \lambda_{max}(\bar{P})L_\phi I\right)\|\tilde{x}\|^2- \\ & \sigma_{max}^2\|\Upsilon\|\|\tilde{\theta}\|^2 + \zeta_1\|\tilde{x}\|\|\tilde{\theta}\| + \zeta_2\|\tilde{x}\| + \zeta_3\|\tilde{\theta}\|\end{aligned} \tag{4.4.34}$$

where $\zeta_1 = \sigma_{max}\lambda_{max}(\bar{P}) + \sigma_{max}\|\psi\|\|\upsilon\| + \sigma_{max}\|\upsilon\|$, $\zeta_2 = 2\theta_{max}\sigma_{max}\lambda_{max}(\bar{P}) + \bar{\epsilon}\lambda_{max}(\bar{P})$, $\zeta_3 = \sigma_{max}^2\theta_{max}\|\Upsilon\|$. Separating the cross terms in (4.4.34) and using Young's inequality, we have $2\|\theta\|\|\tilde{x}\| \leq \|\tilde{\theta}\|^2 + \|\tilde{x}\|^2$, (4.4.34) is written as

$$\begin{aligned}\dot{V}(Z) \leq & -\left(\frac{1}{2}\lambda_{min}(\bar{Q}) - \lambda_{max}(\bar{P})L_\phi I\right)\|\tilde{x}\|^2- \\ & \sigma_{max}^2\|\Upsilon\|\|\tilde{\theta}\|^2 + \zeta_1\|\tilde{x}\|^2 + \zeta_1\|\tilde{\theta}\|^2 + \zeta_2\|\tilde{x}\| + \zeta_3\|\tilde{\theta}\|\end{aligned} \tag{4.4.35}$$

Defining $\zeta_4 = \frac{1}{2}\lambda_{min}(\bar{Q}) - \lambda_{max}(\bar{P})L_\phi I - \zeta_1 > 0$ and $\zeta_5 = \sigma_{max}^2\|\Upsilon\| - \zeta_1 > 0$ we have,

$$\begin{aligned}\dot{V}(Z) &\leq -\zeta_4\|\tilde{x}\|^2 + \zeta_2\|\tilde{x}\| - \zeta_5\|\tilde{\theta}\|^2 + \zeta_3\|\tilde{\theta}\| \\ &\leq -\frac{\zeta_4}{2}\|\tilde{x}\|^2 - \left(\sqrt{\frac{\zeta_4}{2}}\|\tilde{x}\| - \frac{\zeta_2}{\sqrt{2\zeta_4}}\right)^2 + c_1 \\ &\quad - \frac{\zeta_5}{2}\|\tilde{\theta}\|^2 - \left(\sqrt{\frac{\zeta_5}{2}}\|\tilde{\theta}\| - \frac{\zeta_3}{\sqrt{2\zeta_5}}\right)^2 + c_2\end{aligned} \tag{4.4.36}$$

where $c_1 = \frac{\zeta_2^2}{2\zeta_4}$, $c_2 = \frac{\zeta_3^2}{2\zeta_5}$. Since $-\left(\sqrt{\frac{\zeta_4}{2}}\|\tilde{x}\| - \frac{\zeta_2}{\sqrt{2\zeta_4}}\right)^2, -\left(\sqrt{\frac{\zeta_5}{2}}\|\tilde{\theta}\| - \frac{\zeta_3}{\sqrt{2\zeta_5}}\right)^2$ are always negative. $\dot{V}(Z)$ can be written as

$$\dot{V}(Z) \leq -\frac{\zeta_4}{2}\|\tilde{x}\|^2 - \frac{\zeta_5}{2}\|\tilde{\theta}\|^2 + c_1 + c_2 \tag{4.4.37}$$

So $\dot{V}(Z) < 0$ as long as $||\tilde{x}|| > \left(\frac{2(c_1+c_2)}{\zeta_4}\right)^{\frac{1}{2}}$ or $||\tilde{\theta}|| > \left(\frac{2(c_1+c_2)}{\zeta_5}\right)^{\frac{1}{2}}$. By Lyapunov stability, the state estimation error $\tilde{x}$ and NN weight estimation error $\tilde{\theta}$ remain locally UUB. ■

The next section presents with simulation results to validate the model-based fault detection scheme.

4.4.5 Simulation Results and Discussion

Identification of lithium-ion battery electrical model

Experimental studies conducted on cylindrical A12326650 $LiFePO_4$/graphite cells with a capacity of 2.5 Ah are given in Section 3.3.4. The parameters obtained from these experiments are used for simulation.

Validation of the observer in the presence of uncertainties and no fault

MATLAB/Simulink platform is used to perform simulations and is presented in this section to show the effectiveness of the proposed model-based FD scheme. In the plant model, the change in parameters due to SOH degradation in the form (4.4.19) were injected. The coefficients are chosen as $\eta_{11} = \eta_{44} = \eta_{54} = \eta_{61} = \eta_{71} = \eta_{72} = \eta_{73} = \eta_{81} = 0, \eta_{21} = 10^{-7}, \eta_{31} = 10^{-6}, \eta_{41} = \eta_{42} = \eta_{43} = \eta_{51} = \eta_{52} = \eta_{53} = 10^{-8}, \eta_{82} = 10^{-4}$.

The adaptive threshold generators are provided as shown in (4.4.24) with the bounds of these coefficients. The current profile used for the simulation was a drive cycle, as shown in Figure 21. The states and parameters estimated using the observer in the presence of uncertainties are given in Figure 38. All the state estimation errors for SOH, SOC, R_0, T_C are within 1% band with RMSEs = 0.0024, 0.0013, $1.7508E-4$, and 0.0036, respectively. The residual responses for surface temperatures and voltage are shown in Figs. 44(a) and 44(b), respectively, under no-fault conditions. It can be seen that the surface temperature and voltage residuals are within the adaptive threshold values with RMSEs = 0.0038, and 0.0033, respectively.

Validation of the observer under fault

In this section, the effectiveness of the fault detection scheme with two different faults is verified. The same drive cycle current, as shown in Figure 21, was used as an input to LIBs model in (4.4.7) with $T_a \approx 25°C$. First, we verify the online fault learning scheme to learn the faults occurring in T_s.

R_u fault

From (4.4.5), it can be observed that the convective cooling resistance fault affects only the surface temperature dynamics. However, since the change in T_s also affects ohmic resistance dynamics (4.4.3), convective cooling resistance fault also affects voltage dynamics (4.4.4). Therefore the fault can be simulated as $\gamma_5, \gamma_7 \neq 0$, which affects the T_s and V_t residuals.

An abrupt convective cooling resistance fault $0.4Ru$ is injected at $t = 206$ sec. From Figs. 45(a) and 45(b), we can observe that the residuals are within the adaptive threshold

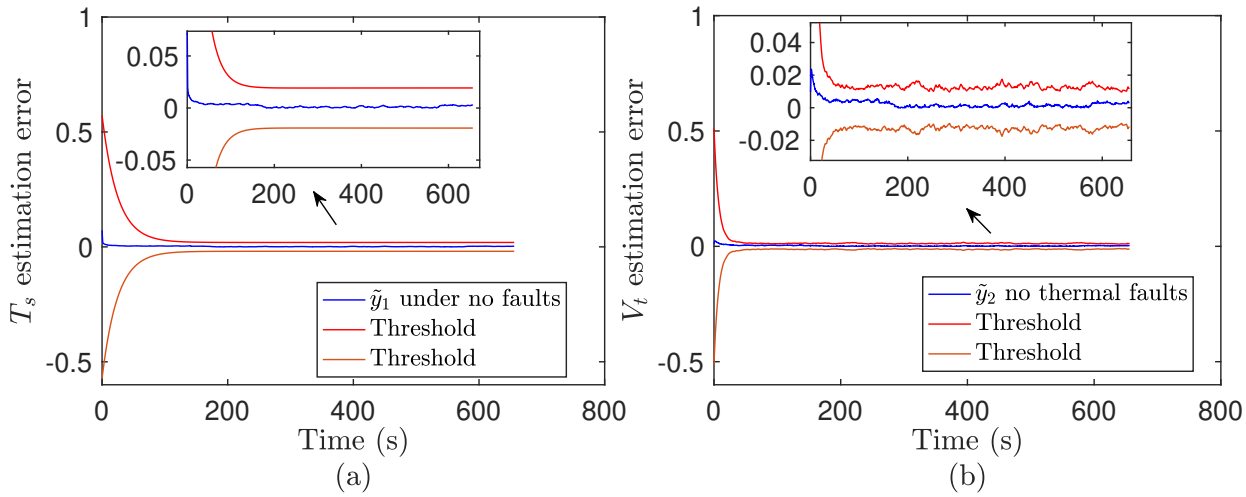

Figure 44: Output residuals and adaptive thresholds a) surface temperature error and b) voltage error under no-fault condition.

value before the occurrence of the fault $t = 206$ sec. This further validates the estimation accuracy of the NLO. Upon the occurrence of the fault, the T_s and V_t residuals exceed the adaptive threshold value after $t = 206$ sec. This implies the detection of a convective cooling resistance fault and is diagnosed at an incipient stage.

Upon detection of the fault, the NN-based observer was deployed to learn the convective cooling resistance fault online. The simulation parameters used were $\Upsilon = diag[.05, 0.001, -5, -.35, -2000, .045, -.09, 5.0], \upsilon = 16 * \Upsilon$. The NN weight $\hat{\theta}$ was initialized at random from a uniform distribution in the interval of [0 0.001]. The number of neurons in the hidden layer is chosen as 20. From Figs. 46(a) and 46(b), we can observe that after the fault is detected at $t = 209$ sec, the NN learns the fault dynamics, which can be verified by the convergence of the residuals T_s and V_t close to zero with RMSEs 0.0041 and 0.0036, respectively. This brings back the residuals below the threshold value, as shown in Figs. 46(a) and 46(b). The convergence of the state estimation errors close to zero with RMSEs within 1% band is shown in Figure 46 (c). Furthermore, the convergence of the estimated NN weight updates is also shown in Figure 46 (d).

Therefore, it can be concluded that the NN was able to learn the fault dynamics and estimate the core temperature SOC and SOH in the presence of a convective cooling resistance fault.

Multiple thermal or side-reaction faults

An abrupt convective cooling resistance $0.4R_u$, internal thermal resistance $0.2R_c$, and thermal runaway 0.02W faults are injected at $t = 206$ sec. From (4.4.5), it can be observed that the convective cooling resistance fault affects only the surface temperature dynamics, thermal runaway affects only core temperature dynamics, whereas internal thermal resistance affects both core and surface temperature dynamics. However, since the change in T_s, T_c also affects ohmic resistance dynamics (4.4.3), multiple thermal or side reaction faults also affect voltage

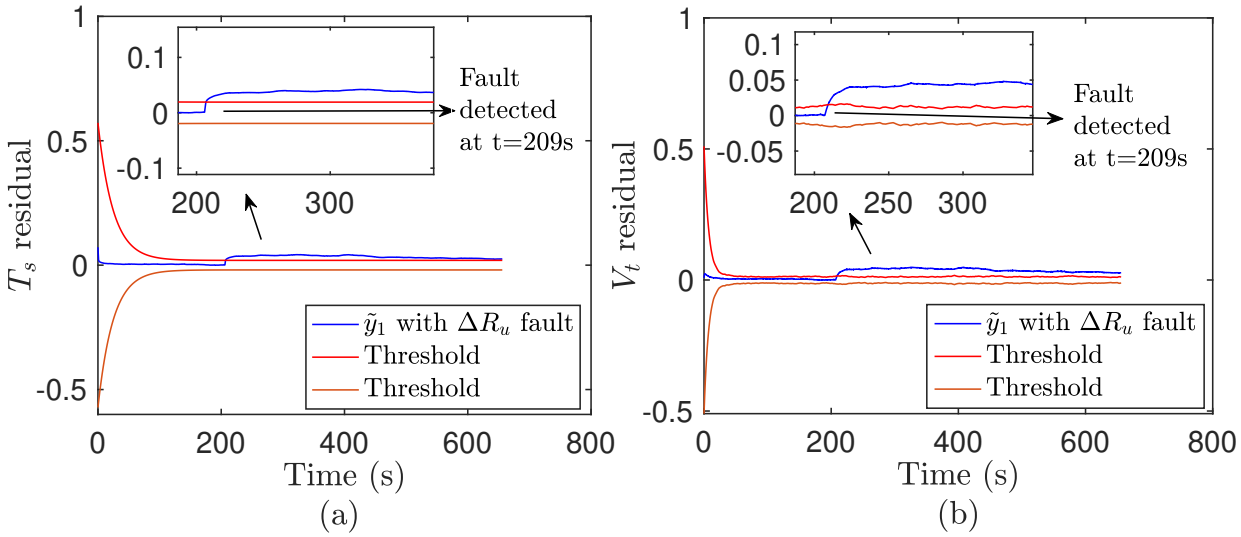

Figure 45: Residual responses under convective cooling resistance fault injected at 206s a) surface temperature error, b) output voltage error.

dynamics (4.4.4). Therefore the fault can be simulated as $\gamma_4, \gamma_5, \gamma_7 \neq 0$, which affects the T_s and V_t residuals. From Figs. 47(a) and 47(b), we can observe that the residuals are within the adaptive threshold value before the occurrence of the fault $t = 206$ sec. This further validates the estimation accuracy of the NLO. Upon the occurrence of the fault, the T_s and V_t residuals exceed the adaptive threshold value after $t = 206$ sec. This implies the detection of the occurrence of multiple thermal or side reaction faults, which are diagnosed at an incipient stage.

Upon the detection of the fault, the NN is deployed to learn the multiple thermal or side reaction faults online. The simulation parameters used were $\Upsilon = diag[.09, 0.01, 0.01, 1, -1900, .08, .02, 10.0], \upsilon = 12\Upsilon$. The NN weight $\hat{\theta}$ was initialized at random from a uniform distribution in the interval of [0 0.001]. The number of neurons in the hidden layer is chosen as 20. From Figure 48(a) and 48(b), we can observe that after the fault is detected at $t = 207$ sec, the NN learns the fault dynamics, which can be verified by the convergence of the residuals T_s and V_t close to zero with RMSEs 0.0087 and 0.0048, respectively. This brings back the residuals below the threshold value, as shown in Figs. 48(a) and 48(b). The convergence of the state estimation errors close to zero with RMSEs within 1% band is shown in Figure 48 (c). Furthermore, the convergence of the estimated NN weight updates is also shown in Figure 48 (d). Therefore, it can be concluded that the NN was able to learn the fault dynamics and estimate the core temperature SOC and SOH in the presence of multiple thermal or side reaction faults.

4.5 Conclusion

Section 4.2 presents an EKF-based SOC and parameter estimation scheme which is further utilized for model-based FD. The novel state-space model of the ECM with an EKF accurately estimates the SOC and nonlinear time-varying internal parameters of the battery as

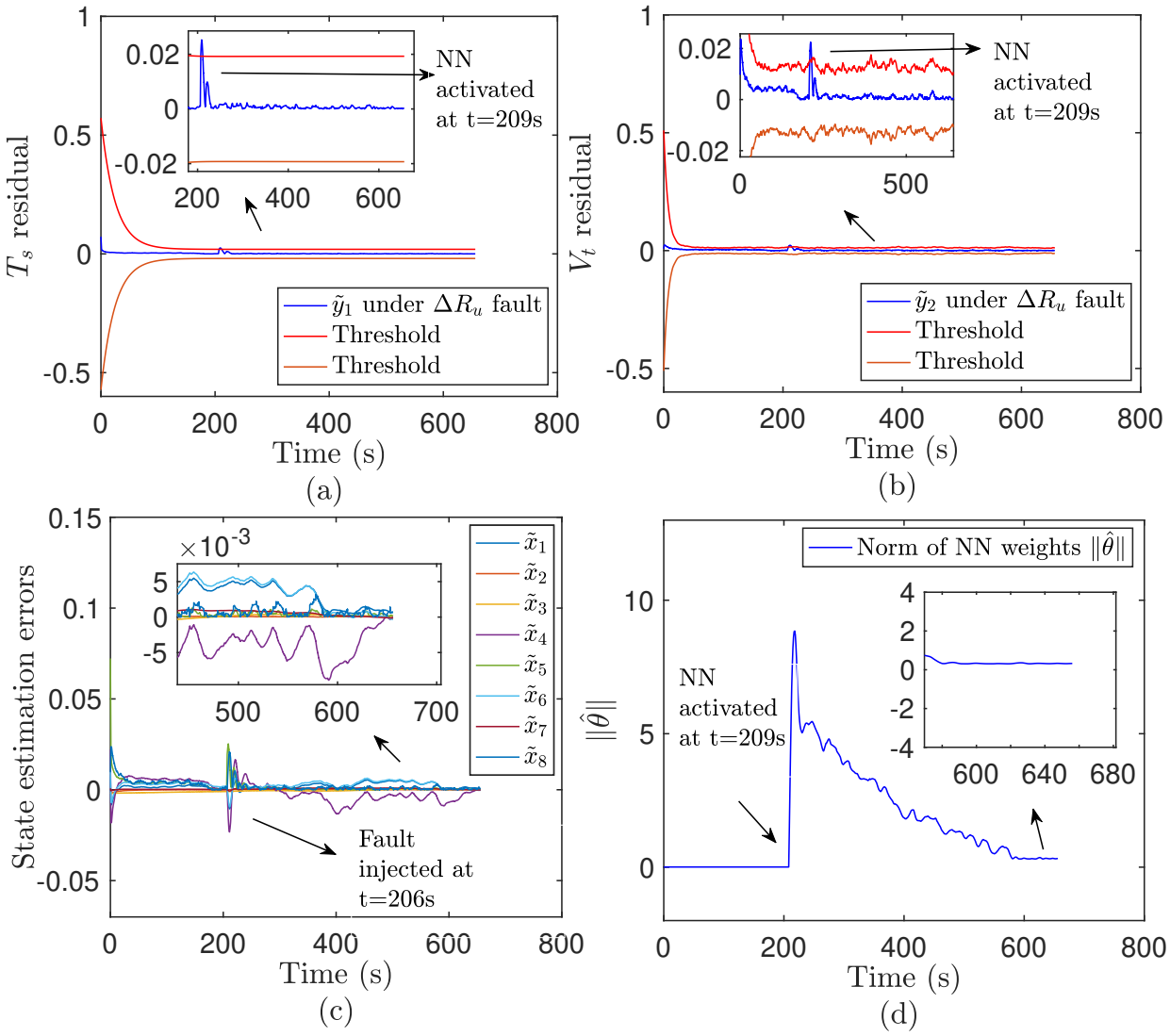

Figure 46: Residual responses with NN under convective cooling resistance fault injected at 206s a) surface temperature error, b) output voltage error, c) state estimation error and d) NN weight estimation.

shown in the simulation. The model-based FD scheme using the EKF was able to detect the internal fault. Estimation of the fault parameter with an online fault estimator will help predict the RUL of LIB and is detailed in Section 4.3 and Section 4.4.

Later in Section 4.3, we have presented an NN-based FD scheme with an adaptive threshold and core temperature estimation scheme under internal thermal faults in LIB. The proposed model-based approach using an NLO guaranteed the estimation of the SOH-coupled ETA model states (SOC, SOH, T_c, T_s) and parameter (R_0). Comparing the output residuals with the proposed adaptive threshold facilitated the detection of thermal faults under health degradation and modeling uncertainties. The online fault learning scheme using NNs for thermal faults showed the potential of accurately estimating the core temperature under fault conditions, which can be used for thermal management by BMS. Learning other

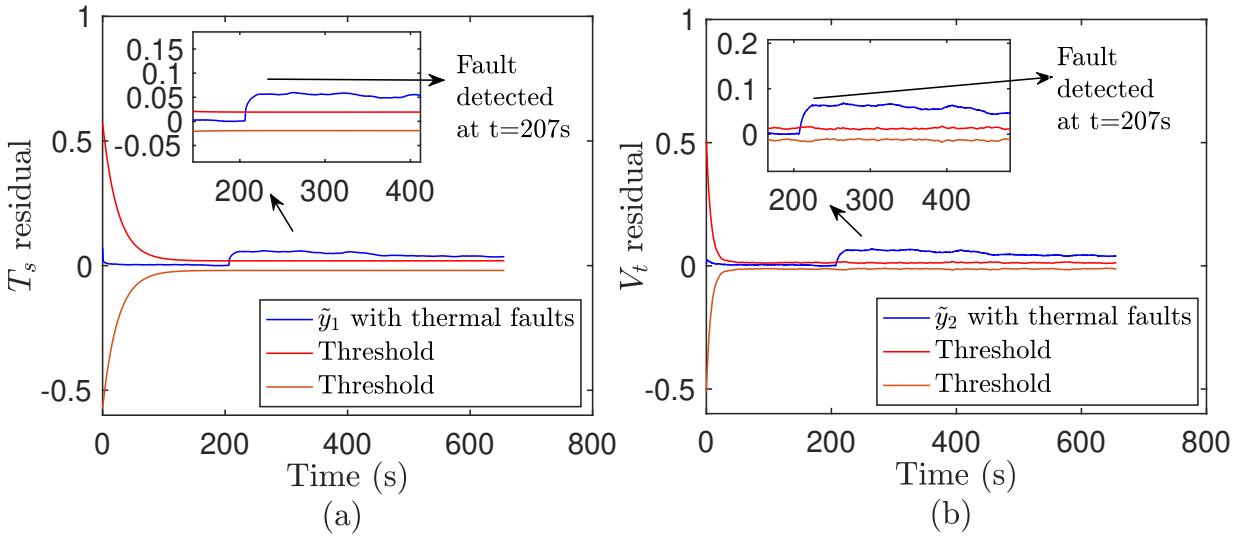

Figure 47: Residual responses under all thermal faults injected at 206s a) surface temperature error, b) output voltage error.

internal faults of the battery online will improve the RUL and battery management and are included in Section 4.4. In addition, ohmic resistance change in the presence of faults has a significant impact on the terminal voltage of the battery [258]. Therefore, tracking the battery's output voltage is indispensable to detecting side reaction faults, which are also included in Section 4.4.

Finally, Section 4.4 presents a modified NN-based FD scheme presented in Section 4.3 to detect thermal and side reaction faults in LIB. A NLO is designed to guarantee the estimation of the states (SOC, SOH, T_c, T_s) and parameter (R_0) of the SOH-coupled ETA model with RMSEs within 1% band. The output residuals generated from the observer are compared against an adaptive threshold designed to account for health degradation and modeling uncertainties. This enabled the detection of thermal and side reaction faults. Faulty state estimation using an NN-based observer showed the convergence of the state estimation errors and NN weight updates, which proved the potential of a learning-based scheme to learn the internal fault dynamics of the system and accurately estimate the core temperature, SOC, and SOH of the battery during faults.

In the next chapter, overall conclusions and future work of this dissertation will be discussed in detail.

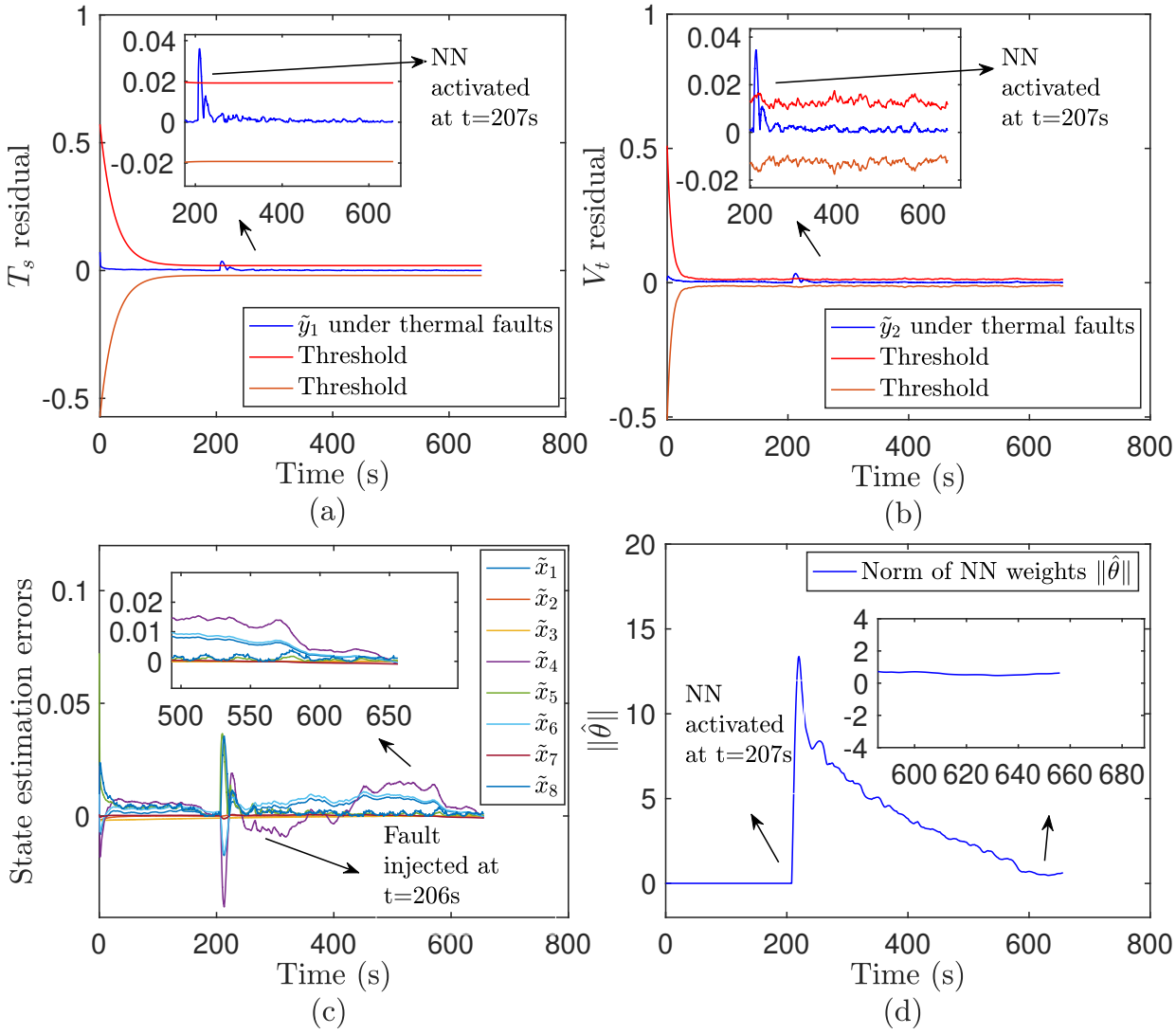

Figure 48: Residual responses with NN under all thermal faults injected at 206s a) surface temperature error, b) output voltage error, c) state estimation error, and d) NN weight estimation.

CHAPTER V

CONCLUSION AND FUTURE WORK

5.1 Conclusion

In this dissertation, we provided an in-depth literature review on LIBs' internal and external degradation mechanisms and SOH estimations. Motivated by the existing gaps in the literature, we developed two different SOC and SOH-based models of LIB to estimate SOC, SOH, and parameters simultaneously using observer/filtering-based approaches. Finally, we developed FD schemes to detect internal (thermal, side reaction) faults in LIB. To this end, we first summarized different internal and external degradation mechanisms of LIB and provided details of the corresponding modeling approaches and correlation with the SOH in chapter II. More specifically, we systematically presented the evolution of the chemical and mechanical degradation starting from the SEI layer formation, fracture, lithium plating, and dendrite formation, along with their governing equations. The inter-relations among these degradation mechanisms and their effects on capacity and power fade were also discussed.

In the later part of chapter II, we have presented the recent and advanced SOH estimation methods, such as OCV-based ICA-DVA techniques, electrochemical methods integrated with internal degradation models, and data-driven methods using DNN and GPR. Further, a summary of empirical models for capacity or power fade, along with the influence of external aging factors on internal degradation mechanisms, were discussed. It was clear from the review that the hybrid approaches, which combine multiple estimation schemes, improve SOH estimation accuracy. It was also observed that real-time machine learning-based approaches are less explored in the area of LIB and gaining popularity in recent times.

Finally, nondestructive quantitative evaluations of the degradation, taking the impact of internal and external aging factors into account, will result in well-optimized cell designs with longer cycle life. Development of real-time machine learning schemes with measured voltage, current, and surface temperature, by leveraging the advancement in NN-based architectures and training schemes, can address the challenges in modeling internal degradation. Further, these learning-based intelligent models can be implemented in BMS for health-conscious decision-making with improved autonomy.

Secondly, in chapter III, two different LIB models were proposed. Both models were developed to accommodate the time-varying parameters to apprehend the effect of aging on SOC and SOH estimations. In the first part of chapter III, a SOC-dependent model was developed. All the parameters in this model are SOC-dependent. A NLO was designed using Lyapunov stability analysis, and the state and parameter estimation errors were guaranteed to be UUB. The simulation results showed that the NLO estimates all the states and parameters with RMSEs within 1% band.

In the later part of chapter III a SOH-coupled ETA model was proposed. The thermal and SOH (capacity fade) dynamics, along with their effects on the ECM parameters, were incorporated into this model. Therefore the ETA model of the battery was developed by integrating or coupling three subsystems: 1) a 2-RC varying parameter ECM, 2) a thermal model, and 3) a semi-empirical aging model

Further, the ETA model was extended to integrate the dynamics of the ohmic resistance to estimate the power fade and internal degradation along with the SOC and SOH of LIB. Finally, both the SOH-coupled and extended SOH-coupled ETA models were validated experimentally and numerically. An EKF was used to estimate the critical battery states such as SOC, SOH, core, and surface temperatures and parameters such as R_0 with RMSEs within 1% band. Comparison results at different C_{rates} and ambient temperatures were also presented to show the effectiveness of the proposed coupled models.

Finally, in chapter IV, FD schemes based on the two different modeling approaches of LIB discussed in chapter III were presented. In the first part of chapter IV FD scheme based on a nonlinear SOC-based model of the battery, which was capable of estimating the nonlinear internal parameters, was proposed. Simulation results with drive cycle input current were presented to show the effectiveness of the proposed model-based FD scheme. In the proposed FD scheme, an EKF was able to estimate the states and parameters accurately in the healthy conditions of the battery. An internal fault was induced in the system by adding an externally time-varying fault to one of the parameter's ohmic resistance. The fault progression was reflected as the rise of voltage residual of the battery. Therefore EKF was able to estimate the output voltage accurately before the fault occurred and could not estimate faulted battery output. This resulted in a large output residual that exceeds the threshold value when the fault occurs. The threshold value to indicate fault was computed based on the run-time maximum values of the internal parameters.

In the second part of chapter IV FD scheme based on an extended SOH-coupled model of the battery (refer to Section 4.3), which can estimate SOC, SOH, and ohmic resistance, was proposed. Integrating the dynamics of ohmic resistance in the SOH-coupled model provided insights into power fade and detection of internal faults (e.g., side-reaction faults) of the battery. Unlike the constant threshold values in Section 4.2, we have designed a residual adaptive generator, which was able to differentiate between the degradation and faults from the residuals, detect faults of smaller magnitude (incipient stage) in normal operating conditions, and account for modeling uncertainties in the system.

First, an NLO was designed using Lyapunov stability analysis, and the state and parameter estimation errors were guaranteed to be asymptotically stable in the absence of fault. Second, an NN-based NLO was designed using Lyapunov stability analysis to estimate the core temperature in the presence of a fault, and the state and weight estimation errors were guaranteed to be UUB. Simulation results with drive cycle input current were presented to validate the fault detection scheme. Faults affecting the core temperature were induced in the system. The first NLO was able to generate the output residuals by comparing the faulty battery and the estimated outputs. All the state estimation errors converged to zero until the fault was introduced into the system with RMSEs within the 1% band. A fault was detected when the residual exceeded the adaptive threshold value designed. Upon detection of the fault, a second NN-based FD observer was able to learn the fault dynamics and estimate the faulty core temperature of the battery with RMSE within 1% band.

In the final part of chapter IV, the FD scheme in Section 4.3 was also modified to estimate the faulty states such as SOC and SOH and detect thermal and side reaction faults in LIB. In this modified scheme, we first designed a NLO with redefined outputs using Lyapunov stability analysis, and the state and parameter estimation errors were guaranteed to be asymptotically stable in the absence of fault. Second, an NN-based modified NLO was designed using Lyapunov stability analysis to estimate the SOC, SOH, and core temperature in the presence of a fault, and the state and weight estimation errors were guaranteed to be UUB. Faults such as thermal and side reaction faults are induced in the system. The first NLO was able to generate the output residuals by comparing the faulty battery and the estimated outputs. All the state estimation errors converged to zero until the fault was introduced into the system with RMSEs within 1% band. When the residual exceeds the adaptive threshold value designed, a fault was detected. Upon detection of the fault, a second NN-based modified FD observer showed the convergence of the state estimation errors and NN weight updates, which proved that the modified NN-based observer was able to learn the fault dynamics and accurately estimate the faulty SOC, SOH, and core temperature of the battery. All the state estimation errors converged close to zero with RMSEs within 1% band.

5.2 Future work

The future work of this dissertation is given as follows:

- Learning the internal faults is helpful in predicting RUL, battery failures, and health management, which is included in our future work.
- Using the proposed SOH-coupled model for the formulation of optimal charge control problem with the minimum-time charge reduced aging charge and balanced charge among pack level batteries.

REFERENCES

[1] G. Suri and S. Onori, "A control-oriented cycle-life model for hybrid electric vehicle lithium-ion batteries," *Energy*, vol. 96, pp. 644–653, 2016.

[2] M. Chen, G. A. Rincon-Mora, *et al.*, "Accurate electrical battery model capable of predicting runtime and iv performance," *IEEE transactions on energy conversion*, vol. 21, no. 2, pp. 504–511, 2006.

[3] C. R. Birkl, M. R. Roberts, E. McTurk, P. G. Bruce, and D. A. Howey, "Degradation diagnostics for lithium ion cells," *Journal of Power Sources*, vol. 341, pp. 373–386, 2017.

[4] J. Vetter, P. Novák, M. R. Wagner, C. Veit, K.-C. Möller, J. Besenhard, M. Winter, M. Wohlfahrt-Mehrens, C. Vogler, and A. Hammouche, "Ageing mechanisms in lithium-ion batteries," *Journal of power sources*, vol. 147, no. 1-2, pp. 269–281, 2005.

[5] Y. Nishi, "Lithium ion secondary batteries; past 10 years and the future," *Journal of Power Sources*, vol. 100, no. 1-2, pp. 101–106, 2001.

[6] N. A. Chaturvedi, R. Klein, J. Christensen, J. Ahmed, and A. Kojic, "Algorithms for advanced battery-management systems," *IEEE Control Systems*, vol. 30, no. 3, pp. 49–68, 2010.

[7] M. Chen, X. Ma, B. Chen, R. Arsenault, P. Karlson, N. Simon, and Y. Wang, "Recycling end-of-life electric vehicle lithium-ion batteries," *Joule*, vol. 3, no. 11, pp. 2622–2646, 2019.

[8] A. Khaligh and M. D'Antonio, "Global trends in high-power on-board chargers for electric vehicles," *IEEE Transactions on Vehicular Technology*, vol. 68, no. 4, pp. 3306–3324, 2019.

[9] X.-G. Yang, Y. Leng, G. Zhang, S. Ge, and C.-Y. Wang, "Modeling of lithium plating induced aging of lithium-ion batteries: Transition from linear to nonlinear aging," *Journal of Power Sources*, vol. 360, pp. 28–40, 2017.

[10] M. Safari, M. Morcrette, A. Teyssot, and C. Delacourt, "Multimodal physics-based aging model for life prediction of li-ion batteries," *Journal of The Electrochemical Society*, vol. 156, no. 3, pp. A145–A153, 2009.

[11] P. Rong and M. Pedram, "An analytical model for predicting the remaining battery capacity of lithium-ion batteries," *IEEE Transactions on Very Large Scale Integration (VLSI) Systems*, vol. 14, no. 5, pp. 441–451, 2006.

[12] H. He, R. Xiong, and J. Fan, "Evaluation of lithium-ion battery equivalent circuit models for state of charge estimation by an experimental approach," *Energies*, vol. 4, no. 4, pp. 582–598, 2011.

[13] K. A. Smith, C. D. Rahn, and C.-Y. Wang, "Model-based electrochemical estimation and constraint management for pulse operation of lithium ion batteries," *IEEE Transactions on Control Systems Technology*, vol. 18, no. 3, pp. 654–663, 2010.

[14] W. Low, J. Aziz, N. Idris, and R. Saidur, "Electrical model to predict current–voltage behaviours of lithium ferro phosphate batteries using a transient response correction method," *Journal of Power Sources*, vol. 221, pp. 201–209, 2013.

[15] D. Di Domenico, A. Stefanopoulou, and G. Fiengo, "Lithium-ion battery state of charge and critical surface charge estimation using an electrochemical model-based extended kalman filter," *Journal of dynamic systems, measurement, and control*, vol. 132, no. 6, p. 061302, 2010.

[16] S. Barcellona and L. Piegari, "Lithium ion battery models and parameter identification techniques," *Energies*, vol. 10, no. 12, p. 2007, 2017.

[17] R. Rao, S. Vrudhula, and D. N. Rakhmatov, "Battery modeling for energy aware system design," *Computer*, vol. 36, no. 12, pp. 77–87, 2003.

[18] S. Nejad, D. Gladwin, and D. Stone, "A systematic review of lumped-parameter equivalent circuit models for real-time estimation of lithium-ion battery states," *Journal of Power Sources*, vol. 316, pp. 183–196, 2016.

[19] S. Buller, M. Thele, E. Karden, *et al.*, "Supercapacitors and lithium-ion batteries for power electronic applications," *IEEE Industry Applications Magazine*, vol. 11, no. 2, pp. 62–67, 2005.

[20] L. Benini, G. Castelli, A. Macii, E. Macii, M. Poncino, and R. Scarsi, "Discrete-time battery models for system-level low-power design," *IEEE Transactions on Very Large Scale Integration (VLSI) Systems*, no. 5, pp. 630–640, 2001.

[21] M. C. Glass, "Battery electrochemical nonlinear/dynamic SPICE model," in *Energy Conversion Engineering Conference, 1996. IECEC 96., Proceedings of the 31st Intersociety*, vol. 1, pp. 292–297, IEEE, 1996.

[22] L. Gao, S. Liu, and R. A. Dougal, "Dynamic lithium-ion battery model for system simulation," *IEEE transactions on components and packaging technologies*, vol. 25, no. 3, pp. 495–505, 2002.

[23] C. Fleischer, W. Waag, H.-M. Heyn, and D. U. Sauer, "On-line adaptive battery impedance parameter and state estimation considering physical principles in reduced order equivalent circuit battery models: Part 1. requirements, critical review of methods and modeling," *Journal of Power Sources*, vol. 260, pp. 276–291, 2014.

[24] W. Li, L. Liang, W. Liu, and X. Wu, "State of charge estimation of lithium-ion batteries using a discrete-time nonlinear observer," *IEEE Trans. Ind. Electron*, vol. 64, no. 11, pp. 8557–8565, 2017.

[25] K. S. Ng, C.-S. Moo, Y.-P. Chen, and Y.-C. Hsieh, "Enhanced coulomb counting method for estimating state-of-charge and state-of-health of lithium-ion batteries," *Applied energy*, vol. 86, no. 9, pp. 1506–1511, 2009.

[26] M. A. Hannan, M. Lipu, A. Hussain, and A. Mohamed, "A review of lithium-ion battery state of charge estimation and management system in electric vehicle applications: Challenges and recommendations," *Renewable and Sustainable Energy Reviews*, vol. 78, pp. 834–854, 2017.

[27] Y. Shen, "Adaptive online state-of-charge determination based on neuro-controller and neural network," *Energy Conversion and Management*, vol. 51, no. 5, pp. 1093–1098, 2010.

[28] Y. Diab, F. Auger, E. Schaeffer, and M. Wahbeh, "Estimating lithium-ion battery state of charge and parameters using a continuous-discrete extended kalman filter," *Energies*, vol. 10, no. 8, p. 1075, 2017.

[29] G. Vennam, A. Sahoo, and S. Ahmed, "A survey on lithium-ion battery internal and external degradation modeling and state of health estimation," *Journal of Energy Storage*, vol. 52, p. 104720, 2022.

[30] J. Li, J. K. Barillas, C. Guenther, and M. A. Danzer, "A comparative study of state of charge estimation algorithms for LiFePO4 batteries used in electric vehicles," *Journal of power sources*, vol. 230, pp. 244–250, 2013.

[31] J. K. Barillas, J. Li, C. Günther, and M. A. Danzer, "A comparative study and validation of state estimation algorithms for li-ion batteries in battery management systems," *Applied energy*, vol. 155, pp. 455–462, 2015.

[32] X. Hu, F. Sun, and Y. Zou, "Estimation of state of charge of a lithium-ion battery pack for electric vehicles using an adaptive luenberger observer," *Energies*, vol. 3, no. 9, pp. 1586–1603, 2010.

[33] C. Lin, A. Tang, and W. Wang, "A review of SOH estimation methods in lithium-ion batteries for electric vehicle applications," *Energy Procedia*, vol. 75, pp. 1920–1925, 2015.

[34] J. Zhang and J. Lee, "A review on prognostics and health monitoring of li-ion battery," *Journal of power sources*, vol. 196, no. 15, pp. 6007–6014, 2011.

[35] H. Tian, P. Qin, K. Li, and Z. Zhao, "A review of the state of health for lithium-ion batteries: Research status and suggestions," *Journal of Cleaner Production*, p. 120813, 2020.

[36] L. Lu, X. Han, J. Li, J. Hua, and M. Ouyang, "A review on the key issues for lithium-ion battery management in electric vehicles," *Journal of power sources*, vol. 226, pp. 272–288, 2013.

[37] M. Berecibar, I. Gandiaga, I. Villarreal, N. Omar, J. Van Mierlo, and P. Van den Bossche, "Critical review of state of health estimation methods of li-ion batteries for real applications," *Renewable and Sustainable Energy Reviews*, vol. 56, pp. 572–587, 2016.

[38] M. H. Lipu, M. Hannan, A. Hussain, M. Hoque, P. J. Ker, M. Saad, and A. Ayob, "A review of state of health and remaining useful life estimation methods for lithium-ion battery in electric vehicles: Challenges and recommendations," *Journal of cleaner production*, vol. 205, pp. 115–133, 2018.

[39] R. Xiong, L. Li, and J. Tian, "Towards a smarter battery management system: A critical review on battery state of health monitoring methods," *Journal of Power Sources*, vol. 405, pp. 18–29, 2018.

[40] M. U. Cuma and T. Koroglu, "A comprehensive review on estimation strategies used in hybrid and battery electric vehicles," *Renewable and Sustainable Energy Reviews*, vol. 42, pp. 517–531, 2015.

[41] M.-K. Tran, S. Panchal, V. Chauhan, N. Brahmbhatt, A. Mevawalla, R. Fraser, and M. Fowler, "Python-based scikit-learn machine learning models for thermal and electrical performance prediction of high-capacity lithium-ion battery," *International Journal of Energy Research*, vol. 46, no. 2, pp. 786–794, 2022.

[42] J. Qiao, X. Liu, and Z. Chen, "Prediction of the remaining useful life of lithium-ion batteries based on empirical mode decomposition and deep neural networks," *IEEE Access*, vol. 8, pp. 42760–42767, 2020.

[43] Y. Li, K. Liu, A. M. Foley, A. Zülke, M. Berecibar, E. Nanini-Maury, J. Van Mierlo, and H. E. Hoster, "Data-driven health estimation and lifetime prediction of lithium-ion batteries: A review," *Renewable and Sustainable Energy Reviews*, vol. 113, p. 109254, 2019.

[44] C. Mikolajczak, M. Kahn, K. White, and R. T. Long, *Lithium-ion batteries hazard and use assessment*. Springer Science & Business Media, 2012.

[45] Z. Liu and H. He, "Sensor fault detection and isolation for a lithium-ion battery pack in electric vehicles using adaptive extended kalman filter," *Applied Energy*, vol. 185, pp. 2033–2044, 2017.

[46] A. Sidhu, A. Izadian, and S. Anwar, "Adaptive nonlinear model-based fault diagnosis of li-ion batteries," *IEEE Transactions on Industrial Electronics*, vol. 62, no. 2, pp. 1002–1011, 2015.

[47] S. Dey and B. Ayalew, "A diagnostic scheme for detection, isolation and estimation of electrochemical faults in lithium-ion cells," in *ASME 2015 Dynamic Systems and Control Conference*, pp. V001T13A001–V001T13A001, American Society of Mechanical Engineers, 2015.

[48] C. Zheng, Y. Ge, Z. Chen, D. Huang, J. Liu, and S. Zhou, "Diagnosis method for li-ion battery fault based on an adaptive unscented kalman filter," *Energies*, vol. 10, no. 11, p. 1810, 2017.

[49] H. Ferdowsi and S. Jagannathan, "Fault diagnosis of a class of distributed parameter systems modeled by parabolic partial differential equations," in *American Control Conference (ACC), IEEE*, pp. 5434–5439, 2014.

[50] W. Chen, W.-T. Chen, M. Saif, M.-F. Li, and H. Wu, "Simultaneous fault isolation and estimation of lithium-ion batteries via synthesized design of luenberger and learning observers," *IEEE Transactions on Control Systems Technology*, vol. 22, no. 1, pp. 290–298, 2014.

[51] A. Singh, A. Izadian, and S. Anwar, "Fault diagnosis of li-ion batteries using multiple-model adaptive estimation," in *Industrial Electronics Society, IECON 2013-39th Annual Conference of the IEEE*, pp. 3524–3529, IEEE, 2013.

[52] S. Dey, Z. A. Biron, S. Tatipamula, N. Das, S. Mohon, B. Ayalew, and P. Pisu, "Model-based real-time thermal fault diagnosis of lithium-ion batteries," *Control Engineering Practice*, vol. 56, pp. 37–48, 2016.

[53] Z. Liu, Q. Ahmed, G. Rizzoni, and H. He, "Fault detection and isolation for lithium-ion battery system using structural analysis and sequential residual generation," in *Dynamic Systems and Control Conference*, vol. 46193, p. V002T36A005, American Society of Mechanical Engineers, 2014.

[54] J. Marcicki, S. Onori, and G. Rizzoni, "Nonlinear fault detection and isolation for a lithium-ion battery management system," in *ASME 2010 Dynamic Systems and Control Conference*, pp. 607–614, American Society of Mechanical Engineers, 2010.

[55] J. Wei, G. Dong, and Z. Chen, "Lyapunov-based thermal fault diagnosis of cylindrical lithium-ion batteries," *IEEE Transactions on Industrial Electronics*, vol. 67, no. 6, pp. 4670–4679, 2019.

[56] S. Dey, H. E. Perez, and S. J. Moura, "Model-based battery thermal fault diagnostics: Algorithms, analysis, and experiments," *IEEE Transactions on Control Systems Technology*, no. 99, pp. 1–12, 2017.

[57] E. Peled, "The electrochemical behavior of alkali and alkaline earth metals in nonaqueous battery systems—the solid electrolyte interphase model," *Journal of The Electrochemical Society*, vol. 126, no. 12, p. 2047, 1979.

[58] C. Uhlmann, J. Illig, M. Ender, R. Schuster, and E. Ivers-Tiffée, "In situ detection of lithium metal plating on graphite in experimental cells," *J Power Sources*, vol. 279, pp. 428–438, 2015.

[59] B. Khanal, B. Bahrami, H. Lu, and Q. Qiao, "Modelling of solid electrolyte interface (SEI) layer of lithium-ion batteries using kinetic monte carlo approach," in *IIE Annual Conference. Proceedings*, pp. 1193–1198, Institute of Industrial and Systems Engineers (IISE), 2017.

[60] A. Wang, S. Kadam, H. Li, S. Shi, and Y. Qi, "Review on modeling of the anode solid electrolyte interphase (SEI) for lithium-ion batteries," *npj Computational Materials*, vol. 4, no. 1, pp. 1–26, 2018.

[61] T. F. Fuller, M. Doyle, and J. Newman, "Simulation and optimization of the dual lithium ion insertion cell," *Journal of the Electrochemical Society*, vol. 141, no. 1, pp. 1–10, 1994.

[62] J. Christensen and J. Newman, "A mathematical model for the lithium-ion negative electrode solid electrolyte interphase," *Journal of The Electrochemical Society*, vol. 151, no. 11, p. A1977, 2004.

[63] Y. Xie, J. Li, and C. Yuan, "Multiphysics modeling of lithium ion battery capacity fading process with solid-electrolyte interphase growth by elementary reaction kinetics," *Journal of Power Sources*, vol. 248, pp. 172–179, 2014.

[64] S. Sankarasubramanian and B. Krishnamurthy, "A capacity fade model for lithium-ion batteries including diffusion and kinetics," *Electrochimica Acta*, vol. 70, pp. 248–254, 2012.

[65] L. Liu and M. Zhu, "Modeling of SEI layer growth and electrochemical impedance spectroscopy response using a thermal-electrochemical model of li-ion batteries," *Ecs Transactions*, vol. 61, no. 27, p. 43, 2014.

[66] M. Doyle, T. F. Fuller, and J. Newman, "Modeling of galvanostatic charge and discharge of the lithium/polymer/insertion cell," *Journal of the Electrochemical society*, vol. 140, no. 6, pp. 1526–1533, 1993.

[67] P. Ramadass, B. Haran, P. M. Gomadam, R. White, and B. N. Popov, "Development of first principles capacity fade model for li-ion cells," *Journal of the Electrochemical Society*, vol. 151, no. 2, pp. A196–A203, 2004.

[68] M. Doyle, J. Newman, A. S. Gozdz, C. N. Schmutz, and J.-M. Tarascon, "Comparison of modeling predictions with experimental data from plastic lithium ion cells," *Journal of the Electrochemical Society*, vol. 143, no. 6, pp. 1890–1903, 1996.

[69] S. Santhanagopalan, Q. Guo, P. Ramadass, and R. E. White, "Review of models for predicting the cycling performance of lithium ion batteries," *Journal of Power Sources*, vol. 156, no. 2, pp. 620–628, 2006.

[70] S. Santhanagopalan and R. E. White, "Online estimation of the state of charge of a lithium ion cell," *Journal of power sources*, vol. 161, no. 2, pp. 1346–1355, 2006.

[71] A. M. Colclasure and R. J. Kee, "Thermodynamically consistent modeling of elementary electrochemistry in lithium-ion batteries," *Electrochimica Acta*, vol. 55, no. 28, pp. 8960–8973, 2010.

[72] F. Single, B. Horstmann, and A. Latz, "Dynamics and morphology of solid electrolyte interphase (sei)," *Physical Chemistry Chemical Physics*, vol. 18, no. 27, pp. 17810–17814, 2016.

[73] F. Single, B. Horstmann, and A. Latz, "Revealing SEI morphology: in-depth analysis of a modeling approach," *Journal of The Electrochemical Society*, vol. 164, no. 11, p. E3132, 2017.

[74] M. Heinrich, N. Wolff, N. Harting, V. Laue, F. Röder, S. Seitz, and U. Krewer, "Physico-chemical modeling of a lithium-ion battery: an ageing study with electrochemical impedance spectroscopy," *Batteries & Supercaps*, vol. 2, no. 6, pp. 530–540, 2019.

[75] J. Christensen and J. Newman, "A mathematical model of stress generation and fracture in lithium manganese oxide," *Journal of The Electrochemical Society*, vol. 153, no. 6, p. A1019, 2006.

[76] R. Deshpande, Y. Qi, and Y.-T. Cheng, "Effects of concentration-dependent elastic modulus on diffusion-induced stresses for battery applications," *Journal of the Electrochemical Society*, vol. 157, no. 8, p. A967, 2010.

[77] R. D. Deshpande and D. M. Bernardi, "Modeling solid-electrolyte interphase (SEI) fracture: coupled mechanical/chemical degradation of the lithium ion battery," *Journal of The Electrochemical Society*, vol. 164, no. 2, p. A461, 2017.

[78] Q. Deng, R. Hu, C. Xu, B. Chen, and J. Zhou, "Modeling fracture of solid electrolyte interphase in lithium-ion batteries during cycling," *Journal of Solid State Electrochemistry*, vol. 23, no. 11, pp. 2999–3008, 2019.

[79] J. Li, K. Adewuyi, N. Lotfi, R. Landers, and J. Park, "A single particle model with chemical/mechanical degradation physics for lithium ion battery state of health (SOH) estimation," *Applied Energy*, vol. 212, pp. 1178–1190, 2018.

[80] A. Barré, B. Deguilhem, S. Grolleau, M. Gérard, F. Suard, and D. Riu, "A review on lithium-ion battery ageing mechanisms and estimations for automotive applications," *Journal of Power Sources*, vol. 241, pp. 680–689, 2013.

[81] K. Nunotani, F. Yoshida, Y. Kamiya, Y. Daisho, K. Abe, M. Kono, and H. Matsuo, "Development and performance evaluation of lithium iron phosphate battery with superior rapid charging performance—second report: Evaluation of battery capacity loss characteristics," in *2011 IEEE Vehicle Power and Propulsion Conference*, pp. 1–4, IEEE, 2011.

[82] P. Arora, M. Doyle, and R. E. White, "Mathematical modeling of the lithium deposition overcharge reaction in lithium-ion batteries using carbon-based negative electrodes," *Journal of The Electrochemical Society*, vol. 146, no. 10, p. 3543, 1999.

[83] R. D. Perkins, A. V. Randall, X. Zhang, and G. L. Plett, "Controls oriented reduced order modeling of lithium deposition on overcharge," *Journal of Power Sources*, vol. 209, pp. 318–325, 2012.

[84] H. Ge, T. Aoki, N. Ikeda, S. Suga, T. Isobe, Z. Li, Y. Tabuchi, and J. Zhang, "Investigating lithium plating in lithium-ion batteries at low temperatures using electrochemical model with nmr assisted parameterization," *Journal of The Electrochemical Society*, vol. 164, no. 6, p. A1050, 2017.

[85] D. Ren, K. Smith, D. Guo, X. Han, X. Feng, L. Lu, M. Ouyang, and J. Li, "Investigation of lithium plating-stripping process in li-ion batteries at low temperature using an electrochemical model," *Journal of The Electrochemical Society*, vol. 165, no. 10, p. A2167, 2018.

[86] X. Zhao, Y. Yin, Y. Hu, and S.-Y. Choe, "Electrochemical-thermal modeling of lithium plating/stripping of Li(Ni06Mn02Co02)O2/carbon lithium-ion batteries at subzero ambient temperatures," *Journal of Power Sources*, vol. 418, pp. 61–73, 2019.

[87] L. Chen, B. Liu, A. N. Abbas, Y. Ma, X. Fang, Y. Liu, and C. Zhou, "Screw-dislocation-driven growth of two-dimensional few-layer and pyramid-like wse2 by sulfur-assisted chemical vapor deposition," *Acs Nano*, vol. 8, no. 11, pp. 11543–11551, 2014.

[88] J. Luo, C.-E. Wu, L.-Y. Su, S.-S. Huang, C.-C. Fang, Y.-S. Wu, J. Chou, and N.-L. Wu, "A proof-of-concept graphite anode with a lithium dendrite suppressing polymer coating," *Journal of Power Sources*, vol. 406, pp. 63–69, 2018.

[89] R. Akolkar, "Mathematical model of the dendritic growth during lithium electrodeposition," *Journal of Power Sources*, vol. 232, pp. 23–28, 2013.

[90] X. Wang, W. Zeng, L. Hong, W. Xu, H. Yang, F. Wang, H. Duan, M. Tang, and H. Jiang, "Stress-driven lithium dendrite growth mechanism and dendrite mitigation by electroplating on soft substrates," *Nature Energy*, vol. 3, no. 3, pp. 227–235, 2018.

[91] C. Monroe and J. Newman, "Dendrite growth in lithium/polymer systems: A propagation model for liquid electrolytes under galvanostatic conditions," *Journal of The Electrochemical Society*, vol. 150, no. 10, p. A1377, 2003.

[92] R. Akolkar, "Modeling dendrite growth during lithium electrodeposition at sub-ambient temperature," *Journal of Power Sources*, vol. 246, pp. 84–89, 2014.

[93] A. K. Sethurajan, J. M. Foster, G. Richardson, S. A. Krachkovskiy, J. D. Bazak, G. R. Goward, and B. Protas, "Incorporating dendrite growth into continuum models of electrolytes: Insights from nmr measurements and inverse modeling," *Journal of The Electrochemical Society*, vol. 166, no. 8, p. A1591, 2019.

[94] Y. Ren, Y. Zhou, and Y. Cao, "Inhibit of lithium dendrite growth in solid composite electrolyte by phase-field modeling," *The Journal of Physical Chemistry C*, 2020.

[95] C. Shen, G. Hu, L.-Z. Cheong, S. Huang, J.-G. Zhang, and D. Wang, "Direct observation of the growth of lithium dendrites on graphite anodes by operando ec-afm," *Small Methods*, vol. 2, no. 2, p. 1700298, 2018.

[96] P. Harks, F. Mulder, and P. Notten, "In situ methods for li-ion battery research: A review of recent developments," *Journal of power sources*, vol. 288, pp. 92–105, 2015.

[97] J. Steiger, D. Kramer, and R. Mönig, "Microscopic observations of the formation, growth and shrinkage of lithium moss during electrodeposition and dissolution," *Electrochimica Acta*, vol. 136, pp. 529–536, 2014.

[98] Z. Guo, J. Zhu, J. Feng, and S. Du, "Direct in situ observation and explanation of lithium dendrite of commercial graphite electrodes," *RSC advances*, vol. 5, no. 85, pp. 69514–69521, 2015.

[99] K. Ando, T. Matsuda, and D. Imamura, "Degradation diagnosis of lithium-ion batteries with a LiNi05Co02Mn03O2 and LiMn2O4 blended cathode using dV/dQ curve analysis," *Journal of Power Sources*, vol. 390, pp. 278–285, 2018.

[100] R. Xu, H. Sun, L. S. de Vasconcelos, and K. Zhao, "Mechanical and structural degradation of LiNixMnyCozO2 cathode in li-ion batteries: an experimental study," *Journal of The Electrochemical Society*, vol. 164, no. 13, p. A3333, 2017.

[101] B. Wu and W. Lu, "A battery model that fully couples mechanics and electrochemistry at both particle and electrode levels by incorporation of particle interaction," *Journal of Power Sources*, vol. 360, pp. 360–372, 2017.

[102] Y. Zhang, C. Zhao, and Z. Guo, "Simulation of crack behavior of secondary particles in li-ion battery electrodes during lithiation/de-lithiation cycles," *International Journal of Mechanical Sciences*, vol. 155, pp. 178–186, 2019.

[103] S.-c. Yang, Y. Hua, D. Qiao, Y.-b. Lian, Y.-w. Pan, and Y.-l. He, "A coupled electrochemical-thermal-mechanical degradation modelling approach for lifetime assessment of lithium-ion batteries," *Electrochimica Acta*, vol. 326, p. 134928, 2019.

[104] P. S. Sabet, A. J. Warnecke, F. Meier, H. Witzenhausen, E. Martinez-Laserna, and D. U. Sauer, "Non-invasive yet separate investigation of anode/cathode degradation of lithium-ion batteries (nickel–cobalt–manganese vs. graphite) due to accelerated aging," *Journal of Power Sources*, vol. 449, p. 227369, 2020.

[105] K. A. Smith, C. D. Rahn, and C.-Y. Wang, "Control oriented 1d electrochemical model of lithium ion battery," *Energy Conversion and management*, vol. 48, no. 9, pp. 2565–2578, 2007.

[106] R. Mehta and A. Gupta, "An improved single-particle model with electrolyte dynamics for high current applications of lithium-ion cells," *Electrochimica Acta*, vol. 389, p. 138623, 2021.

[107] W. Mei, Q. Duan, P. Qin, J. Xu, Q. Wang, and J. Sun, "A three-dimensional electrochemical-mechanical model at the particle level for lithium-ion battery," *Journal of The Electrochemical Society*, vol. 166, no. 14, p. A3319, 2019.

[108] R. Deshpande, M. Verbrugge, Y.-T. Cheng, J. Wang, and P. Liu, "Battery cycle life prediction with coupled chemical degradation and fatigue mechanics," *Journal of the Electrochemical Society*, vol. 159, no. 10, p. A1730, 2012.

[109] I. Laresgoiti, S. Käbitz, M. Ecker, and D. U. Sauer, "Modeling mechanical degradation in lithium ion batteries during cycling: Solid electrolyte interphase fracture," *Journal of Power Sources*, vol. 300, pp. 112–122, 2015.

[110] C. Miehe, H. Dal, L.-M. Schänzel, and A. Raina, "A phase-field model for chemo-mechanical induced fracture in lithium-ion battery electrode particles," *International Journal for Numerical Methods in Engineering*, vol. 106, no. 9, pp. 683–711, 2016.

[111] S. Abada, M. Petit, A. Lecocq, G. Marlair, V. Sauvant-Moynot, and F. Huet, "Combined experimental and modeling approaches of the thermal runaway of fresh and aged lithium-ion batteries," *Journal of Power Sources*, vol. 399, pp. 264–273, 2018.

[112] G. Liu and W. Lu, "A model of concurrent lithium dendrite growth, sei growth, sei penetration and regrowth," *Journal of the Electrochemical Society*, vol. 164, no. 9, p. A1826, 2017.

[113] L. Liang, Y. Qi, F. Xue, S. Bhattacharya, S. J. Harris, and L.-Q. Chen, "Nonlinear phase-field model for electrode-electrolyte interface evolution," *Physical Review E*, vol. 86, no. 5, p. 051609, 2012.

[114] K. Wang, Y. Xiao, P. Pei, X. Liu, and Y. Wang, "A phase-field model of dendrite growth of electrodeposited zinc," *Journal of The Electrochemical Society*, vol. 166, no. 10, p. D389, 2019.

[115] Y. Gao, J. Jiang, C. Zhang, W. Zhang, Z. Ma, and Y. Jiang, "Lithium-ion battery aging mechanisms and life model under different charging stresses," *Journal of Power Sources*, vol. 356, pp. 103–114, 2017.

[116] L. Su, J. Zhang, C. Wang, Y. Zhang, Z. Li, Y. Song, T. Jin, and Z. Ma, "Identifying main factors of capacity fading in lithium ion cells using orthogonal design of experiments," *Applied Energy*, vol. 163, pp. 201–210, 2016.

[117] S. S. Zhang, "The effect of the charging protocol on the cycle life of a li-ion battery," *Journal of power sources*, vol. 161, no. 2, pp. 1385–1391, 2006.

[118] S. S. Choi and H. S. Lim, "Factors that affect cycle-life and possible degradation mechanisms of a li-ion cell based on licoo2," *Journal of Power Sources*, vol. 111, no. 1, pp. 130–136, 2002.

[119] S. Saxena, C. Hendricks, and M. Pecht, "Cycle life testing and modeling of graphite/LiCoO2 cells under different state of charge ranges," *Journal of Power Sources*, vol. 327, pp. 394–400, 2016.

[120] R. P. Ramasamy, R. E. White, and B. N. Popov, "Calendar life performance of pouch lithium-ion cells," *Journal of Power Sources*, vol. 141, no. 2, pp. 298–306, 2005.

[121] F. Leng, C. M. Tan, and M. Pecht, "Effect of temperature on the aging rate of li ion battery operating above room temperature," *Scientific reports*, vol. 5, p. 12967, 2015.

[122] C. Akkaldevi, S. D. Chitta, J. Jaidi, S. Panchal, M. Fowler, and R. Fraser, "Coupled electrochemical-thermal simulations and validation of minichannel cold-plate water-cooled prismatic 20 ah lifepo4 battery," *Electrochem*, vol. 2, no. 4, pp. 643–663, 2021.

[123] V. Choudhari, A. Dhoble, S. Panchal, M. Fowler, and R. Fraser, "Numerical investigation on thermal behaviour of 5× 5 cell configured battery pack using phase change material and fin structure layout," *Journal of Energy Storage*, vol. 43, p. 103234, 2021.

[124] S. D. Chitta, C. Akkaldevi, J. Jaidi, S. Panchal, M. Fowler, and R. Fraser, "Comparison of lumped and 1d electrochemical models for prismatic 20ah lifepo4 battery sandwiched between minichannel cold-plates," *Applied Thermal Engineering*, vol. 199, p. 117586, 2021.

[125] T. Waldmann, M. Wilka, M. Kasper, M. Fleischhammer, and M. Wohlfahrt-Mehrens, "Temperature dependent ageing mechanisms in lithium-ion batteries–a post-mortem study," *Journal of Power Sources*, vol. 262, pp. 129–135, 2014.

[126] S. Zhang, K. Xu, and T. Jow, "Electrochemical impedance study on the low temperature of li-ion batteries," *Electrochimica acta*, vol. 49, no. 7, pp. 1057–1061, 2004.

[127] M. Ouyang, Z. Chu, L. Lu, J. Li, X. Han, X. Feng, and G. Liu, "Low temperature aging mechanism identification and lithium deposition in a large format lithium iron phosphate battery for different charge profiles," *Journal of Power Sources*, vol. 286, pp. 309–320, 2015.

[128] S. Watanabe, M. Kinoshita, T. Hosokawa, K. Morigaki, and K. Nakura, "Capacity fading of LiAlyNi1- x- yCoxO2 cathode for lithium-ion batteries during accelerated calendar and cycle life tests (effect of depth of discharge in charge–discharge cycling on the suppression of the micro-crack generation of LiAlyNi1- x- yCoxO2 particle)," *Journal of Power Sources*, vol. 260, pp. 50–56, 2014.

[129] N. Omar, M. A. Monem, Y. Firouz, J. Salminen, J. Smekens, O. Hegazy, H. Gaulous, G. Mulder, P. Van den Bossche, T. Coosemans, *et al.*, "Lithium iron phosphate based battery–assessment of the aging parameters and development of cycle life model," *Applied Energy*, vol. 113, pp. 1575–1585, 2014.

[130] J. de Hoog, J.-M. Timmermans, D. Ioan-Stroe, M. Swierczynski, J. Jaguemont, S. Goutam, N. Omar, J. Van Mierlo, and P. Van Den Bossche, "Combined cycling and calendar capacity fade modeling of a nickel-manganese-cobalt oxide cell with real-life profile validation," *Applied Energy*, vol. 200, pp. 47–61, 2017.

[131] J. R. Belt, C. D. Ho, C. G. Motloch, T. J. Miller, and T. Q. Duong, "A capacity and power fade study of li-ion cells during life cycle testing," *Journal of Power Sources*, vol. 123, no. 2, pp. 241–246, 2003.

[132] M. Ouyang, D. Ren, L. Lu, J. Li, X. Feng, X. Han, and G. Liu, "Overcharge-induced capacity fading analysis for large format lithium-ion batteries with liyni1/3co1/3mn1/3o2+ liymn2o4 composite cathode," *Journal of power sources*, vol. 279, pp. 626–635, 2015.

[133] J. Schmalstieg, S. Käbitz, M. Ecker, and D. U. Sauer, "A holistic aging model for Li(NiMnCo)O2 based 18650 lithium-ion batteries," *Journal of Power Sources*, vol. 257, pp. 325–334, 2014.

[134] R. Guo, L. Lu, M. Ouyang, and X. Feng, "Mechanism of the entire overdischarge process and overdischarge-induced internal short circuit in lithium-ion batteries," *Scientific reports*, vol. 6, no. 1, pp. 1–9, 2016.

[135] M. Broussely, P. Biensan, F. Bonhomme, P. Blanchard, S. Herreyre, K. Nechev, and R. Staniewicz, "Main aging mechanisms in li ion batteries," *Journal of power sources*, vol. 146, no. 1-2, pp. 90–96, 2005.

[136] J. Belt, V. Utgikar, and I. Bloom, "Calendar and PHEV cycle life aging of high-energy, lithium-ion cells containing blended spinel and layered-oxide cathodes," *Journal of Power Sources*, vol. 196, no. 23, pp. 10213–10221, 2011.

[137] H. J. Ploehn, P. Ramadass, and R. E. White, "Solvent diffusion model for aging of lithium-ion battery cells," *Journal of The Electrochemical Society*, vol. 151, no. 3, pp. A456–A462, 2004.

[138] R. Hausbrand, G. Cherkashinin, H. Ehrenberg, M. Gröting, K. Albe, C. Hess, and W. Jaegermann, "Fundamental degradation mechanisms of layered oxide li-ion battery cathode materials: Methodology, insights and novel approaches," *Materials Science and Engineering: B*, vol. 192, pp. 3–25, 2015.

[139] S. F. Schuster, T. Bach, E. Fleder, J. Müller, M. Brand, G. Sextl, and A. Jossen, "Non-linear aging characteristics of lithium-ion cells under different operational conditions," *Journal of Energy Storage*, vol. 1, pp. 44–53, 2015.

[140] J. Cannarella and C. B. Arnold, "Stress evolution and capacity fade in constrained lithium-ion pouch cells," *Journal of Power Sources*, vol. 245, pp. 745–751, 2014.

[141] Z. Li, J. Huang, B. Y. Liaw, V. Metzler, and J. Zhang, "A review of lithium deposition in lithium-ion and lithium metal secondary batteries," *Journal of power sources*, vol. 254, pp. 168–182, 2014.

[142] J. Christensen and J. Newman, "Cyclable lithium and capacity loss in li-ion cells," *Journal of the Electrochemical Society*, vol. 152, no. 4, p. A818, 2005.

[143] A. Farmann, W. Waag, A. Marongiu, and D. U. Sauer, "Critical review of on-board capacity estimation techniques for lithium-ion batteries in electric and hybrid electric vehicles," *Journal of Power Sources*, vol. 281, pp. 114–130, 2015.

[144] C. Weng, Y. Cui, J. Sun, and H. Peng, "On-board state of health monitoring of lithium-ion batteries using incremental capacity analysis with support vector regression," *Journal of Power Sources*, vol. 235, pp. 36–44, 2013.

[145] M. Safari and C. Delacourt, "Aging of a commercial graphite/LiFePO4 cell," *Journal of The Electrochemical Society*, vol. 158, no. 10, p. A1123, 2011.

[146] X. Li, Z. Wang, L. Zhang, C. Zou, and D. D. Dorrell, "State-of-health estimation for li-ion batteries by combing the incremental capacity analysis method with grey relational analysis," *Journal of Power Sources*, vol. 410, pp. 106–114, 2019.

[147] J. Tian, R. Xiong, and Q. Yu, "Fractional-order model-based incremental capacity analysis for degradation state recognition of lithium-ion batteries," *IEEE Transactions on Industrial Electronics*, vol. 66, no. 2, pp. 1576–1584, 2018.

[148] M. Lewerenz and D. U. Sauer, "Evaluation of cyclic aging tests of prismatic automotive linimncoo2-graphite cells considering influence of homogeneity and anode overhang," *Journal of Energy Storage*, vol. 18, pp. 421–434, 2018.

[149] S. K. Rechkemmer, X. Zang, W. Zhang, and O. Sawodny, "Calendar and cycle aging study of a commercial limn2o4 cell under consideration of influences by cell progress," *Journal of Energy Storage*, vol. 30, p. 101547, 2020.

[150] Y. Gao, J. Jiang, C. Zhang, W. Zhang, and Y. Jiang, "Aging mechanisms under different state-of-charge ranges and the multi-indicators system of state-of-health for lithium-ion battery with li (nimnco) o2 cathode," *Journal of Power Sources*, vol. 400, pp. 641–651, 2018.

[151] M. Dubarry, C. Truchot, and B. Y. Liaw, "Synthesize battery degradation modes via a diagnostic and prognostic model," *Journal of power sources*, vol. 219, pp. 204–216, 2012.

[152] D. Anseán, V. M. García, M. González, C. Blanco-Viejo, J. C. Viera, Y. F. Pulido, and L. Sánchez, "Lithium-ion battery degradation indicators via incremental capacity analysis," *IEEE Transactions on Industry Applications*, vol. 55, no. 3, pp. 2992–3002, 2019.

[153] X. Han, M. Ouyang, L. Lu, and J. Li, "Cycle life of commercial lithium-ion batteries with lithium titanium oxide anodes in electric vehicles," *Energies*, vol. 7, no. 8, pp. 4895–4909, 2014.

[154] I. Bloom, L. K. Walker, J. K. Basco, D. P. Abraham, J. P. Christophersen, and C. D. Ho, "Differential voltage analyses of high-power lithium-ion cells. 4. cells containing nmc," *Journal of Power Sources*, vol. 195, no. 3, pp. 877–882, 2010.

[155] Y. Li, M. Abdel-Monem, R. Gopalakrishnan, M. Berecibar, E. Nanini-Maury, N. Omar, P. van den Bossche, and J. Van Mierlo, "A quick on-line state of health estimation method for li-ion battery with incremental capacity curves processed by gaussian filter," *Journal of Power Sources*, vol. 373, pp. 40–53, 2018.

[156] T. Shibagaki, Y. Merla, and G. J. Offer, "Tracking degradation in lithium iron phosphate batteries using differential thermal voltammetry," *Journal of Power Sources*, vol. 374, pp. 188–195, 2018.

[157] M. Berecibar, M. Garmendia, I. Gandiaga, J. Crego, and I. Villarreal, "State of health estimation algorithm of lifepo4 battery packs based on differential voltage curves for battery management system application," *Energy*, vol. 103, pp. 784–796, 2016.

[158] J. Zhu, M. S. D. Darma, M. Knapp, D. R. Sørensen, M. Heere, Q. Fang, X. Wang, H. Dai, L. Mereacre, A. Senyshyn, *et al.*, "Investigation of lithium-ion battery degradation mechanisms by combining differential voltage analysis and alternating current impedance," *Journal of Power Sources*, vol. 448, p. 227575, 2020.

[159] S. Zhang, X. Guo, X. Dou, and X. Zhang, "A rapid online calculation method for state of health of lithium-ion battery based on coulomb counting method and differential voltage analysis," *Journal of Power Sources*, vol. 479, p. 228740, 2020.

[160] Q. Zhang, X. Li, Z. Du, and Q. Liao, "Aging performance characterization and state-of-health assessment of retired lithium-ion battery modules," *Journal of Energy Storage*, vol. 40, p. 102743, 2021.

[161] C. Weng, J. Sun, and H. Peng, "A unified open-circuit-voltage model of lithium-ion batteries for state-of-charge estimation and state-of-health monitoring," *Journal of power Sources*, vol. 258, pp. 228–237, 2014.

[162] L. Wang, X. Zhao, L. Liu, and C. Pan, "State of health estimation of battery modules via differential voltage analysis with local data symmetry method," *Electrochimica acta*, vol. 256, pp. 81–89, 2017.

[163] L. Wang, C. Pan, L. Liu, Y. Cheng, and X. Zhao, "On-board state of health estimation of LiFePO4 battery pack through differential voltage analysis," *Applied energy*, vol. 168, pp. 465–472, 2016.

[164] X. Hu, W. Liu, X. Lin, and Y. Xie, "A comparative study of control-oriented thermal models for cylindrical li-ion batteries," *IEEE Transactions on Transportation Electrification*, vol. 5, no. 4, pp. 1237–1253, 2019.

[165] G. L. Plett, "Extended kalman filtering for battery management systems of LiPB-based HEV battery packs: Part 3. state and parameter estimation," *Journal of Power sources*, vol. 134, no. 2, pp. 277–292, 2004.

[166] J. Li, N. Lotfi, R. G. Landers, and J. Park, "A single particle model for lithium-ion batteries with electrolyte and stress-enhanced diffusion physics," *Journal of The Electrochemical Society*, vol. 164, no. 4, p. A874, 2017.

[167] J. Li, R. G. Landers, and J. Park, "A comprehensive single-particle-degradation model for battery state-of-health prediction," *Journal of Power Sources*, vol. 456, p. 227950, 2020.

[168] Y. Gao, X. Zhang, J. Yang, and B. Guo, "Estimation of state-of-charge and state-of-health for lithium-ion degraded battery considering side reactions," *Journal of the electrochemical society*, vol. 165, no. 16, p. A4018, 2018.

[169] Y. Bi, Y. Yin, and S.-Y. Choe, "Online state of health and aging parameter estimation using a physics-based life model with a particle filter," *Journal of Power Sources*, vol. 476, p. 228655, 2020.

[170] T. R. Tanim and C. D. Rahn, "Aging formula for lithium ion batteries with solid electrolyte interphase layer growth," *Journal of Power Sources*, vol. 294, pp. 239–247, 2015.

[171] T. Mesbahi, N. Rizoug, P. Bartholomeüs, R. Sadoun, F. Khenfri, and P. Le Moigne, "Dynamic model of li-ion batteries incorporating electrothermal and ageing aspects for electric vehicle applications," *IEEE Transactions on industrial electronics*, vol. 65, no. 2, pp. 1298–1305, 2018.

[172] M. Ecker, J. B. Gerschler, J. Vogel, S. Käbitz, F. Hust, P. Dechent, and D. U. Sauer, "Development of a lifetime prediction model for lithium-ion batteries based on extended accelerated aging test data," *Journal of Power Sources*, vol. 215, pp. 248–257, 2012.

[173] M.-K. Tran, M. Mathew, S. Janhunen, S. Panchal, K. Raahemifar, R. Fraser, and M. Fowler, "A comprehensive equivalent circuit model for lithium-ion batteries, incorporating the effects of state of health, state of charge, and temperature on model parameters," *Journal of Energy Storage*, vol. 43, p. 103252, 2021.

[174] H. E. Perez, X. Hu, S. Dey, and S. J. Moura, "Optimal charging of li-ion batteries with coupled electro-thermal-aging dynamics," *IEEE Transactions on Vehicular Technology*, vol. 66, no. 9, pp. 7761–7770, 2017.

[175] X. Hu, Y. Zheng, X. Lin, and Y. Xie, "Optimal multistage charging of nca/graphite lithium-ion batteries based on electrothermal-aging dynamics," *IEEE Transactions on Transportation Electrification*, vol. 6, no. 2, pp. 427–438, 2020.

[176] A. Cordoba-Arenas, S. Onori, Y. Guezennec, and G. Rizzoni, "Capacity and power fade cycle-life model for plug-in hybrid electric vehicle lithium-ion battery cells containing blended spinel and layered-oxide positive electrodes," *Journal of Power Sources*, vol. 278, pp. 473–483, 2015.

[177] J. Wang, P. Liu, J. Hicks-Garner, E. Sherman, S. Soukiazian, M. Verbrugge, H. Tataria, J. Musser, and P. Finamore, "Cycle-life model for graphite-lifepo4 cells," *Journal of Power Sources*, vol. 196, no. 8, pp. 3942–3948, 2011.

[178] M. Swierczynski, D.-I. Stroe, A.-I. Stan, R. Teodorescu, and S. K. Kær, "Lifetime estimation of the nanophosphate $LiFePO_4/C$ battery chemistry used in fully electric vehicles," *IEEE Transactions on industry Applications*, vol. 51, no. 4, pp. 3453–3461, 2015.

[179] D.-I. Stroe, M. Świerczyński, A.-I. Stan, R. Teodorescu, and S. J. Andreasen, "Accelerated lifetime testing methodology for lifetime estimation of lithium-ion batteries used in augmented wind power plants," *IEEE Transactions on Industry Applications*, vol. 50, no. 6, pp. 4006–4017, 2014.

[180] D.-I. Stroe, M. Swierczynski, S. K. Kær, and R. Teodorescu, "Degradation behavior of lithium-ion batteries during calendar ageing—the case of the internal resistance increase," *IEEE Transactions on Industry Applications*, vol. 54, no. 1, pp. 517–525, 2017.

[181] F. Todeschini, S. Onori, and G. Rizzoni, "An experimentally validated capacity degradation model for li-ion batteries in PHEVs applications," *IFAC Proceedings Volumes*, vol. 45, no. 20, pp. 456–461, 2012.

[182] S. Grolleau, A. Delaille, H. Gualous, P. Gyan, R. Revel, J. Bernard, E. Redondo-Iglesias, J. Peter, and S. Network, "Calendar aging of commercial graphite/lifepo4 cell–predicting capacity fade under time dependent storage conditions," *Journal of Power Sources*, vol. 255, pp. 450–458, 2014.

[183] G. Zubi, R. Dufo-López, M. Carvalho, and G. Pasaoglu, "The lithium-ion battery: State of the art and future perspectives," *Renewable and Sustainable Energy Reviews*, vol. 89, pp. 292–308, 2018.

[184] M. Jafari, K. Khan, and L. Gauchia, "Deterministic models of li-ion battery aging: It is a matter of scale," *Journal of Energy Storage*, vol. 20, pp. 67–77, 2018.

[185] A. Ahmadian, M. Sedghi, A. Elkamel, M. Fowler, and M. A. Golkar, "Plug-in electric vehicle batteries degradation modeling for smart grid studies: Review, assessment and conceptual framework," *Renewable and Sustainable Energy Reviews*, vol. 81, pp. 2609–2624, 2018.

[186] J. Tian, R. Xu, Y. Wang, and Z. Chen, "Capacity attenuation mechanism modeling and health assessment of lithium-ion batteries," *Energy*, vol. 221, p. 119682, 2021.

[187] T. Goh, M. Park, M. Seo, J. G. Kim, and S. W. Kim, "Capacity estimation algorithm with a second-order differential voltage curve for li-ion batteries with nmc cathodes," *Energy*, vol. 135, pp. 257–268, 2017.

[188] H. Pan, Z. Lü, H. Wang, H. Wei, and L. Chen, "Novel battery state-of-health online estimation method using multiple health indicators and an extreme learning machine," *Energy*, vol. 160, pp. 466–477, 2018.

[189] B. Jia, Y. Guan, and L. Wu, "A state of health estimation framework for lithium-ion batteries using transfer components analysis," *Energies*, vol. 12, no. 13, p. 2524, 2019.

[190] V. Klass, M. Behm, and G. Lindbergh, "A support vector machine-based state-of-health estimation method for lithium-ion batteries under electric vehicle operation," *Journal of Power Sources*, vol. 270, pp. 262–272, 2014.

[191] A. Nuhic, T. Terzimehic, T. Soczka-Guth, M. Buchholz, and K. Dietmayer, "Health diagnosis and remaining useful life prognostics of lithium-ion batteries using data-driven methods," *Journal of power sources*, vol. 239, pp. 680–688, 2013.

[192] D. Andre, C. Appel, T. Soczka-Guth, and D. U. Sauer, "Advanced mathematical methods of SOC and SOH estimation for lithium-ion batteries," *Journal of Power Sources*, vol. 224, pp. 20–27, 2013.

[193] A. Zenati, P. Desprez, and H. Razik, "Estimation of the SOC and the SOH of li-ion batteries, by combining impedance measurements with the fuzzy logic inference," in *IECON 2010-36th Annual Conference on IEEE Industrial Electronics Society*, pp. 1773–1778, IEEE, 2010.

[194] K. Yang, Z. Chen, Z. He, Y. Wang, and Z. Zhou, "Online estimation of state of health for the airborne li-ion battery using adaptive dekf-based fuzzy inference system," *Soft Computing*, pp. 1–10, 2020.

[195] D. Liu, J. Pang, J. Zhou, Y. Peng, and M. Pecht, "Prognostics for state of health estimation of lithium-ion batteries based on combination gaussian process functional regression," *Microelectronics Reliability*, vol. 53, no. 6, pp. 832–839, 2013.

[196] X. Qin, Q. Zhao, H. Zhao, W. Feng, and X. Guan, "Prognostics of remaining useful life for lithium-ion batteries based on a feature vector selection and relevance vector machine approach," in *2017 IEEE International Conference on Prognostics and Health Management (ICPHM)*, pp. 1–6, IEEE, 2017.

[197] Y. Che, Z. Deng, X. Lin, L. Hu, and X. Hu, "Predictive battery health management with transfer learning and online model correction," *IEEE Transactions on Vehicular Technology*, vol. 70, no. 2, pp. 1269–1277, 2021.

[198] Y. Fan, F. Xiao, C. Li, G. Yang, and X. Tang, "A novel deep learning framework for state of health estimation of lithium-ion battery," *Journal of Energy Storage*, vol. 32, p. 101741, 2020.

[199] S. Shen, M. Sadoughi, X. Chen, M. Hong, and C. Hu, "A deep learning method for online capacity estimation of lithium-ion batteries," *Journal of Energy Storage*, vol. 25, p. 100817, 2019.

[200] K. Kaur, A. Garg, X. Cui, S. Singh, and B. K. Panigrahi, "Deep learning networks for capacity estimation for monitoring soh of li-ion batteries for electric vehicles," *International Journal of Energy Research*, vol. 45, no. 2, pp. 3113–3128, 2021.

[201] W. Pan, X. Luo, M. Zhu, J. Ye, L. Gong, and H. Qu, "A health indicator extraction and optimization for capacity estimation of li-ion battery using incremental capacity curves," *Journal of Energy Storage*, vol. 42, p. 103072, 2021.

[202] J.-z. Kong, F. Yang, X. Zhang, E. Pan, Z. Peng, and D. Wang, "Voltage-temperature health feature extraction to improve prognostics and health management of lithium-ion batteries," *Energy*, vol. 223, p. 120114, 2021.

[203] Z. Deng, X. Hu, X. Lin, L. Xu, Y. Che, and L. Hu, "General discharge voltage information enabled health evaluation for lithium-ion batteries," *IEEE/ASME Transactions on Mechatronics*, 2020.

[204] P. Guo, Z. Cheng, and L. Yang, "A data-driven remaining capacity estimation approach for lithium-ion batteries based on charging health feature extraction," *Journal of Power Sources*, vol. 412, pp. 442–450, 2019.

[205] L. Liao and F. Köttig, "Review of hybrid prognostics approaches for remaining useful life prediction of engineered systems, and an application to battery life prediction," *IEEE Transactions on Reliability*, vol. 63, no. 1, pp. 191–207, 2014.

[206] J. Wei, G. Dong, and Z. Chen, "Remaining useful life prediction and state of health diagnosis for lithium-ion batteries using particle filter and support vector regression," *IEEE Transactions on Industrial Electronics*, vol. 65, no. 7, pp. 5634–5643, 2017.

[207] X. Zheng and H. Fang, "An integrated unscented kalman filter and relevance vector regression approach for lithium-ion battery remaining useful life and short-term capacity prediction," *Reliability Engineering & System Safety*, vol. 144, pp. 74–82, 2015.

[208] Z. Ma, R. Yang, and Z. Wang, "A novel data-model fusion state-of-health estimation approach for lithium-ion batteries," *Applied energy*, vol. 237, pp. 836–847, 2019.

[209] D. Liu, X. Yin, Y. Song, W. Liu, and Y. Peng, "An on-line state of health estimation of lithium-ion battery using unscented particle filter," *Ieee Access*, vol. 6, pp. 40990–41001, 2018.

[210] S. Li, H. He, C. Su, and P. Zhao, "Data driven battery modeling and management method with aging phenomenon considered," *Applied Energy*, vol. 275, p. 115340, 2020.

[211] C. Hu, B. D. Youn, P. Wang, and J. T. Yoon, "Ensemble of data-driven prognostic algorithms for robust prediction of remaining useful life," *Reliability Engineering & System Safety*, vol. 103, pp. 120–135, 2012.

[212] Z. Chen, Q. Xue, R. Xiao, Y. Liu, and J. Shen, "State of health estimation for lithium-ion batteries based on fusion of autoregressive moving average model and elman neural network," *IEEE Access*, vol. 7, pp. 102662–102678, 2019.

[213] X. Feng, J. Li, M. Ouyang, L. Lu, J. Li, and X. He, "Using probability density function to evaluate the state of health of lithium-ion batteries," *Journal of Power Sources*, vol. 232, pp. 209–218, 2013.

[214] B. Gou, Y. Xu, and X. Feng, "State-of-health estimation and remaining-useful-life prediction for lithium-ion battery using a hybrid data-driven method," *IEEE Transactions on Vehicular Technology*, vol. 69, no. 10, pp. 10854–10867, 2020.

[215] Y. Song, D. Liu, H. Liao, and Y. Peng, "A hybrid statistical data-driven method for on-line joint state estimation of lithium-ion batteries," *Applied Energy*, vol. 261, p. 114408, 2020.

[216] M. Dubarry and D. Beck, "Big data training data for artificial intelligence-based li-ion diagnosis and prognosis," *Journal of Power Sources*, vol. 479, p. 228806, 2020.

[217] K. S. Mayilvahanan, K. J. Takeuchi, E. S. Takeuchi, A. C. Marschilok, and A. C. West, "Supervised learning of synthetic big data for li-ion battery degradation diagnosis," *Batteries & Supercaps*, vol. 5, no. 1, p. e202100166, 2022.

[218] M. Kabir and D. E. Demirocak, "Degradation mechanisms in li-ion batteries: a state-of-the-art review," *International Journal of Energy Research*, vol. 41, no. 14, pp. 1963–1986, 2017.

[219] B. Stiaszny, J. C. Ziegler, E. E. Krauss, J. P. Schmidt, and E. Ivers-Tiffée, "Electrochemical characterization and post-mortem analysis of aged LiMn2O4–Li (Ni0. 5Mn0. 3Co0. 2) O2/graphite lithium ion batteries. part i: Cycle aging," *J Power Sources*, vol. 251, pp. 439–450, 2014.

[220] S. S. Zhang, K. Xu, and T. Jow, "Study of the charging process of a LiCoO2-based li-ion battery," *Journal of Power Sources*, vol. 160, no. 2, pp. 1349–1354, 2006.

[221] A. M. Colclasure, K. A. Smith, and R. J. Kee, "Modeling detailed chemistry and transport for solid-electrolyte-interface (SEI) films in li–ion batteries," *Electrochimica Acta*, vol. 58, pp. 33–43, 2011.

[222] J. M. Reniers, G. Mulder, and D. A. Howey, "Review and performance comparison of mechanical-chemical degradation models for lithium-ion batteries," *Journal of The Electrochemical Society*, vol. 166, no. 14, p. A3189, 2019.

[223] U. Janakiraman, T. R. Garrick, and M. E. Fortier, "Lithium plating detection methods in li-ion batteries," *Journal of the Electrochemical Society*, vol. 167, no. 16, p. 160552, 2020.

[224] X. Zhang, J. Lu, S. Yuan, J. Yang, and X. Zhou, "A novel method for identification of lithium-ion battery equivalent circuit model parameters considering electrochemical properties," *Journal of Power Sources*, vol. 345, pp. 21–29, 2017.

[225] G. Vennam and A. Sahoo, "Simultaneous state and parameter estimation of lithium-ion battery: An observer based approach," in *2019 American Control Conference (ACC)*, pp. 4485–4490, IEEE, 2019.

[226] A. Sahoo and V. Narayanan, "Differential-game for resource aware approximate optimal control of large-scale nonlinear systems with multiple players," *Neural Networks*, vol. 124, pp. 95–108, 2020.

[227] W. Yan, B. Zhang, G. Zhao, S. Tang, G. Niu, and X. Wang, "A battery management system with a lebesgue-sampling-based extended kalman filter," *IEEE transactions on industrial electronics*, vol. 66, no. 4, pp. 3227–3236, 2018.

[228] L. Zheng, J. Zhu, D. D.-C. Lu, G. Wang, and T. He, "Incremental capacity analysis and differential voltage analysis based state of charge and capacity estimation for lithium-ion batteries," *Energy*, vol. 150, pp. 759–769, 2018.

[229] X. Tang, X. Mao, J. Lin, and B. Koch, "Li-ion battery parameter estimation for state of charge," in *American Control Conference (ACC), 2011*, pp. 941–946, IEEE, 2011.

[230] H. Dai, X. Wei, and Z. Sun, "State and parameter estimation of a hev li-ion battery pack using adaptive kalman filter with a new soc-ocv concept," in *Measuring Technology and Mechatronics Automation, 2009. ICMTMA'09. International Conference on*, vol. 2, pp. 375–380, IEEE, 2009.

[231] H. He, R. Xiong, X. Zhang, F. Sun, and J. Fan, "State-of-charge estimation of the lithium-ion battery using an adaptive extended kalman filter based on an improved thevenin model," *IEEE Transactions on Vehicular Technology*, vol. 60, no. 4, pp. 1461–1469, 2011.

[232] J. S. Goud, R. Kalpana, and B. Singh, "An online method of estimating state of health of a li-ion battery," *IEEE Transactions on Energy Conversion*, vol. 36, no. 1, pp. 111–119, 2020.

[233] C. Park and A. K. Jaura, *Dynamic thermal model of li-ion battery for predictive behavior in hybrid and fuel cell vehicles*. SAE international, 2011.

[234] X. Lin, H. E. Perez, S. Mohan, J. B. Siegel, A. G. Stefanopoulou, Y. Ding, and M. P. Castanier, "A lumped-parameter electro-thermal model for cylindrical batteries," *Journal of Power Sources*, vol. 257, pp. 1–11, 2014.

[235] H. Pang, L. Guo, L. Wu, J. Jin, F. Zhang, and K. Liu, "A novel extended kalman filter-based battery internal and surface temperature estimation based on an improved electro-thermal model," *Journal of Energy Storage*, vol. 41, p. 102854, 2021.

[236] N. Guo, X. Zhang, Y. Zou, L. Guo, and G. Du, "Real-time predictive energy management of plug-in hybrid electric vehicles for coordination of fuel economy and battery degradation," *Energy*, vol. 214, p. 119070, 2021.

[237] K. Liu, C. Zou, K. Li, and T. Wik, "Charging pattern optimization for lithium-ion batteries with an electrothermal-aging model," *IEEE Transactions on Industrial Informatics*, vol. 14, no. 12, pp. 5463–5474, 2018.

[238] A. Cordoba-Arenas, S. Onori, and G. Rizzoni, "A control-oriented lithium-ion battery pack model for plug-in hybrid electric vehicle cycle-life studies and system design with consideration of health management," *Journal of Power Sources*, vol. 279, pp. 791–808, 2015.

[239] M. Al-Gabalawy, K. Mahmoud, M. M. Darwish, J. A. Dawson, M. Lehtonen, and N. S. Hosny, "Reliable and robust observer for simultaneously estimating state-of-charge and state-of-health of lifepo4 batteries," *Applied Sciences*, vol. 11, no. 8, p. 3609, 2021.

[240] NASA, "Development of battery packs for space applications."

[241] G. Vennam, A. Sahoo, and S. Ahmed, "A novel coupled electro-thermal-aging model for simultaneous soc, soh, and parameter estimation of lithium-ion batteries," in *2022 American Control Conference (ACC)*, pp. 5259–5264, IEEE, 2022.

[242] L. Lam, P. Bauer, and E. Kelder, "A practical circuit-based model for li-ion battery cells in electric vehicle applications," in *Telecommunications Energy Conference (INTELEC), 2011 IEEE 33rd International*, pp. 1–9, IEEE, 2011.

[243] X. Chen, W. Shen, M. Dai, Z. Cao, J. Jin, and A. Kapoor, "Robust adaptive sliding-mode observer using rbf neural network for lithium-ion battery state of charge estimation in electric vehicles," *IEEE Transactions on Vehicular Technology*, vol. 65, no. 4, pp. 1936–1947, 2016.

[244] H. E. Perez, J. B. Siegel, X. Lin, A. G. Stefanopoulou, Y. Ding, and M. P. Castanier, "Parameterization and validation of an integrated electro-thermal cylindrical lfp battery model," in *Dynamic Systems and Control Conference*, vol. 45318, pp. 41–50, American Society of Mechanical Engineers, 2012.

[245] M. Gholizadeh and F. R. Salmasi, "Estimation of state of charge, unknown nonlinearities, and state of health of a lithium-ion battery based on a comprehensive unobservable model," *IEEE Transactions on Industrial Electronics*, vol. 61, no. 3, pp. 1335–1344, 2013.

[246] X. Bian, L. Liu, J. Yan, Z. Zou, and R. Zhao, "An open circuit voltage-based model for state-of-health estimation of lithium-ion batteries: Model development and validation," *Journal of Power Sources*, vol. 448, p. 227401, 2020.

[247] J.-M. Tarascon and M. Armand, "Issues and challenges facing rechargeable lithium batteries," in *Materials For Sustainable Energy: A Collection of Peer-Reviewed Research and Review Articles from Nature Publishing Group*, pp. 171–179, World Scientific, 2011.

[248] G. Vennam and A. Sahoo, "A dynamic soh-coupled lithium-ion cell model for state and parameter estimation," *IEEE Transactions on Energy Conversion*, 2022.

[249] B. Xia, Y. Shang, T. Nguyen, and C. Mi, "A correlation based fault detection method for short circuits in battery packs," *Journal of Power Sources*, vol. 337, pp. 1–10, 2017.

[250] B. Xia, Z. Chen, C. Mi, and B. Robert, "External short circuit fault diagnosis for lithium-ion batteries," in *Transportation Electrification Conference and Expo (ITEC), 2014 IEEE*, pp. 1–7, 2014.

[251] Z. Gao, C. Cecati, and S. X. Ding, "A survey of fault diagnosis and fault-tolerant techniques—part i: Fault diagnosis with model-based and signal-based approaches," *IEEE Transactions on Industrial Electronics*, vol. 62, no. 6, pp. 3757–3767, 2015.

[252] G. Dong and M. Lin, "Model-based thermal anomaly detection for lithium-ion batteries using multiple-model residual generation," *Journal of Energy Storage*, vol. 40, p. 102740, 2021.

[253] A. Sidhu, A. Izadian, and S. Anwar, "Adaptive nonlinear model-based fault diagnosis of li-ion batteries," *IEEE Transactions on Industrial Electronics*, vol. 62, no. 2, pp. 1002–1011, 2014.

[254] D. Belov and M.-H. Yang, "Failure mechanism of li-ion battery at overcharge conditions," *Journal of Solid State Electrochemistry*, vol. 12, no. 7, pp. 885–894, 2008.

[255] X. Zhang, M. M. Polycarpou, and T. Parisini, "A robust detection and isolation scheme for abrupt and incipient faults in nonlinear systems," *IEEE transactions on automatic control*, vol. 47, no. 4, pp. 576–593, 2002.

[256] H. K. Khalil, *Nonlinear control*, vol. 406. Pearson New York, 2015.

[257] J. M. Steele, *The Cauchy-Schwarz master class: an introduction to the art of mathematical inequalities*. Cambridge University Press, 2004.

[258] J. Wei, G. Dong, and Z. Chen, "Model-based fault diagnosis of lithium-ion battery using strong tracking extended kalman filter," *Energy Procedia*, vol. 158, pp. 2500–2505, 2019.

VITA

Geetika Vennam

Candidate for the Degree of

Doctor of Philosophy

Dessertation: LITHIUM-ION CELL MODELING, STATE ESTIMATION, AND FAULT DETECTION CONSIDERING STATE OF HEALTH FOR BATTERY MANAGEMENT SYSTEMS

Major Field: Electrical Engineering

Biographical:

Education:

Completed the requirements for the Doctor of Philosophy in Electrical Engineering at Oklahoma State University, Stillwater, Oklahoma in December, 2022.

Completed the requirements for the Master of Science in Electrical Engineering at Oklahoma State University, Stillwater, Oklahoma in 2017.

Completed the requirements for the Master of Technology in Power Systems at SASTRA University, Thanjavur, India in 2014.

Completed the requirements for the Bachelor of Technology in Electrical and Electronics Engineering at SASTRA University, Thanjavur, India in 2014.

Experience:

Assistant System Engineer at Tata Consultancy Services Limited (TCS), 2014-2015

Professional Membership:

IEEE Student Member